High-intracavity-power thin-disk laser for the alignment of molecules

Dissertation

zur Erlangung des Doktorgrades
des Department Physik
der Universität Hamburg

vorgelegt von

Bastian Deppe

aus München

Hamburg
2018

Gutachter der Dissertation:	Dr. habil. C. Kränkel Prof. Dr. J. Küpper
Gutachter der Disputation:	Dr. habil. C. Kränkel Prof. Dr. J. Küpper Prof. Dr. G. Huber Prof. Dr. P. Schmelcher Prof. Dr. U. Frühling
Datum der Disputation:	22.11.2018
Vorsitzender des Promotionsausschusses:	Prof. Dr. P. Schmelcher
Dekan der Fakultät für Mathematik, Informatik und Naturwissenschaften:	Prof. Dr. H. Graener

Abstract

The subject of this thesis was the development of a thin-disk laser with a continuous wave intracavity intensity of more than $10^{10}\,\mathrm{W\,cm^{-2}}$ for the adiabatic alignment of molecules. In particular, this necessitates an intracavity power of more than 100 kW, an internal focus with a radius of 20 µm, a well-defined and stable polarization, and benefits from fundamental transverse mode operation. For this purpose, ytterbium-doped host materials were compared in various resonators, exploring their losses and their suitability for such a laser system. The study focused on the possible implementation of such a laser setup, notably for pump powers below 500 W, which allow resonator losses of approx. 5×10^{-3}. A characterization of Yb:$Y_3Al_5O_{12}$ and Yb:Lu_2O_3 in an efficient and short linear multi-transverse-mode resonator revealed resonator internal losses in the order of 2×10^{-4}. No dependency on the gain material could be resolved. Measurements of the losses with more than 20 thin disks pointed towards losses originating at their surface. An intracavity power of 130 kW could be demonstrated. This corresponds to an enhancement by a factor of 2500 with respect to the incident pump power of 54 W. Further scaling of the pump intensity was restrained by optical damage, mostly in the form of nodular point defects, which were observed at optics and disks. The optical damage is believed to be caused by defects in the highly reflective coatings. The resonator internal losses for linear single-transverse-mode resonators increased up to 9×10^{-4}, which might have been caused by additional diffraction losses. The application of a Brewster window to ensure a stable polarization additionally led to an increase of losses to 1.5×10^{-3}. Supposedly, it was caused by stress-induced birefringence in the isotropic gain materials. This induced a rotation of the polarization and eventually contributed to significant reflection losses at the Brewster plate. Additionally, an intrinsic polarization was measured, which was less stable than the before mentioned polarization but avoided additional losses. Similar behaviors were detected for folded resonators. Those were more suitable for acquiring a tight internal focus. Imaging the Rayleigh scattering at atmospheric molecules allowed an in vitro determination of the caustic. Here, an intracavity-focus-radius in the order of 20 µm was measured. However, resonator losses of approx. 5 % and the prevalent optical damage obstructed the achievement of the required intracavity powers with the available pump powers. Comparisons and calculations of possible losses suggested the diffraction losses, caused by astigmatic distortions of the disks, being responsible. To accomplish the goals, a combination of a decrease of losses and an increase of the pump power might be necessary.

Kurzfassung

Der Gegenstand dieser Arbeit war die Entwicklung eines Dauerstrich-Scheibenlasers mit resonatorinternen Intensitäten von mehr als $10^{10}\,\mathrm{W\,cm^{-2}}$ zur adiabatischen Ausrichtung von Molekülen. Für diesen Zweck wird eine resonatorinterne Leistung von mehr als 100 kW, ein interner Fokus mit einem Radius von 20 µm und eine definierte Polarisation benötigt. Zusätzlich wird von der Oszillation auf der Grundmode profitiert. Ytterbium dotierte Wirtskristalle wurden bei geringen Pumpleistungen in verschiedenen Resonatoren hinsichtlich intrinsischer Verluste und ihrer generellen Eignung für solch ein Lasersystem verglichen. Die Priorität lag dabei in der Entwicklung eines Lasersystems bei Pumpleistungen von weniger als 500 W. Diese tolerieren Resonatorverluste von ca. 5×10^{-3}. Eine Charakterisierung von Yb:$Y_3Al_5O_{12}$ und Yb:Lu_2O_3 in einem effizienzoptimierten Resonator ergab Verluste von ca. 2×10^{-4}. Eine signifikante Abhängigkeit vom Lasermaterial konnte hierbei nicht festgestellt werden. Vergleichende Untersuchungen der Verluste an mehr als 20 Scheiben deuteten jedoch auf Oberflächenverluste, z. B. an dielektrischen Beschichtungen hin. Es konnten resonatorinterne Leistungen von mehr als 130 kW demonstriert werden. Dies entspricht einer 2500-fachen Überhöhung für eine Pumpleistung von 54 W. Eine weitere Steigerung der Pumpintensität war aufgrund optischer Defekte nicht möglich. Die gemessenen Resonatorverluste erhöhten sich im Grundmodenbetrieb auf 9×10^{-4}. Verantwortlich hierfür sind möglicherweise Beugungsverluste an der Scheibe. Resonatoren mit einem Brewster-Element zeigten ebenfalls erhöhte Verluste von bis zu 1.5×10^{-3}, vermutlich verursacht durch stressinduzierte Depolarisation in der Laserscheibe, welche zu einer partiellen Rotation des elektrischen Feldes führte. Zusätzlich konnte ohne die Nutzung von zusätzlichen optischen Elementen eine intrinsische Polarisation mit einem niedrigeren Extinktionsverhältnis und geringerer Stabilität festgestellt werden. Vergleichbare Verluste und Effekte konnten dabei auch für gefaltete Resonatoren beobachtet werden, welche sich als besser geeignet herausstellten, um einen internen Fokus im Resonator zu erzielen. In einem zu diesem Zweck entwickelten Resonator konnte anhand der Rayleigh Streuung an atmosphärischen Molekülen der resonatorinterne Strahlverlauf gemessen werden. Hierbei wurde eine Strahltaille von 20 µm bestimmt. Hohe Resonatorverluste von mehr als 5 % verhinderten ein Erreichen der benötigten internen Leistung. Diese Verluste wurden vermutlich durch Beugung aufgrund von astigmatischen Störungen in der Laserscheibe verursacht. Daher werden eine Reduzierung der Verluste und eine Erhöhung der Pumpleistung für weitere Experimente empfohlen.

Contents

1. Introduction

Movies display and allow to unravel dynamics. Depending on the spatial and temporal resolution of the film camera, even ultrafast dynamics of atoms and electrons in molecules, proteins, or in larger particles like viruses can be captured.

120 years ago, one of the first true motion pictures was recorded by the Lumiere brothers in France.[1] "Sortie de l'usine Lumiere de Lyon" was shot in black and white on 35 mm film with a rather poor temporal resolution of 16 frames per second. This frame rate allowed to resolve temporal dynamics, which develop significantly over time spans longer than approx. 60 ms. For processes which take place on faster timescales only the initial and the final state were determined; back then, the intermediate dynamics and states remained hidden.

The intermediate states and dynamics occurring in chemical reactions are of great interest for chemistry [1, 2]. Femtochemistry comprises the area of physical chemistry which occurs in the femtosecond range. In the low femtosecond regime vibrations of the atomic nucleus, which extend spatially over distances in the order of 100 pm, can be investigated. Extending the time spans up to approx. 100 fs still permits to observe some molecular vibrations. The detailed spatial and temporal insight into such processes allows the understanding of many secrets of life, which are hidden behind numberless chemical reactions.

Movies with atomic and femtosecond resolutions are called molecular movies. To record a molecular movie there are two essential key requirements. The dimensions of interest can be in the order of 100 pm. In general, this resolution can be obtained with methods like scanning transmission electron microscopes, which are suitable for the investigation of static spatial structures. However, to record a three-dimensional (3d) molecular movie, diffraction based methods are necessary [3–5]. Diffraction imaging requires a coherent particle or light source with a wavelength short enough to resolve the structures of interest. The particle or photon flux must be sufficient to obtain a high signal to noise ratio. To achieve a suitable temporal resolution the diffraction source must illuminate the sample with pulses, whose durations are short enough to unravel the dynamics of interest.

To investigate processes on a sub-fs timescale, mainly attosecond based high harmonic generation (HHG) experiments were able to probe atomic processes with attosecond resolution. However, the common repetition rates of such HHG-systems are nowadays not comparable with modern x-ray light sources and the photon flux is still unreasonably low for efficient operation. Electron and x-ray diffraction-based sources can provide beams with wavelengths short enough to resolve atomic structures and with pulse durations below 100 fs [6]. In this day and age, especially free-electron lasers (FELs) and synchrotrons can

[1] Leland Stanford Muybridge (Sallie Gardner at a Gallop, 1878) and Louis de Prince (Roundhay Garden Scene, 1888) are only two of further mentionable directors of this early era of film.

provide short bunches of coherent radiation at MHz repetition rates. Future generations of energy recovering linear accelerators might be operated at a 1 GHz repetition rate [7].

These days, the diffraction pattern of a single molecule suffers from a low signal-to-noise ratio (SNR). In principle, this can be enhanced by two different approaches. The diffraction source can be optimized to cause more scattered photons, albeit electronic damage and too long x-ray pulse durations may constitute limitations [8]. Alternatively, the total signal can be amplified by the usage of an ensemble of molecules in the gas-phase instead of single particles. However, when a diffraction image is generated by such an ensemble, the equality of all molecules must be ensured. Otherwise a decrease of the local contrast could be observed and the diffraction pattern would smear out. In this context, equality denotes quantum properties like internal states as well as the angular alignment of single molecules with respect to a fixed axis in the laboratory. An equal alignment and orientation of all single entities from an ensemble increases the local SNR.

Molecules can be aligned by strong electric fields. In principle, there are three distinctive ways to do so. The nonadiabatic alignment relies on laser pulses with a pulse duration much shorter than the rotational period. The pulse leaves a system in a coherent superposition of rotational states. In this case, the alignment of the molecular ensemble occurs periodically under field-free conditions with a period corresponding to the rotational period of the molecules [9]. In contrast, the alignment in the continuous wave (CW) limit (termed adiabatic alignment), i.e., for pulse durations much longer than the rotational period, directly follows the envelope of the electric field. During the laser's turning-on phase, each eigen state of the field-free Hamiltonian evolves adiabatically into the corresponding state of the complete Hamiltonian [10]. Once the laser has been turned off, the alignment is abolished. In addition, the intermediate alignment with pulse durations between these limits can be placed between the adiabatic and the impulsive alignment. To reach molecular alignment, the laser system has to grant several requirements. Depending on the rotational period and polarizability of the molecule, intensities typically larger than $1 \times 10^{10}\,\mathrm{W\,cm^{-2}}$ are required and the electric field must be polarized [11, 12]. The specific kind of polarization depends on the molecule. While the alignment of symmetric molecules only requires a linear polarization of the electromagnetic laser field, other kinds of molecules might need an elliptical one.

Why does the necessary electric field intensity set such high requirements to the alignment laser-system? To understand this, one must consider the planned application of x-ray diffraction experiments. First, the molecular or biological samples could be destroyed by high x-ray intensities, which would alter the diffraction images. However, diffraction before destruction or the usage of a low intensity [13, 14] can prevent this. As the alignment laser must provide a volume of homogenously aligned molecules to the x-ray source, this subsequently causes further requirements regarding the minimum focus radius and the laser's Rayleigh length. Second, as mentioned earlier, the repetition rate of x-ray sources can be in magnitudes of MHz and prospectively even GHz. Time-efficient measurements therefore demand aligned molecules available at the repetition rate of the x-ray sources. The required laser pulse duration for adiabatic alignment must be longer than the rotational period of

the samples, which can already possess nanoseconds for large molecules. Considering the required long alignment laser pulse durations of nanoseconds and the envisioned x-ray repetition rates, a continuous alignment laser source is required. The latter would further provide the flexibility to work with arbitrary x-ray sources, independent from their specific and variable repetition rate.

Neglecting the duty cycle of the x-ray sources, this yields into a necessary average optical power of 1 MW. It is reasonable to assume that laser sources with such a direct output power will not be available in the future. The issue of high average power can be dealt with by accessing the field intensities inside of a cavity instead of outside in an outcoupled laser beam. In a so-called enhancement cavity, which in fact every common laser resonator constitutes, high average intracavity powers can be accessed for low resonator losses at rather low average pump powers for the gain medium. Therefore, the gain material must have low intrinsic losses and oscillate at wavelengths which are non-resonant to transitions in the molecules of interest.

A laser scheme seeming suitable for such a purpose is the thin-disk laser (TDL). The gain medium, acting as an active mirror, typically has a thickness of only a few 100 µm. This allows for a very efficient cooling from its rear side. The necessary power scaling can be achieved by increasing the pump spot diameter, while the pump absorption of the thin gain medium is ensured by a multi-pass pumping scheme onto the active medium.

In this thesis, the feasibility and development of a CW-TDL-system, suitable for the intracavity alignment of gas-phase molecules is presented. The general concept is depicted in Figure 1.1. Such a system will allow for a continuous adiabatic alignment of molecules. It is further conceivable to use such a setup for the trapping and guiding of molecules and many more strong-field physics experiments, such as CW HHG. The theoretical frame work is introduced in Chapter 2, including a brief introduction into the required electric field intensities for the alignment of small gas-phase molecules and summarizing the different necessary requirements for CW TDL based alignment. Thereafter, a physical model of a solid-state laser, in particular a TDL, is presented. The chapter ends with a focus on possible resonator internal losses and a discussion of the realizability of such a TDL based system. Chapter 3 describes and compares the optical and thermomechanical properties of two different host materials, Yb:$Y_3Al_5O_{12}$ and Yb:Lu_2O_3, which were tested as low-loss gain materials for the laser experiments described in Chapter 4 and 5. Chapter 4 contains the details of the used experimental setup, shortly describing the vacuum chamber but mainly focussing on the laser system. The description of the latter covers the used optical elements, the pump diodes as well as the different resonators. In Chapter 5 the results of the performed measurements are presented and discussed. Intrinsic losses of different gain materials and resonator geometries are compared. The final Chapter 6 provides a conclusion and an outlook for the suggested development towards an MW intracavity power CW laser for molecular alignment.

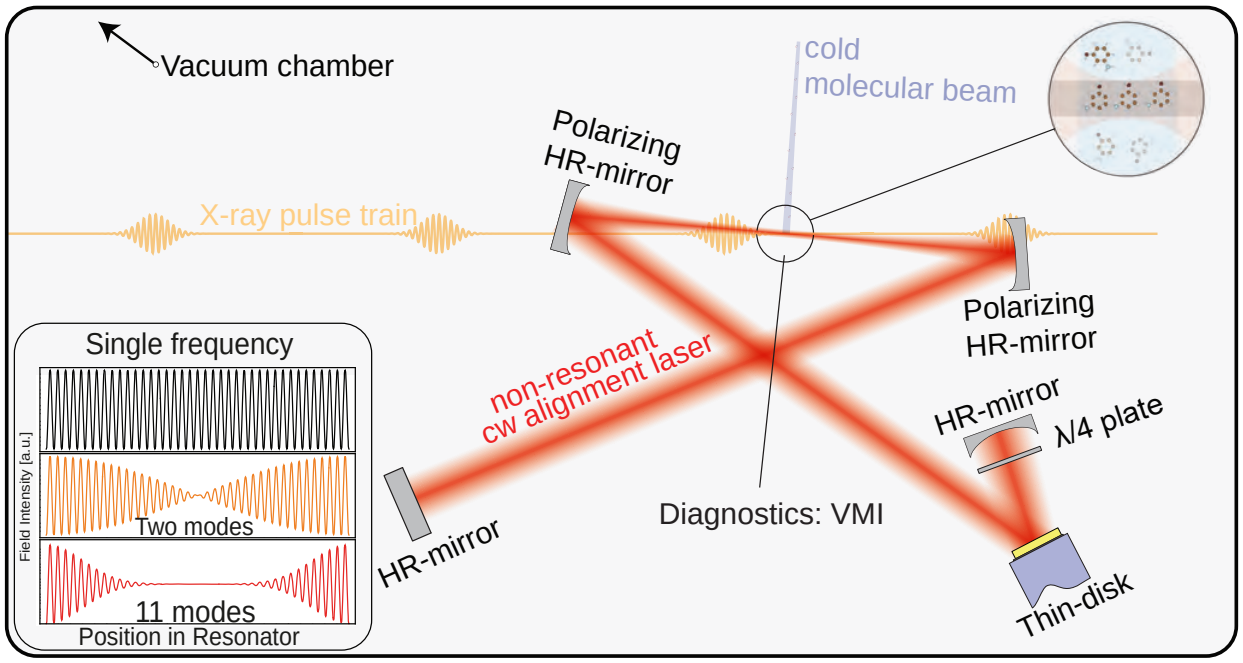

Figure 1.1: Concept for CW alignment of molecules: A thin-disk pump module is part of a resonator with high mirror reflectivities, which are required for a high intracavity power at moderate pump powers. The complete setup is integrated into a vacuum chamber. The required intensity is ensured by a suitable combination of mirrors and resonator design. The x-ray and the laser beam are colinearly overlapped, with a molecular beam perpendicular to them. To achieve a defined laser polarization, mirrors with polarization-dependent reflectivity or optical windows at the Brewster angle could be used. In the resonator internal focus, the x-ray pulse, the cold molecular beam and the laser overlap. The cold molecules are adiabatically aligned for sufficient field intensities. The alignment is probed by diagnostics like VMI. Inset: Mode averaging of a broad gain bandwidth end-pumped laser in the resonator yields to a smooth intensity distribution.

2. Continuous adiabatic alignment

This chapter is divided as follows. First, a basic concept of molecule alignment by the use of lasers is introduced. Second, the requirements, arising from this theory, on a CW laser are discussed. Third, a physical model of a TDL is presented with details on different loss mechanisms. Finally, the feasibility of CW laser based adiabatic alignment with a TDL is examined.

2.1 Alignment of gas-phase molecules

Tomografic reconstruction approaches and photoelectron holography experiments at molecular samples typically require a high degree of aligned molecules [15, 16]. Diffractive imaging of aligned molecules benefits from the use of molecular ensembles, i.e., due to the low diffraction signal of single molecules [4, 17]. This corresponds to a narrow statistical distribution of the physical properties which manifests itself in the temperature of the ensemble, but other properties like spatial orientation, alignment and the occupied quantum state must be controlled and selected as well [18, 19].

One of the birthplaces of the separation of quantum states can be found in Hamburg, where Wrede, a graduate student of Stern recognized the deflection of molecular beams in an inhomogeneous electric field [20]. Today's molecular samples can be cooled down by a supersonic expansion [21] into a molecular beam [22], with translational and rotational temperatures below 1 K [21, 23]. This low internal temperature leads to an occupation of only a few quantum states. Molecules in different quantum states can subsequently be separated by an external electric field. This is possible due to the quantum state depending interaction of the neutral molecule's effective dipole moment with an inhomogeneous direct current (DC) electric field [18, 24], called Stark effect. The required field strengths for a sufficient degree of spatial separation are in the order of 100 kV/cm.

Already the selection of lower rotational quantum states out of a molecular beam generates a spatial alignment of the molecular ensemble. A scheme of the differences between an isotropic, an aligned, and an oriented ensemble of molecules is illustrated in Figure 2.1. An early concept to brute-force orient molecules was published by Loesch and Remscheidt [25] and independently by Friedrich and Herschbach [26]. In both publications, strong DC fields are used to align the molecule's dipole moments along the electric field lines. This was experimentally demonstrated in the same decade [27]. The approach is known as brute-force orientation [28]. Molecules can also be aligned in strong polarized alternating current (AC) electric fields. This results from the interaction between the molecular anisotropic polarizability and a non-resonant electric field, where an induced dipole moment forces the molecules to align along the field's polarization. A laser could provide fields of sufficient

strength. This was demonstrated in the early 90s [29] with a Nd:$Y_3Al_5O_{12}$ laser (30 ps, $10^{15}\,\mathrm{W\,cm^{-2}}$). For small cold molecules, field intensities in the order of $10^{10}\,\mathrm{W\,cm^{-2}}$ to $10^{12}\,\mathrm{W\,cm^{-2}}$ are adequate. In particular, this depends on the rotational temperature of the molecular beam [11, 12]. Previously, those high field intensities were typically delivered by pulsed injected-seeded Nd:$Y_3Al_5O_{12}$ lasers, with repetition rates in the order of 10 Hz. Nowadays these field strengths and high degrees of alignment can be obtained in experiments at kHz repetition rates with amplified titanium-sapphire laser systems [15, 30].

The duration τ_{las} of a Gaussian laser pulse, in which the electric field is applied to the molecules, defines different types of alignment: adiabatic, intermediate, and impulsive alignment. For time spans $\tau_{rot} \ll \tau_{las}$ much longer than the rotational period of the molecule, the alignment is called adiabatic, as it follows the envelope of the laser intensity. The rotational period is in the order of 10×10^{-12} s for simple diatomic molecules [31] and up to nanoseconds and longer for larger molecules [32, 33]. The intermediate regime $\tau_{rot} \approx \tau_{las}$ can behave similarly to the adiabatic one during the pulse [33], while the impulsive alignment with $\tau_{rot} \gg \tau_{las}$ differs from the adiabatic alignment by periodic revivals of the angular confinement after the field has been turned off.

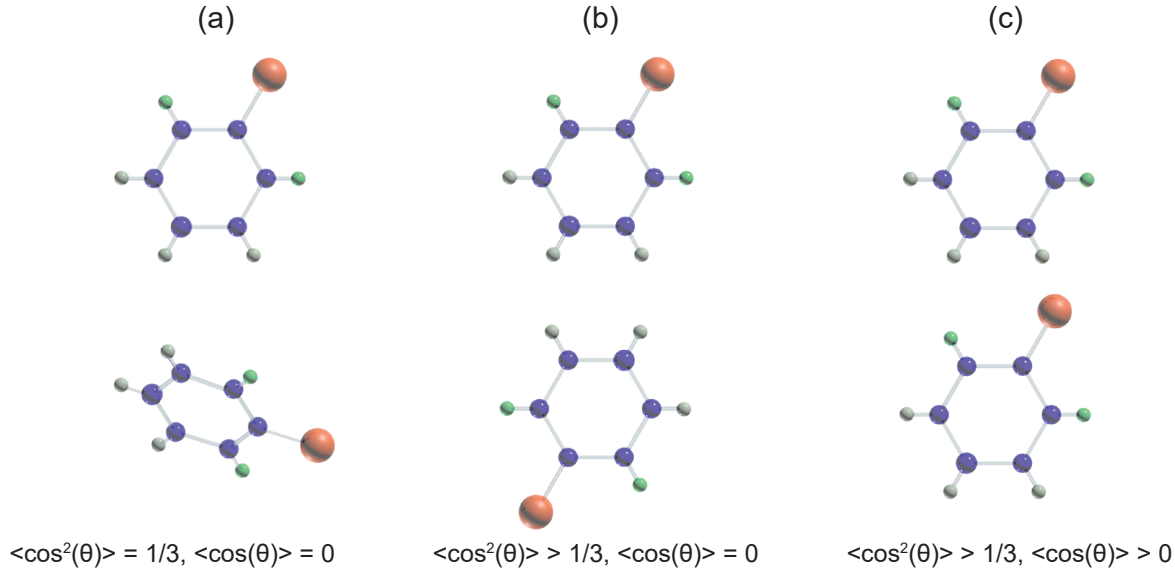

Figure 2.1: (a): Randomly aligned molecules (1,3-dichloro-2-iodobenzene - $C_6H_3Cl_2I$), as they would be present in a molecular ensemble in the gas phase. (b): Molecules which are aligned with respect to a fixed axis, but still retain inversion symmetry. (c): In comparison to the aligned molecules the inversion symmetry is broken for an oriented ensemble.

2.2 Requirements of x-ray experiments with aligned molecules

The degree of a molecular ensemble's adiabatic alignment by a laser beam depends on several physical properties. It can be characterized by the thermal averaged expectation value $\langle \cos^2(\theta)_T \rangle$, with θ denoting the angle between the z-axis of the molecular frame and the z-axis in the space fixed frame. Besides a sufficient field intensity, also the polarization of the laser and the field distribution must be considered. The theory of molecular alignment can be gained from various publications, like [10, 19, 34–39]. An overview is given in [10].

Properties of the electric field Figure 2.2 illustrates the necessary field intensities for a few small molecules, which depend on the rotational constant B of the molecule or the rotational temperature. The alignment laser must operate on wavelengths non-resonant to electronic, rotational, and vibrational transitions in the molecules. Linearly polarized electrical fields can only be used for one-dimensional (1d) alignment. 3d alignment of, for instance, asymmetric top molecules, requires controllable elliptically polarized fields and adiabatic mixed-field orientation requires the addition of a moderate DC electric field [10, 11]. The degree of adiabatic alignment follows the envelope of the electric field [34]. It, therefore, requires the application of the AC electric field over timespans comparable to - or much longer than - the rotational period of the molecule. The rotational periods can range from tens of picoseconds for small molecules to nanoseconds or even microseconds for larger molecules [31].

Special requirements for x-ray diffraction experiments Pump-probe experiments with aligned molecules require the spatial and temporal overlap of the molecular beam, the alignment laser and the probe pulse. In the case of an x-ray pump-probe diffraction experiment, the x-ray beam is typically focused to a beam radius $w_{0,\mathrm{FEL}} > 10\,\mu\mathrm{m}$ [40] to

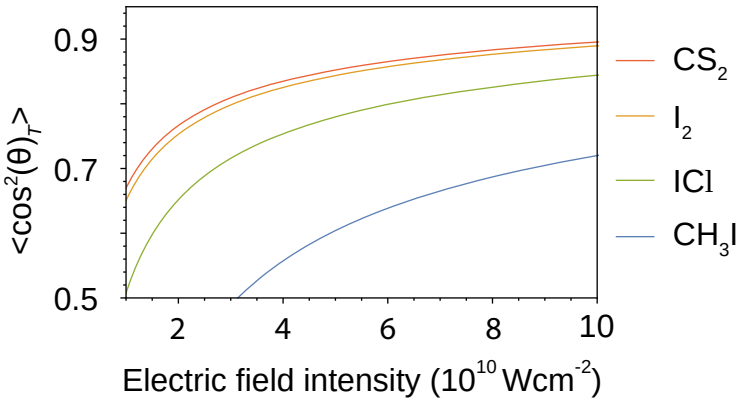

Figure 2.2: Calculated expectation value of $\langle \cos^2(\theta)_T \rangle$ according to [34] in dependency of the electric field intensity for different molecules, for a rotational temperature of 0.3 K. The molecular parameters were taken from [35, 36].

avoid radiation damage of the molecular beam which has a typical width of several mm [14, 41, 42]. An alignment laser must provide a smooth temporal and spatial field intensity over the interaction volume defined by the intersection of the molecular and x-ray beam to ensure an appreciable degree of adiabatic alignment. Alignment experiments rely on molecular ensembles of low rotational temperatures. Typically, such ensembles are provided by the expansion of supersonic molecular beams into the ultra-high-vacuum [43]. The cold molecular beam must be delivered to the interaction zone and the degree of alignment needs to be monitored, for instance, through Coulomb explosion VMI [44]. At the current state, the dimensions of the delivery mechanics and the VMI device require a clear space of tens of cm around the focal point. Besides spatial overlap, diffraction experiments necessitate temporal overlap between the x-ray and alignment laser. Time efficient measurements thus benefit from a coincident repetition rate of x-ray source and alignment laser [4, 33]. Nowadays FELs can provide macro pulses at repetition rates of some 10 Hz (Linac Coherent Light Source (LCLS): 120 Hz [45]) up to MHz in the micro bunch (X-Ray Free-Electron Laser (XFEL): 4.5 MHz [46, 47]).

Synchrotrons can operate at even higher repetition rates of up to 500 MHz (Positron-Elektron-Tandem-Ring-Anlage (PETRA), Berliner Elektronenspeicherring-Gesellschaft für Synchrotronstrahlung (BESSY) [48]), depending on the bucket filling pattern [49]. Even repetition rates of 1 GHz are envisaged for energy recovering linear accelerators [7]. The currently available and the trend towards even higher repetition rates require alignment laser systems for the alignment of molecules which are already suitable for operating at repetition rates up to 1 GHz and provide nanosecond pulse durations. Neglecting the duty cycle of modern light sources, this can only be fulfilled with a CW laser beam for a repetition rate of 1 GHz and a pulse duration of 1 ns.

State-of-the-art experiments with aligned molecules Diffraction experiments of quasi-adiabatic aligned 2,5-diiodothiophene were reported by Küpper et al. at a repetition rate of the x-ray laser and alignment laser of 60 Hz [40] and by Kierspel et al. at 120 Hz [33]. Table-top alignment experiments were performed at repetition rates of 1 kHz with an amplified femtosecond laser system and iodobenzene molecules [15] or carbonylsulfide [30], in addition x-ray probe experiments were demonstrated with aligned bromotrifluoromethane at the Advanced Photon Source at 1 kHz [50]. The highest repetition rate used for the alignment of molecules was achieved by Benko et al. where nitrous oxide was aligned at a repetition rate of 154 MHz in a fiber frequency comb laser seeded enhancement cavity [51] but not good enough for diffractive imaging.

Continuous alignment with CW lasers has not been demonstrated yet. The average laser power needed for the alignment of small molecules exceeds the power level of lasers which are currently available on the market. For large biomolecules, e.g., viruses or proteins at low sample temperatures, calculations predict that commercially available CW laser systems with output powers up to 1 kW might be suitable for a degree of alignment which allows to calculate the molecular structure with nm resolution from diffraction images [52].

2.3 Thin-disk lasers and resonators

2.3.1 Physical model of a thin-disk laser

The gain material of a solid-state laser consists of a host material, e.g., a glass or a crystal doped with optically active ions. The energy levels of the dopant determine the spectroscopic properties of the gain material. These energy levels are determined by the spin-orbit interaction, the Coulomb interaction and the energy between the electrons and the nucleus [53]. Described by the Stark effect, the energy levels are further split in Stark multiplets which can consist of several Stark levels [54]. The single Stark levels are coupled by phonons and a thermal equilibrium of the occupation of the energy levels is obtained. Depending on the energetic splitting, different laser schemes can be denoted, which are depicted in Figure 2.3. This work focuses on ytterbium doped host materials. Therefore, the discussion is restricted to quasi-three-level systems. More details can be gained from [55–58].

The relative occupation $f_{\mathrm{m,i}}$ of an energy level $E_{\mathrm{m,i}}$ at a temperature t in a multiplet m with the degeneracy $g_{\mathrm{m,i}}$ is given by the Boltzmann occupation

$$f_{\mathrm{m,i}} = \frac{1}{Z_{\mathrm{m}}} g_{\mathrm{m,i}} \exp\left(-\frac{E_{\mathrm{m,i}}}{\mathrm{k_B} t}\right) \tag{2.1}$$

with the partition function Z_{m} of the canonical ensemble

$$Z_{\mathrm{m}} = \sum_j g_{\mathrm{m,j}} \exp\left(-\frac{E_{\mathrm{m,j}}}{\mathrm{k_B} t}\right). \tag{2.2}$$

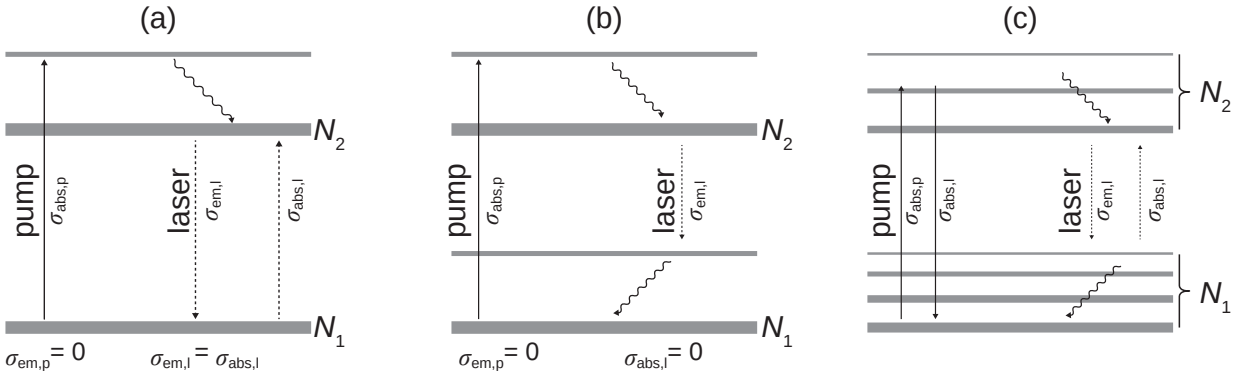

Figure 2.3: Scheme of laser n-level systems (n=3, 4, quasi-3-level). The horizontal lines represent energy levels, the height is proportional to the energy. (a) Three-level system. The laser transition ends in the ground state. (b) Four-level system. The laser transition ends in a level which can be quickly depopulated by phonons. (c) Quasi-three-level system. The laser transition ends in a thermally occupied energy level. The thickness of the level represents the occupation density.

Stimulated absorption rate Knowledge of the relative occupation of the energy levels allows to describe the absorption of pump photons according to

$$W_\mathrm{p} = (f_\mathrm{d,p} N_1 - f_\mathrm{u,p} N_2)\sigma_\mathrm{p} \frac{E_\mathrm{p,eff}}{h\nu_\mathrm{p}} = (\sigma_\mathrm{abs,p} N_1 - \sigma_\mathrm{em,p} N_2)\frac{E_\mathrm{p,eff}}{h\nu_\mathrm{p}}. \tag{2.3}$$

Here, $h\nu_\mathrm{p}$ is the energy of a pump photon, $N_{1,2}$ the ion density in the lower (1) and the upper (2) multiplet with the relative occupation $f_\mathrm{d,p}$ and $f_\mathrm{u,p}$ of the pump level inside the upper (u) or lower (d) multiplet, the effective pump density $E_\mathrm{p,eff}$ and σ_p the spectroscopic cross section, which can be excluded by introduction of the effective emission cross section $\sigma_\mathrm{ems,p}$ and absorption cross section $\sigma_\mathrm{abs,p}$ at the pump wavelength λ_p. These effective cross sections

$$\sigma_\mathrm{abs,p} = f_\mathrm{d,p}\sigma_\mathrm{p} \tag{2.4a}$$

$$\sigma_\mathrm{ems,p} = f_\mathrm{u,p}\sigma_\mathrm{p} \tag{2.4b}$$

are related by the McCumber theory [59] according to

$$\sigma_\mathrm{ems,p} = \frac{Z_1}{Z_2}\exp\left(\frac{E_\mathrm{zpl} - \frac{hc}{\lambda_\mathrm{p}}}{k_\mathrm{B}T}\right)\sigma_\mathrm{abs,p}. \tag{2.5a}$$

Induced emission rate The induced emission rate W_l is described analogously to Equation 2.3 as

$$W_\mathrm{l} = (\sigma_\mathrm{em,l} N_2 - \sigma_\mathrm{abs,l} N_1)\frac{E_\mathrm{r,eff}}{h\nu_\mathrm{l}} \tag{2.6}$$

with the effective emission and absorption cross sections at the laser wavelength $\sigma_\mathrm{em,l}$ and $\sigma_\mathrm{abs,l}$ respectively. $E_\mathrm{r,eff}$ denotes the (possible) superposition of different intracavity radiation fields, which can be influenced by the resonator scheme.

Spontaneous emission rate The spontaneous emission rate W_f

$$W_\mathrm{f} = \frac{N_2}{\tau} \tag{2.7}$$

is characterized by the lifetime τ of the transition between the two multiplets and the occupation density N_2 of the upper multiplet.

Rate equations As the occupation of the multiplets is connected by

$$N_1 + N_2 = N_\mathrm{dop}, \tag{2.8}$$

with the doping concentration N_dop, it is sufficient to consider one multiplet. The balance of the spontaneous emission, the induced absorption and the induced emission is then given by

$$\frac{\mathrm{d}N_2}{\mathrm{d}t} = \frac{E_\mathrm{p,eff}}{h\nu_\mathrm{p}}\left(\left(N_\mathrm{dop} - N_2\right)\sigma_\mathrm{abs,p} - N_2\sigma_\mathrm{em,p}\right) - \frac{N_2}{\tau} - \frac{E_\mathrm{r,eff}}{h\nu_\mathrm{l}}\left(N_2\sigma_\mathrm{em,l} - \left(N_\mathrm{dop} - N_2\sigma_\mathrm{abs,l}\right)\right). \tag{2.9}$$

Rate equations for the intracavity power The intracavity power P_{int} can be calculated with the knowledge of the resonator roundtrip time T_{rt} and the stored energy Q_{r} by integration over the resonator volume V_{res}

$$P_{\mathrm{int}} = \frac{Q_{\mathrm{r}}}{T_{\mathrm{rt}}} = \int_{V_{\mathrm{res}}} q_{\mathrm{r}} \frac{c}{2L_{\mathrm{r,eff}}} \mathrm{d}V \tag{2.10}$$

with the energy density q_{r} connected to the effective power density $E_{\mathrm{r,eff}}$ by

$$E_{\mathrm{r,eff}} = q_{\mathrm{r}} \frac{c}{n} \tag{2.11}$$

with the refractive index n and the effective resonator length (optical path length)

$$L_{\mathrm{r,eff}} = L_{\mathrm{r}} + \frac{M_{\mathrm{r}}}{2}(n_{\mathrm{cr}} - 1) l_{\mathrm{cr}} \tag{2.12}$$

with the resonator length L_{r} and a gain medium of length l_{cr} and refractive index n_{cr} which is passed M_r times per round trip [60, p. 304]. The gain of the active medium results in an increase of the effective power density $E_{\mathrm{r,eff}}$ according to

$$\frac{\mathrm{d}E_{\mathrm{r,eff}}}{\mathrm{d}t} = \frac{\mathrm{d}E_{\mathrm{r,eff}}}{\mathrm{d}z} \frac{c}{n_{\mathrm{cr}}} = E_{\mathrm{r,eff}} g \frac{c}{n_{\mathrm{cr}}} \tag{2.13}$$

with the gain g given by

$$g = \sigma_{\mathrm{em,l}} N_2 - \sigma_{\mathrm{abs,l}} N_1. \tag{2.14}$$

With the previous equations it is possible to transform Equation 2.10 into

$$\frac{\mathrm{d}P_{\mathrm{int}}}{\mathrm{d}t} = -\frac{P_{\mathrm{int}}}{\tau_{\mathrm{res}}} = \int_{V_{\mathrm{r}}} \frac{\mathrm{d}q_{\mathrm{r}}}{\mathrm{d}t} \frac{c}{2L_{\mathrm{r,eff}}} \mathrm{d}V = \int_{V_{\mathrm{cr}}} g E_{\mathrm{r,eff}} \frac{c}{2L_{\mathrm{r,eff}}} \mathrm{d}V \tag{2.15}$$

with τ_{res} as the lifetime of photons in the resonator, which defines the decay of the intracavity power, ideally only depending on the internal resonator losses L_{int} and transmission losses T_{oc} at the output coupling mirrors which leads, for negligible internal resonator losses L_{int}, from

$$(1 - L_{\mathrm{int}})(1 - T_{\mathrm{oc}}) P_{\mathrm{int}} = \exp\left(-\frac{T_{\mathrm{rt}}}{\tau_{\mathrm{res}}}\right) P_{\mathrm{int}} \tag{2.16}$$

to

$$\tau_{\mathrm{res}} = -\frac{T_{\mathrm{rt}}}{\ln(R_{\mathrm{oc}})}. \tag{2.17}$$

Here, R_{oc} denotes the product of the reflectivities R_{i}

$$R_{\mathrm{oc}} = \prod_{i=1}^{n} R_{\mathrm{i}} \tag{2.18}$$

of the resonator mirrors. From Equation 2.16 we can alternatively find the resonator lifetime to be

$$\frac{1}{\tau_{\mathrm{res}}} = -\frac{\ln(1 - L_{\mathrm{int}}) + \ln(1 - T_{\mathrm{oc}})}{T_{\mathrm{rt}}} = -\left(\ln(1 - L_{\mathrm{int}}) + \ln(1 - T_{\mathrm{oc}})\right) \frac{c}{2L_{\mathrm{r,eff}}}, \tag{2.19}$$

which yields for the time derivative of the intracavity power with the gain volume V_{cr}

$$\frac{\mathrm{d}P_{\mathrm{int}}}{\mathrm{d}t} = -\frac{P_{\mathrm{int}}}{\tau_{\mathrm{res}}} = \frac{c}{2L_{\mathrm{r,eff}}}\left[\int_{V_{\mathrm{cr}}} g E_{\mathrm{r,eff}} \mathrm{d}V + \ln(1-L_{\mathrm{int}}) + (\ln(1-T_{\mathrm{oc}}))\, P_{\mathrm{int}}\right]. \tag{2.20}$$

A CW laser operates at a constant intracavity power and a fixed occupation density in the upper multiplet according to

$$\frac{\mathrm{d}P_{\mathrm{int}}}{\mathrm{d}t} = \frac{\mathrm{d}N_2}{\mathrm{d}t} = 0. \tag{2.21}$$

Considering this, we find for the intracavity power, as balance between losses and gain,

$$P_{\mathrm{int}}\,(-\ln(1-L_{\mathrm{int}}) - \ln(1-T_{\mathrm{oc}})) = \int_{V_{\mathrm{cr}}} g E_{\mathrm{r,eff}}, \mathrm{d}V \tag{2.22}$$

and for the constant occupation of the upper multiplet

$$N_2 = \frac{\frac{E_{\mathrm{p,eff}}}{h\nu_{\mathrm{p}}}\sigma_{\mathrm{abs,p}} + \frac{E_{\mathrm{r,eff}}}{h\nu_{\mathrm{l}}}\sigma_{\mathrm{abs,l}}}{\frac{E_{\mathrm{p,eff}}}{h\nu_{\mathrm{p}}}(\sigma_{\mathrm{abs,p}} + \sigma_{\mathrm{em,p}}) + \frac{E_{\mathrm{r,eff}}}{h\nu_{\mathrm{l}}}(\sigma_{\mathrm{abs,l}} + \sigma_{\mathrm{em,l}}) + \frac{1}{\tau}} N_{\mathrm{dop}}. \tag{2.23}$$

When we combine Equation 2.22 and Equation 2.23 we find the following expression for the intracavity power

$$P_{\mathrm{int}} = \frac{N_{\mathrm{dop}}}{-\ln(1-L_{\mathrm{int}}) - \ln(1-T_{\mathrm{oc}})} \cdot \int_{V_{\mathrm{cr}}} \left[\frac{\left(E_{\mathrm{r,eff}}(\sigma_{\mathrm{em,l}} + \sigma_{\mathrm{abs,l}})\right)\frac{E_{\mathrm{p,eff}}}{h\nu_{\mathrm{p}}}\sigma_{\mathrm{abs,p}} + \frac{E_{\mathrm{r,eff}}}{h\nu_{\mathrm{l}}}\sigma_{\mathrm{abs,l}}}{\frac{E_{\mathrm{p,eff}}}{h\nu_{\mathrm{p}}}(\sigma_{\mathrm{abs,p}} + \sigma_{\mathrm{em,p}}) + \frac{E_{\mathrm{r,eff}}}{h\nu_{\mathrm{l}}}(\sigma_{\mathrm{abs,l}} + \sigma_{\mathrm{em,l}}) + \frac{1}{\tau}} - \sigma_{\mathrm{abs,l}} E_{\mathrm{r,eff}}\right] \mathrm{d}V. \tag{2.24}$$

The intracavity power is finally connected to the laser output power P_{l}, which is in most cases transmitted by one mirror with the transmission T_{oc} according to

$$P_{\mathrm{int}} = \frac{P_{\mathrm{l}}}{T_{\mathrm{oc}}} = \int_{A_{\mathrm{cr}}} E_{\mathrm{r}} \mathrm{d}A \tag{2.25}$$

by integration of the internal power density over the cross section of the gain medium.

2.3.2 The thin-disk laser

The TDL was invented by the group of A. Giesen in 1992 [61, 62]. The purpose of a TDL is the efficient conversion of a low beam quality laser diode into a laser of higher beam quality even at large output power. Especially the conversion over a large power range is typically not the case in common solid state laser concepts, such as bulk or rod lasers, which can suffer from thermal induced lenses in the gain medium. The induced heat originates mainly from the quantum defect which corresponds in this context to the energetic difference between pump and laser photons.

In the TDL laser setup the generation of a strong thermal lense is avoided by usage of a gain medium with a very small thickness, which is mostly in the order of only a few 100 µm. This small thickness leads to an almost 1d heat gradient perpendicular to the disk's surface, while the radial heat gradient, parallel to the disk's surface, nearly vanishes.

Sufficient absorption of the thin-disk, which due to the high-reflective (HR) coating on its backside behaves as a mirror, is achieved by a multipass pumping scheme. This is implemented by a combination of a parabolic mirror and deflecting prisms [63], as sketched in Figure 2.4. Up to 48 pump passes through the laser medium can be achieved and even 72 pump passes are envisioned [64]. This can ensure a pump power absorption larger than 90 % in the gain medium.

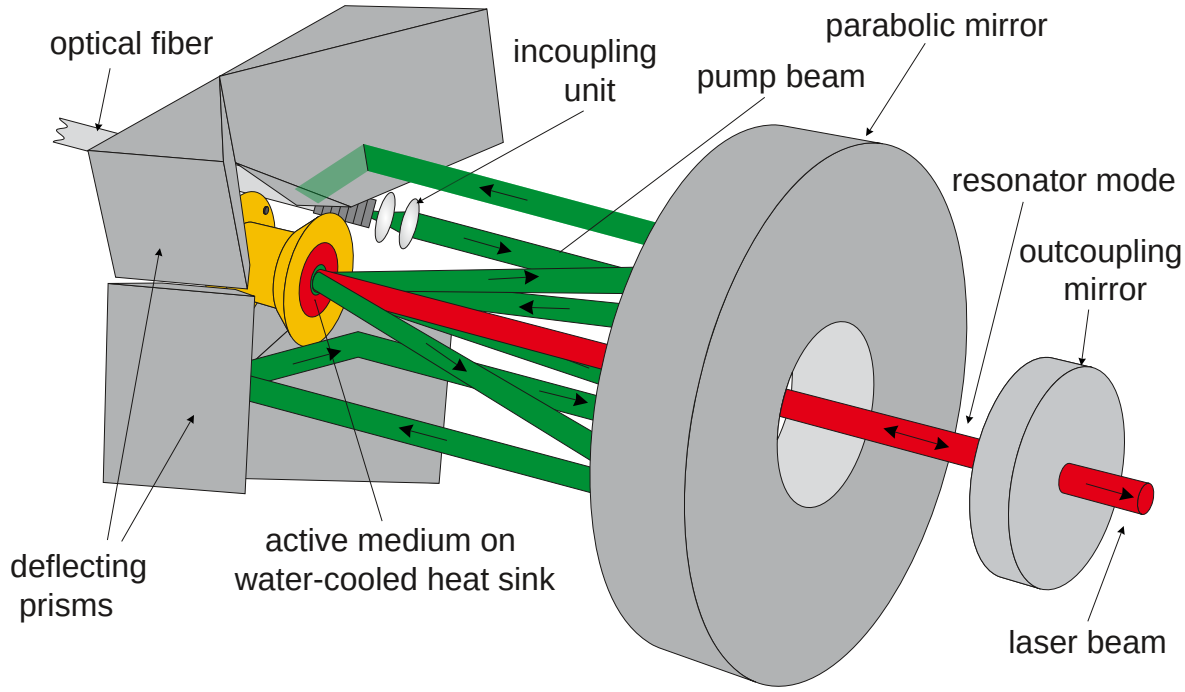

Figure 2.4: Thin-disk laser setup [65]. The output of a fiber coupled diode laser of a low beam quality is collimated by an incoupling unit. By a combination of a parabolic mirror and deflecting prisms the pump beam is focused multiple times onto the thin active medium, which is glued or soldered on a fluid-cooled heatsink.

2.3.3 Analytical model of the thin-disk laser

A key parameter of a laser is the intracavity power given by Equation 2.24. As this equation is generally not solvable in the given form, simplifications are necessary to calculate the intracavity power. Voss [66] and Contag [67] developed the zero-dimensional model for the TDL. The model assumes all laser relevant properties to be homogeneous inside of the gain medium[1].

Under the assumption of a low gain per pass we find for the effective intracavity power density $E_{\mathrm{r,eff}}$

$$E_{\mathrm{r,eff}} \approx M_{\mathrm{r}} E_{\mathrm{r}} \tag{2.26}$$

composed by the product of the intracavity power density E_{r} and the passes through the crystal in one resonator roundtrip M_{r}. The logarithm in Equation 2.22 can be approximated for low internal losses L_{int} and low output coupling transmissions T_{oc} to

$$-\ln(1-L_{\mathrm{int}}) - \ln(1-T_{\mathrm{oc}}) \approx L_{\mathrm{int}} + T_{\mathrm{oc}} \tag{2.27}$$

and Equation 2.22 reads for a constant power density in the gain medium of the length l_{cr}

$$L_{\mathrm{int}} + T_{oc} = (N_2(\sigma_{\mathrm{em,l}} + \sigma_{\mathrm{abs,l}}) - N_{\mathrm{dop}}\sigma_{\mathrm{abs,l}}) M_{\mathrm{r}} l_{\mathrm{cr}}. \tag{2.28}$$

In parallel, it is possible to define for a constant pump power density E_{p} an effective pump power density $E_{\mathrm{p,eff}}$ by

$$E_{\mathrm{p,eff}} = E_{\mathrm{p}} \frac{\eta_{\mathrm{abs}}}{\alpha l_{\mathrm{cr}}} \tag{2.29}$$

with the attenuation (absorption) length α and the absorption efficiency η_{abs}, which is given by

$$\eta_{\mathrm{abs}} = 1 - \exp\left(-M_{\mathrm{p}} \alpha l_{\mathrm{cr}}\right) = 1 - \exp\left(-M_{\mathrm{p}} \sigma_{\mathrm{abs,p}} f_{\mathrm{b}} N_{\mathrm{dop}} l_{\mathrm{cr}}\right). \tag{2.30}$$

The factor f_{b} denotes in this case a bleaching factor

$$f_{\mathrm{b}} = 1 - \frac{\sigma_{\mathrm{abs,p}} + \sigma_{\mathrm{em,p}}}{\sigma_{\mathrm{abs,p}}} \frac{N_2}{N_{\mathrm{dop}}}, \tag{2.31}$$

which reflects the decreasing absorption of pump power with the decreasing population density in the lower laser multiplet. This directly influences the Lambert–Beer law according to

$$I(l) = I_0 \exp\left(-\sigma_{\mathrm{abs,p}} N_{\mathrm{dot}} l f_{\mathrm{b}}\right). \tag{2.32}$$

For $P_{\mathrm{p}} \to \infty \Rightarrow f_{\mathrm{b}} \to 0$ a maximum inversion $\beta = N_2/N_{\mathrm{dop}}$ of

$$\beta_{\mathrm{max}} = \frac{\sigma_{\mathrm{abs,p}}}{\sigma_{\mathrm{em,p}} + \sigma_{\mathrm{abs,p}}} \tag{2.33}$$

[1] Spatial variation of the pump radiation was considered by Taira [68]. A new approach can be found in the work of P. Wittmuess [69].

can be obtained. The rate equation of the upper multiplet can, under consideration of Equation 2.29, be rewritten to

$$\frac{\mathrm{d}N_2}{\mathrm{d}t} = \frac{E_\mathrm{p}}{h\nu_\mathrm{p}}\frac{\eta_\mathrm{abs}}{l_\mathrm{cr}} - \frac{N_2}{\tau} - M_\mathrm{r}\frac{E_\mathrm{r}}{h\nu_\mathrm{l}}(N_2(\sigma_{\mathrm{em,l}} + \sigma_{abs,l}) - N_{dop}\sigma_{abs,l}). \tag{2.34}$$

We find with the threshold condition $T_\mathrm{oc} + L_\mathrm{int} = M_\mathrm{r} g$

$$N_{2,\mathrm{th}} = N_\mathrm{dot}\frac{\sigma_\mathrm{abs,l}}{\sigma_\mathrm{em,l} + \sigma_\mathrm{abs,l}} + \frac{L_\mathrm{int,l} + T_\mathrm{ges,l}}{M_\mathrm{r} l(\sigma_\mathrm{em,l} + \sigma_\mathrm{abs,l})}. \tag{2.35}$$

For steady state laser operation $\dot{N}_2 = 0$, Equation 2.34 becomes $\dot{N} = 0$ and thus

$$N_{2,th} = \frac{\frac{E_\mathrm{p}}{h\nu_\mathrm{p}}\frac{\eta_\mathrm{abs}}{l_\mathrm{cr}} + M_\mathrm{r}\frac{E_\mathrm{r}}{h\nu_\mathrm{l}}\sigma_\mathrm{abs,l}N_\mathrm{dop}}{M_\mathrm{r}\frac{E_\mathrm{r}}{h\nu_\mathrm{l}}(\sigma_\mathrm{em,l} + \sigma_\mathrm{abs,l}) + \frac{1}{\tau}} \tag{2.36}$$

for the occupation density N_2 of the upper multiplet at the threshold. Both deductions of the occupation density N_2 allow to calculate the intracavity power density by

$$E_\mathrm{r} = \frac{1}{T_\mathrm{oc} + L_\mathrm{int}}\eta_\mathrm{St}\eta_\mathrm{ov}\eta_\mathrm{abs}(E_\mathrm{p} - E_\mathrm{p,th}) \tag{2.37}$$

with the Stokes efficiency $\eta_\mathrm{St} = \nu_\mathrm{l}/\nu_\mathrm{p}$, the absorption efficiency η_abs, the overlap efficiency $\eta_\mathrm{ov} \approx w_0/w_p$ [70, p. 81] with the radius of the pump mode w_p and of the laser mode w_l, and the pump power density $E_\mathrm{p,th}$ at the threshold given by

$$E_\mathrm{p,th} = \frac{h\nu_\mathrm{p}}{\tau\eta_\mathrm{abs}}l_\mathrm{cr}N_\mathrm{2,th}. \tag{2.38}$$

The pump power at the threshold can be written as follows

$$P_\mathrm{th} = A_\mathrm{p}E_\mathrm{p,th} = \frac{A_\mathrm{p}h\nu_\mathrm{p}}{\tau\eta_\mathrm{abs}}\frac{\sigma_\mathrm{abs,l}}{\sigma_\mathrm{abs,l} + \sigma_\mathrm{em,l}}N_\mathrm{dot}l_\mathrm{cr} + \frac{A_\mathrm{p}h\nu_\mathrm{p}}{\tau\eta_\mathrm{abs}}\frac{L_\mathrm{int,l} + T_\mathrm{ges,l}}{M_\mathrm{r}(\sigma_\mathrm{em,l} + \sigma_\mathrm{abs,l})}. \tag{2.39}$$

The threshold power includes a temperature dependent contribution for reaching transparency on the laser wavelength, caused by the absorption of photons at the laser wavelength and a contribution to compensate for the total resonator losses.

The power $P_\mathrm{l,i}$ transmitted by a resonator mirror with the transmission T_i ($T_\mathrm{oc} = \sum_i T_\mathrm{i}$)

$$P_\mathrm{l,i} = \frac{T_\mathrm{i}E_\mathrm{r}}{A_\mathrm{p}} = \underbrace{\frac{T_\mathrm{i}}{L_\mathrm{int} + T_\mathrm{oc}}}_{\eta_\mathrm{oc}}\eta_\mathrm{St}\eta_\mathrm{abs}\eta_\mathrm{ov}(P_\mathrm{p} - P_\mathrm{th}) \tag{2.40}$$

increases from the threshold with the slope efficiency

$$\eta_\mathrm{sl} = \eta_\mathrm{oc}\eta_\mathrm{St}\eta_\mathrm{abs}\eta_\mathrm{ov}. \tag{2.41}$$

The total optical-to-optical efficiency can be obtained by dividing P_l by P_p

$$\eta_\mathrm{opt} = \frac{T_\mathrm{oc}}{L_\mathrm{int,l} + T_\mathrm{oc}}\eta_\mathrm{St}\eta_\mathrm{ov}\eta_\mathrm{abs}\left(1 - \frac{P_\mathrm{th}}{P_\mathrm{p}}\right). \tag{2.42}$$

2.3.4 Optical resonators

The key for the achievement of requirements, sufficient for the intracavity alignment of molecules, can be seen in a great extend in the underlying laser resonator. Common requirements, which can be influenced by the specific resonator configuration, are the waist or oscillation of a specific transversal mode profile. These requirements can be fulfilled by a selection of a coordinated set of parameters, which includes the shape of the resonator, the mirrors, distances between mirrors and further intracavity elements. A complete synopsis of resonator configurations and designs is beyond the scope of this thesis and can be found in a magnitude of textbooks [71–76]. Instead, only the main relevant properties of resonators are introduced.

The Gaussian beam

In the simplest case, a resonator consists of two mirrors M_i with a specific radius of curvature (ROC) ROC_i separated by the distance l. If the resonator configuration is stable, a defined set of electro-magnetic eigenmodes can be excited. These eigenmodes decay with a time which depends on the finesse, or the quality of the optical resonator.

Starting with the Maxwell equations, which allow for the derivation of a wave equation

$$c^2 \Delta \vec{E}(\vec{r},t) = \ddot{\vec{E}}(\vec{r}). \tag{2.43}$$

With the ansatz

$$\vec{E}(\vec{r},t) = \vec{e}E(\vec{r})\exp(iwt) \tag{2.44}$$

the wave equation Equation 2.43 can be transformed into the Helmholtz equation

$$\Delta \vec{E}(\vec{r}) + k^2 \vec{E}(\vec{r}) = 0 \tag{2.45}$$

with the angular wavenumber $k = |\vec{k}| = w/c = 2\pi/\lambda$ and the electric field $\vec{E}$. Plane waves are a solution to Equation 2.45 with a constant amplitude over the complete space. For a spatially restricted laser beam, the ansatz

$$E(\vec{r}) = E_0 X(x,z) Y(y,z) e^{(-ikz)} \tag{2.46}$$

with the propagation direction z is common. Together with the paraxial approximation

$$\left| 2ik \frac{\partial \vec{E}}{\partial z} \right| \gg \left| \frac{\partial^2 \vec{E}}{\partial z^2} \right|, \tag{2.47}$$

which denotes the slow change of the transversal beam profile in respect to the propagation direction z, Equation 2.45 transforms into the paraxial wave equation

$$Y \frac{\partial^2 X}{\partial x^2} + X \frac{\partial^2 Y}{\partial y^2} - 2ikX \frac{\partial X}{\partial z} - 2ikY \frac{\partial Y}{\partial z} = 0. \tag{2.48}$$

This can be separated into equations for $X(x,z)$ and $Y(y,z)$

$$\left(\frac{\partial^2}{\partial x^2} - 2ik\frac{\partial}{\partial z}X(x,z)\right) \text{and} \tag{2.49a}$$

$$\left(\frac{\partial^2}{\partial y^2} - 2ik\frac{\partial}{\partial z}Y(y,z)\right). \tag{2.49b}$$

A complete set of solutions of Equation 2.48 is given with the Hermite polynomials $H_{\mathrm{m,n}}$[2] in the astigmatic case by

$$X_{\mathrm{m}}(x,z) = \sqrt{\frac{w_{0,\mathrm{x}}}{w_{\mathrm{x}}(z)}}H_{\mathrm{m}}\left(\frac{\sqrt{2}x}{w_{\mathrm{x}}(z)}\right)\left(\exp\left(-\frac{x^2}{w_{\mathrm{x}}^2(z)} - i\frac{kx^2}{2R_{\mathrm{x}}(z)} + i\frac{2m+1}{2}\xi_{\mathrm{x}}(z)\right)\right) \tag{2.50a}$$

$$Y_{\mathrm{n}}(y,z) = \sqrt{\frac{w_{0,\mathrm{y}}}{w_{\mathrm{y}}(z)}}H_{\mathrm{n}}\left(\frac{\sqrt{2}y}{w_{\mathrm{y}}(z)}\right)\left(\exp\left(-\frac{y^2}{w_{\mathrm{y}}^2(z)} - i\frac{ky^2}{2R_{\mathrm{y}}(z)} + i\frac{2n+1}{2}\xi_{\mathrm{y}}(z)\right).\right) \tag{2.50b}$$

Here, $\xi_{\mathrm{x,y}}$ denotes the Gouy-phase, describing the phase accumulation of a Gaussian beam with respect to a plane wave

$$\xi_{\mathrm{x,y}} = \arctan\frac{z_{\mathrm{x,y}}}{z_{0,\mathrm{x,y}}}. \tag{2.51}$$

$R_{\mathrm{x,y}}$ describes the propagation dependent radius of curvature of the beam

$$R_{\mathrm{x,y}}(z) = z\left(1 + \left(\frac{z_{\mathrm{R,x,y}}}{z}^2\right)\right) \tag{2.52}$$

with the Rayleigh length

$$z_{\mathrm{R,x,y}} = \frac{\pi w_{\mathrm{x,y}}^2}{\lambda} \tag{2.53}$$

as the required distance for the beam to double its cross-sectional area, or to increase the radius by $\sqrt{2}$. Equation 2.50 describes a set of solutions of the paraxial wave equations corresponding to the fundamental Gaussian beam if $n = m = 0$.

By introduction of the complex beam parameter (q-parameter), which specifies the state of a Gaussian beam at every position

$$\frac{1}{q_{\mathrm{x,y}}(z)} = \frac{1}{z_{\mathrm{x,y}} + iz_{\mathrm{R,x,y}}} = \frac{1}{R_{\mathrm{x,y}}(z)} - \frac{i\lambda}{\pi w_{\mathrm{x,y}}(z)^2}, \tag{2.54}$$

it is, e.g., possible to rewrite Equation 2.50a into

$$X_{\mathrm{m}}(x,z) = \left(\frac{\sqrt{2/\pi}}{2^m m!\, w_{0,\mathrm{x}}}\right)^{\frac{1}{2}}\left(\frac{q_{0,\mathrm{x}}}{q_{\mathrm{x}}(z)}\right)^{\frac{1}{2}}\left(-\frac{q_{\mathrm{x}}^*}{q_{\mathrm{x}}(z)}\right)^{\frac{m}{2}}H_{\mathrm{m}}\left(\frac{\sqrt{2}x}{w_{\mathrm{x}}(z)}\right)\exp\left(-i\frac{kx^2}{2q(z)}\right). \tag{2.55a}$$

[2] Different symmetry dependent solution sets are discussed in [72]

The Gaussian beam in a resonator

As analytical solutions of Equation 2.48 are only available for simple resonators, a general procedure for the calculation of the resonator's caustic is presented in the following. A circular Gaussian beam profile can be written as

$$E_\mathrm{r}(z) = \frac{1}{q(z)} \exp\left(-\frac{ikr^2}{2q(z)}\right) \tag{2.56}$$

which is altered linearly with the distance of an optical system [77, p. 117]. When a Gaussian beam passes an optical system, the q-parameter is transformed with a matrix

$$M_\mathrm{i} = \begin{pmatrix} A & B \\ C & D \end{pmatrix} \tag{2.57}$$

according to

$$q_2 = \frac{Aq_1 + B}{Cq_1 + D} \tag{2.58}$$

with the solution

$$q_\pm = \frac{(A-D) \pm \sqrt{(A+D)^2 - 4}}{2C}. \tag{2.59}$$

With this, the caustic inside the resonator can be calculated [72, p. 107].

Mode spectrum The mode spectrum of a resonator with a medium with the group index n_g and the length L_R is separated by the axial mode spacing, the free spectral range (FSR)

$$\Delta\upsilon = \frac{c}{2n_\mathrm{g}L_\mathrm{R}}. \tag{2.60}$$

Due to the accumulated Gouy phase shift ξ of the higher transversal modes during one resonator roundtrip a narrower separation of the resonator mode exists. The eigenmodes are characterized by the transverse mode indices n and m and the axial mode number q by

$$\upsilon_\mathrm{nmq} = \upsilon_0 + q\Delta\upsilon + (n+m)\frac{\Delta\upsilon \cdot \xi}{2\pi}. \tag{2.61}$$

According to [78–80] the total accumulated Gouy phase shift ξ can be calculated from the resonator's roundtrip matrix M_res by

$$\xi = \mathrm{sgn}(B)\cos^{-1}\left(\frac{A+D}{2}\right). \tag{2.62}$$

Its knowledge allows to calculate the length of the cavity by observing the beat frequencies of the different axial modes [71]. In parallel, the accumulated phase shift can be considered in the resonator design to avoid a reduction of the beam quality which can be caused by mode degeneracies [81–83].

2.4 Losses in solid-state lasers

2.4.1 Measurement of resonator losses

Findlay-Clay method Findlay and Clay developed a method to determine the internal resonator losses of an active cavity by measuring the output coupler (OC) transmission dependent laser threshold [84]. Steady state operation of a laser requires the balance of losses and amplification for a roundtrip in the cavity. For a laser resonator consisting of two mirrors with the reflectivities R_1 and R_2, an active medium of the length l_{cr}, the equally distributed volume losses α and the small-signal gain at the threshold g_{thr} this can, according to [77], be written as

$$R_1 R_2 \exp(-2\alpha l_{\mathrm{cr}}) \exp(2 g_{\mathrm{thr}} l_{\mathrm{cr}}) = 1. \tag{2.63}$$

Rearrangements and the assumption of a constant optical loss $\alpha = \alpha_0$ and $R_1 = 1$ lead to

$$2 g_{\mathrm{thr}} l_{\mathrm{cr}} = 2\alpha_0 l_{\mathrm{cr}} - \ln(R_2). \tag{2.64}$$

The threshold pump power P_{thr} can be assumed to be proportional to $2 g_{\mathrm{thr}} l_{\mathrm{cr}}$ [60] and with $L = 2 l_{\mathrm{cr}} \alpha_0$ and the constant K, Equation 2.64 can be written as

$$P_{\mathrm{thr}} = K \left(L - \ln(R_2) \right). \tag{2.65}$$

This considers only homogeneously distributed losses inside the gain medium, phenomena like diffraction at the interfaces are neglected. A more detailed derivation considering scattering and diffraction losses L_{scat} and L_{diff} is shown in [60].

Caird analysis Here, resonator losses are determined by measurement of the slope efficiency [85]. The slope efficiency η_{sl} of a laser is, according to Equation 2.40 the product of the single efficiencies, which can include, e.g.,

$$\eta_{\mathrm{sl}} = \eta_{\mathrm{oc}} \eta_{\mathrm{St}} \eta_{\mathrm{abs}} \eta_{\mathrm{ov}}. \tag{2.66}$$

Segregation of the latter three efficiencies to η_{tot} and applying rearrangements leads to

$$\frac{1}{\eta_{\mathrm{sl}}} = \frac{L_{\mathrm{int}}}{\eta_{\mathrm{tot}}} \frac{1}{T_{\mathrm{oc}}} + \frac{1}{\eta_{\mathrm{tot}}}. \tag{2.67}$$

This allows to derive the resonator losses L_{int} from a linear fit of the reciprocal slope efficiencies versus the reciprocal OC transmissions. Alternatively, a direct nonlinear fit of

$$\eta_{\mathrm{sl}} = \frac{T_{\mathrm{oc}}}{T_{\mathrm{oc}} + L_{\mathrm{int}}} \eta_{\mathrm{tot}} \tag{2.68}$$

can be performed. With both different fits, the internal losses as well as the total resonator efficiency can be determined. Note, that the Caird plot may not lead to reasonable results at higher OC transmissions, where the slope efficiency decreases due to loss processes at high inversion densities which are not covered by the underlying rate equations [86].

Relaxation oscillations Any disturbance of an operating laser leads to relaxation oscillations [71, 87]. The frequency of the relaxation oscillations f_{ro} is given by

$$f_{\mathrm{ro}} = \frac{1}{2\pi}\left(\frac{L_{\mathrm{int}}P_{\mathrm{int}}}{T_{\mathrm{rt}}E_{\mathrm{sat}}} - \frac{1}{4}\left(\frac{1}{\tau} + \frac{P_{\mathrm{int}}}{E_{\mathrm{sat}}}\right)^2\right)^{\frac{1}{2}} \tag{2.69}$$

with the saturation energy E_{sat}. For upper state lifetimes much larger than the cavity dumping time, Equation 2.69, can according to [88] be rewritten as

$$f_{\mathrm{ro}} \approx \frac{1}{2\pi}\left(\frac{L_{\mathrm{int}}P_{\mathrm{int}}}{T_{\mathrm{rt}}E_{\mathrm{sat}}}\right)^{\frac{1}{2}} \tag{2.70}$$

and rearrangements yield to

$$L_{\mathrm{int}} \approx \frac{4\pi^2 T_{\mathrm{rt}} f_{\mathrm{ro}}^2 E_{\mathrm{sat}}}{P_{\mathrm{int}}}. \tag{2.71}$$

The advantage of this method is, that the losses of the system can in principle be determined from a single measurement. A similar method is described in [89].

The cavity linewidth The definition of the Q factor [71, 88]

$$Q = \frac{\upsilon_0}{\delta\upsilon} = \upsilon_0 T_{\mathrm{rt}} \frac{2\pi}{L_{\mathrm{int}}} \tag{2.72}$$

directly yields to the calculation of the losses

$$L_{\mathrm{int}} = \frac{2\pi T_{\mathrm{rt}}}{\delta\upsilon}. \tag{2.73}$$

The linewidth $\delta\upsilon$ can be scanned in seeded enhancement cavities with piezo actuators. A possible way for measuring this in active laser cavitities could be the detection of longitudinal mode beating [71] with a radio frequency (RF) spectrum analyzer. The linewidth can in principle be deduced from the linewidth of the beating. However, mode competition effects can hinder the assignment.

The cavity lifetime The principle of measuring the resonator losses from the lifetime of the photons in the cavity can be done with cavity ring down (CRD) spectroscopy [90]. This method is used for measuring very low absorptions or high reflectivities of cavity mirrors [91]. When a light pulse is coupled into a cavity, the intensity in the cavity decays exponentially by

$$I(t) = I_{\upsilon_0} \exp\left(-\frac{t}{\tau_{\mathrm{res}}}\right). \tag{2.74}$$

The decay constant τ_{res} depends on the different losses of the cavity according to

$$\tau_{\mathrm{res}} = \frac{n}{c} \cdot \frac{L_{\mathrm{r}}}{1 - \prod_i R_i + X + \alpha l} \tag{2.75}$$

and can consider besides reflection R_i and absorption losses α additional losses X.

Spectral gain measurement The technique described by Zaho [92] is based on spectral measurements of the laser oscillation wavelength. It does not require separate measurements and can be performed at any laser output power levels, thus allowing a dynamic optimization of the laser performance. The intracavity losses can be calculated from the loss dependent peak gain coefficient due to the balance of losses and gain

$$R_{\mathrm{oc}}\,(1-L_{\mathrm{int}})\exp(g(\lambda_{\mathrm{las}}))=1. \tag{2.76}$$

Here, $g(\lambda_{\mathrm{las}})$ is the wavelength-dependent effective gain coefficient. Thus, the intracavity losses can be calculated once the gain coefficient and the reflectivity of the OC are known. The gain coefficient can be calculated by determination of the laser wavelength according to

$$g(\lambda_{\mathrm{las}})=2N_{dop}l_{\mathrm{cr}}\,(\beta\sigma_{\mathrm{em}}(\lambda_{\mathrm{las}})-(1-\beta)\sigma_{\mathrm{abs}}(\lambda_{\mathrm{las}}))\,. \tag{2.77}$$

This method allows the on-line calculation of the resonator losses, but relies on precise measurements of the cross sections and the laser wavelength. Even though this method might be applicable for materials with a continuous change of the laser wavelength, its application can be difficult for materials like Yb:$Y_3Al_5O_{12}$ with smooth gain spectra, where only large differences can be distinguished. This is depicted in Figure 2.8 where λ_{las} is plotted against the total resonator losses and only large steps of resonator losses can be spectrally resolved.

Simple approximations from energy conservation laws An estimation of the maximum possible losses can be made by consideration of energy conservation per

$$\eta_{\mathrm{sl}}\leq\frac{T_{\mathrm{oc}}}{T_{\mathrm{oc}}+L_{\mathrm{int}}}\eta_{\mathrm{St}}\eta_{\mathrm{sl}}. \tag{2.78}$$

Subsequent rearrangements yield into

$$L_{\mathrm{int}}\leq\left(\frac{\eta_{\mathrm{St}}}{\eta_{\mathrm{sl}}}-1\right)T_{\mathrm{oc}}. \tag{2.79}$$

Equation 2.78 allows to calculate an upper limit of the resonator losses by measuring the slope efficiency for only one OC transmission. A high precision requires the use of OCs with low and precisely determined transmissions.

2.4.2 Losses in solid state lasers

Scattering losses Scattering can, e.g., be understood as absorption and reemission processes of incident light, without a change of the photon energy [93]. Irregularities on surfaces or enclosed in volumes, cause scattering. The scattering in volumes can be calculated for simple scatter centers, such as spheres. For diameters with $\lambda > d/n_{\text{medium}}$ the process is described by Rayleigh scattering, $\lambda \approx d/n_{\text{medium}}$ by Mie scattering and $\lambda < d/n_{\text{medium}}$ by geometrical scattering theory [93, p. 277]. According to [94], the Rayleigh scattering intensity can be described by

$$I = I_0 \left(\frac{1+\cos^2(\theta)}{2R^2} \right) \left(\frac{2\pi}{\lambda} \right)^4 \left(\frac{n^2-1}{n^2+2} \right)^2 \left(\frac{d}{2} \right)^6 . \tag{2.80}$$

Here, I_0 is the intensity of the incident beam, R the distance to the particle, θ the scattering angle, n the refractive index of the scattered object with the diameter d. For molecules with the polarizability α, Equation 2.80 simplifies to

$$I = I_0 \frac{8\pi^4\alpha^2}{\lambda^4 R^2} \left(1+\cos^2(\theta)\right). \tag{2.81}$$

The angular average of Equation 2.80 results in the Rayleigh cross section [95]

$$\sigma_s = \frac{2\pi^5}{3} \frac{d^6}{\lambda^4} \left(\frac{n^2-1}{n^2+2} \right)^2 . \tag{2.82}$$

For given cross sections, which were measured in [96] for nitrogen and theoretical values for air gas mixtures in [97], it is possible to calculate the scattered power. For a resonator with a length of 0.5 m and a wavelength of 1 µm this results into roundtrip losses of approx. 1 ppm. Concerning the resonator, scattering occurs mainly at surfaces. The simplest model describes surface scattering at single layers. The concept of the total integrated scatter (TIS) is based on work by Bennett [98] who determined the fraction of specular and total reflected power as

$$\frac{R_s}{R_t} = \exp\left(\left(\frac{4\pi\cos(\theta)\sigma}{\lambda} \right)^2 \right), \tag{2.83}$$

where R_s is the specular reflectance, R_t the total reflectance, θ the incident angle, λ the wavelength and σ the root mean square (RMS) roughness of the surface [99]. The TIS then follows from the classical definition with $R_d = R_t - R_s$ as diffuse reflectance as

$$TIS = \frac{R_t - R_s}{R_t} = 1 - \exp\left(\left(\frac{4\pi\cos(\theta)\sigma}{\lambda} \right)^2 \right). \tag{2.84}$$

The previous declarations are only valid for surfaces with a normal distributed height. Then the RMS roughness is equal to the standard deviation of the height distribution. Further height distributions are discussed in [99, 100]. The description of scattering in multilayer systems involves further effects, such as inlayer scattering or radiation trapping. Theories for scattering from multilayer systems can be found in [101–103]. In general, those methods do not rely on simple sums of the single scattering from single surfaces due to interference effects [104, 105]. Numerical implementations of these theories can be found in [106].

Absorption losses Absorption in a TDL can be separated into absorption at the pump wavelength and absorption at the laser wavelength. Essential for the laser operation is sufficient absorption of the laser medium at the pump wavelength. Absorption at the laser wavelength can be beneficial for transversal mode selection, as it suppresses the oscillation of higher order modes [107]. Absorption of the laser radiation in the resonator atmosphere decreases the slope efficiency. These losses can be calculated from the absorption cross section of the gas mixture in the resonator. Data for gas mixtures can be obtained from the HITRAN database [108]. The absorption of air in one 1 m is up to 100 ppm between 1000 nm and 1050 nm and up to 1000 ppm between 1050 nm and 1100 nm. However, exact predictions depend on the specific resonator and gain medium, and must consider the FSR as well as the gain cross section.

Optical damage by small defects Absorption in optical coatings is one of the mechanisms responsible for optical damage in CW lasers[3]. The absorption occurs due to defects, deficient localized oxidation of the sputtered raw materials, stoichiometric deficiencies or contaminants in the coating material [93]. The nodular defects typically have diameters in the order of 10 µm. Depending on the composition they can absorb pump or laser power. In dependence of the local embedding of the defect in the coating structure, different thermal processes can occur [117].

State of the art optimized ion beam sputtering (IBS) coatings can exhibit total losses of 0.2 ppm while typical sputtered coatings have losses in the order of 5 ppm to 10 ppm [118, 119]. Reduction of the absorption to 0.2 ppm is possible by annealing of the coatings [120, 121]. Possible reasons for this improvement are an improvement of crystalline properties and grain size [122], decrease of organic contaminations, structural reconstruction or stress relaxation of the thin films [123, 124].

Defects in the order of several µm can be modelled as circular apertures. If a Gaussian beam with the power P and the beam radius w hits an on-axis aperture with the radius r_a, the transmitted power is given by

$$P_\mathrm{tr}(r,z) = P_0\left(1-\exp\left(-2\frac{r_\mathrm{a}^2}{w^2}\right)\right). \tag{2.85}$$

A derivation for off-axis apertures is presented in [125]. Generally, the transmission losses P_tr/P_0 are insufficient to describe the total losses at a small aperture. The field distribution of a Gaussian beam, reflected by a surface with an aperture or hole, has a hole. When coupling into higher order modes is avoided, the overlap between the fundamental mode and the reflected field distribution is reduced by $\exp\left(-2r_{\mathrm{a}^2}/w^2\right)$. This was experimentally shown in [126]. A theoretical description of this effect is given in [79, 127]. According to these publications, the diffraction and absorption losses of an absorbing defect on a mirror L_def can be approximated by

$$L_\mathrm{def} = 1-\exp\left(-4\frac{r_\mathrm{a}^2}{w^2}\right). \tag{2.86}$$

[3]Details about different loss channels in optical coatings are given, e.g., in [93, 109–116].

Transmission losses The energy balance at an optical element, neglecting absorption and scattering, can be approximated by

$$T = 1 - R \tag{2.87}$$

with the transmittance T and reflectance R. Mirrors with reflectivities in the order of 0.99 can be based on metallic coatings. Higher reflectivities are facilitated with dielectric mirrors. A possible mirror design is the quarter-wave stack (QWS). Such mirrors contain alternating layers of dielectric materials with a high refractive index n_h and a low refractive index n_l. If each layer in this stack has the same optical thickness $t = \lambda_\mathrm{t}/4n_\mathrm{i}$ for the target center wavelength λ_t and the specific refractive index of the layer material n_i, this results in constructive interference of the light beams reflected at the particular interfaces. Reflection at a single interface is described by the Fresnel equations. The description of the reflection at a multilayer system becomes complex due to the number of different partial waves, arising at each interface. This complexity can be avoided by the transfer-matrix method [128]. This method allows an approximation of the reflectivity R_qws of a QWS multilayer system with a large number N of layer pairs by [93, p. 405]

$$R_\mathrm{qws} = 1 - 4n_0 n_\mathrm{s} \frac{n_\mathrm{l}^{2N}}{n_\mathrm{h}^{2(N+1)}}. \tag{2.88}$$

Here, n_s is the substrate's refractive index and n_0 the refractive index of the ambient medium. Equation 2.88 illustrates that a high reflectivity can be achieved by increasing the number of layer pairs N and the contrast between n_l and n_h. However, the number of layer pairs cannot be increased without disadvantages. Thin dielectric sputtered layers can have a low thermal conductivity in the order of $1\,\mathrm{W\,m^{-1}\,K^{-1}}$, which depends on the coating method [129]. In particular, for TDL a further disadvantage exists due to different numbers of layer pairs of the HR coating on the backside of the disk and the anti-reflective (AR) coating on the frontside of the disk, which can yield to a concave form of the disk. [130].

Diffraction losses Diffraction losses L_d occur in open resonators due to the finite extend of optical elements. No analytical solutions for the calculation of diffraction losses in generalized resonators are known. Most publications dealt with the numerical calculations of the diffraction losses of symmetric resonators, and a few analyzed symmetric resonators with one or two apertures or general asymmetric resonators [131, 132]. According to [31, 60], the diffraction losses can be approximated for symmetric resonators with the mirror diameter a by the Fresnel number F according to

$$L_\mathrm{d} \approx \frac{1}{F} = \frac{\lambda \cdot L_\mathrm{r}}{a^2}. \tag{2.89}$$

A different estimation of the diffraction losses is proposed in [133]. Here, a Gaussian beam with the radius w, which gets reflected from a mirror, experiences a (clipping) power loss of $\exp\left(-a^2/w^2\right)$. A general numerical approach is described in [134, 135].

Depopulation losses Depopulation losses can be understood as processes, which depopulate the upper laser level of an excited gain material [57]. Any depopulation of the upper laser level decreases the maximum achievable gain. Effects are, e.g., amplified spontaneous emission (ASE) or the occurrence of parasitic modes and prelasing [67, 136]. In addition, also inter-ionic energy transfers can occur especially in highly doped materials and depopulate the upper laser level. These transfers are unlikely in ytterbium-doped gain materials and explained elsewhere [88, 137]. ASE describes the amplification of a spontaneous emission without optical feedback. It becomes relevant when the spontaneous emission can be amplified along a long optical path. The optical path can hereby be extended by internal reflections at surfaces. Therefore, ASE is of special interest in TDLs where it results in a decrease of the upper state lifetime. In particular, in a TDL the power scalability is achievable by the increase of the pump spot diameter and might be limited by ASE [138–140] in parallel to thermal aberrations [141, 142]. More details can be found in [143, 144].

Depolarization losses An isotropic crystal does not exhibit birefringence. However, the temperature distribution as well as electric voltages and mechanical stress can influence the refractive index and induce birefringence [72]. This can be disadvantageous if additional polarization selective elements are added into the resonator. In this case, the polarization axis can, e.g., be predetermined by a window in the Brewster angle. The induced birefringence of the active medium rotates the predetermined polarization and thus exhibits a loss at the polarization selective element. The depolarization losses were analyzed for TDL in [67]. The calculated depolarization losses are for a disk with a thickness of 200 µm for pump spot diameters between 1 mm to 6 mm in the order of 2.5×10^{-4} to 5×10^{-4}. The depolarization losses can be minimized by using a Faraday rotator, a $\lambda/4$ plate, a different crystal orientation, or by adjusting the Gouy phase shift of the resonator [88, 145, 146].

Nonlinear losses In this context nonlinear losses denote losses which result from nonlinear optics as well as inversion dependent losses. The latter occurs at high inversion densities in TDL and yields to decreased laser efficiencies. Inversion dependent losses are described in [53, 86]. Nonlinear optics describe the nonlinear response of the dielectric polarizability in respect to the electric field. Effects by nonlinear optics can be assigned firstly to the group of frequency mixing processes which consist, e.g., of second harmonic generation (SHG), third harmonic generation (THG), and HHG. Another group of nonlinear processes involves the optical Kerr effect. The intensity dependency of the refractive index $n = n_0 + n_2 I$ with the nonlinear refractive index n_2 can yield to different effects, such as self-focusing, Kerr-lens mode locking, self-phase modulation or optical solitons. As n_2 is for transparent glasses and crystals typically in the order of $10^{-16}\,\mathrm{cm^2\,W^{-1}}$, it requires intensities of $\mathrm{GW\,cm^{-2}}$ for significant variations of the refractive index [71]. Finally, if the laser power is higher than the critical power

$$P_{\mathrm{cr}} = 1.9 \frac{\lambda^2}{4\pi n_0 n_2}, \tag{2.90}$$

a whole-beam self-focusing can occur [71, 147] and lead to optical damage.

2.5 Feasibility of continuous adiabatic alignment with thin-disk lasers

Electrical field intensity The envisioned range for the adiabatic alignment of molecules is between an electrical field intensity of $10^{10}\,\mathrm{W\,cm^{-2}}$ and $10^{12}\,\mathrm{W\,cm^{-2}}$. The purpose of diffraction experiments requires the alignment beam to cover the x-ray beam as homogeneously as possible. Typically, the x-ray beams can be kept at a radius in the order of 10 µm [14, 40] to avoid radiation damage at the samples by the XFEL-beams [148, 149].

A smooth field intensity distribution is required in the interaction volume of the molecular beam, alignment laser, and x-ray beam. The optical power P of a Gaussian laser beam, necessary to achieve a field intensity of $10^{10}\,\mathrm{W\,cm^{-2}}$ at a distance of 5 µm $= w_{0,\mathrm{FEL}}$ from the center in dependence of the Gaussian beam radius, is depicted in Figure 2.6. It is possible to obtain the required field intensity at the beam radius of the FEL beam with a laser power of 21 kW and a waist of 7 µm. This corresponds to an enhanced optical peak intensity in the center of the laser beam

$$I_\mathrm{p} = \frac{2P}{\pi w_0^2} \tag{2.91}$$

of $2.7 \times 10^{10}\,\mathrm{W\,cm^{-2}}$. In contrast, an alignment laser radius of $w_{0,\mathrm{las}} = 25\,\mu\mathrm{m}$ requires a power of 106 kW and yields a peak intensity of $1.1 \times 10^{10}\,\mathrm{W\,cm^{-2}}$. This large beam radius corresponds to a smooth field intensity distribution over the interaction zone as it is shown in Figure 2.5. Thus, a compromise must be found between a high intracavity power and a high enhancement of the peak intensity. For a molecular beam, perpendicular to the x-ray and alignment laser, the molecules would experience a pulse duration of 0.16 µs if a beam with a velocity of $300\,\mathrm{m\,s^{-1}}$ was assumed [150]. The temporal derivative of the field intensity during the pass across the alignment laser is shown in Figure 2.5.

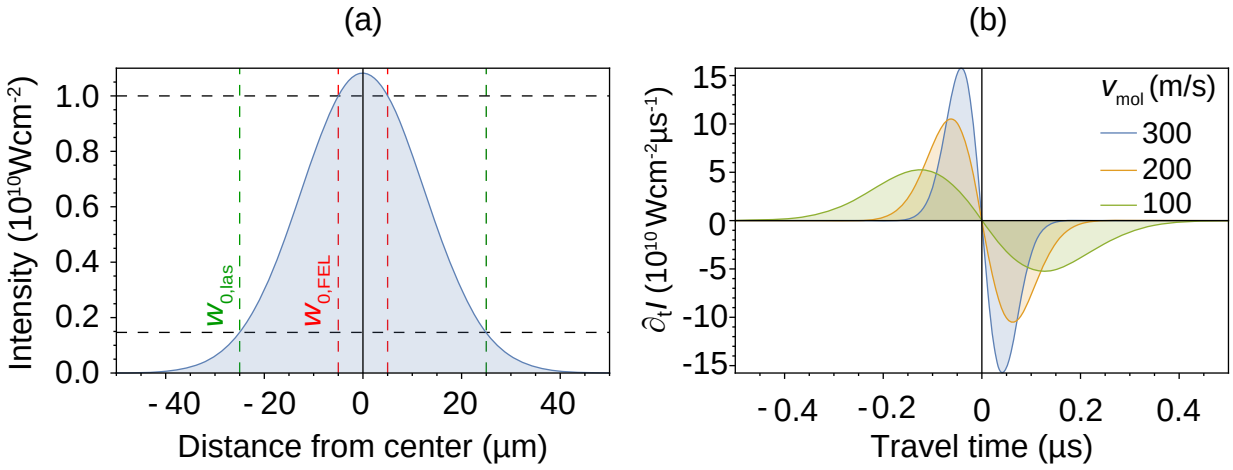

Figure 2.5: (a) A Gaussian transversal intensity distribution with $w_{0,\mathrm{las}} = 25\,\mu\mathrm{m}$. The intensity exceeds $10^{10}\,\mathrm{W\,cm^{-2}}$ in the area where the Gaussian beam overlaps the x-ray probe beam with $w_{0,\mathrm{FEL}} = 5\,\mu\mathrm{m}$. (b) Effective temporal derivative of the intensity for molecules passing the alignment laser perpendicularly with different velocities.

Intracavity alignment with thin-disk lasers The laser powers between approx. 0.1 MW and 10 MW which are necessary to realize peak intensities from 10^{10} W cm^{-2} to 10^{12} W cm^{-2} trigger the subsequent discussion of possible CW laser sources.

100 kW-class CW lasers have been realized as fiber lasers [151], as CO_2 lasers [152, 153], and as chemical DF-lasers [154]. Coherent beam combining [155] is also a viable approach to achieve a laser output at this power level [156]. The TDL geometry has been shown to be suited for very high CW output powers in combination with Yb^{3+}-doped gain materials [61]. Output powers exceeding 27 kW were demonstrated [157] and 100 kW-systems are expected [157, 158]. However, so far these output powers of TDL and fiber lasers are only available at beam qualities that do not allow for tight focusing, necessary to achieve the intended focal intensities [151, 158]. In contrast, carbon dioxide or chemical lasers exhibit good beam qualities at even higher output powers, but the huge space required by the systems and the potentially toxic gain materials are a significant drawback for using these systems as a mobile user facility at modern x-ray light sources. Moreover, operating and propagating any laser at such high output power levels imposes serious safety risks. The identified problems can be avoided by accessing the required field strengths in an enhancement cavity. Enhancement cavities denote resonators, which typically enhance an external laser seeded into a cavity. The cavity finesse, which depends on the overall optical losses of the cavity, defines the maximum enhancement of the seeded laser. This enhancement can be comparable to 2×10^5 [159]. Passive enhancement cavities are widely used with low intracavity powers in quantum optics [160], typically in combination with narrow linewidth CW seed lasers and just recently also with pulsed lasers and high intracavity peak powers for nonlinear optics, e.g., for HHG [161, 162]. Important key parameters of such seeded systems are a high stability of the resonator, a narrow laser linewidth and a high-power seed laser. Especially the operation of a high-power laser with a narrow linewidth is technically challenging. However, the Advanced LIGO gravitational wave detector has an intracavity

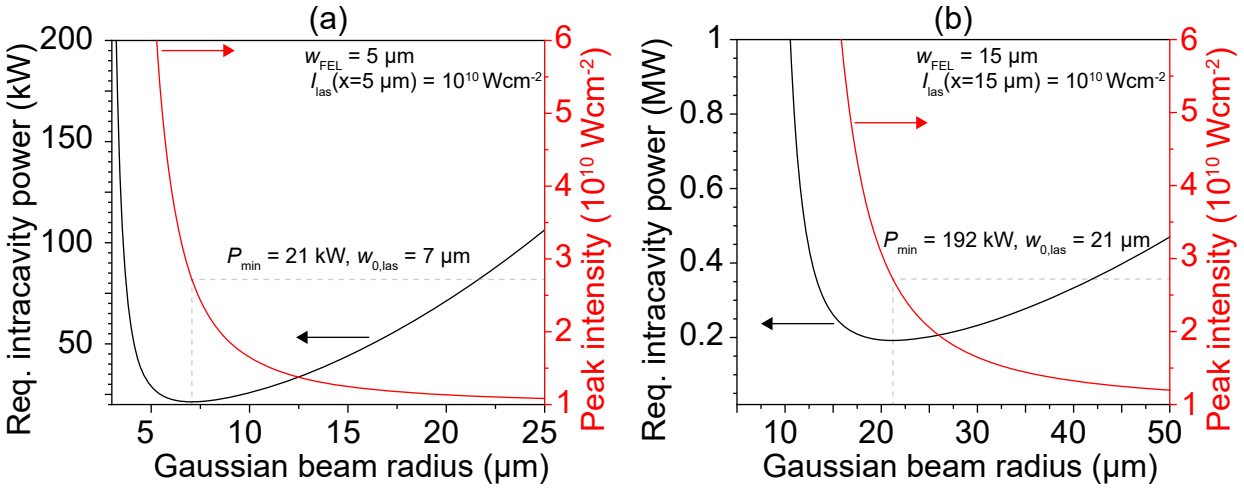

Figure 2.6: The black curve represents the optical power, which is necessary for a Gaussian laser beam to obtain at the radius of an x-ray beam of (a) $w_{0,\mathrm{FEL}} = 5\,\mu\mathrm{m}$ and (b) $w_{0,\mathrm{FEL}} = 15\,\mu\mathrm{m}$ an intensity of $10^{10}\,\mathrm{W\,cm^{-2}}$. The red curve depicts the peak intensity in the center.

power of 700 kW, seeded with an optical power of up to 125 W provided by a Nd:YAG laser system [163], which demonstrates the general feasibility of an intracavity power close to 1 MW with a passive enhancement cavity. A calculation of the achievable intracavity and threshold pump power in dependence of the total resonator losses with a TDL for the laser material Yb:$Y_3Al_5O_{12}$, is depicted in Figure 2.7 (b). In this plot the impact of the bleaching on the absorption efficiency, given by Equation 2.31, and on the threshold power given by Equation 2.39, which is shown in Figure 2.7 (a), are considered. We can learn from this, that an intracavity power of 100 kW can, e.g., be achieved with a pump power of 50 W and losses of approximately 5×10^{-4} or with 600 W of pump power and maximum losses of approximately 5×10^{-3}, which therefore provides an estimation of the upper limit for the maximum tolerable total resonator losses for a given pump power. A homogeneous longitudinal field can be achieved inside the TDL resonator through multi-longitudinal-mode operation. The different modes average out the field distribution around the interaction point. For only a few modes a longitudinally practically homogeneous field is achieved. Under these conditions, spatial hole burning could only occur close to the end mirrors.

Polarization of the electric field For the alignment of linear molecules a polarization extinction ratio (PER) of 100 : 1 is typically used. Polarization selective optical elements can induce a linear polarization. Such optical elements are, e.g., windows in the Brewster's angle, mirrors, with different σ and π reflectivities and un-isotropic gain materials. Losses induced by depolarization, which were previously determined in the order of 1×10^{-3} [136], must be considered. Circular or elliptical polarization eigenstates are possible, if skewed Brewster windows [164] or non-planar ring resonators are used [165, 166].

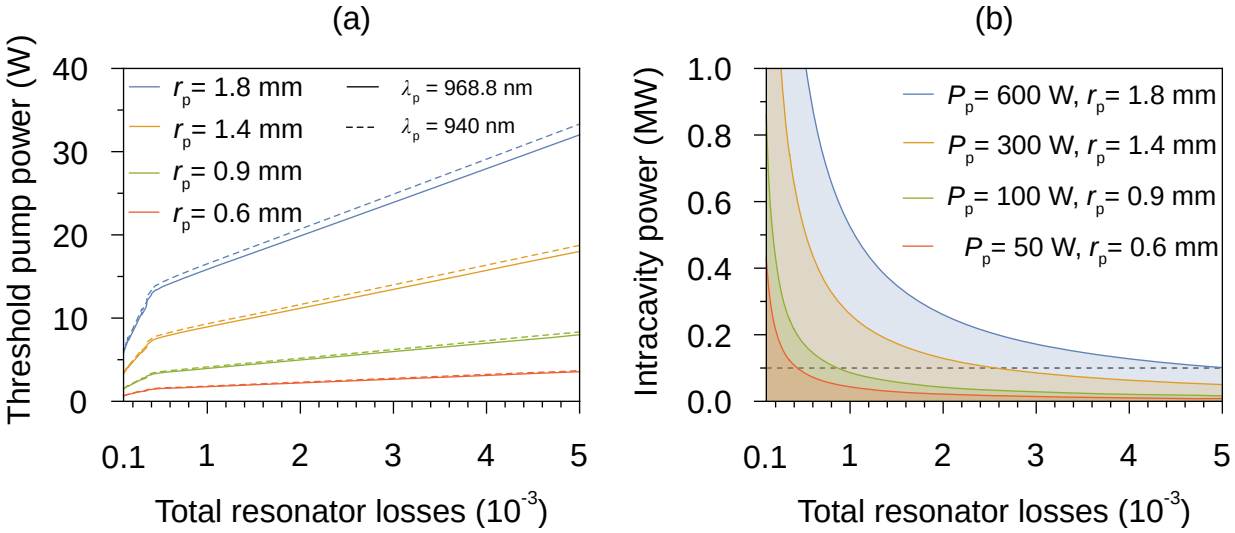

Figure 2.7: Calculation of the (a) threshold pump power and (b) achievable intracavity power with a 200 µm 7 at. % doped Yb:$Y_3Al_5O_{12}$ disk for pump powers and pump spot radii.

Special requirements for x-ray diffraction experiments Diffractive imaging of aligned molecules requires the spatial and temporal overlap of the alignment laser, x-ray, and molecular beam in UHV vacuum. This facilitates two concepts for intracavity alignment with a TDL. The disk and the pump module could be placed outside of a vacuum chamber with optical vacuum windows, transparent on the laser wavelength, while the remaining parts of the resonator would be located inside of the vacuum chamber. This could be beneficial, as it would not require special adaptations at the pump module. The disadvantages of this solution would be that the resonator parts inside and outside of the vacuum chamber were decoupled, which might decrease the resonator stability. In addition, the optical windows could induce additional losses to the laser resonator and endanger the vacuum operation, e.g., by absorption of laser power and subsequent heating. The second possibility would be to place the complete resonator, including the disk and pump module inside of a vacuum chamber. This would require technical modifications of the laser system, due to the lack of convective cooling and the selection of vacuum compatible materials. However, the concept could benefit from an increased resonator stability, possible enhanced cooling possibilities and less sensitivity with respect to external parameters like humidity or dust.

Thin-disk laser at low doping concentration The gain must compensate the losses of a laser during one roundtrip. Typical solid-state laser resonators operate with OC transmissions of a few percent. As the intrinsic resonator losses are usually magnitudes lower, the total resonator losses can be approximated by the losses induced by transmission of the dielectric coatings in the resonator. The calculations shown in Figure 2.7 predict tolerable losses in the order of 10^{-3} to 10^{-4}. This reduces the maximum necessary gain for the loss compensation in comparison to typical laser resonators, which are optimized for high output powers. Therefore, it is possible to reduce the doping concentration or thickness of the host material. This can be beneficial in respect to the thermal management due to an increased thermal conductivity and further energy migration losses [86, 88]. The maximum possible inversion β_{max} at a given pump wavelength can be calculated from the absorption cross section and the emission cross section according to Equation 2.33. The gain cross section is calculated for an arbitrary inversion $\beta \ll \beta_{\mathrm{max}}$ as

$$\sigma_{\mathrm{gain}}(\lambda_{\mathrm{las}}) = \beta\sigma_{\mathrm{em}}(\lambda_{\mathrm{las}}) - (1-\beta)\sigma_{\mathrm{abs}}(\lambda_{\mathrm{las}}). \tag{2.92}$$

The steady state laser condition requires the belance of losses and gain during one roundtrip

$$T + L = 2\sigma_{\mathrm{gain}} N_{\mathrm{dop}} l_{\mathrm{cr}}. \tag{2.93}$$

This can be rearranged to

$$N_{\mathrm{dot}} = \frac{T+L}{2\sigma_{\mathrm{gain}} l_{\mathrm{cr}}} \tag{2.94}$$

which allows to calculate the minimum required doping concentration to achieve steady state operation. The minimum required ytterbium doping concentration is depicted in Figure 2.9. We can learn from this, that lower doping concentration could be used to compensate losses below 10^{-3}. However, a decrease of the doping concentration causes

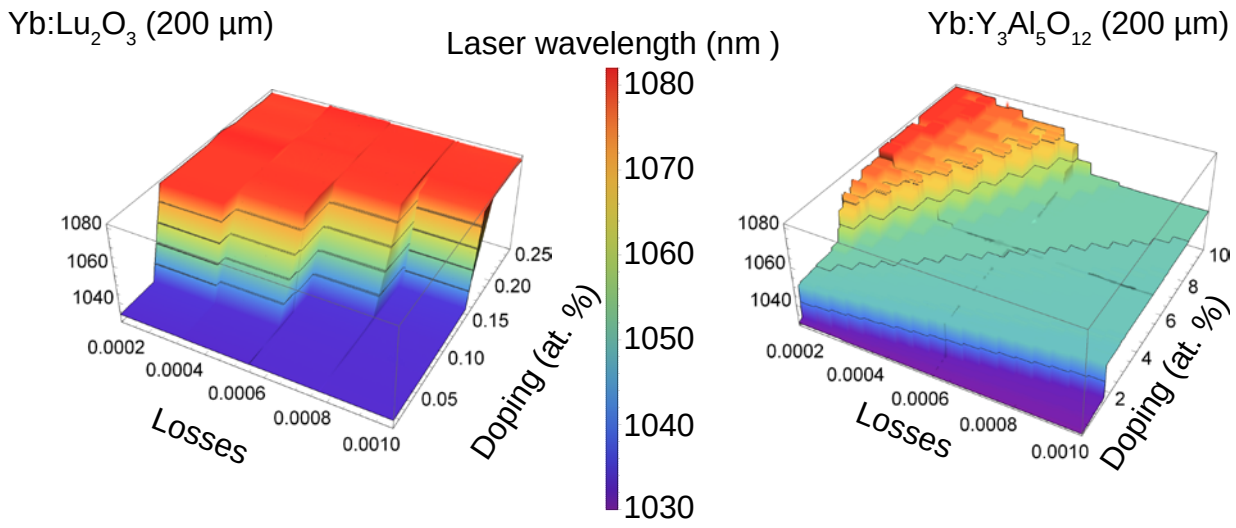

Figure 2.8: Calculated laser wavelength for a 200 µm (a) Yb:Lu_2O_3 and a (b) Yb:$Y_3Al_5O_{12}$ disk.

a decrease of the absorption of the disk. To calculate this, it must be considered, that the absorption efficiency decreases according to Equation 2.31. The absorption efficiency of the disk can then be calculated with Equation 2.30 and is shown in Figure 2.9 (b) for a 200 µm Yb:$Y_3Al_5O_{12}$ disk and losses of 10^{-4}. It is visible, that the doping concentrations which would be sufficient to balance the losses by the gain are not suitable to achieve sufficient absorption, for today's TDLs. A further increase of the pump passes would allow the use of thinner disks with a lower doping concentration. This, however, would increase the requirements to the beam quality of the high-power diode pump sources, the alignment sensitivity of the pump module and to the spherical form accuracy of the disks.

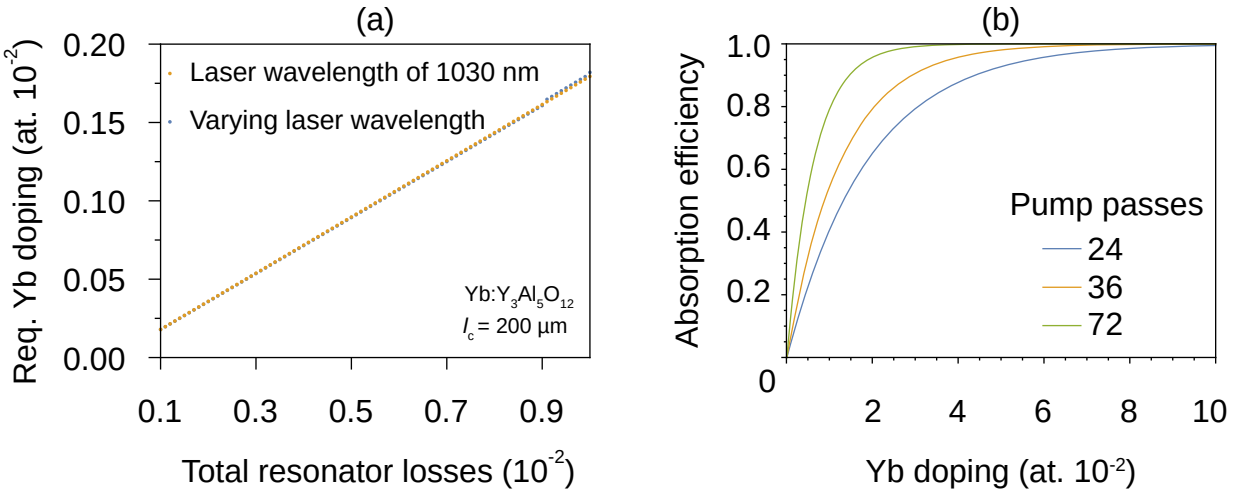

Figure 2.9: (a) The minimum doping concentration for a 200 µm Yb:$Y_3Al_5O_{12}$ disk, which is required to balance the total resonator losses. The loss and doping laser wavelength is depicted in Figure 2.8 (b) Plot of the absorption efficiency of a 200 µm Yb:$Y_3Al_5O_{12}$ disk.

3. The gain materials

This chapter comprises a compact introduction into the spectroscopic and the thermo-mechanic properties of Yb:$Y_3Al_5O_{12}$ and Yb:Lu_2O_3. First, the general requirements for TDL materials and the suitability of ytterbium doped host materials are discussed, which is followed by a set of the most relevant spectroscopic and thermo-mechanic properties of Yb:$Y_3Al_5O_{12}$ and Yb:Lu_2O_3. While the spectroscopy is relevant for the selection of pump sources and the design of coatings, unsuitable key parameters like the thermal conductivity can prevent the use of a laser material in a high-power TDL.

3.1 Requirements for thin-disk laser gain materials

A gain material can be suitable for high-power TDL, if it exhibits a high power-conversion-efficiency, a high thermal conductivity, large absorption cross sections for available pump sources, large gain cross-sections for low threshold-pump powers and if it is available at a good optical quality. The highest conversion efficiency for diode-pumped solid state lasers can be achieved for quasi-three-level systems [62]. In contrast to four-level lasers these materials have a small quantum defect and thus a large optical-to-optical efficiency. The laser medium must exhibit sufficient absorption cross sections which can be accessed by available high-power laser diodes. The intended application for alignment of molecules requires the circumvention of resonances between the alignment laser and transitions in the molecules. Suitable for the application is therefore a laser operation in the near infrared spectral region, especially between 800 nm and 1200 nm [167, p. 5]. In case of quasi-three-level gain materials a high thermal occupation of the lower laser level must be avoided for a high optical-to-optical efficiency. Therefore, the temperature of the laser medium must be controlled. The quantum defect typically depicts the main contribution of heat [168, 169]. The conducted heat must be dissipated from the disk. Therefore, a high thermal conductivity of the gain medium is beneficial [170]. The thin disks are mounted on fluid cooled heatsinks for efficient heat removal. A low thermal resistance of the heatsink is necessary for an efficient cooling. Suitable materials are metal alloys or chemical vapour deposition (CVD) diamonds [136]. The heatsink's material benefits from a comparable coefficient of thermal expansion (CTE) to avoid deformation and damage of the gain material [171]. Additionally, the thin disk can be deformed by a different thickness of its AR and HR coating. The design of the coatings requires knowledge of the refractive index of the gain materials. Besides the thermal conductivity and the CTE also the refractive index n is temperature dependent. Depending on the spatial profile of the laser and pump mode a radial varying temperature profile can thus lead to a similar profile of the refractive index. This influences as an additional lens the resonator stability and materials with low temperature dependence are favorable.

3.2 Common ytterbium-doped thin-disk laser materials

Since the first demonstration of the TDL a multitude of different host materials and dopants were tested. The first laser material which was used in a TDL was Yb:$Y_3Al_5O_{12}$ in 1994 [61, 172]. Since that time ytterbium-doped host materials are prevalent in commercial TDL. Besides ytterbium, other ions were used for thin-disk materials, e.g., thulium, holmium or neodymium [61]. A recent comparison of ytterbium doped host materials for TDL can be found in [173], which was recently enlarged by titanium-sapphire lasers [174] and Yb:$Gd_3Ga_5O_12$ [175]. Yb:$Y_3Al_5O_{12}$ is suitable for the TDL concept because of its small quantum defect. Due to the simple energy scheme of Yb:$Y_3Al_5O_{12}$ parasitic effects are improbable. Furthermore, Yb:$Y_3Al_5O_{12}$ has a thermal conductivity sufficient for high pump densities and can be manufactured in a high optical quality. A similar material is Yb:$Lu_3Al_5O_{12}$[176–178]. For both the spectroscopic properties are comparable with but Yb:$Lu_3Al_5O_{12}$ has the advantage of a higher thermal conductivity. Output powers higher than 5 kW were demonstrated for both materials [176]. For the generation of ultra-short pulses, gain materials with a broad and smooth gain bandwidth are favorable. Here, Yb:Lu_2O_3 [179, 180] attracted attention in the last decade. Its broad gain bandwidth introduces it as a suitable gain medium for the generation of ultra-short pulses. Additionally, the high thermal conductivity allows for high pump densities. However, crystals of Yb:Lu_2O_3 are, nowadays, not available at a constant high optical quality. This is a prerequisite for commercial acceptance for high power lasers and causes that this laser material is not used industrially.

3.3 Properties of the laser materials Yb:$Y_3Al_5O_{12}$ and Yb:Lu_2O_3

3.3.1 Phonons

Phonons describe lattice vibrations in solids as a quantum mechanical quantization of excited vibrational modes. The different modes can be categorized into acoustical and optical phonons. Acoustical phonons describe coherent movements of the atoms and optical phonons out-of-phase movements of the atoms in the lattice. Optical phonons exist in crystals with polyatomic unit cells. In an ionic crystal this leads to opposite movements of different atoms, which corresponds to an oscillating electric dipole moment [31]. Electromagnetic waves can couple to that dipole moment and the crystal is called to be infrared-active [181]. Depending on the energy of the phonons, they can broaden electronic transition lines or lead to unwanted pure phonon-assisted transitions between different energy levels. This is suppressed for materials with low phonon energies. In parallel to the influence of the phonons on the optical properties of a crystal, they effect the thermal and electrical conductivity. The published maximum phonon energies for Lu_2O_3 and $Y_3Al_5O_{12}$ are 618 cm^{-1} and 857 cm^{-1}, respectively [182, 183]. In general its magnitude depends on the coordination and size of the cation site. Small cations which are located on sites with a low coordination, are bound more strongly than on high coordinated sites with a larger vibrational energy. This description is consistent as the unit cell of $Y_3Al_5O_{12}$ contains tetravalent sites.

3.3.2 Thermal conductivity

The thermal conductivity can be expressed as integration up to the Debye frequency ω_D

$$\lambda_{th} = \frac{1}{3}\int_0^{\omega_D} c_v(\omega) v_s^2(\omega)\tau(\omega)\mathrm{d}\omega, \tag{3.1}$$

with the heat capacity c_v, the speed of sound v_s and the mean relaxation time t. In dielectric crystals the relaxation time is mainly determined by scattering at defects, by Umklapp processes or phonon-phonon interaction [181] which contribute according to

$$\frac{1}{\tau} = A\omega^4 + B\omega^2 = \frac{V}{4\pi v^3}\underbrace{\frac{c_i(M_i - \sum_i c_i M_i)^2}{\sum_i c_i M_i}}_{\epsilon}\omega^4 + B\omega^2. \tag{3.2}$$

to the relaxation time. The first summand of Equation 3.2 describes the scattering at point defects with the constant A. Additionally, V denotes the atomic volume and the second term describes with the element's/dopant's specific concentration c_i and masses M_i the strength of the scattering at point defects which are combined to the parameter ϵ. For the two hosts the process of ϵ is shown in Figure 3.1 (a). The second summand of Equation 3.2 describes with the constant B the Umklapp processes. If no other processes contribute to the relaxation time, Equation 3.1 can be transformed [53, 184], under the condition of temperatures above the Debye temperature, into

$$\lambda_{th} = (C\lambda_{c=1} + (1-C)\lambda_{c=0})\frac{1}{\chi}\sqrt{\frac{T}{\epsilon}}\arctan\left(\chi\sqrt{\frac{\epsilon}{T}}\right). \tag{3.3}$$

Within Equation 3.3 all parameters were combined into χ and additionally depend on the introduced scattering parameter ϵ. A fit to data of [53, 176, 180] is depicted in Figure 3.1 (b).

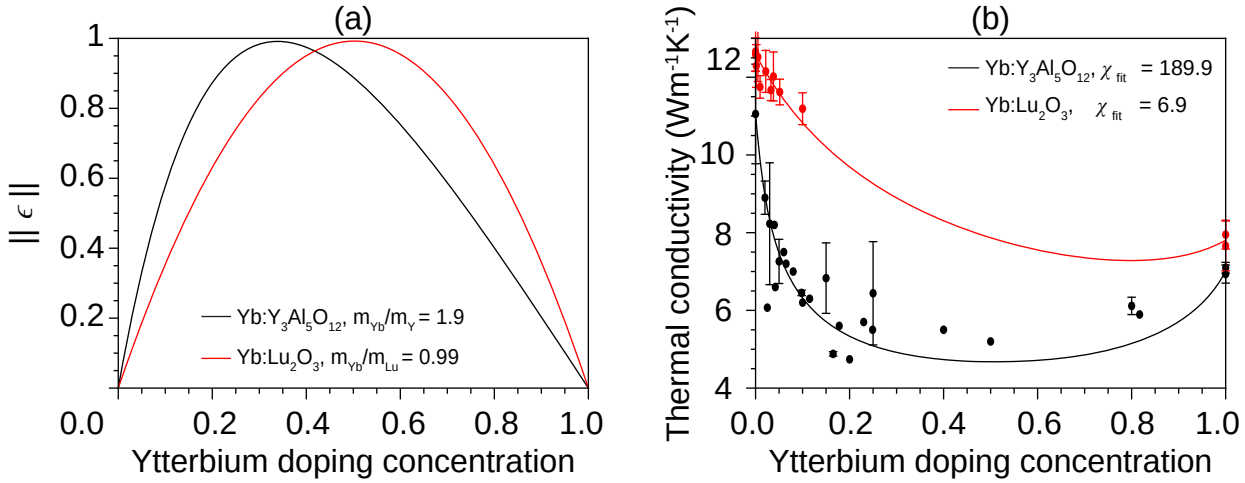

Figure 3.1: (a) Normed scattering parameter ϵ for Yb:Lu_2O_3 and Yb:$Y_3Al_5O_{12}$ according to Equation 3.2. (b) Doping concentration dependent thermal conductivity. Data taken from [53, 180].

3.3.3 Coefficient of thermal expansion

The CTE is inverse proportional to the bond energy of the material. Therefore, solids with higher bond energies typically have a low thermal expansion, a high melting point and vice versa [185]. Data of the CTE of Yb:$Y_3Al_5O_{12}$ exists since decades. This interest was mainly motivated by research for cryogenic ytterbium lasers [168, 186, 187]. Data for $Y_3Al_5O_{12}$ for the temperature range higher than 25 °C was measured interferometrically for a wavelength of 633 nm by Larionov [136]. The data can be described by a fit according to

$$\alpha_{\mathrm{th}}(T) = 9.46 \cdot 10^{-6} \left(1 - \exp\left(-\frac{T}{191.2}\right)\right)^{1.71}. \tag{3.4}$$

However, the mathematical description of this fit, which is depicted in Figure 3.2, is without any physical meaning. A general theoretical description can be found in the work of Reeber [188–191]. In contrast to $Y_3Al_5O_{12}$, the CTE of Lu_2O_3 was not of high interest in the past. Most publications rely on data published by Gmelin [192]. Here, a value for α_{th} of $8.6 \times 10^{-6}\,\mathrm{K}^{-1}$ is specified. Two samples of a 1.5 at. % doped Yb:Lu_2O_3 were polished by Forschungsinstitut f. Mineral u. Metallische Werkstoffe Edelsteine Edelmetalle (FEE). One sample was analyzed by the Physikalisch-Technische Bundesanstalt (PTB) with a phase-stepping interferometer [193]. The second sample was analyzed by P.A. Loiko at the Technical University of Minsk with a dilatometer. The results are depicted in Figure 3.2. Details of the measurement can be found in the corresponding publication [194]. A cubic fit was performed by the PTB according to

$$\alpha_{\mathrm{th}}(T) = -1.69 \times 10^{-6}\,\mathrm{K}^{-1} + 4.51 \times 10^{-8}\,\mathrm{K}^{-2} T - 7.3 \times 10^{-8}\,\mathrm{K}^{-11} T^2 + 3.68 \times 10^{-14}\,\mathrm{K}^{-11} T^3. \tag{3.5}$$

Note, that the polynomial fit in the publication did not include the data from the PTB. The PTB measured a CTE of $5.88 \times 10^{-6}\,\mathrm{K}^{-1}$ at room temperature.

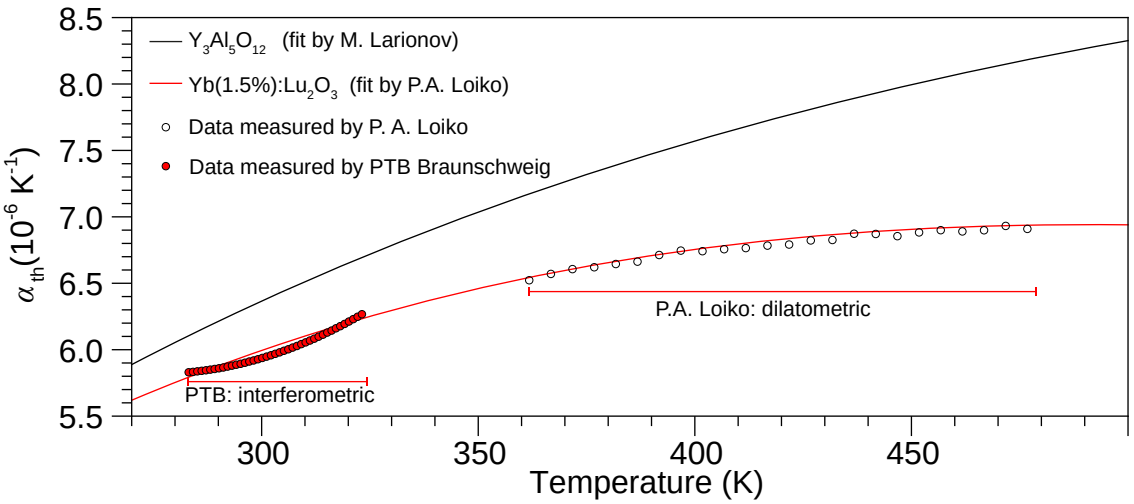

Figure 3.2: Coefficient of thermal expansion of undoped $Y_3Al_5O_{12}$ and 1.5 at. % doped Yb:Lu_2O_3. The function for $Y_3Al_5O_{12}$ originates from a fit by Larionov [136] according to Equation 3.4.

3.3.4 Refractive index

The refractive index n describes the decrease of wavelength and phase velocity of an electromagnetic wave in a medium in comparison to vacuum. In a microscopic view, this deceleration is caused by a phase shift of a reemitted wave by the electrons of the medium in contrast to a laser, where the photons are emitted in phase. This makes it difficult to relate the refractive index of a crystal to its crystallographic properties. However, for glasses, the refractive index typically increases with its density [195].

The disk acts as an active mirror, it has an HR dielectric coating on its backside and an AR dielectric coating on its front side. The optimal selection of the dielectric coating materials to design the required reflectivity requires knowledge of the refractive index of the substrate, or in this case of the laser disk [196]. In parallel, also the temperature dependency of the refractive index is important. This is described by the thermo-optic coefficient $\partial n/\partial T$. A non-constant temperature profile of the thin-disk yields to a varying refractive index, which acts like a thermally induced lens [197].

The refractive index can be measured by the minimum deviation method [128]. A current description of the refractive index of Lu_2O_3 was done by Zelmon et al.[198]. Their measurements were fitted with a temperature dependent Sellmeier equation [199]. The refractive index of $Y_3Al_5O_{12}$ was analyzed by Haynes et al. [200]. They performed the measurements of the wavelength dependent refractive index for different doping concentrations up to 10 at. % ytterbium. The analysis revealed an increase of the refractive index by 1.6×10^{-4} per at. % ytterbium in the near infrared. For a constant wavelength the temperature dependency of the refractive index for Lu_2O_3 can be calculated from the temperature dependent Sellmeier equation. For $Y_3Al_5O_{12}$ measurements at a fixed wavelength were performed for 633 nm and 1064 nm by Aggarwal and Zelmon [198, 201] for temperatures between 80 K and 300 K. The fits of their measurements are shown with the partial derivative in respect to the temperature in Figure 3.3 (b).

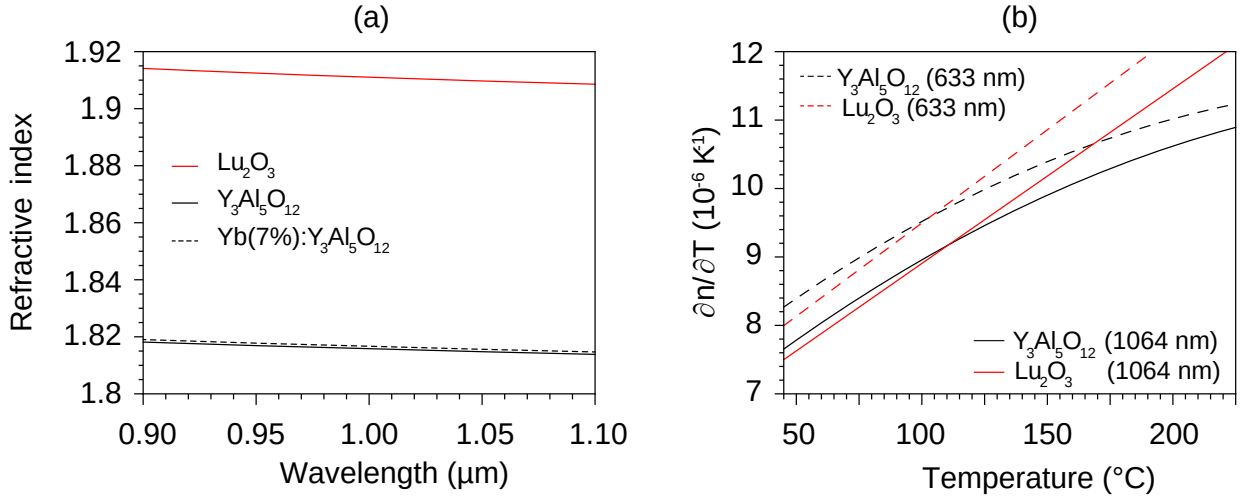

Figure 3.3: (a) Refractive index and (b) thermo-optic coefficient of Yb:$Y_3Al_5O_{12}$ and Yb:Lu_2O_3.

3.3.5 Energy levels of trivalent ytterbium in Lu_2O_3 and $Y_3Al_5O_{12}$

Details and compositions about different assignments and measurements of energy Stark levels in Yb:$Y_3Al_5O_{12}$ can be found in a number of publications [53, 65, 182, 203, 204]. A set of levels which is commonly used, was measured by Bogomolova [202] for a ytterbium doping concentration of 1 at. %. The corresponding energy levels E_i are depicted in Figure 3.4 (a) together with the relative occupation in the specific multiplet N_i/N_{tot} calculated at a temperature of 300 K.

The measurement of Bogomolova determined the zero-phonon line (ZPL) to be at 968.34 nm. The ZPL assignment can be compared with the absorption properties of the laser material. However, as most spectroscopic experiments are performed at room temperature, small differences have to be expected [202]. Böttger measured a thermal shift of the ZPL of 0.271 nm for temperatures between 3 K (968.571 nm) and 300 K (968.842 nm) in vacuum and Voss a shift of 3 pm K^{-1} for temperatures higher than 213 K [66]. The fixing of the ZPL at room temperatures varies in the literature between 968.8 nm and 968.9 nm [67, 136].

Data for Yb:Lu_2O_3 was measured by Mix, Peters and Guyot [182, 205, 206]. A comparison of the three datasets with the absorption spectrum showed the highest compatibility with the data by Mix, even though the data by Peters is used in literature more frequently. The assignment of Mix is shown in Figure 3.4 (b). The measured wavelength of the ZPL of Yb:Lu_2O_3 by Mix is 975.61 nm.

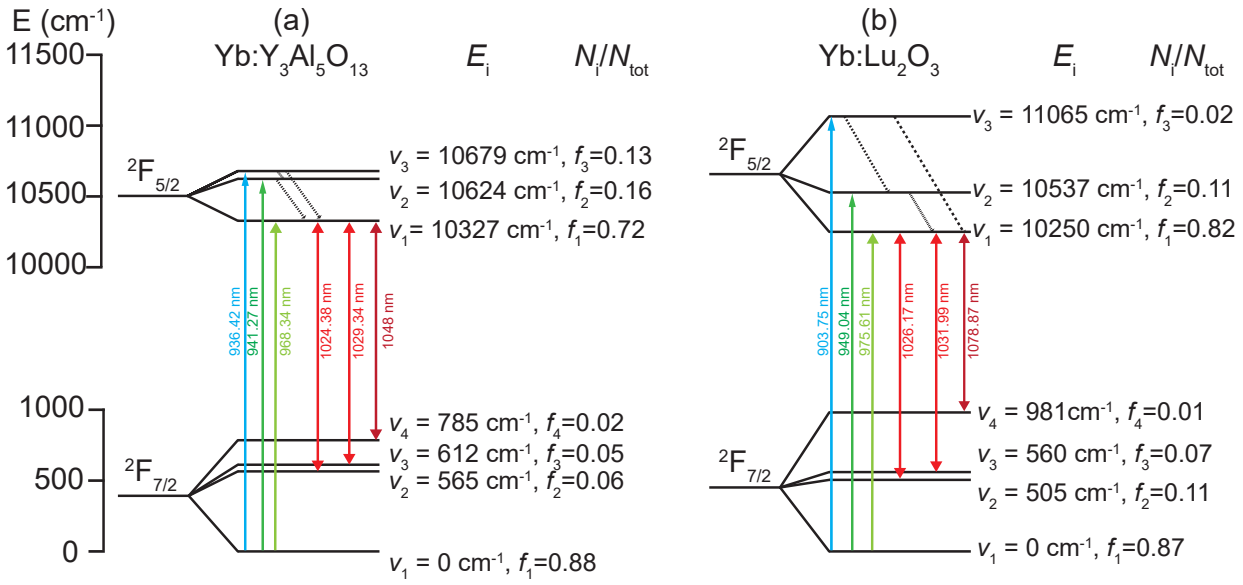

Figure 3.4: Energy levels and relative occupation for Yb:$Y_3Al_5O_{12}$ (a) and Yb:Lu_2O_3 (b). The levels for Yb:Lu_2O_3 refer to the C_2 site. Data of the energy levels is taken from [182, 202]

3.3.6 Lifetime of the excited multiplet

For the planned CW operation, the knowledge of the upper state lifetime of a laser material has mainly one motivation. Its determination is required for the calculation of the emission cross section with the Füchtbauer–Ladenburg equation. The fluorescence lifetime τ can be determined by measuring the time dependent decay of the fluorescence intensity $I(t)$ after an excitation and an initial intensity I_0 according to

$$I(t) = I_0 e^{-\frac{t}{\tau}}. \tag{3.6}$$

The lifetime should be measured with the pinhole method for quasi-three level systems because of radiation trapping [65, 207]. Doping concentration dependent lifetimes can be seen in Figure 3.5. The lifetime of Yb:$Y_3Al_5O_{12}$ remains nearly constant on a value of approx. 950 µs to a doping of 80 %. When all yttrium ions are replaced by ytterbium the lifetime decreases to 850 µs. The constant trend up to high doping concentrations contradicts with the measurement by Peng [204]. Furthermore, Contag measured a strong decrease of the lifetime with an increasing doping concentration for Yb:$Y_3Al_5O_{12}$ [67].

Due to the measured strong decrease of the interatomic distances, a change of the local crystal field could be expected. A different trend shows Yb:Lu_2O_3 with the data measured by Peters [180]. From a doping of approx. 3 % and a value of 820 µs, an increasing behaviour can be seen up to a lifetime of 970 µs. The reason for this effect could not be explained yet, but a link to an increased radiation trapping or a change in the local crystal field cannot be ruled out [180].

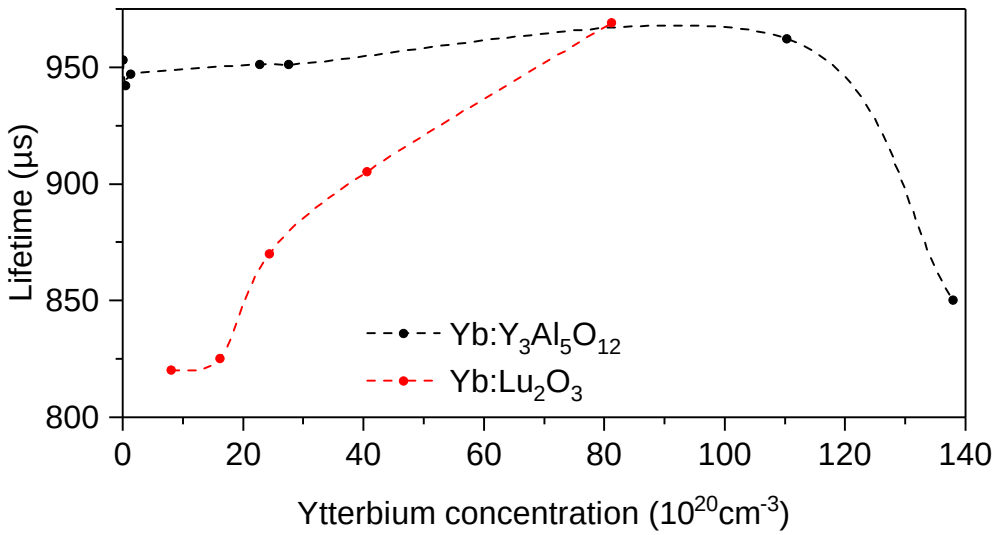

Figure 3.5: Upper state radiative lifetimes for Yb:$Y_3Al_5O_{12}$ [53] and Yb:Lu_2O_3 [180]. The connection between the data points depicts a guide to the eye.

3.3.7 Absorption cross sections

If an initial photon flux Φ_0 passes an isotropic medium, the flux Φ changes according to

$$\frac{d\Phi}{dz} = -\alpha\Phi_0 \tag{3.7}$$

with the absorption coefficient α, which is solved by the Beer-Lambert law

$$\Phi = \Phi_0 e^{-\alpha(\lambda) l_{cr}}. \tag{3.8}$$

To obtain a form which is independent of the doping density n_{dop}, a total cross section can be introduced by

$$\sigma_{tot} = \frac{\alpha(\lambda)}{N_{dop}} = \sigma_{abs} + \sigma_{scat} + \sigma_{lum}. \tag{3.9}$$

The total cross section σ_{tot} includes the sum of absorption σ_{abs}, scattering σ_{scat} and luminescence cross section σ_{lum}. The absorption cross section can be calculated with the measured transmission $T = \Phi/\Phi_0$ at a length l_{cr}, which allows the determination of the absorption cross section according to

$$\sigma_{abs} = \frac{\ln(T)}{l_{cr} \cdot N_{dop}}. \tag{3.10}$$

The transmission measurements were done with a Cary 5000 UV-VIS NIR. The results are depicted in Figure 3.6. It is recognizable, that the ZPLs of both materials can be pumped, e.g., by InGaAs diode lasers, which are commercially available with high output powers.

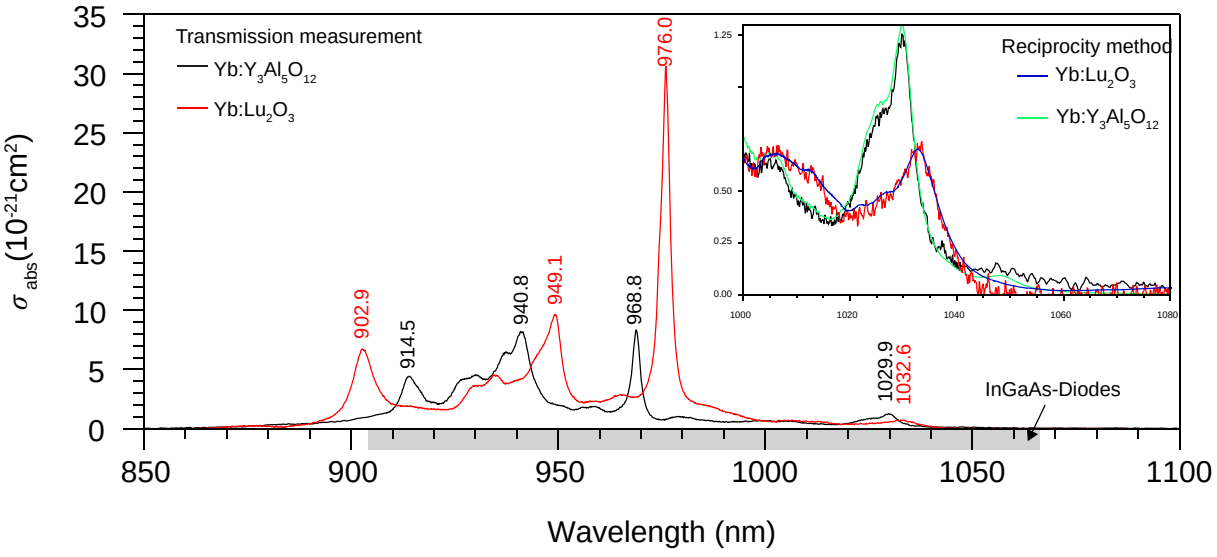

Figure 3.6: Absorption cross sections of Yb:$Y_3Al_5O_{12}$ and Yb:Lu_2O_3. The inset shows the same data between 1000 nm and 1100 nm and cross sections calculated with Equation 3.11 (reciprocity method), which provides a larger SNR for long wavelengths.

3.3.8 Emission cross sections

The emission cross sections are typically constructed with the McCumber relation [59] and the Füchtbauer-Ladenburg relation [208]. The McCumber relation connects the absorption cross section σ_{abs} with the emission cross section σ_{em} according to

$$\sigma_{em}(\lambda) = \sigma_{em}(\lambda)\frac{Z_l}{Z_u}\exp\left(\frac{E_{ZPL} - \frac{hc}{\lambda}}{k_B T}\right). \tag{3.11}$$

In this equation E_{ZPL} denotes the energy of the ZPL and T is the temperature of the absorption measurement. An alternative possibility to determine the emission cross section is the Füchtbauer-Ladenburg relation, according to

$$\sigma_{em}(\lambda) = \frac{\lambda^5}{8\pi c n^2 \tau_{rad}}\frac{I(\lambda)}{\int I(\lambda)\mathrm{d}\lambda}, \tag{3.12}$$

with the spectral shape of fluorescence light $I(\lambda)$. Emission cross sections are typically constructed by a combination of both methods. The McCumber relation in Equation 3.11 is used for the determination of the absolute cross sections. The results of the Füchtbauer-Ladenburg method are adjusted to the ones by the McCumber equation for long wavelengths. Vice versa, the absorption cross sections can be constructed from the emission cross sections to reduce the SNR at long wavelengths, as it is depicted in the inset of Figure 3.6.

The emission cross sections are shown for both laser materials in Figure 3.7.

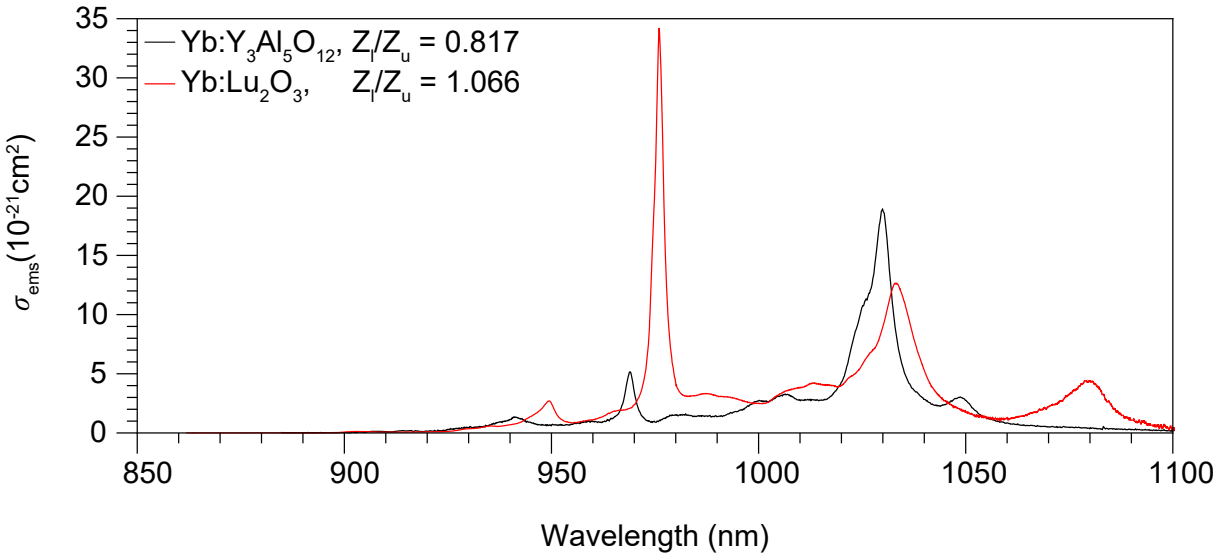

Figure 3.7: Emission cross sections of Yb:$Y_3Al_5O_{12}$ and Yb:Lu_2O_3. The data for the partition functions was taken from Bogomolova [202] and Peters [205] for Yb:$Y_3Al_5O_{12}$ and Yb:Lu_2O_3, respectively.

3.3.9 Gain cross sections

The gain cross section σ_{gain} allows predictions about the expected central laser wavelength in dependence of the total resonator losses. This is essential for the mirror coating design and the thermal management of the laser system. It specifies the minimal length, or doping concentration required for the balance between the total resonator gain and the losses according to Equation 2.93. The gain cross section can be calculated from Equation 2.92. Vice versa, the required inversion can be calculated for a laser wavelength λ_{las} from

$$\beta(\lambda_{\text{las}}) = \frac{\frac{L}{M_r l_{\text{cr}} N_{\text{dop}}} + \sigma_{\text{abs}}(\lambda_{\text{las}})}{\sigma_{\text{abs}}(\lambda_{\text{las}}) + \sigma_{\text{em}}(\lambda_{\text{las}})}. \tag{3.13}$$

The gain cross section of Yb:$Y_3Al_5O_{12}$ und Yb:Lu_2O_3 can be seen in Figure 3.8. For Yb:Lu_2O_3 the calculation was done for two different partition functions from Mix and Peters. The absorption spectrum was calculated from the emission spectrum by the McCumber relation. This increases the SNR for long wavelengths. The gain cross section shows, that both materials, in principle, even allow laser operation around 1100 nm for low inversions of 5×10^{-3}. However, because of the low required losses, these wavelengths can typically not be seen in usual laser experiments.

At the threshold the laser tends to oscillate at the wavelength of its lowest required inversion. Here, Equation 3.13 in principle, allows, to include even wavelength dependent losses. The lowest inversion can be found mathematically by searching for the global minimum. A calculation of the threshold's laser oscillation wavelength in dependence on the inversion, and according to Equation 3.13 thus on the doping concentration N_{dop} and on the total resonator losses L, is presented in Figure 2.8.

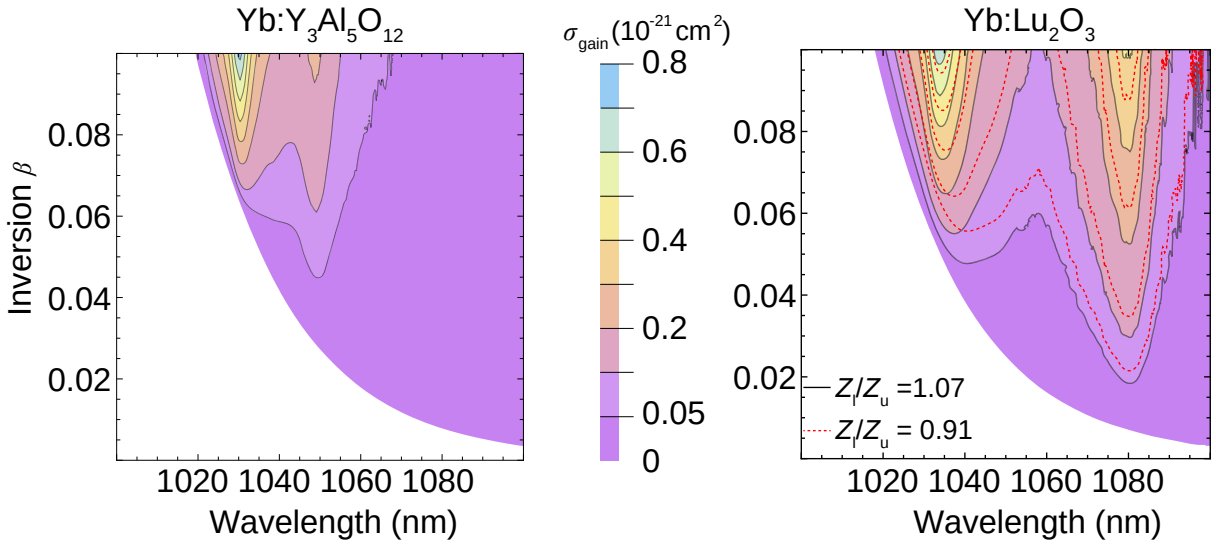

Figure 3.8: Gain cross sections of $Y_3Al_5O_{12}$ and Yb:Lu_2O_3. The smaller partition function for Yb:Lu_2O_3 (red, dashed) yields a smaller gain cross section due to the reduced emission cross section.

4. Experimental setup

The laser experiments not only consisted in the implementation, but also in the design, set up and characterization of TDL resonators with different gain materials. In this chapter, the focus lies on the laser-experiment's setup. First, the available pump sources at that time are depicted. Then, the thin disk's preparation, including, e.g., polishing or contacting is described. The chapter is completed with the presentation of certain methods, such as the determination of the intracavity focus or the measurement of the laser disk's surface maps, by which the resonators may be characterized.

4.1 The InGaAs pump laser diodes

Two different TDL modules (IFSW Stuttgart) with 24 pump passes were employed for the laser experiments. For pump powers up to approx. 70 W and 700 W pump spot diameters of 1.2 mm and up to 3.6 mm were used, respectively. Depending on the gain material, four pump sources based on fiber coupled InGaAs laser diodes with fiber diameters of 600 µm were available. The properties of the diodes are summarized in Table 4.1.

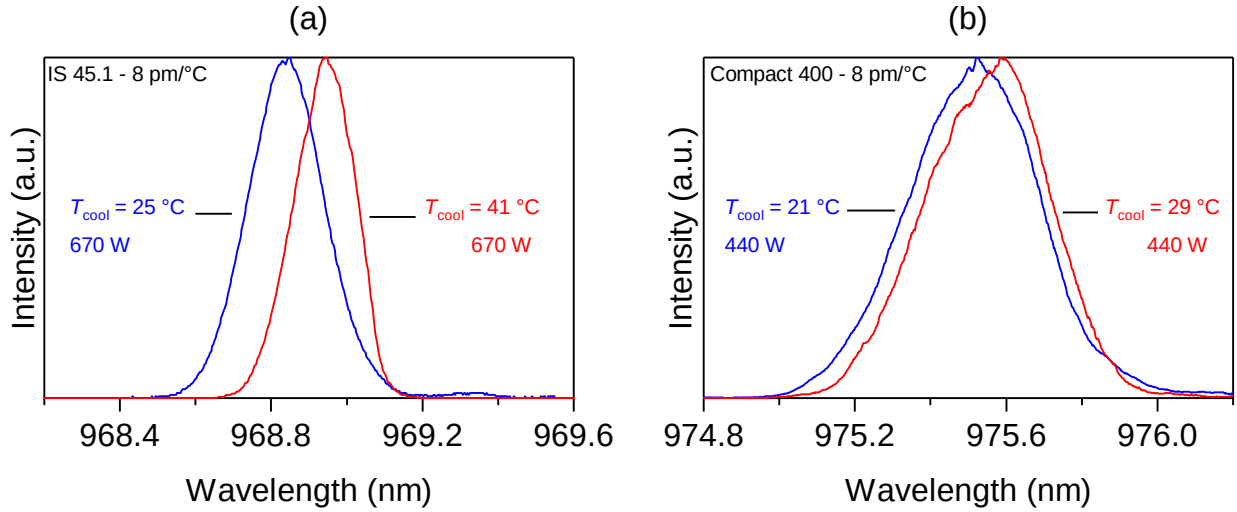

Figure 4.1: Spectral profile of (a) the DILAS IS45.1(VBG) diode and (b) of the the DILAS Compact 400(VBG) diode. Both diodes exhibit a shift of the Gaussian peak central wavelength of approx. 8 pm $°C^{-1}$.

Pump sources for Yb:$Y_3Al_5O_{12}$ For Yb:$Y_3Al_5O_{12}$ two different diodes were available. For a pump target wavelength of 941 nm, one diode laser with two internal diode bars for pump powers up to 75 W with a central wavelength of 938 nm was used (Jenoptik, JOLD-75-CPXF-2P). This diode was employed with a 600 µm fiber to ensure the required pump spot diameter for the available imaging optics. The usage of a 600 µm fiber instead of a 400 µm fiber is beneficial, because the larger fiber core diameter homogenizes the diode laser (optical stacking) and reduces the numerical aperture. The wavelength of the diode laser was adjusted to 941 nm with two water-cooled thermoelectric Peltier elements, which were placed below the diode bars. The temperature was set to 35 °C for the experiments with this laser diode. Emission profiles for the JOLD-75 diode can be found in [53, p. 105].

For the ZPL of Yb:$Y_3Al_5O_{12}$ of 968.8 nm a pump power up to 700 W was available from a volume Bragg grating (VBG) stabilized diode (DILAS,IS45.1-VBG). The electrical power supply of the laser diode was ensured by a high stability driver (Delta Elektronika, SM66-AR-110). The wavelength of the laser diode was adjusted by the cooling-water temperature of the diode system [209, 210]. The regulation of the pump wavelength was necessary as 968.8 nm could only be obtained for a diode current of 35 A at a cooling temperature of 25 °C. The wavelength of the pump source was measured with an optical spectrum analyzer (Yokogawa, AQ6370C). This allowed the automatic adaptation of the water chiller's cooling temperature with LabView. The water temperature was for this purpose controlled with a high stability chiller (Lauda, WC2000W). With this, the central wavelength could be shifted with a temperature dependence of 8 pm $°C^{-1}$ within the recommended cooling range between 10 °C and 40 °C. The temperature dependent shift of the central wavelength is depicted in Figure 4.1 (a). In addition, the diode current dependence of the Gaussian peak central wavelength and the peak's FWHM are shown in Figure 4.2.

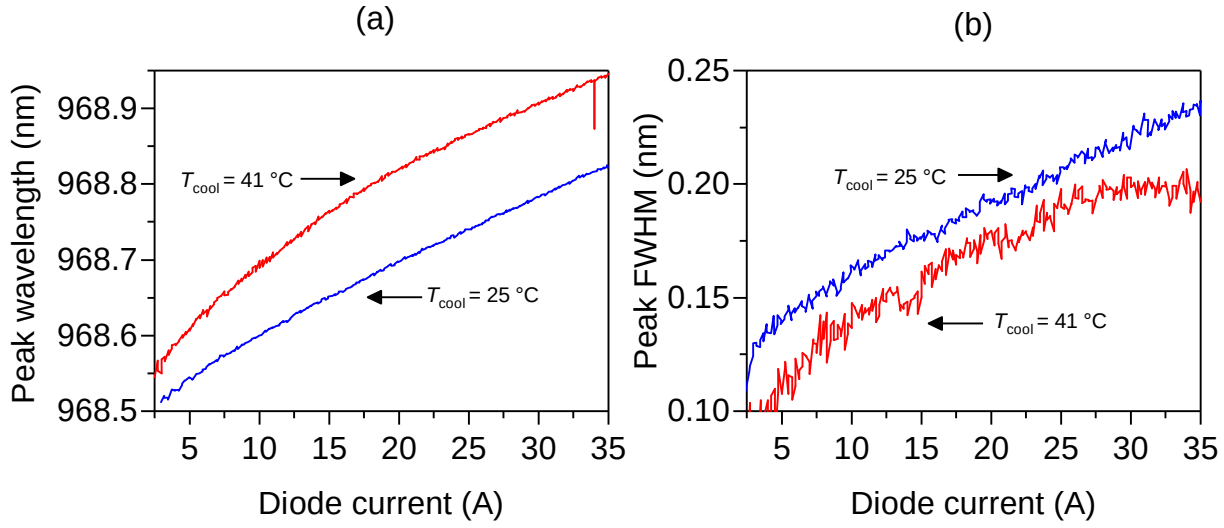

Figure 4.2: Current dependent (a) shift of the peak wavelength and (b) peak FWHM of the emission bandwidth for two different water cooling temperatures for the IS45 diode laser.

	Jenoptik Jold 50	Jenoptik Jold 75	DILAS Compact 400	DILAS IS45.1
Max. power (W)	55	70	450	700
Central wavelength (nm) (25 °C)	980	938	975.6	968.8
Spectral bandwidth (nm) (FWHM)	2.3	5	0.40	0.23
Fiber diameter (µm)	600	400	600	600
Numerical aperture	0.22	0.22	>0.22	<0.12
Comments		used with 600 µm fiber	inaccurate fiber incoupling	

Table 4.1: Relevant properties of the pump sources which were used in the experiments.

Pump sources for Yb:Lu_2O_3 Two pump sources were available for Yb:Lu_2O_3. A diode laser (Jenoptik, JOLD-50-CPXF-2P) for pump powers up to 50 W and wavelengths between 972 nm and 985 nm was used to pump the ZPL of Yb:Lu_2O_3 at 976 nm. The temperature of the diode bars had to be adjusted between 20 °C and 8 °C for this purpose. Emission profiles for this diode can be found in [180]. Pump powers up to 440 W were provided by an integrated VBG stabilized diode laser system (DILAS, Compact 400/600) with a central wavelength of 975.56 nm. A spectrum of the diode is depicted in Figure 4.1 (b). It is noticeable, that the FWHM of the Compact400 system is twice as broad as the one from the newer IS45. This could have been caused by further development at the VBGs. Despite the comparable wavelength shift of approx. 8 pm $°C^{-1}$, the center could only be shifted to a wavelength of approx. 975.6 nm, because of the accessible cooling range of the integrated diode laser system. Furthermore, a sub-optimal fiber-in-coupling of the laser diode caused a donut shaped intensity profile at the fiber nearfield.

4.2 Preparation of the thin laser disks

Gain materials Yb:$Y_3Al_5O_{12}$ disks with a ytterbium doping concentration of 7 at. % were obtained from Dausinger + Giesen (D+G). The disks from D+G had a specified thickness of 220 µm and an average ROC of approx. 5 m. Details about soldering and coating of the disks were not provided, however the use of gold coated copper–tungsten alloy heatsinks (W80/Cu20, cf. [136]) can be presumed. Additional Yb:$Y_3Al_5O_{12}$ disks and a Yb:$Lu_3Al_5O_{12}$ disk with a doping concentration of 10 at. % were provided by the Deutsches Zentrum für Luft- und Raumfahrt (DLR). These disks were polished and coated by LAYERTEC and soldered at 315 °C on copper-tungsten alloy heatsinks (W80/Cu20) from WHS Sondermetalle (WHS) with solder by GPS Technologies GmbH.

Raw material of Yb:Lu_2O_3 was not commercially available in a high optical quality. Therefore 3 at. % doped crystals were grown for this purpose in the Institut für Laser-Physik (ILP) with the heat exchanger method (HEM). In-growth annealing allowed to obtain color free crystals. Despite that, investigations of the boules under crossed polarizers showed significant birefringence. Strong depolarization of the disks was confirmed by the IFSW Stuttgart. Details about the HEM crystal growth can be found in [180].

Polishing The disks must be lapped to a thickness of a few 100 µm and polished to decrease scattering losses. All Yb:Lu_2O_3 disks were lapped and polished by FEE. Despite less inclusions and defects in comparison to previous crystals, the disks were difficult to polish, due to braking shivers from the edges. Measurements by FEE with laser scanning microscope at comparable crystal samples yielded a RMS roughness of approx. 5 nm. In contrast to that, investigations on coated disks with a white light interferometer (WLI) at DESY exhibited a RMS roughness between 0.4 nm and 2 nm. This is consistent with observations from LAYERTEC, who observed that polishing of Yb:Lu_2O_3 was more challenging compared to Yb:$Y_3Al_5O_{12}$ [211]. A higher sensitivity to fracture, caused by larger mechanical stress from the HEM method could be the reason [211].

Coating All coatings on the disks were sputtered at LAYERTEC. For that purpose, the standard procedures for Yb:$Y_3Al_5O_{12}$ had to be adapted to Yb:Lu_2O_3. The number of layer pairs of the HR coating was increased to ensure a reflectivity larger than 0.9999 for wavelengths between 1000 nm and 1100 nm. In addition, also the reflectivity of the ZPL pump wavelength at 976 nm was designed to be larger than 0.9999 for an angle of incidence (AOI) up to 25°. Increase of the layer pairs can be beneficial for disks on diamond heatsinks. These disks are glued onto the diamond and the transmission of the HR coating can depict a substantial loss. The AR coating was designed to have a reflectivity lower than 0.2 % from 1030 nm to 1080 nm and lower than 0.5 % for 976 nm and an AOI between 10° and 43°. The calculated influence of the number of layer pairs is depicted for an exemplary coating in Figure 4.3. The calculations show, that already QWS systems with approx. 15 layer-pairs can achieve reflectivities in the order of 0.9999.

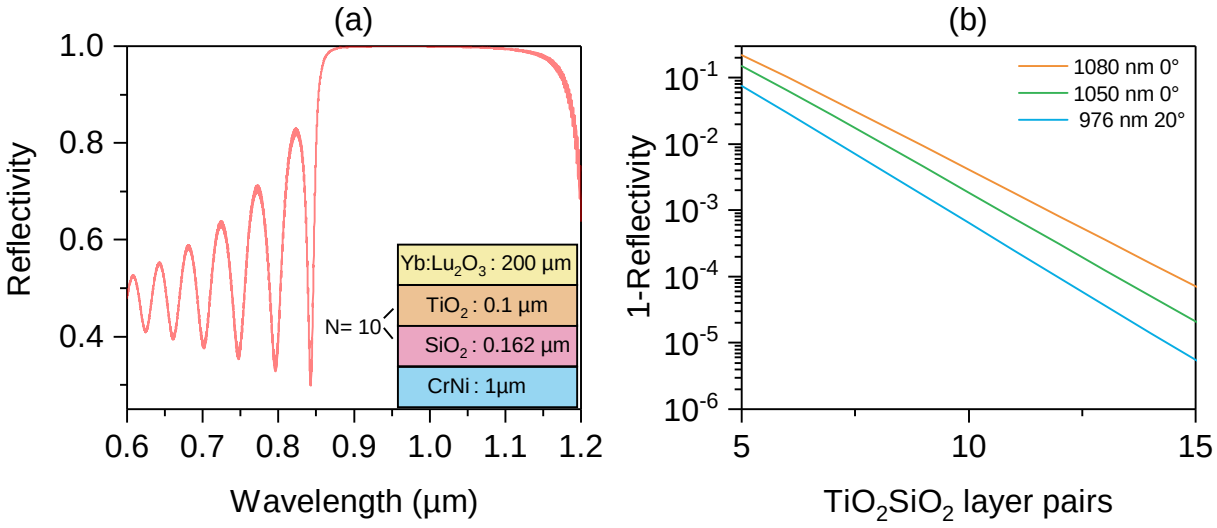

Figure 4.3: (a) Calculation of the reflectance of a QWS coating structure, designed for a center wavelength of 1 µm. (b) Dependence of the transmission on the number of oxide layer pairs. The refractive indices of the oxide layer materials were taken from [212].

Contacting Details about different contacting methods can be obtained from [136, 173, 213]. The contacting of the Yb:Lu_2O_3 disks was done with two methods. Three disks were contacted on CVD diamond heatsinks by D+G. This contacting has mainly two advantages. First, because of the stiff contacting method, the ROC of the disk remains nearly constant for different pump intensities [214]. This is beneficial for the resonator design, as no dynamic changes of the disk's variable lens must be considered. Additionally, the thermal management can be improved because of the high thermal conductivity of the CVD diamond [173]. The disadvantages are the production costs of the heatsinks and mechanical stress for an increased pump intensity because of the stiff contacting and the different CTEs. Most of the unsoldered Yb:Lu_2O_3 disks showed an ROC between 0.5 m and 1 m. Therefore, CVD diamond heatsinks with a comparable ROC were used in order reduce the mechanical stress in the crystal-diamond system during laser operation.

Until then, copper-tungsten alloy heatsinks (W80/Cu20) with a CTE of $8.8 \times 10^{-6}\,K^{-1}$ were used for Yb:$Y_3Al_5O_{12}$ and Yb:Lu_2O_3. In this work, the PTB refined the CTE of Yb:Lu_2O_3 to $5.88 \times 10^{-6}\,K^{-1}$. Therefore, W90/Cu10 (pseudo) alloy heat sinks were used. Those are with a CTE of approx. $6.5 \times 10^{-6}\,K^{-1}$ better suited than W80/Cu20. The heat sinks were galvanically coated with 3 µm nickel and 1 µm gold by WHS to ensure the wettability for the soldering [136]. Alternatively, a tungsten high density alloy (W90NiFe/W90NiCu) with a CTE of $5.8 \times 10^{-6}\,K^{-1}$ could be used. The disks were soldered onto the heatsinks by D+G. It must be noted that D+G observed irregularities of the heatsinks and a lower contact of the disks as usual. The irregularities (small bubbles) can also be seen in the Nomarski interference contrast image in Figure 4.4. With this method, optical path differences (OPDs) become visible as image contrast. An insufficient wetting and contact between disk and heatsink has impact on the thermal resistance of the system, which finally might have been lower than expected.

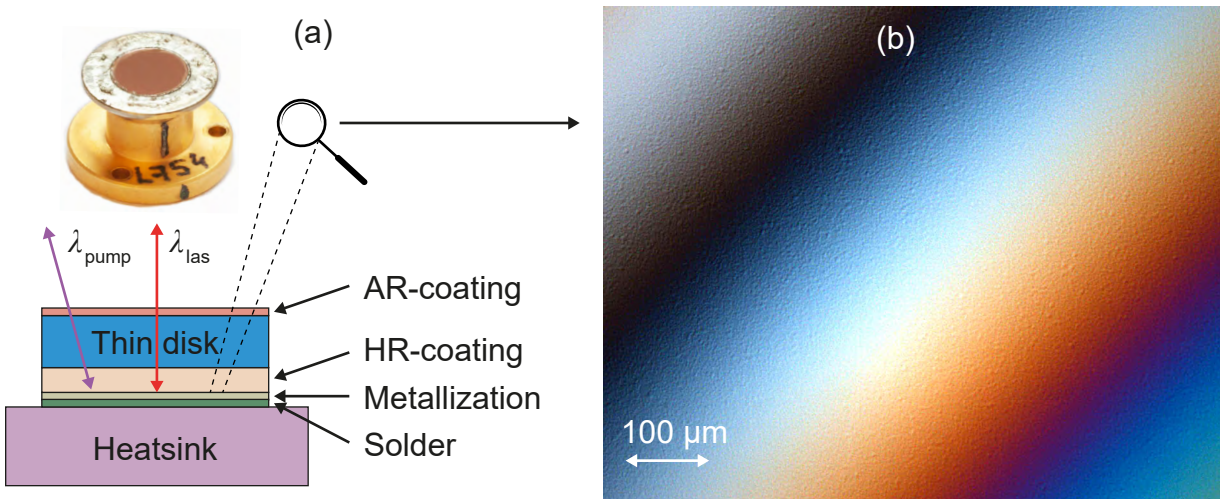

Figure 4.4: (a) Top: Yb:$Y_3Al_5O_{12}$ disk soldered on a copper-tungsten alloy heatsink. Bottom: Scheme of the different layers of the thin-disk. (b) Nomarski microscope image of the disk's rear side, which shows the roughness and the insufficient contacting of the heatsink/metallization system.

4.3 Characterization of the laser resonators

4.3.1 Wavefront measurements

A Shack–Hartmann wavefront sensor (SHWFS) measures the local tilt of an incident wavefront [215, 216]. The spatial resolution is determined by the pitch of a micro-lens-array, which images the local tilt of the wavefront on a camera sensor. A subsequent mathematical fit of the wavefront with Zernike polynomials allows to analyze the profile and to reconstruct the wavefront. To obtain a height profile of a surface, the sample must be illuminated and imaged onto the CMOS sensor.

This was done with the optical setup depicted in Figure 4.5. A diode pumped Nd:YAG (Altechna, DPSL1064) with a wavelength of 1064 nm was used as illumination. The further setup consisted of two telescopes and a beam splitter. The first telescope with $f_1 = 25\,\text{mm}$ and $f_2 = 100\,\text{mm}$ was used for the adjustment of the beam size on the disk and to obtain a flat wavefront.The second telescope with $f_3 = f_4 = 200\,\text{mm}$ imaged the disturbed wavefront onto the SHWFS. A flat super polished mirror (ATFilms) was used as reference to correct for any remaining optical disturbances of the optical system. The determination of the radius of curvature and additional optical perturbations of the disk were done using the software MrBeam (LL Göttingen).

In principle, the presented optical setup would also be suitable for the live survey of disks inside of a resonator. However, this would require a bandpass filter at the illumination laser wavelength to suppress the fluorescence originating from the pumped laser disk. Preliminary tests with a laser line filter for 1064 nm were unsuccessful because of strong wavefront distortions by the filter, which could not be compensated.

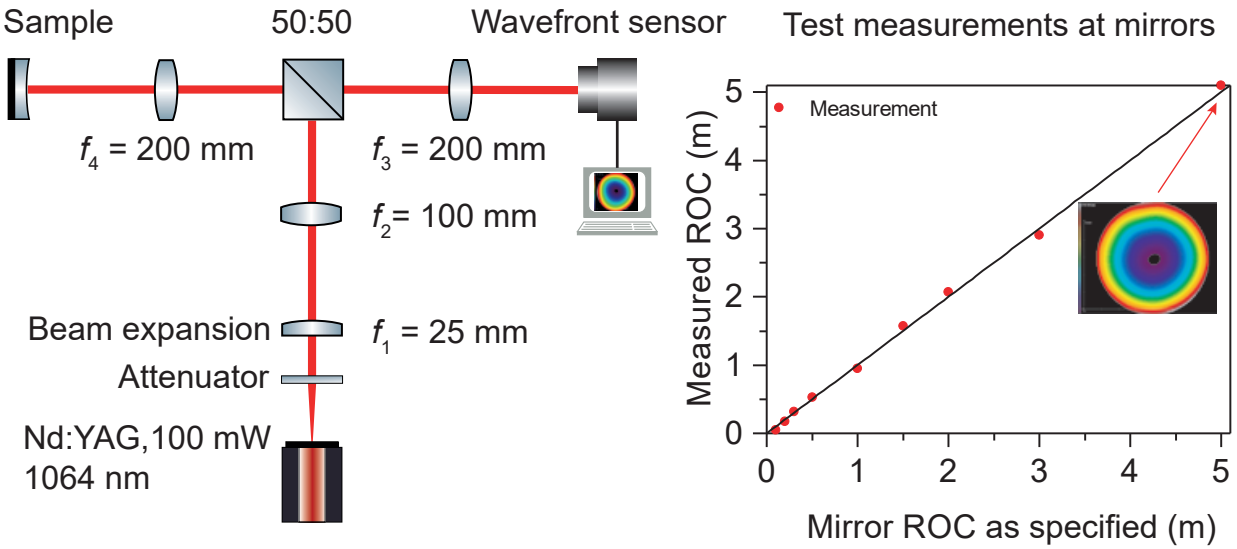

Figure 4.5: Setup for the determination of ROC of laser disks. The right part shows the measured data for mirrors with defined ROC.

4.3.2 Intracavity beam radius

The intracavity peak intensity depends on the Gaussian beam waist w_0 according to

$$I_\mathrm{p} = \frac{2P}{\pi w_0^2}. \tag{4.1}$$

Therefore, measurement of the intracavity beam radius is essential to ensure intensities which are sufficient for the adiabatic alignment of molecules. However, measurement of the intracavity caustic must be noninvasive in respect to the intracavity laser beam. In principle, an optical imaging system behind the OC mirror could be used for this purpose. By measuring of the far field beam divergence angle θ it is possible to calculate the Gaussian beam radius w_0 with the beam quality M^2 according to

$$\frac{w_0\theta}{4} = M^2\frac{\lambda}{\pi}. \tag{4.2}$$

It must be considered that the beam gets disturbed by the OC. This can be avoided by an imaging system set up perpendicular to the laser beam. As no direct beam can be imaged here, only light-matter interaction can be observed. In case of a laser resonator in air, this corresponds to Rayleigh or Mie scattering at atmospheric molecules or larger particles. This direct measurement has the advantage that in comparison to Equation 4.2, knowledge of the precise beam quality is unnecessary. The Rayleigh scattering cross section depicts losses in the order of a few ppm for meter long cavities in air at a wavelength of 1 µm. Because of the low losses, this makes it ideal to image the intracavity beam radius. In principle, this scheme is also applicable for a cold molecular beam in vacuum, given that the scattering cross section of the molecules is large enough to scatter enough photons for the

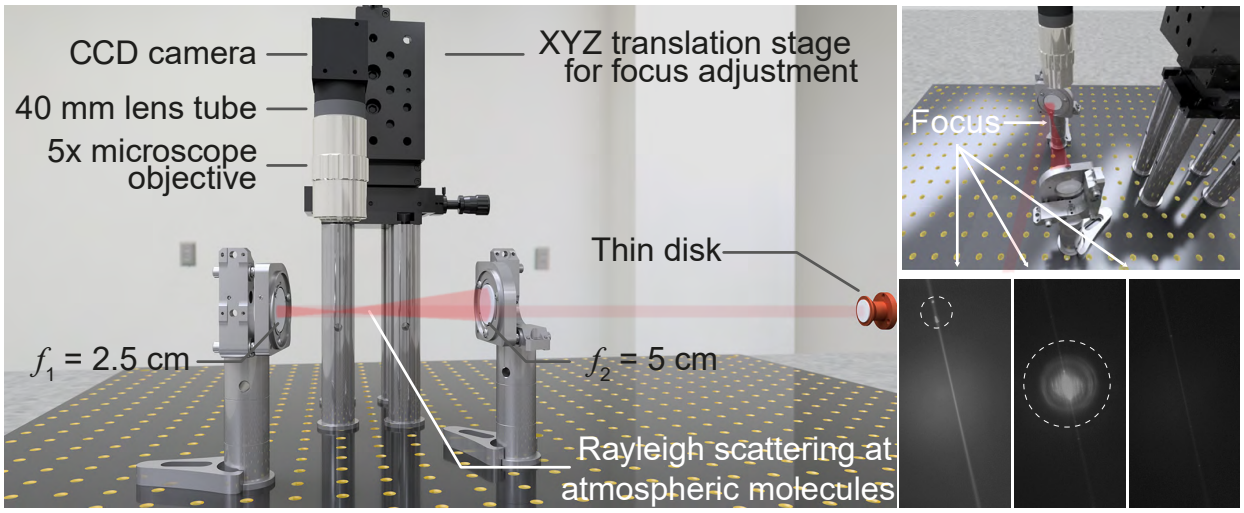

Figure 4.6: Left: Setup for the determination of the intracavity focus size. Right: Successive images of a resonator's internal focus with an exposure time of 30 s. The white circles show particles, moving towards or trapped in the focus.

complementary metal-oxide-semiconductor (CMOS) camera [217]. A patent, describing a similar application can be found in [218]. A scheme of the setup is shown in Figure 4.6. The determination of the focus radius was carried out utilizing a CMOS camera (The Imaging Source, DMK 23UP031m) with a quantum efficiency of approx. 2 % at a wavelength of 1 µm. The Rayleigh scattering of the intracavity beam was imaged onto the CMOS sensor through a 4 cm lens tube and a 5× microscope objective (Mitutoyo, 5× Plan Apo Infinity Corrected Long WD Objective). The optical setup was calibrated with a 1 mm microscope scale. With this, the resolution of the final setup was determined to 1.56 µm per pixel. The setup can suffer from vibrations, which can, e.g., originate from the cooling water supplies. These vibrations can influence the laser resonator as well as the optical imaging setup. The inaccuracy was determined to be in the order of 2 µm for CMOS exposure times of 30 s. The workflow can be described as following: first, the resonator's internal focus had to be localized. This was possible, as high-field-seeking particles experienced a dipole force and moved towards the highest optical intensity and were trapped for several seconds until they burned [219, 220][1]. Centering and focusing at this point defined the focal plane and the position of the intracavity focus. Subsequently, images were recorded with an exposure time of 30 s for a high SNR. A successive series of images can be seen in the right part of Figure 4.6. The exposure times were caused by the low amount of scattered photons the low sensitivity of microscope and CMOS sensor for wavelengths longer than 1 µm. More than 99 % of the images were overexposed by the strong light scattering from larger particles. The particle free images were aligned and a background signal was subtracted. The profiles were fitted with a Gaussian function in the form

$$I(x) = B + a \exp\left(-\frac{2(x-x_0)^2}{w^2}\right) \tag{4.3}$$

considering a background B and center x_0. This procedure was subsequently repeated over the entire beam. The Gaussian radii in the propagation direction of the laser were approximated by a function according to

$$w(z) = w_0 \sqrt{1 + \left(\frac{z_x + z}{Z_R}\right)} \tag{4.4}$$

to determine the longitudinal position z_x, the radius of the beam waist w_0 and the Rayleigh length Z_R. The setup could be improved by the use of a charge-coupled device (CCD) or CMOS cameras with a higher sensitivity at 1 µm to reduce the exposure time and sensitivity to external vibrations.

Beam quality The parameter M^2 is commonly used as a beam quality factor. A further insight into description of the beam quality using the entropy can be found in [221]. The beam quality M^2, according to Equation 4.2, was determined with a commercial beam profiler (Ophir, M^2-200). The M^2 parameter was monitored after re-alignment and during

[1] The same effect can lead to the observation of dust particles which are pulled towards mirror surfaces. Here they can get burned and decrease the laser performance.

the laser experiments in parallel by measurement of transversal mode beating between the fundamental mode and corresponding higher order modes [71] with a RF analyzer (Agilent, N9320B). The different axial and transversal modes generate a beating in the frequency spectrum. In case of the axial modes this corresponds to the FSR $\Delta\upsilon$, as shown in Figure 4.7. Thus, measurement of the radio frequency spectrum of the laser beam allows calculating the resonator length with $L_\mathrm{r} = c/2\Delta\upsilon$. According to Equation 2.61 also the higher transversal eigenmodes can become visible in the frequency spectrum and allow thus an approximation and live-monitoring of the beam quality. Vice versa, a comparison with Equation 2.62 shows, that the measurement of the transversal mode spacing allows to calculate properties, like the ROC of optical elements in simple resonators.

Resonator alignment and data acquisition The resonators were set up with vacuum-compatible high-stability open-loop piezo-controllable optical mounts (Newport, 8817-8-V) on motorized XYZ-stages. The alignment was done automatically with LabView. For this purpose, the value and the slope of the output power was measured for variations of all axes. Subsequently the position of the maximum output power was approximated with sufficient agreement in comparison to manual alignment. Together with the output power and diode operation parameters, also other values were monitored and saved in LabView. This includes, e.g., the spectrum of the laser with a fast spectrometer (OceanOptics, HR2000+) or slower and with a higher precision with an optical spectrum analyzer (Yokogawa, AQ6370C).

Measurement of output and intracavity power Different power meters were used for determination of the pump power P_p and the laser power P_l. This was necessary due to different power levels, which exceeded the dynamic range of single power meters. The power meters which were used for the characterization of lasers and pump diodes are

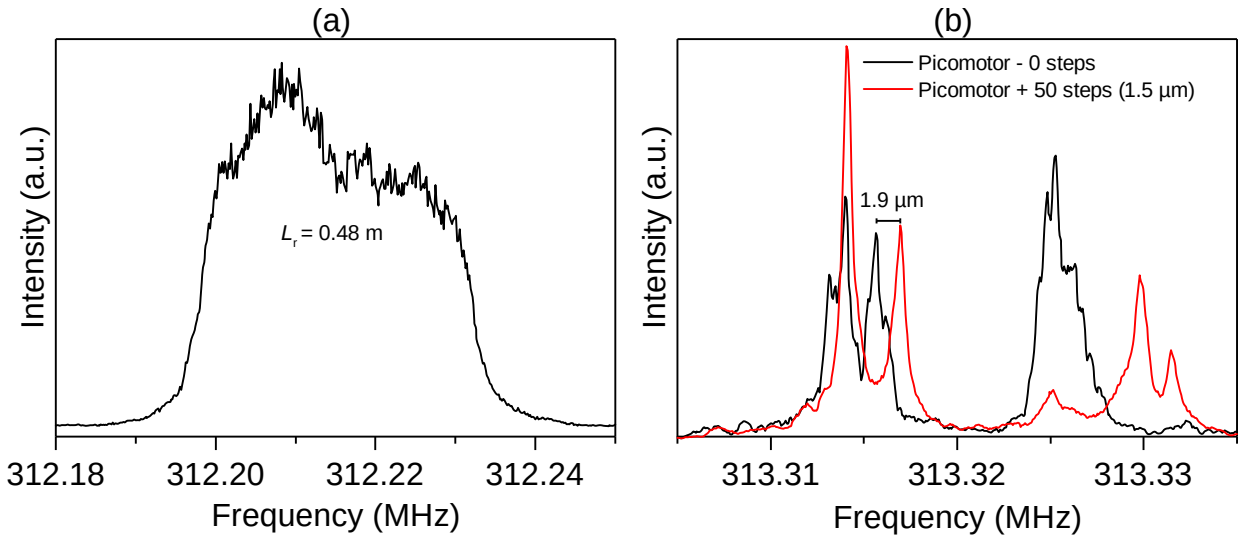

Figure 4.7: (a) Measurement of the axial modes' beating, which corresponds to a resonator length of 48 cm. (b) Influence of the movement of a piezo actuator by approx 1.5 µm on the beating.

Name	PD300-UV	LM-3	LM-100	LM-1000
Manufacturer	Ophir	Coherent	Coherent	Coherent
Spectral range (nm)	200 – 1100	250 – 10600	250 – 10600	250 – 10600
Power range	20 pW – 300 mW	10 mW – 3 W	100 mW – 100 W	1 W – 1 kW
Resolution	1 pW	10 µW	10 mW	20 mW
Calibration wavelength (nm)	1064	10600	10600	10600
Cooling	n.a.	air	air	water
Sensor	silicon	thermopile	thermopile	thermopile

Table 4.2: Overview about the power meters which were used in the laser experiments.

listed in Table 4.2. A comparison of the diode calibration curves for different power meters can be found in the appendix. The intracavity power was determined with $P_{\mathrm{int}} = P_{\mathrm{l}}/T_{\mathrm{oc}}$. It has to be noted that an older publication suggested the measurement of the Rayleigh scattering for the determination of the intracavity power [222].

Disk temperature measurement The temperature of the front side of the coated laser disks was measured with a thermographic camera (Flir, SC645). To correct for the temperature dependent and laser material specific emissivity, a calibration curve was measured. For this purpose, the disks were heated to a specific temperature T_{disk} on an electric stove, which was controlled by a thermo element. The temperature T_{meas} which was measured on the disk surface with the infrared camera could now be correlated with the actual temperature of the disk. For both materials the measured and the actual temperature of the disk can be approximated by $T_{\mathrm{meas}} = 0.94T_{\mathrm{disk}}$ for Yb:$Y_3Al_5O_{12}$ and $T_{\mathrm{meas}} = 0.85T_{\mathrm{disk}}$ for Yb:Lu_2O_3. This behaviour and the corresponding emissivity are depicted in Figure 4.8.

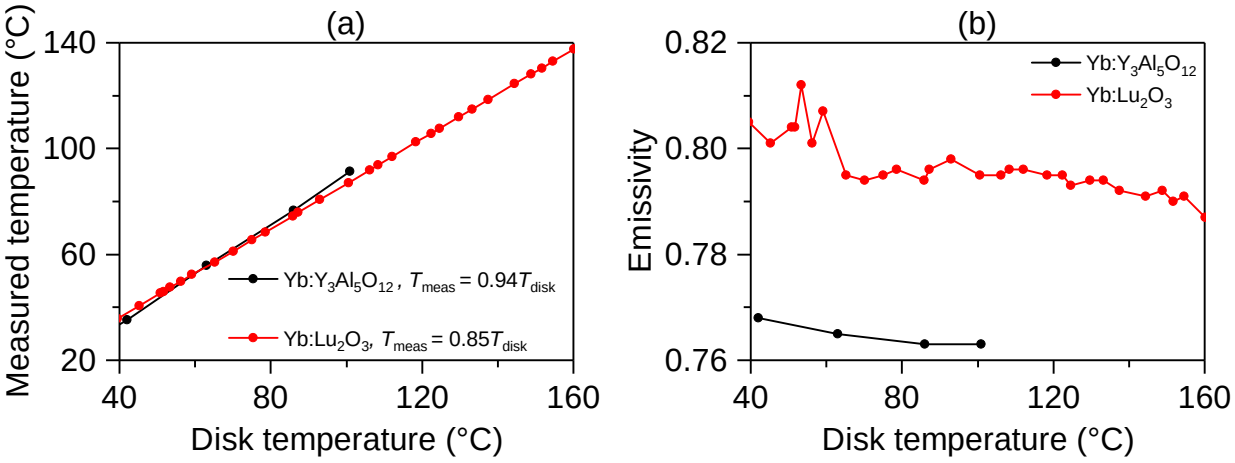

Figure 4.8: (a) Measured temperature vs. oven (disk) temperature for Yb:$Y_3Al_5O_{12}$ and Yb:Lu_2O_3. Data for Yb:$Y_3Al_5O_{12}$ was taken from [86]. (b) Trend of the emissivity of both laser materials.

5. Laser experiments and discussion

This chapter begins with an introduction to the linear resonator's design. An elaborated design is necessary to plan application-oriented resonators, e.g., for a high beam quality or a high laser efficiency. After that, laser experiments with efficient multi-transverse-mode, single-transverse-mode and polarized single-transverse-mode resonators are presented. A focus is set on the discussion of the resonator's internal losses. A comparison of the losses of the different resonators allows to recognize different loss mechanism, such as scattering, absorption or diffraction. Afterward, the attention is put on folded resonators, because an internal focus can be achieved more appropriately with folded resonators than with linear resonators. The chapter is finished by measurements of the beam waist.

5.1 Design of the linear resonators for thin-disk lasers

In many cases linear resonators consist of two facing mirrors. Depending on the curvature and the distance between the two mirrors, the linear resonator can be separated into different types [71]. For the resonators which were set up for this thesis only concave and plane mirrors were used. The design of a linear resonator can be adapted to its purpose. It can be distinguished between resonators suitable to achieve single-transverse-mode operation or resonators which are optimized for high laser efficiencies. Concave-convex cavities have not been used, due to their high alignment sensitivity. However, they can be suitable in order to achieve single-transverse-mode operation TDLs [223].

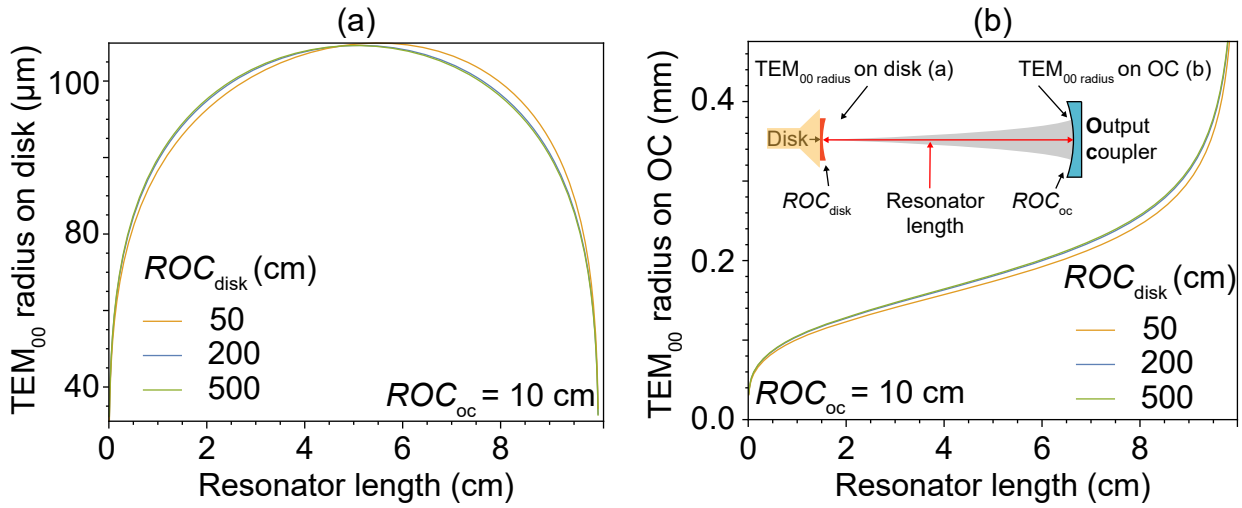

Figure 5.1: First stability zone: Calculated fundamental mode radius on the (a) disk and on the (b) OC for different ROCs of the thin disk in dependence on the resonator length.

Resonator design for multi-transverse-mode operation An efficient multi-transverse-mode resonator requires a small fundamental mode size in the pumped volume. This facilitates the oscillation of higher order transverse modes which can efficiently fit into the pumped gain area. This leads to less re-absorption losses compared to the fundamental mode, with a beam radius sufficiently large for a sufficient overlap with the pump beam. An efficient resonator with a small fundamental mode on the thin disk requires the operation in the first stability zone. Details regarding the stability zones of resonators with internal thermal lenses can be found in [63, 224].

The fundamental mode radius on the thin disk and on the OC, in the first stability zone, is depicted in Figure 5.1 for different ROCs of the thin disk. The ROC of the output mirror is 0.1 m, because this focal length is well suited for the available TDL modules. For soldered disks, the ROC of a thin disk typically increases with higher pump intensities [214]. Common values of the ROC are between 0.5 m and 5 m. However, this value depends on the thickness of the disk and coating. A resonator length below 6 cm is often impractical because of the dimensions of todays TDL pump modules. Therefore, a suitable operation point is next to the maximum possible resonator length. Additionally, operation at the maximum distance between disk and mirror increases the Gaussian beam radius on the OC, as it can be seen in Figure 5.1 (b). This decreases the impact of dirt and defects on the dielectric coatings.

The smaller beam radius on the disk constitutes one disadvantage of this resonator concept. Here, the highest field intensity in the resonator is kept in the area of the thin disk. This creates the possibility of high-field-seeking particles or molecules getting pulled toward the disk surface. When sticking to the surface, optical damage might occur. Therefore, an optimum resonator length must be found. In addition, diffraction losses at the mirrors due to the possibly large mode size on the OC must be considered.

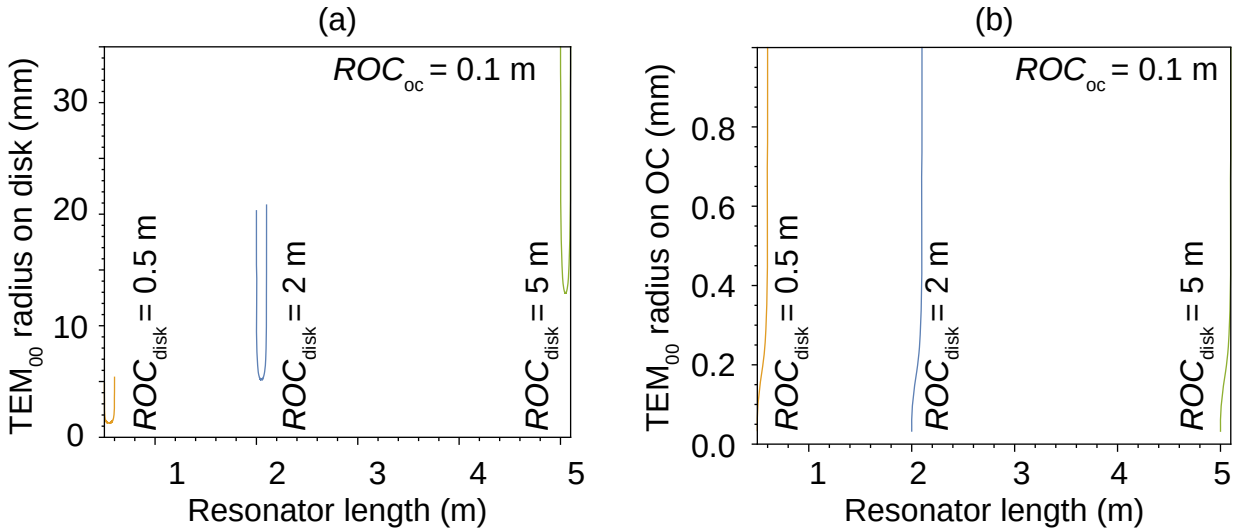

Figure 5.2: Second stability zone: Calculated Gaussian mode radius on the (a) thin disk and on the (b) OC for different ROCs of the thin disk in dependence on the total resonator length.

The fundamental mode radii on the thin disk and on the OC, in the second stability zone, are depicted in Figure 5.2. This configuration has two main characteristics. First, the possible fundamental mode radius on the disk is larger than the one in the first stability zone. Therefore, this configuration requires larger pump spot radii. While the configuration is achievable for the presented ROC of 0.5 m and a pump spot diameter of 1.2 mm, it might become technically challenging for larger ROCs. Second, the influence of the fundamental mode radius on the OC is increased. With a larger ROC of the disk, also the required resonator length gets longer, which has a negative impact on the alignment sensitivity.

Single-transverse-mode operation The intention of a single-transverse-mode resonator is to suppress the oscillation of higher order modes. This can be achieved by significant differences of the losses for the different modes. Resonator internal apertures as well as a careful selection of the size ratio between pump beam and laser mode are options for a TDL to induce losses for higher order modes. For a flat-top pump beam, which can be approximated by a super Gaussian function, a ratio of fundamental mode radius/pump mode radius of approx. 0.8 to 0.85 is suitable to obtain efficient TEM_{00} operation [63, 68, 107, 136]. This reduces the overlap efficiency to approx. 60 % to 70 % [70]. Therefore, optical-to-optical efficiencies in the order of 50 % are typical for single-fundamental mode operation. Fundamental mode operation is easy to achieve with a resonator consisting of a concave thin disk and a plane OC. The application can become more difficult in case of a concave OC. Typical pump spot radii of TDL with an output power below 1 kW are between 0.6 mm and 1.8 mm. Consequently, this requires a fundamental mode radius on the disk between 0.5 mm and 1.5 mm. It is evident in Figure 5.1 that these radii can only be achieved for strongly curved disks with $ROC_{\text{disk}} \approx 0.5\,\text{m}$, which are difficult to manufacture. One

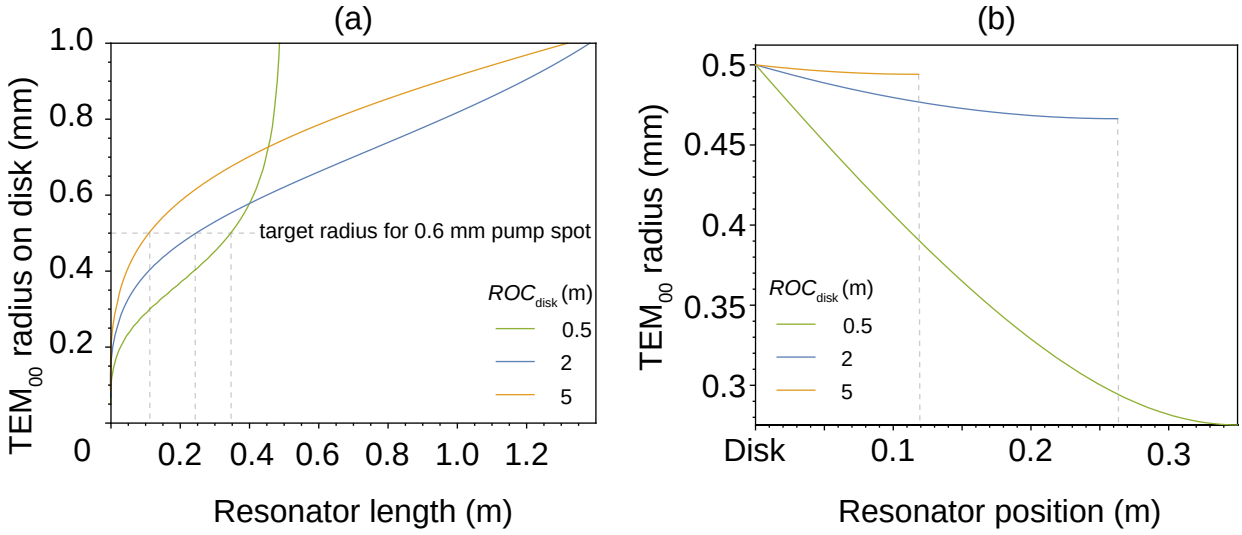

Figure 5.3: (a) Fundamental mode radius on the disk for several ROCs and a plane OC. The dashed grey line depicts the required beam radius on the disk. This yields to a necessary resonator length with the corresponding caustic - the beam radius inside of the resonator - shown in (b).

disadvantage of the second stability zone is its angular alignment sensitivity. Additionally, the fundamental beam radius is smaller on the OC. This makes the OC a possible target for high feeld seeking particles and consequently for optical damage. The trapping and guiding of particles towards resonator positions of higher field intensities is presented in Figure 4.6. These observations imply, that in case of a resonator design with the highest field intensity on the disk or on the OC, the usage of dust deflecting coating designs is beneficial. Results of the calculations of the beam radius for different ROCs of a thin disk between 0.5 m and 5 m and a plane OC are listed in Figure 5.3 (a). A flat-top pump spot radius of 0.6 mm requires a fundamental mode radius of approx. 0.5 mm, which is depicted by the grey line. The intersections with the fundamental mode radius on the disk yield the required resonator length. The caustic for the specific ROC can be found in Figure 5.3 (b).

Linear resonators with an internal focus It is possible to achieve a tight intracavity focus, even in case of a linear resonator. However, this requires a fine adjustment of the resonator length in the second stability zone with a concave OC. This is exemplarily shown in Figure 5.4 (a). The concept can be simplified as follows: the disk acts as a lens which creates a focus. The focal point must be imaged back to this point which can be done by a subsequent 4f-image by the curved OC. This resonator concept has two main draw backs. With an increasing ROC of the disk also the mode radius on the disk becomes bigger, which can require large pump spot radii. In addition, the total resonator length mainly depends on the ROC of the thin disk which can reach several meters. Long resonators are difficult to align and might require folding over additional plane mirrors, which induce further losses. However, it is beneficial in this concept that no astigmatism can be generated by the folding mirrors or the disk in comparison to folded resonators, as shown in Figure 5.27.

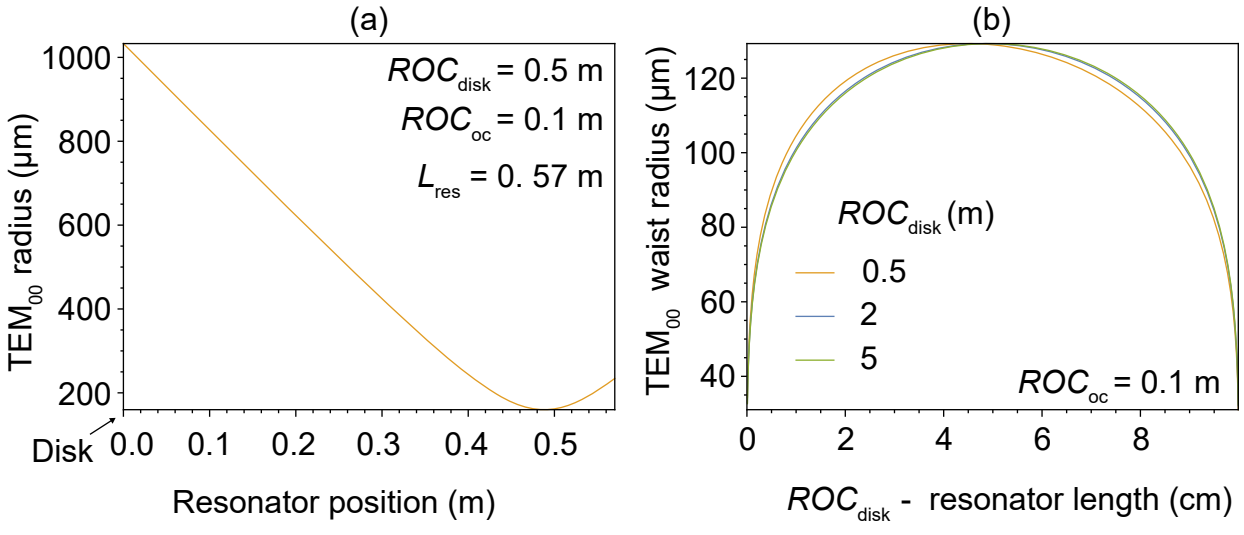

Figure 5.4: (a) Caustic of a linear resonator in the first stability zone with an ROC of the disk of 0.5 m and an ROC of the OC of 0.1 m. The waist is 159 µm. (b) Achievable intracavity focus for different disk ROCs. The abscissa corresponds to the subtraction of the ROC minus the total resonator length.

5.2 Results of laser experiments with linear resonators

5.2.1 Efficient linear resonators at low pump powers

Motivation for experiments with efficient multi-transverse-mode resonators At first, laser experiments with different gain materials in short multi-transverse-mode resonators are presented. These experiments served different purposes. Measurements of the laser performance, especially at low OC transmissions enable a precise determination of the resonator losses. Previously, the losses were estimated to be in the order of 10^{-3} [53, 136]. A multi-mode resonator depicts the optimal prerequisite to refine the resonator losses and to obtain high power efficiencies. Subsequently, a comparison with more complex resonators allows the assignment of additional loss channels. Second, a low-loss high-efficiency resonator can achieve high intracavity powers at low pump powers, which is necessary to explore the general suitability of optics and disks at high intracavity intensities.

Specific setup A linear resonator with a length of approx. 7 cm was set up. The ROC of the OC was 10 cm. The resonator was adjusted for a maximum output power. It should be considered that an optimization of the output power does not mandatorily optimize the intracavity power as well. While an optical defect in an HR OC might increase the outcoupled power, it decreases the intracavity power. Different gain materials were compared. Details about the laser disks can be obtained from Table A.1. The disks were water cooled to approx. 9 °C. Yb:$Y_3Al_5O_{12}$ and Yb:$Lu_3Al_5O_{12}$ were pumped over a pump spot diameter of 1.2 mm. The pump wavelength was 940 nm for Yb:$Y_3Al_5O_{12}$ and 976 nm for Yb:Lu_2O_3.

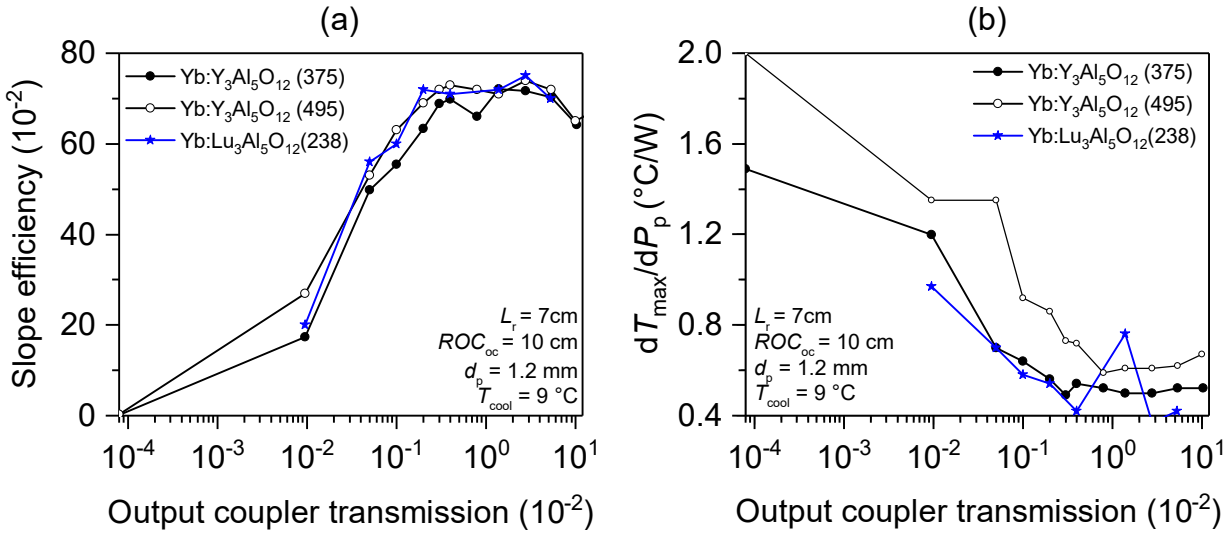

Figure 5.5: (a) OC transmission dependent slope efficiencies for different disks. Data for Yb:$Lu_3Al_5O_{12}$ is incomplete because of accumulation of optical damage in the form of nodular defects on the disk. (b) OC dependent slope of the maximum surface temperature of the laser disks.

Laser performance: Yb:$Y_3Al_5O_{12}$ and Yb:$Lu_3Al_5O_{12}$ Results of the laser experiments of Yb:$Y_3Al_5O_{12}$ and Yb:$Lu_3Al_5O_{12}$ are shown in Figure 5.5 and listed in Table 5.1. Here, the slope efficiency of the output power (a) can be seen together with the slope of the temperature in respect to the input power (b). The calculation of the temperature's slope allows approximations of the power scalability in respect to thermal issues. The maximum slope efficiency of 0.75 was measured for an OC transmission of 2.8×10^{-2} for Yb:$Lu_3Al_5O_{12}$. Under considerations of errors in the power measurement of approx. 5 % all disks are comparable, especially at high OC transmissions. The laser efficiency is similarly deceasing for $T_{oc} > 2.8 \times 10^{-2}$ and more significantly for $T_{oc} < 4 \times 10^{-4}$. The slope efficiencies for $T_{oc} = 9 \times 10^{-5}$ for all three disks deviate from the trend in respect to the results with the surrounding OC transmissions, which could be caused by a wrong mirror transmission.

Intracavity power: Yb:$Y_3Al_5O_{12}$ and Yb:$Lu_3Al_5O_{12}$ A maximum intracavity power of 134 kW was obtained for $T_{oc} = 9.5 \times 10^{-5}$ for Yb:$Y_3Al_5O_{12}$ (375) and a pump power of $P_p = 56.5$ W. This corresponds on the pump spot to an electric field intensity of 1.1 TW cm^{-2}, which is magnitudes larger than recommended by thin disk manufacturers. The behavior of the intracavity power of the disk 375 for $T_{oc} < 4 \times 10^{-3}$ is depicted in Figure 5.6. The trend of the intracavity power was disturbed for an OC transmission of 8×10^{-7} at high pump powers. In parallel, a high surface temperature was measured. Because of the irregular behaviour no further increase was done for this OC.

Nevertheless, this demonstrates the feasibility of TDL resonators with pump powers in the order of 50 W which are capable of containing powers in the 100 kW regime. Optical damage and high disk temperatures have to be considered as a limiting factor at high intracavity powers.

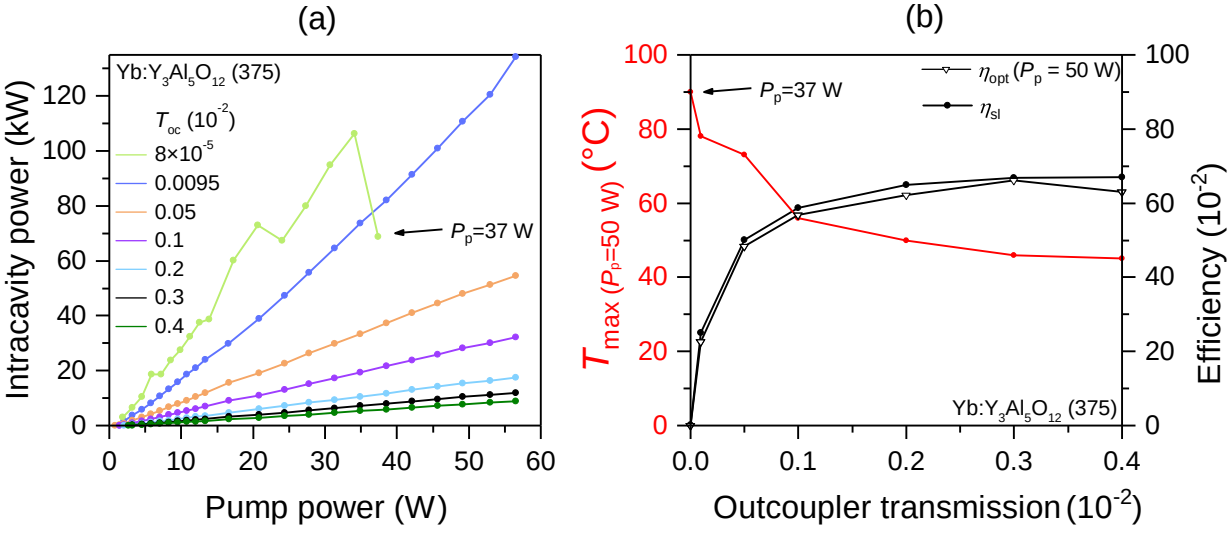

Figure 5.6: (a) Input output curves for Yb:$Y_3Al_5O_{12}$ (375). Scaling of the pump power was stopped for $T_{OC} = 8 \times 10^{-7}$ at $P_p = 37$ W due to the sudden decrease of the output power and the high surface temperature. (b) Maximum measured surface temperature (red) on the disk for $P_p = 50$ W and the corresponding slope efficiency η_{sl} and optical-to-optical efficiency η_{opt}.

Disk	Output coupler transmission (10^{-2})											
	8×10^{-5}	0.0095	0.05	0.1	0.2	0.3	0.4	0.8	1.4	2.4	5.4	10
495	0.2	17	50	56	63	69	70	66	**72**	71	70	64
375	0.3	27	53	63	69	72	**73**	72	71	74	72	65
238	-	20	56	60	72	-	71	-	72	**75**	70	-

Table 5.1: Slope efficiency (10^{-2}) of Yb:$Y_3Al_5O_{12}$ and Yb:$Lu_3Al_5O_{12}$ in the 7 cm short multi-mode resonator. Data for Yb:$Lu_3Al_5O_{12}$ (238) is incomplete due to optical damage of the disk.

Thermal analysis: Yb:$Y_3Al_5O_{12}$ and Yb:$Lu_3Al_5O_{12}$ An analysis can be carried out from the measurements shown in Figure 5.5 (b). The 'thermal slope' decreased from 2 °C W^{-1} to approx. 0.6 °C W^{-1} (disk 495) and increased for the larger OC transmissions. Thus, for losses in the gain material, the amount of depleted heat became larger. For an increasing OC transmission and OC efficiency, the heat, generated by losses in or at the disk, decreased and originated to a great extent from the quantum defect [169]. Therefore, this resulted in a lower sensitivity in respect to additional loss channels due to a large OC efficiency. In contrast to the expected constant trend of the slope, the depleted heat increased again for larger OC transmissions. Explanations for this effect can be found in [86].

The results, shown in Figure 5.5 (b), allow an estimation of the disk's temperature for higher pump powers. Generally, a lower temperature is beneficial. An increase of the gain medium's temperature yields to a higher thermal occupation of the lower laser level. A higher occupation increases the gain threshold and the pump threshold. In parallel, also the thermal conductivity can be decreased. It must be considered that the properties of the dielectric coatings might change at higher temperatures and become sensitive to optical damage. Details can be found, e.g., in [225]. As expected the slope of the intracavity power in Figure 5.6 is the largest for $T_{oc} = 8 \times 10^{-7}$.

Despite the observation that the experiments in Figure 5.6 showed a disturbed behavior for larger pump powers, further scaling of the pump power may be possible. With an increase of 1.5 °C W^{-1} a pump power of 100 W would be feasible and could be sufficient to achieve an intracavity power of more than 300 kW.

Laser performance: Yb:Lu_2O_3 The results of three different laser disks are depicted in Figure 5.7 and Table 5.2. No data is presented for $T_{oc} = 8 \times 10^{-7}$ due to optical damage of the corresponding mirror. All samples show a slope efficiency of $\eta_{sl} \approx 0.2$ for $T_{oc} = 9.5 \times 10^{-5}$. Due to the sensitivity of the laser performance to internal losses at low OC transmissions, a possible interpretation of the observation of comparable slope efficiencies is the presence of similar intrinsic losses. The highest slope efficiency of $\eta_{sl} = 0.78$ was measured for disk 147 for $T_{oc} = 1.4 \times 10^{-2}$. For larger OC transmissions, the disks show a comparable laser performance. Advantages of disks mounted on diamond heatsinks are the higher thermal conductivity of the diamond and the higher stiffness of the disk-heatsink system. The larger thermal conductivity reduces the temperature in the disk which leads to a reduced occupation of the lower laser level and thus a lower threshold.

Disk	Output coupler transmission (10^{-2})											
	8×10^{-5}	0.0095	0.05	0.1	0.2	0.3	0.4	0.8	1.4	2.4	5.4	10
124	-	21	46	52	62	64	65	68	**70**	67	60	55
128	-	23	46	59	70	72	73	**75**	74	78	**75**	52
147	-	24	53	62	71	69	70	74	76	**78**	75	65

Table 5.2: Slope efficiency (10^{-2}) of Yb:Lu_2O_3 in the multi-transverse-mode resonator.

Intracavity power: Yb:Lu_2O_3 The highest intracavity power of 118 kW was realized for disk 128 at an OC transmission of 9.5×10^{-5} and a pump power of 50 W. The corresponding input-output curves are depicted in Figure 5.8. Here, the possible impact of different cleaning methods on the laser performance at low OC efficiencies is shown. The disk and the mirrors were cleaned with the "brush", or the "drop and drag" technique, which can leave residuals on the optics. One can see that the average output power was approx. 20 % higher for optics cleaned with the "drop and drag" technique.

Thermal analysis: Yb:Lu_2O_3 The general trend of Yb:Lu_2O_3's OC transmission dependent temperature's behaviour is comparable to the trend observed for Yb:$Y_3Al_5O_{12}$. At the lowest OC transmission of 9.5×10^{-5}, the measured surface temperature and its increase is higher than the one for Yb:$Y_3Al_5O_{12}$. A possible explanation could be local inhomogeneities in Yb:Lu_2O_3 which were observed by Wentsch [173, p. 62]. The lowest increase of the temperature was determined for disk 147, which was contacted on diamond. This observation could have been caused by the higher thermal conductivity of the heatsink.

Experiments with Yb:Lu_2O_3 and Yb:$Y_3Al_5O_{12}$ showed comparable laser results. Diamond contacted disks exhibited lower temperatures due to their higher thermal conductivity, as expected.

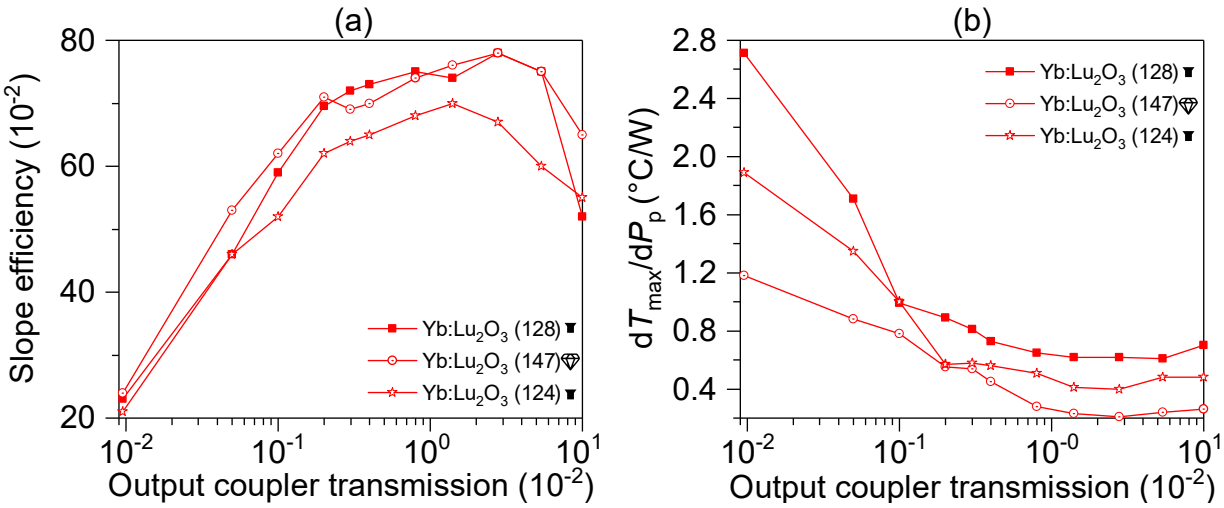

Figure 5.7: (a) OC dependent slope efficiencies for different disks (147 was contacted on diamond). (b) OC dependent slope of the maximum measured surface temperature of the laser disks.

Thermal analysis: FEM simulations Measurement of the temperature with a thermographic camera had several disadvantages. First, due to the available camera lense, the resolution over the pump spot with a diameter of 1.2 mm was limited to approx. 3×3 pixel. Therefore, the maximum temperature, measured with the camera, was an average over the pump spot. Second, the correlation to the actual temperature depended on the calibration curve, with an error of approx. 10 %. Furthermore, it has to be considered that measurements within a range of 20 °C higher than room temperature are less reliable [226]. A comparison with calculated temperatures allows the evaluation of the measurement and conclusions about power scalability. In comparison to approximations [86, 136] precise finite element method (FEM) simulations can be made with commercially available software. While the actual simulation is 'drag and drop' in modern FEM solutions, a precise knowledge of the thermal parameters and thicknesses of the layers is required. A list of tentative parameters is given in Table 5.3. It must be considered that the thermal conductivity of the dielectric coatings can strongly depend on the substrates thus leading to possibly large error bounds. The simulations of the average and the maximum disk temperature are performed for two scenarios in Figure 5.9. In Figure 5.9 (a) a Yb:$Y_3Al_5O_{12}$ disk with a thickness of 220 µm is depicted. The inset shows a central slice cut through the disk, revealing the deviations from a purely one-dimensional longitudinal heat flow. The experimental data is taken from the multi-mode experiment of Yb:$Y_3Al_5O_{12}$ (495) with an OC transmission of 1.4×10^{-2}. The dataset was chosen because of its highest measured slope and optical efficiency. This increases the probability that most of the heat was caused due to the quantum defect. Therefore, the heat rate was approximated as $P_{\mathrm{vol}} = P_{\mathrm{p}}(1-(\lambda_{\mathrm{las}}/\lambda_{\mathrm{pump}}))$. The calculated average temperature is in good agreement with the maximum temperature, measured with the thermographic camera. In Figure 5.9 (b) a Yb:Lu_2O_3 disk with a thickness of 150 µm is simulated. The temperature measurements were taken from the multi-mode experiment of Yb:Lu_2O_3 (218) with an OC transmission of 9.5×10^{-2}. This

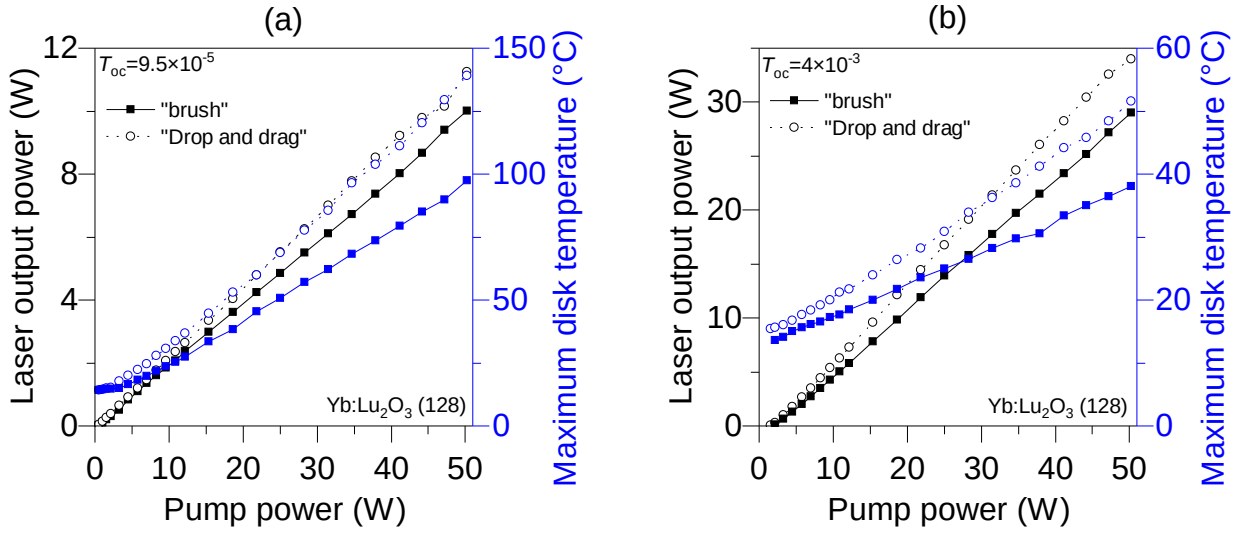

Figure 5.8: Impact of two cleaning methods of laser disk and mirror on the laser performance (black) and the disk temperature (blue) for an OC transmission of (a) 9.5×10^{-5} and (b) 4×10^{-3}.

	Value	Thickness	Source
Thermal resistance HR coating	$6\,\mathrm{K\,m^2\,W^{-1}}$	5 µm	[136, p. 49]
Thermal conductivity solder	$57\,\mathrm{W\,m^{-1}\,K^{-1}}$ (Au80Sn20)	40 µm	[227]
Thermal conductivity glue	$0.25\,\mathrm{W\,m^{-1}\,K^{-1}}$	0.2 µm	[173, 213]
Thermal conductivity CuW (80/20)	$140\,\mathrm{W\,m^{-1}\,K^{-1}}$–$220\,\mathrm{W\,m^{-1}\,K^{-1}}$	1 mm	MatWeb
Thermal conductivity CVD	$1800\,\mathrm{W\,m^{-1}\,K^{-1}}$	1 mm	MatWeb
Thermal conductivity SiO_2	$1\,\mathrm{W\,m^{-1}\,K^{-1}}$–$2\,\mathrm{W\,m^{-1}\,K^{-1}}$	$\lambda_l/4n$	[129]
Thermal conductivity TiO_2	$2\,\mathrm{W\,m^{-1}\,K^{-1}}$–$5\,\mathrm{W\,m^{-1}\,K^{-1}}$	$\lambda_l/4n$	[129]

Table 5.3: Suggested values for the FEM simulations of the thin disk's temperature.

particular experiment exhibited the highest measured maximum disk temperature and slope efficiency for this OC transmission for Yb:Lu_2O_3. The high temperatures suggest that additional loss channels beside the quantum defect induced the heat. In Figure 5.9 (b) the heat rate was assumed to be $P_{\mathrm{vol}} = P_{\mathrm{p}} - P_{\mathrm{l}}$, which yields to a good agreement of the simulated and the measured temperature.

FEM simulations indicate that the maximum measured surface temperatures correspond to the average temperatures in the pump spot. Additionally, they might confirm a significant power conversion in the volume of the pump spot for a Yb:Lu_2O_3 disk.

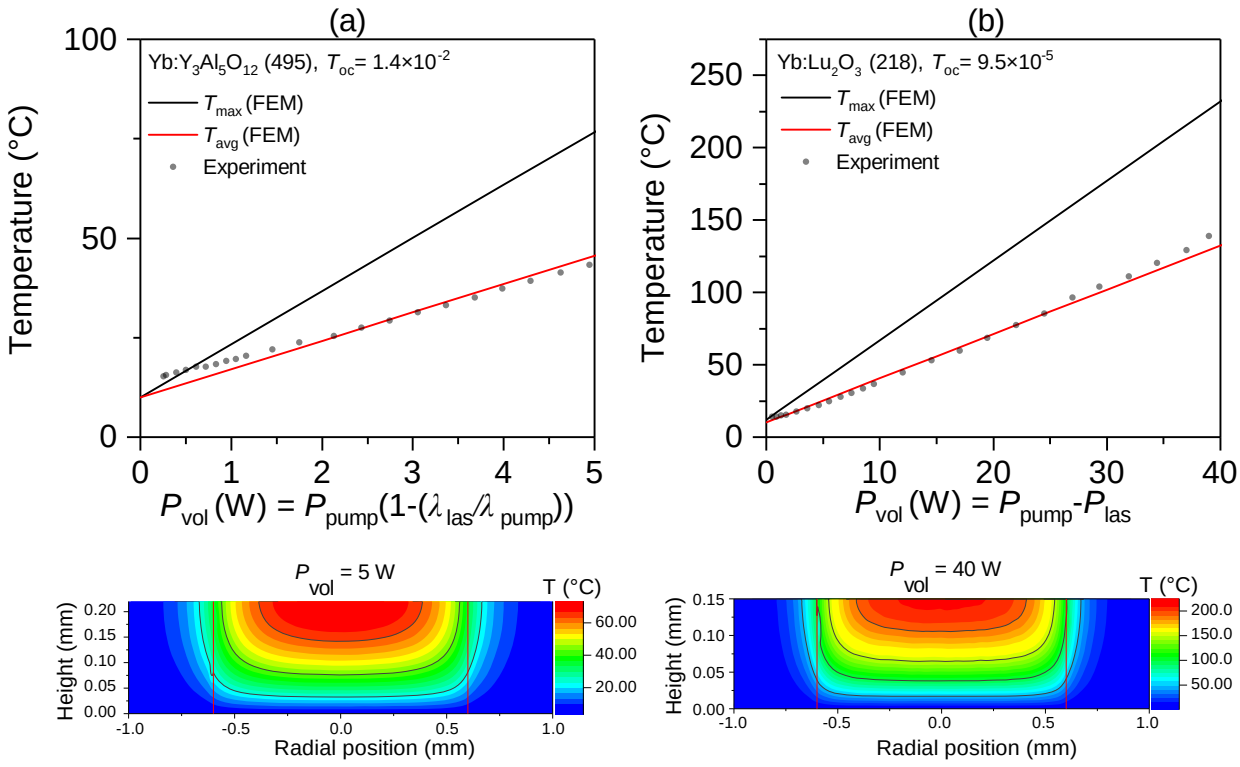

Figure 5.9: FEM calculations of the disk's temperature and emissivity corrected measurements with a thermographic camera for (a) a 220 µm thin Yb:$Y_3Al_5O_{12}$ disk and (b) a 150 µm thin Yb:Lu_2O_3 disk.

Laser spectra Typical OC transmission dependent spectra are shown in Figure 5.10 for Yb:$Y_3Al_5O_{12}$ and Yb:Lu_2O_3. Spectra for Yb:$Lu_3Al_5O_{12}$ are comparable to the ones of Yb:$Y_3Al_5O_{12}$. For Yb:Lu_2O_3 two different types of spectra were found. For an OC transmission of $\geq 4 \times 10^{-3}$ the laser oscillation was observed at a wavelength of approx. 1033 nm and for a mirror transmission of $\leq 5 \times 10^{-4}$ the laser was oscillating at a wavelength of approx. 1080 nm. In parallel, a Yb:$Y_3Al_5O_{12}$ laser at a wavelength of 1080 nm could be operated for OC transmissions lower than 9.5×10^{-5}, which is coherent to the results of calculations, shown in Figure 2.8. Therefore, a comparison of a laser spectrum with the calculated ones allows estimations about the losses for a comparable disk, regarding doping and thickness. In principle, this corresponds to a determination of the losses described in [92]. Additionally, the laser spectrum can change with the pump power, which is observed and shown in Figure 5.11. Here, for increasing pump power, the spectra shifted to longer wavelengths. The laser oscillation wavelengths depend on the loss dependent gain profile and on the resonator's FSR. Due to spatial hole burning, there exist areas in the gain material where the inversion density is not efficiently dissipated. For an increasing pump power it is possible that there are wavelengths which reach the threshold power and can use the available excitation density. This has to be considered for the OC transmission which was used for the determination of the intracavity power. For Yb:$Y_3Al_5O_{12}$ also visible changes of the luminescence could be detected. It was noticed for $T_{oc} < 4 \times 10^{-3}$ that the luminescence was centered at a wavelength of 489 nm, while for $T_{oc} > 4 \times 10^{-3}$ it was centered at 529 nm. According to [228] the cyan emission is caused by cooperative luminescence and the greenish emission might be up-conversion energy transfers to rare earth impurities of the raw materials.

The laser oscillation spectra can shift pump and OC transmission dependent. This alters the intracavity power. A precise determination of the latter requires a continuous measurement of laser spectra and a comparison with the mirror's OC transmission.

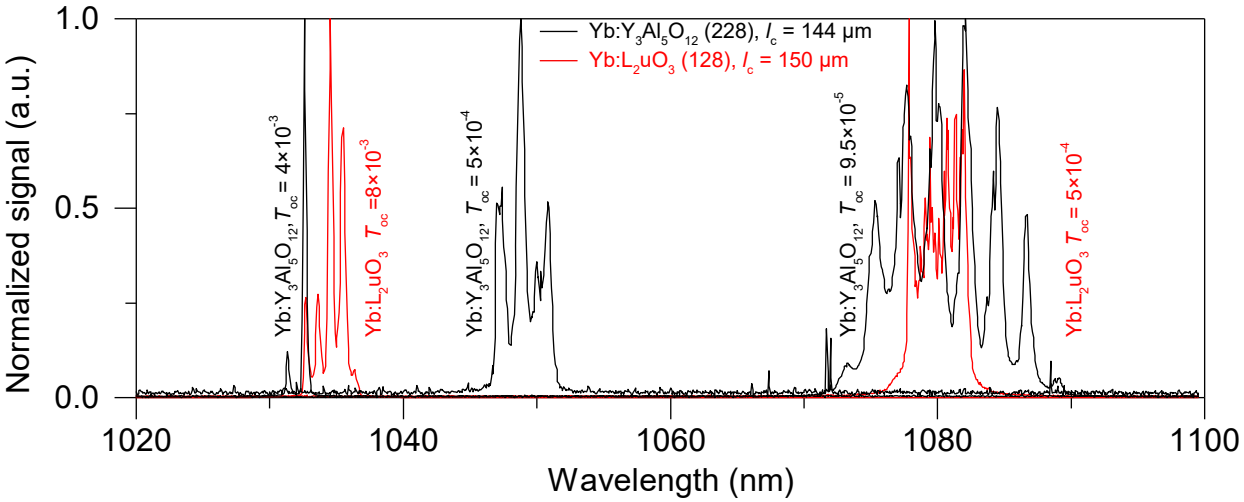

Figure 5.10: OC transmission dependent normalized measured spectra for Yb:$Y_3Al_5O_{12}$ (black) and Yb:Lu_2O_3 (red). The spectra were measured at a diode current of 10 A.

Disk	Caird fit		Energy conservation	
	$L_{\mathrm{int}}(10^{-4})$	$\eta_{\mathrm{abs}} \cdot \eta_{\mathrm{ov}}$	$L_{\mathrm{int}}(10^{-4})$ $T_{\mathrm{oc}} = 9.5 \times 10^{-5}$	$L_{\mathrm{int}}(10^{-4})$ $T_{\mathrm{oc}} = 5 \times 10^{-4}$
Yb:$Y_3Al_5O_{12}$ (495)	3.2	0.85	3.8	3.1
Yb:$Y_3Al_5O_{12}$ (375)	1.6	0.82	1.8	2.6
Yb:$Lu_3Al_5O_{12}$ (228)	2.8	0.91	2.8	2.1
Yb:Lu_2O_3 (128)	2.1	0.82	2.4	3.8
Yb:Lu_2O_3 (147)	2.0	0.84	2.2	2.7
Yb:Lu_2O_3 (124)	1.6	0.72	2.2	3.8

Table 5.4: Results of the Caird plot and energy conservation by Equation 2.78 with $\eta_{\mathrm{abs}}\eta_{\mathrm{ov}} = 0.9$.

Resonator losses in efficient resonators The amount of internal losses to a great extent determines the pump power necessary to achieve a required intracavity power. For TDL, the determined and assumed losses usually range from 10^{-3} [53] to 3×10^{-4} [180]. This already illustrates the importance of a refinement of the loss investigations. For an exact determination they were calculated with the Caird method, according to Equation 2.68. The Caird plots are shown in Figure 5.12 with the results listed in Table 5.4. Inclusion of $T_{\mathrm{oc}} = 8 \times 10^{-7}$ into the calculations yields to losses of $L_{\mathrm{int}} < 1 \times 10^{-7}$ for particular disks. Such losses do not seem realistic under consideration of, e.g., scattering. Therefore, the mirrors with $T_{\mathrm{oc}} = 8 \times 10^{-7}$ were not included in the calculation by the Caird method. The reason is the strong impact of the large inverse transmission on the linear fit. This makes it sensitive to errors in the determination of the wavelength dependent transmission. The smallest losses were determined for Yb:Lu_2O_3 with $L_{\mathrm{int}} = 1.6 \times 10^{-4}$ and the largest for Yb:$Y_3Al_5O_{12}$ with $L_{\mathrm{int}} = 3.2 \times 10^{-4}$. All available laser disks were characterized in a 70 mm short efficient multi-transverse-mode resonator with $T_{\mathrm{oc}} = 5 \times 10^{-4}$ and an ROC of 100 mm

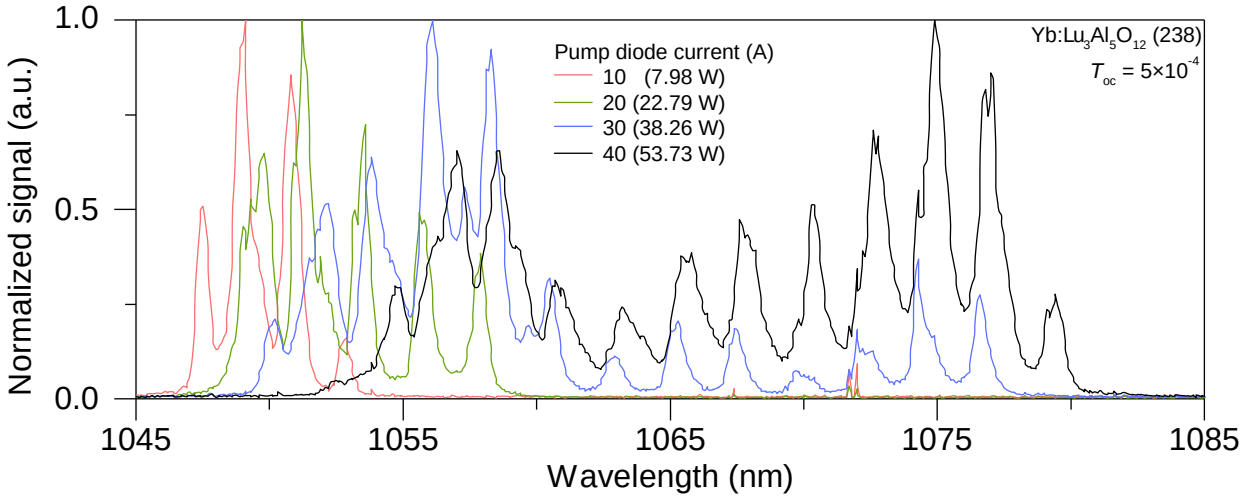

Figure 5.11: Pump-diode-current dependent normalized measured spectra for Yb:$Lu_3Al_5O_{12}$. Similar spectra were observed for Yb:$Y_3Al_5O_{12}$ as well. Ripples were caused by the disk's FSR.

to obtain statistics in dependence of the different disk's properties. Because of optical damage of the mirror with $T_{oc} = 5 \times 10^{-4}$ and an ROC of 100 mm, some experiments had to be conducted with an ROC of 150 mm. However, this only slightly increased the fundamental mode radius on the disk and the OC. The resonator length was kept constant within ±1 mm between the different experiments. Mainly, a change of the disks and the adjustment for maximum output power were performed to ensure a high degree of comparability between the different laser experiments.

The results of the laser experiments, performed with the available disks, are depicted in Figure 5.13. The analysis can be seen in Figure 5.14. The length of the disks was verified by spectral measurements of the FSR according to $\delta\nu = c/2n_g L$. In Figure 5.13 (a) an increase of the temperature with the disk's thickness is observable. This is expected because of a uniform heat depletion in the gain medium. Within the accuracy of the measurements for an OC transmission of 5×10^{-4}, no significant correlation of the losses L_{int} with the disk's thickness, a wedge of the laser disk, the ROC or the surface roughness could be resolved.

This supports the hypothesis, that a significant amount of the intracavity power is lost at the surfaces. Surface losses from scattering were already discussed in subsection 2.4.2. However, scattering losses do not necessarily yield into a subsequent absorption and the depletion of heat. In contrast, the absorption of optical power at point defects, especially at the coatings is often connected to a strong local heating. This can in principle lead to a local melting and subsequently to an optical damage. A distinct assignment of losses to a specific coating or side of the disk cannot be made. Losses at the front side, e.g., originating from absorption losses of the AR coating and point defects would be visible in Figure 5.14 (a) and add an additional dependency of the temperature on the thickness of the disk. Losses at the backside of the disk can be caused by absorption of point defects or even by a residual transmission of the HR coating. Subsequently, the transmission of the coated disks was measured. Samples of coating runs, which were used by Fredrich and Peters [53, 180], exhibited a transmission of 8×10^{-4} at a wavelength of 1080 nm. The Yb:Lu_2O_3 disks of

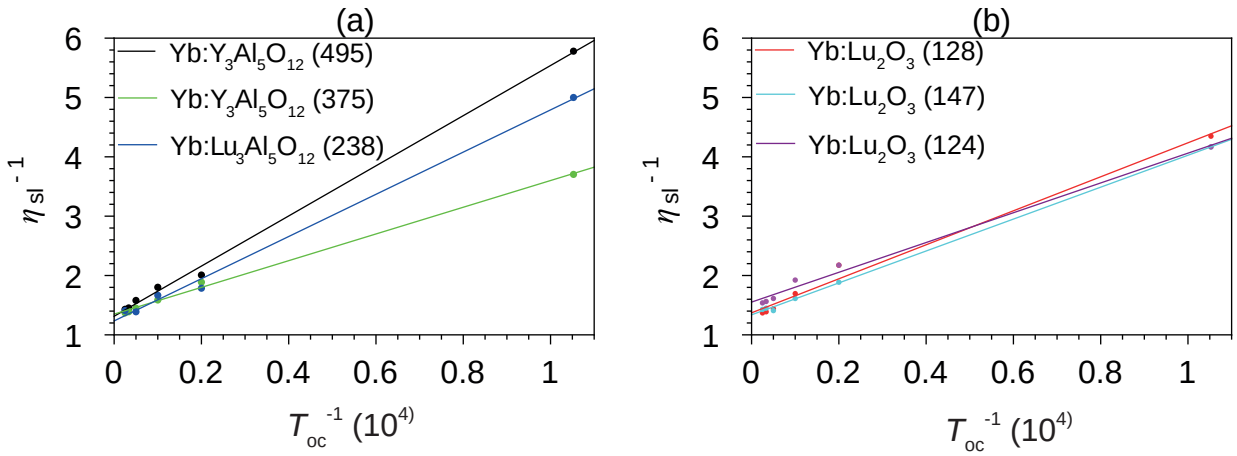

Figure 5.12: Plot of the Caird analysis for (a) Yb:$Y_3Al_5O_{12}$ and Yb:$Lu_3Al_5O_{12}$ and (b) Yb:Lu_2O_3. The calculations only included OC transmissions between 9.5×10^{-5} and 4×10^{-3}.

this thesis were coated with more layer pairs. For this disks a transmission of 9.3×10^{-5} was measured. The Yb:Lu_2O_3 disks were metallized with chromium by LAYERTEC for soldering on copper-tungsten heat sinks. The optical properties of the optical multilayer system were determined with the IMD-XOP software [106]. For a wavelength of 1 µm this yielded an absorption of approx. 3×10^{-5}. The transmission through the metallization layer can be neglected due to the exponential decay of the field intensity in chromium. However, the exact transmission and reflectivity of the disks cannot be calculated, as material properties and dimensions of the glue, solder or metallization were unknown.

Optimized multi-transverse-mode resonators with Yb:$Y_3Al_5O_{12}$ or Yb:Lu_2O_3 can exhibit resonator losses in the order of 2×10^{-4}, which in principle enables the obtainment of high intracavity powers. Neither of the laser materials shows significant advantages over the other.

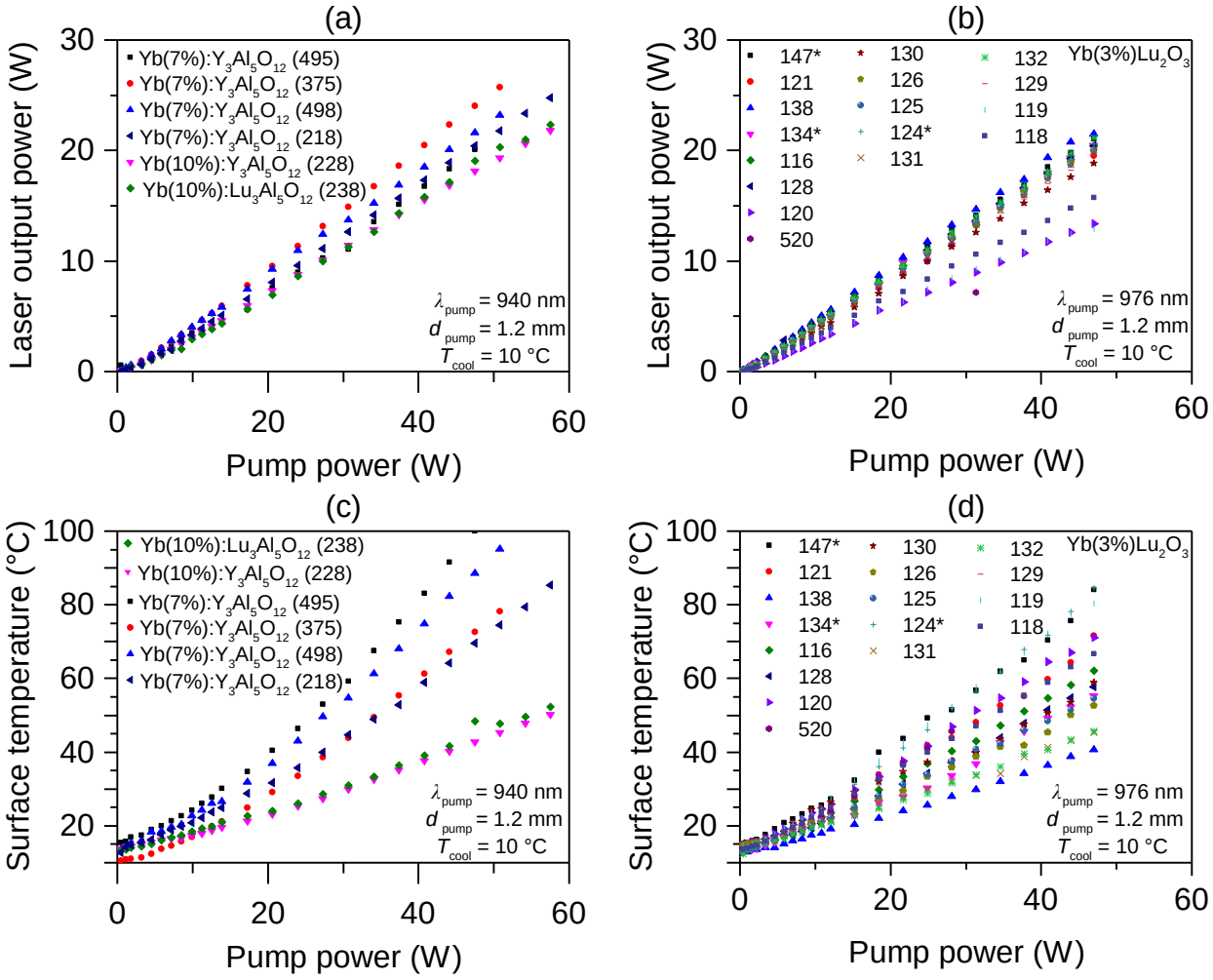

Figure 5.13: Pump power P_p and laser output power P_{out} for (a) Yb:$Y_3Al_5O_{12}$ and Yb:$Lu_3Al_5O_{12}$ and (b) Yb:Lu_2O_3 for $T_{oc} = 5 \times 10^{-5}$. The emissivity corrected corresponding maximum surface temperatures of the disk in the pump spot are depicted in (c) and (d).

Intracavity power scalability with larger pump spot diameters A correlation between the resonator losses L_{int} and the area used by the laser modes, can be analyzed in a multimode resonator by an increase of the pump spot diameter. In addition, this allows the increase of the pump power due to a lower disk temperature. For this purpose, two disks ($Yb:Y_3Al_5O_{12}$ (498) and $Yb:Lu_2O_3$ (129)) were selected. They were integrated into a short linear resonator with a length of approx. 15 cm. The OC mirror had a transmission of 5×10^{-4} and an ROC of 300 mm.The disks were pumped with a pump spot diameter of $d_{\mathrm{p}} = 3.6\,\mathrm{mm}$ at their ZPLs. For $Yb:Y_3Al_5O_{12}$ and $Yb:Lu_2O_3$ a slope efficiency of 0.55 and 0.4 was measured and a maximum intracavity power of 150 kW and 200 kW, respectively. In this configuration, the maximum optical-to-optical efficiencies were 0.5 and 0.37. This resulted into maximum possible losses of 2.5×10^{-4} and 5×10^{-4}, under consideration of ZPL pumping and $\eta_{\mathrm{sl}} = 0.5$. Despite the high intracavity powers, for both materials, the measured surface temperatures were below 100 °C and in a tolerable range.

Despite the 5× larger pump and laser mode area in comparison to the experiments with a pump spot diameter of 1.2 mm, no significant increase of the losses could be measured for any of the disks. In contrast, the $Yb:Y_3Al_5O_{12}$ disk 498 showed a 17 % higher performance for the larger pump spot and ZPL pumping. Even considering the restricted resolution of determining the losses with an OC transmission of $T_{\mathrm{oc}} = 5 \times 10^{-4}$, a linear scaling of the losses with the surface would have been noticed. This can point towards volume losses or surfaces losses, which are not uniformly distributed, as shown in Figure 6.1.

An intracavity power of 200 kW was obtained with a 3.6 mm pump spot diameter for $Yb:Lu_2O_3$. This power would be sufficient for the alignment of molecules if appreciably focused. No significant scaling of the losses with the mode size could be determined. In fact the laser performance was increased by 17 % in the case of $Yb:Y_3Al_5O_{12}$ and ZPL pumping. Further scaling was limited by optical damage.

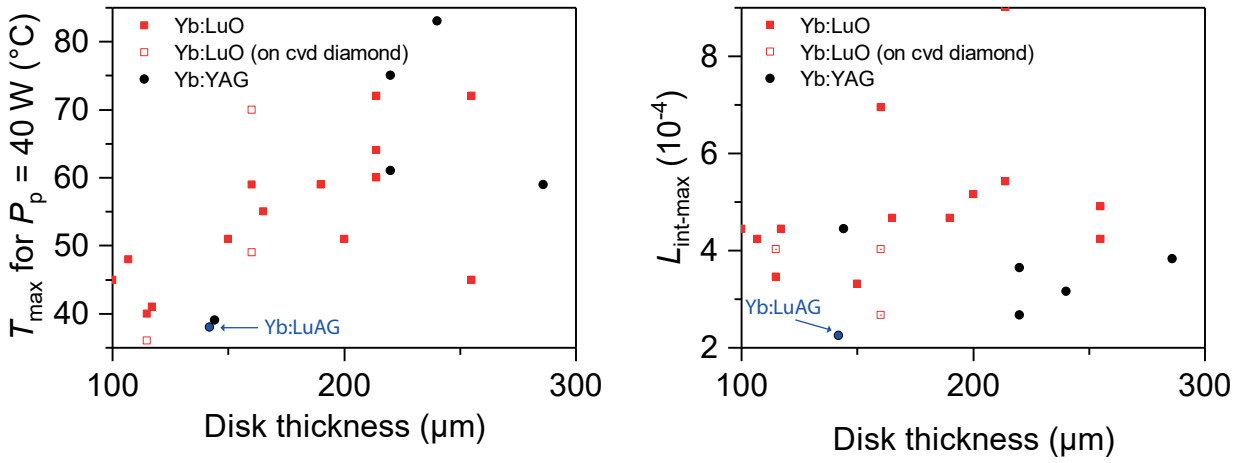

Figure 5.14: Analysis of Figure 5.13. (a) Maximum surface temperatures of the laser disks for $P_{\mathrm{p}} = 40\,\mathrm{W}$. (b) Estimation of the losses, according to Equation 2.78, assuming $\eta_{\mathrm{abs}}\eta_{\mathrm{ov}} = 0.9$.

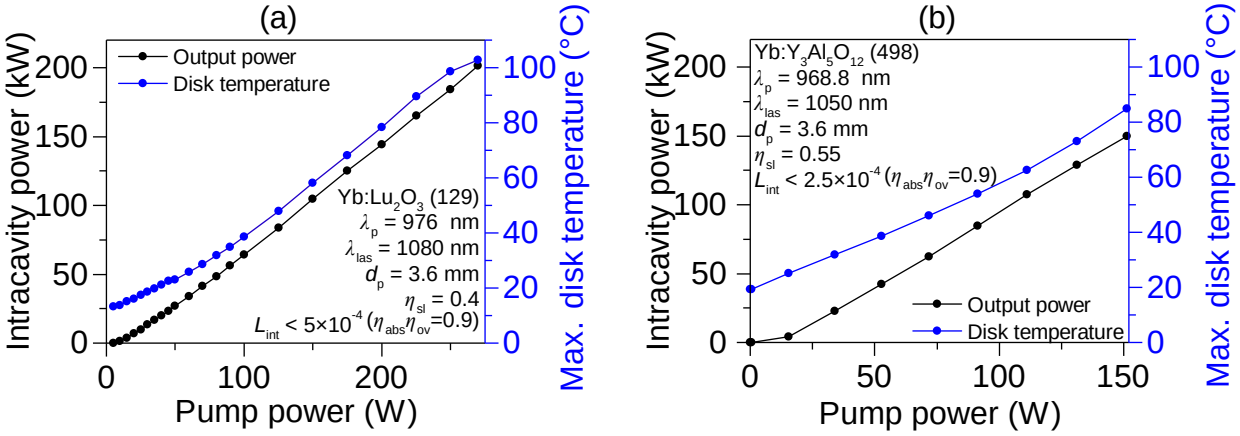

Figure 5.15: Results of pump power scaling experiments for a pump spot diameter of $d_p = 3.6\,\text{mm}$.

Optical damage Both disks were damaged at the highest intracavity power. However, the type of optical damage was different. The Yb:Lu_2O_3 disk obtained cracks through the surface. In contrast, the Yb:$Y_3Al_5O_{12}$ disk had a nodular point defect with a diameter of 10 µm close to its center. While the trigger for the crack of the Yb:Lu_2O_3 disk could not be assigned, a crack points to an excess of thermo-mechanical properties. The pump intensity of quality-insurance laser experiments done by D+G with this specific disk was more than three times higher compared to the investigations presented in Figure 5.15. Therefore, the pump intensity might have not have been responsible for the optical defect. In addition, the temperature of the laser disk was uncritical. This makes it probable, that the intracavity intensity was the reason for the optical damage. This is supported by observations that the optical defect regularly occurred at the position of highest intensity. Pictures of typical defects are shown in Figure 5.16.

The accumulation of nodular defects with diameters of approx. 10 µm [229] was observed for all mirrors and disks which were used in the experiments. Those defects can exhibit significant losses and have to be considered for further scaling of the intracavity power and intensity.

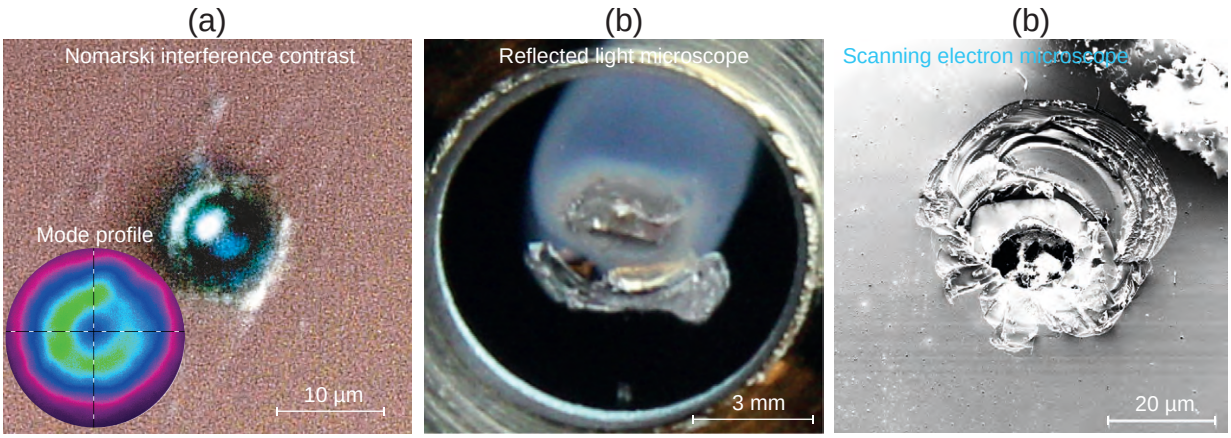

Figure 5.16: Images of different optical defects which were observed for disks and mirrors.

5.2.2 Linear resonators with a high beam quality

Specific setup All following experiments and descriptions are restricted to Yb:$Y_3Al_5O_{12}$, due to better experiences in respect to the beam quality, which were gained in initial experiments. At the Yb:$Y_3Al_5O_{12}$ disk 495 an ROC of $R_x = 6.3\,\mathrm{m}$ and $R_y = 6.2\,\mathrm{m}$ was measured. For a flat OC and a resonator length of $l_{res} = 8\,\mathrm{cm}$ this yields to a fundamental mode radius of $w_0 = 486\,\mu\mathrm{m}$. According to the calculations presented in section 5.1 this denotes a ratio of $w_0/w_p = 0.8$ which should have ensured a high probability of fundamental mode operation. To reduce the risk of optical damage, the maximum pump power was reduced in order to avoid intracavity powers higher than 10 kW.

Beam quality For the largest OC transmission, an M^2 of 1.03 was measured and for $T_{oc} < 1 \times 10^{-3}$ an $M^2 \approx 1.1$. The OC dependent trend is depicted in Figure 5.17 (b). The beam quality factor did not exhibit a strong dependence on the OC transmission in the case of the single-transverse-mode resonator. However, it improved with increasing OC transmission for the multi-transverse-mode resonator. A significant decrease of the M^2 factor is visible around an OC transmission of approx. 4×10^{-3} from $M^2 \approx 13$ to $M^2 \approx 7$. For the latter a decrease of the laser wavelength from 1050 nm to 1030 nm was observed. The shorter wavelength increases the absorption losses for the higher order modes. Subsequently, the beam quality factor can decrease because of the reduced contribution of higher order modes.

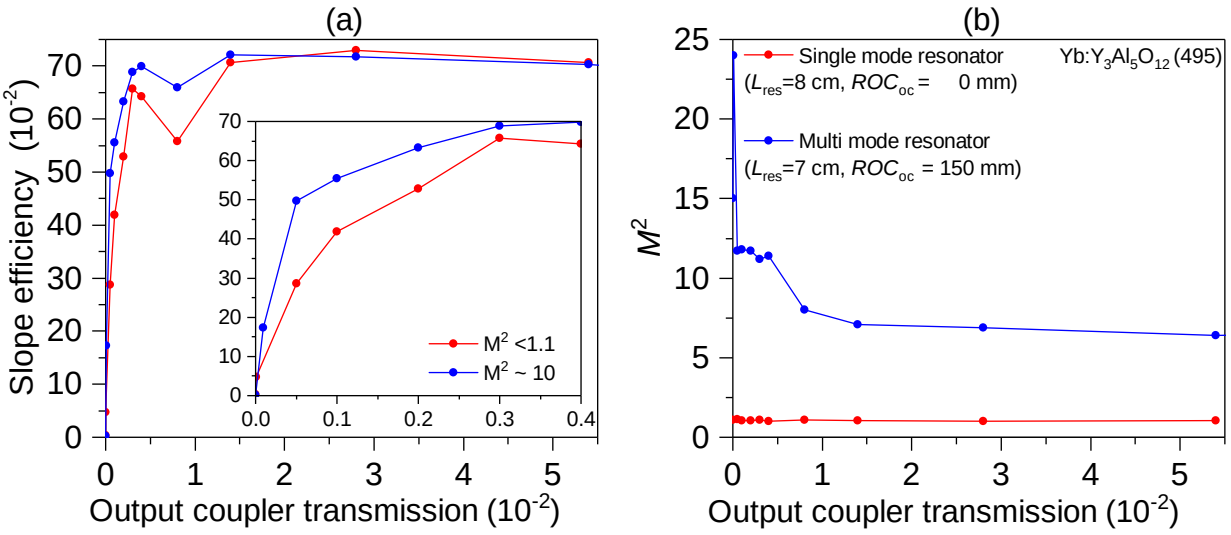

Figure 5.17: (a) Measured slope efficiencies of the TEM_{00} resonator with Yb:$Y_3Al_5O_{12}$ (495) in comparison to the results achieved in multi-mode operation from Figure 5.5. The inset shows a magnification of the data for lower OC transmissions. (b) M^2 measurements for the data of (a).

Mode	L_{res} (cm)	Clear aperture diameter (mm)				
		1	2	3	4	5
HG_{00}	7	4.5×10^{-2}	6.8×10^{-5}	4.3×10^{-10}	3.3×10^{-16}	6.6×10^{-16}
HG_{01}	7	12×10^{-2}	6.7×10^{-4}	5.1×10^{-9}	1.1×10^{-16}	6.6×10^{-16}
HG_{02}	7	23×10^{-2}	3.8×10^{-3}	7.6×10^{-8}	2.3×10^{-15}	8.8×10^{-16}
HG_{00}	30	31×10^{-2}	1.7×10^{-3}	4.7×10^{-7}	6.4×10^{-9}	9.8×10^{-14}
HG_{01}	30	65×10^{-2}	7.4×10^{-3}	6.4×10^{-4}	1.6×10^{-7}	1.3×10^{-9}
HG_{02}	30	41×10^{-2}	17×10^{-2}	4.2×10^{-3}	2.3×10^{-6}	4.9×10^{-11}

Table 5.5: Calculated diffraction losses for a linear 30 cm and a 7 cm long resonator, with a plane OC and an ROC of the disk of 5 m. The aperture is set to the diameter of the mirror and disk.

Laser performance The results are depicted in Figure 5.17. For OC transmissions of $T_{oc} < 4 \times 10^{-3}$ the laser performance of the single-transverse-mode operation is lower compared to the multi-transverse-mode operation. The difference becomes smaller for OC transmissions of $T_{oc} > 4 \times 10^{-3}$, where a maximum slope efficiency of $\eta_{sl} = 0.73$ was measured. The laser performance at low OC transmissions is of importance. For $T_{oc} = 5 \times 10^{-4}$ a slope efficiency of 0.29 ($\eta_{opt\text{-}max} = 0.22$) was measured and for $T_{oc} = 9.5 \times 10^{-5}$ a slope efficiency of 4.5×10^{-4} ($\eta_{opt\text{-}max} = 4 \times 10^{-4}$). The maximum intracavity power of 7.1 kW was obtained for $T_{oc} = 1.0 \times 10^{-3}$ and a pump power of $P_p = 20$ W. For an OC transmission of $T_{oc} = 5.0 \times 10^{-4}$ and a pump power of $P_p = 13$ W an intracavity power of 6.1 kW was achieved at a measured maximum disk temperature of approx. 22 °C. The slope of the intracavity power for $T_{oc} = 5.0 \times 10^{-4}$ of $dP_{int}/P_{pump} = 580$, would require for intracavity powers higher than 100 kW pump powers in the order of 200 W.

Loss analysis A Caird analysis of the data depicted in Figure 5.17 yielded losses of $L_{int} = 9 \times 10^{-4}$ and an efficiency of $\eta_{abs} \cdot \eta_{ov} = 0.89$. In contrast to multi-transverse-mode resonators, quasi-three level lasers with a Gaussian pump and laser mode might show a non-linear input-output power curve. While a nonlinear input-output curve can also be caused by the thermal occupation of the energy levels, this behavior can be further increased for Gaussian pump and laser shapes. Here, the relation between gain and doping concentration is not fixed, due to a broadened degree of transversal doping-ion excitation of the gain medium. Therefore, in this case the slope efficiency can rise for an increasing pump power. The single-transverse-mode experiments were conducted at low pump powers to decrease the risk of optical damage. This implies that the measured slope efficiencies could have been higher for larger pump powers, which would have corresponded to lower losses. An increase of losses can be caused by absorption losses [230, 231] and by an increase of diffraction losses. The calculated diffraction losses are listed in Table 5.5.

A resonator, designed for and operating on the fundamental mode exhibited losses of approx. 10^{-3}. A laser performance at low OC transmissions would require pump powers in the order of 200 W to achieve intracavity powers higher than 100 kW. The increase of losses could have been caused by diffraction and absorption losses at the disk.

5.2.3 Fundamental mode I-resonators with defined polarization

The following extension of the previous experiments consists of influencing and analyzing the resonator's polarization state, because a defined and stable polarization is required for the alignment of molecules. Each of the electromagnetic transversal modes has two possible degrees of polarizations, which are orthogonal. Those can be seen as self-contained modes of the resonator. The modes which experience lower losses in a resonator will start oscillating at first [133]. As elliptical and cylindrical polarizations are challenging to achieve in a resonator, this chapter only deals with the generation of linearly polarized fields.

Dependency of the beam quality and laser efficiency on the pump/laser mode overlap
The previous resonators were too short to add polarization selective elements. Therefore, the influence of the resonator length on laser performance and beam quality had to be investigated. The polarization was measured with a Glan-Thompson-polarizer mounted on a LabView controlled rotation stage (Standa, 8MR151). During the experiments the Yb:$Y_3Al_5O_{12}$ disk 495 accumulated optical defects and was found less suitable for further experiments. Instead, the Yb:$Y_3Al_5O_{12}$ disk 218 was used, which exhibited comparable losses and efficiencies in multi-transverse-mode and single-transverse-mode laser experiments. However, this reduced the comparability between the different laser experiments. The dependency of the laser performance on the resonator length and thus on the ratio of laser mode/pump radius was measured for an OC transmission of 4×10^{-4}. The results are shown in Figure 5.18. For resonators with a length up to 30 cm no strong decrease of the slope efficiency η_{sl} and the optical-to-optical efficiency η_{opt} could be observed.

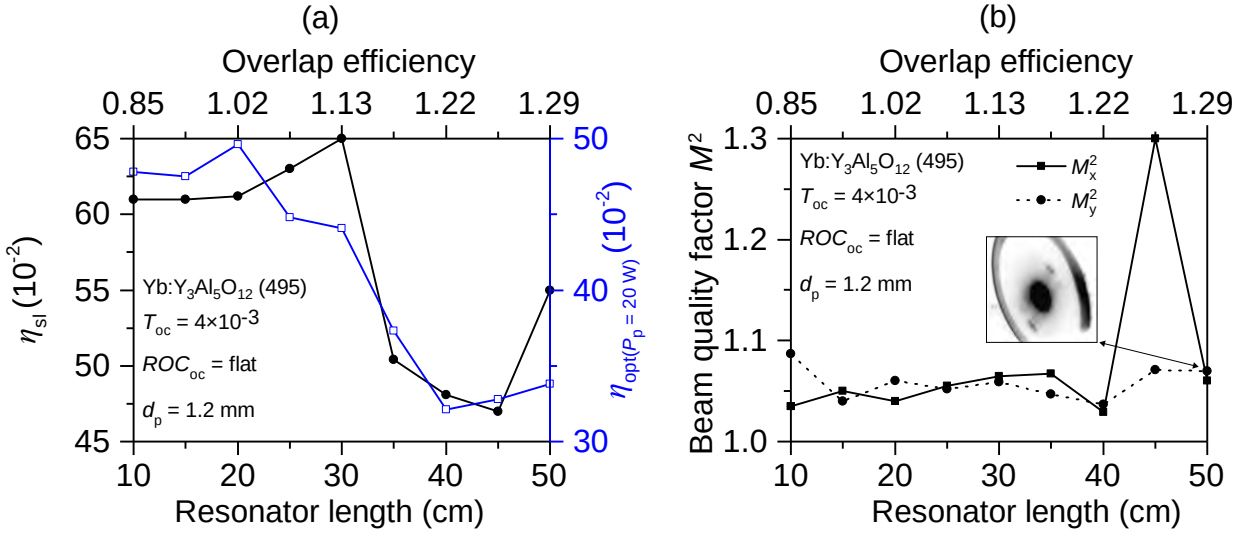

Figure 5.18: (a) Dependency of the slope efficiency η_{sl} and optical-to-optical efficiency η_{opt} on the resonator length and equivalent on the ratio between laser mode radius and pump mode radius. The maximum pump power was 20 W. (b) Corresponding beam quality factors M_x^2 and M_y^2. The inset depicts a camera image of the thin disk, showing the oscillation of higher order modes.

Additional losses by a window in the Brewster's angle An optical window inside of a laser beam in a resonator will induce additional losses. Depending on the material and the manufacturing, this can, e.g., be absorption or scattering losses. For a first test, a SiO_2 window with a thickness of 1 mm was perpendicularly included in a 30 cm long resonator. The measured maximum possible losses, with $L_{\mathrm{int}} = 2.8 \times 10^{-3}$, were approximately three times higher than obtained from the results shown in Figure 5.17. No influence of different materials on the laser performance could be determined.

A 30 cm long resonator was set up with a 1 mm plate of fused silica in the Brewster angle. The setup is shown in Figure 5.19 (b) together with the resonator's caustic for an ROC of the thin disk of 5 m. When oriented in Brewster's angle, a window exhibits lower losses for p polarized light than for s polarized light. Thus the gain medium tends to start with laser oscillation with p polarized light. The gain medium's temperature gradient causes mechanical stress and radially varying birefringence. The latter distorts an intrinsically linear polarisation state and exhibits losses at the Brewster plate [57, p. 420]. The laser output power P_{out} and the power reflected at all surfaces of the Brewster window P_{Bi}, were measured to determine the total losses at the Brewster plate.

Laser performance The results of the experiments are depicted in Figure 5.19 (a). For this resonator and disk the losses at the Brewster window were in the order of 1×10^{-3} with a decreasing trend for increasing OC transmissions. Additionally, the OC efficiency $\eta_{\mathrm{oc}} = T_{\mathrm{oc}}/(T_{\mathrm{oc}} + L_{\mathrm{int}})$ was reduced, due to the losses at the Brewster window. More details can be gained from the laser performance at two OC transmissions in Figure 5.20. For an OC transmission of 5×10^{-5} the output coupling efficiency was low due to losses and the power reflected at the Brewster plate was large. The losses at the Brewster window were in

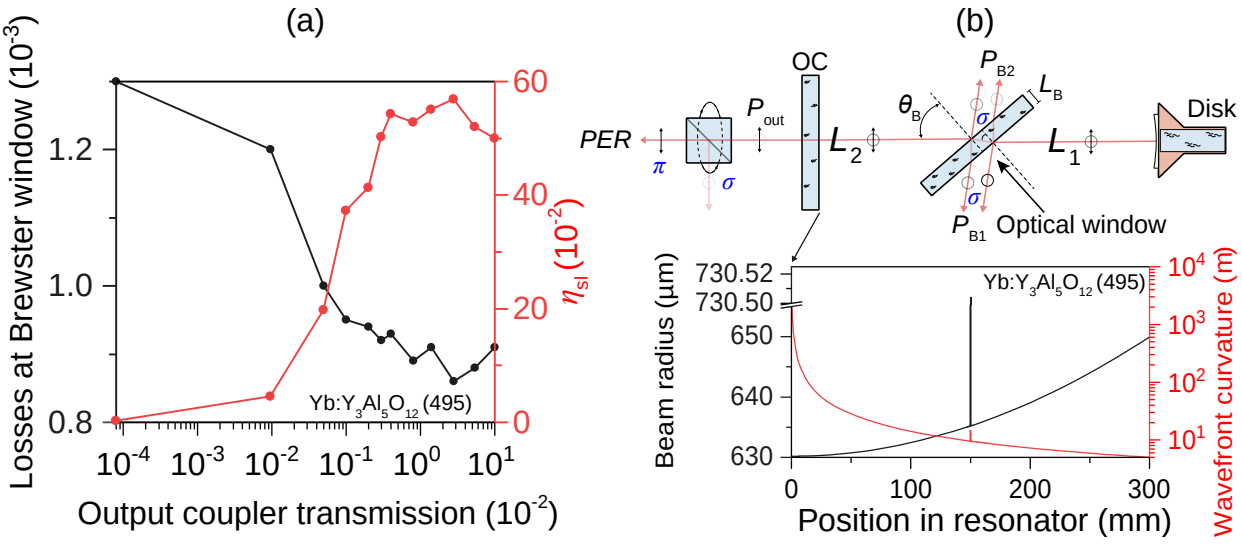

Figure 5.19: (a) Slope efficiency (red) and losses (black) at the Brewster window for a pump power of 20 W against the output coupler transmission of a 30 cm long fundamental mode resonator. (b) Scheme of the resonator with the corresponding caustic for an ROC of the disk of $R_{\mathrm{x}} = R_{\mathrm{y}} = 5$ m.

the order of 10^{-3} and did not change significantly over a pump power range between 10 W and 20 W. The losses were calculated by $L_{\mathrm{Brewster}} = T_{\mathrm{oc}} \cdot (\sum P_{\mathrm{Bi}})/P_{\mathrm{out}}$. For an OC transmission of 2.7×10^{-2} the behavior was different. The output coupling efficiency was larger and the power reflected at the Brewster window was lower than before. The calculated losses decreased from 9.3×10^{-4} at 10 W pump power towards 8.5×10^{-4} at 20 W. The behavior shown in Figure 5.20 illustrates an important problem of the proposed setup. In principle, no OC transmission is required. However, this would conduct the intracavity power into loss channels, which might be difficult to control. The slope of the intracavity power at $T_{\mathrm{oc}} = 5.0 \times 10^{-4}$ of $\partial P_{\mathrm{int}}/\partial P_{\mathrm{pump}} = 380$ necessitates pump powers in the order of 260 W for the envisioned intracavity powers higher than 100 kW. This pump powers require the use of larger pump spot diameters to reduce the pump intensity on the disk. Under consideration of the measured efficiencies and the available pump spot diameters, up to 1 cm in commercially available TDL modules, intracavity powers up to 1 MW seem achievable with pump powers less than 5 kW, given that the losses at the coatings and on the disks are comparable.

Loss analysis The evaluation of the laser performance by the Caird method of the disk 495 for different linear resonators is listed in Table 5.6. Two different data sets were considered, which illustrates the influence of larger OC on the determination of the losses. A closer look into the different losses is necessary to evaluate the possibility of an assignment to specific channels. The simplest scenario consists of a multi-mode resonator without additional optics such as Brewster elements. Therefore, this resonator consists of a disk, an OC and a medium of the resonator. It can be assumed that the losses are mainly composed of scattering, absorption, transmission and diffraction losses. However, even in this simple resonator, an assignment of the determined losses in the order of 3×10^{-4} to specific loss

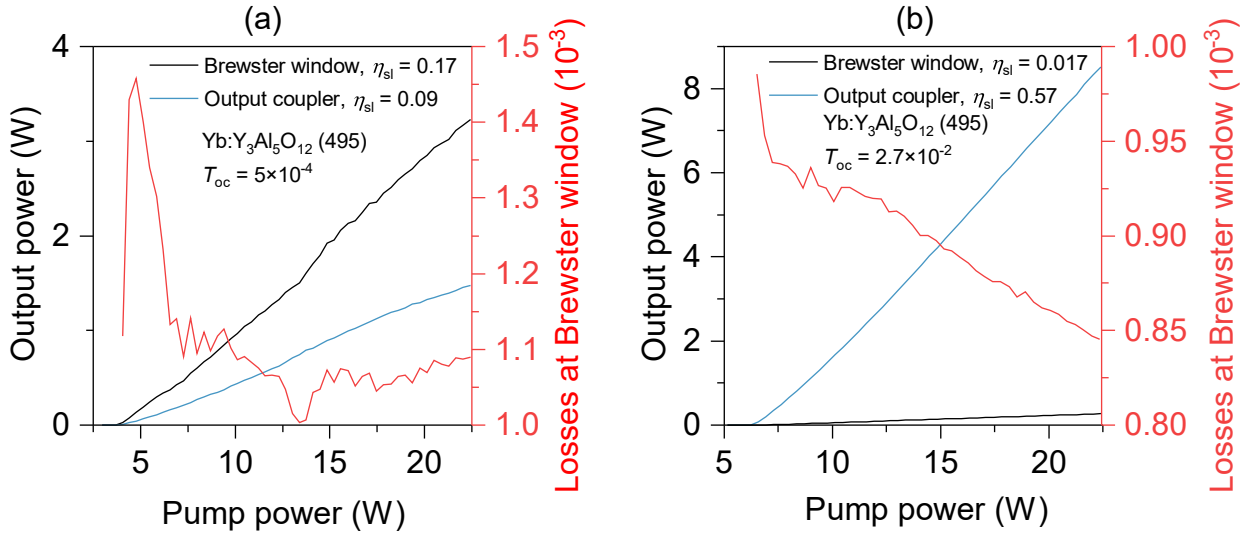

Figure 5.20: Output power transmitted through the OC (cyan), reflected at the Brewster window (black) and measured losses (red) at the optical window in the Brewster's angle according to the setup, shown in Figure 5.19 for an OC transmission of (a) 5×10^{-4} and (b) 2.7×10^{-2}.

Resonator	Caird fit		Nonlinear model fit	
	$L_{\mathrm{int}}(10^{-4})$	$\eta_{\mathrm{abs}} \cdot \eta_{\mathrm{ov}}$	$L_{\mathrm{int}}(10^{-4})$	$\eta_{\mathrm{abs}} \cdot \eta_{\mathrm{ov}}$
Multi-mode - linear	3.2 (2.9)	0.85 (0.82)	2.8 (2.8)	0.82 (0.82)
Single-mode - linear	8.9 (8.1)	0.89 (0.85)	9.4 (7.3)	0.91 (0.83)
Single-mode - linear - Brewster	15 (12)	0.85 (76)	11 (8)	0.76 (0.68)

Table 5.6: Calculated losses (10^{-4}) for different resonators and Yb:$Y_3Al_5O_{12}$ (495) with the Caird method and a direct nonlinear fit. The values in brackets include OC transmissions between 8×10^{-7} and 2.8×10^{-2} while the first include only OC transmissions between 9.5×10^{-5} and 4.0×10^{-3}.

channels was not possible. Two reasons can be given. First, the exact magnitude of different losses was unknown. This was the case due to the unavailability of precise information of the disk's surface and coating structure, which is required to calculate the transmission, diffraction and scattering losses. Second, losses, such as scattering depend on parameters like the geometric roughness, which can vary significantly over the disk and therefore over the laser mode. The tested disks from D+G exhibited a roughness R_{q} between 4 Å and 9 Å. This corresponds to a TIS between 3×10^{-5} and 10^{-4}. In parallel, measurements at the OC yielded a TIS of approx. 5×10^{-5}. Therefore, already the sum of the single scattering losses is in the order of the losses, which were determined with the Caird method. The transition to a single-transverse-mode resonator changes mainly two things. First, the overlap efficiency decreases and second, the diffraction losses differ in the multi-transverse-mode operation, already by the transition from a multi-mode to a single-mode system. In addition, the suppression of higher modes yields to increased diffraction losses for the fundamental mode.

A detailed investigation into the calculation of the diffraction losses can be found in [232]. A MATLAB based code to calculate the eigenmodes, eigenvalues and therefore diffraction losses of an optical cavity can be found here [233]. This MATLAB code was adapted to the cavity shown in Figure 5.19. The influence of the OPD originating from astigmatic and thermally induced phase distortions of thin-disks were not considered. This could in principle be measured with an SHWFS as demonstrated in [234] or calculated with FEM packages [232]. The results are listed in Table 5.5. When an optical window is added to a resonator in the Brewster's angle, new loss channels are possible. Scattering losses occur at all surfaces, which depend on the actual AOI, the wavelength of the laser and the surface roughness. Commercial fused silica Brewster windows are available with a surface quality of 10-5 scratch-dig and a surface roughness less than 1 nm. Therefore, as shown in Figure 5.21 (b), they can already significantly contribute to the resonator's internal roundtrip losses: according to Equation 2.83 the losses at a single surface can be in the order of 100 ppm for an AOI of 45° and a wavelength of 1 µm. Additionally, the Brewster window can exhibit absorption losses depending on the specific material. However, the absorption of fused silica glasses at a wavelength of 1 µm can be neglected [235]. Furthermore, comparative experiments with Suprasil 3001, which has the lowest fused silica absorption coefficient of $3 \times 10^{-7}\,\mathrm{cm}^{-1}$ at a wavelength of 1064 nm, showed no significant difference of the laser's performance.

The reflectivity of the window vanishes only for the Brewster's angle. Any physical beam has a divergence greater than zero according to Equation 4.2. Thus, only the central part of the beam does not experience reflection losses. This becomes relevant for an increasing beam divergence. The 30 cm long resonator of these experiments exhibits a beam divergence angle of 0.03°, which is negligible. However, the losses can become visible for resonators with a tight focus, because they exhibit a large beam divergence. In the case of folded resonators, the placement of the Brewster window in the arm with the lowest divergence is beneficial. An approximation of the reflection losses is shown in Figure 5.21 (a).

A significant fraction of the intracavity power is reflected out of the cavity at the Brewster window. The possible reason for this is (stress) induced birefringence in the gain material. Here, the polarization is rotated and subsequently reflected at the Brewster plate, where it represents an unwanted loss. A theoretical insight into losses caused by thermo-mechanically induced depolarization can be found in [72]. Calculations for the TDL and Yb:$Y_3Al_5O_{12}$ were made in [67]. These simulations yielded losses in the order of 5×10^{-4} for disk and resonator parameters comparable to the present ones. In addition, 25 % lower efficiencies in the polarized operation of a TDL experiments were reported [236]. Methods to minimize the depolarization losses are known [88, 145, 146] and the depolarization losses might be even avoided by the use of radially polarized lasers [237]. The disadvantage of most techniques is the integration of additional elements, which induce even larger losses. However, there are techniques, such as the use of cut optimized crystals [146, 238], which should be explored, if the use of polarization selective elements cannot be avoided.

A fundamental mode resonator with a Brewster plate exhibited losses of 1.5×10^{-3}, which were caused in a great extend by stress induced depolarization in the thin disk. For fundamental mode resonators an intrinsic polarization was observed, which was less stable but avoided additional losses.

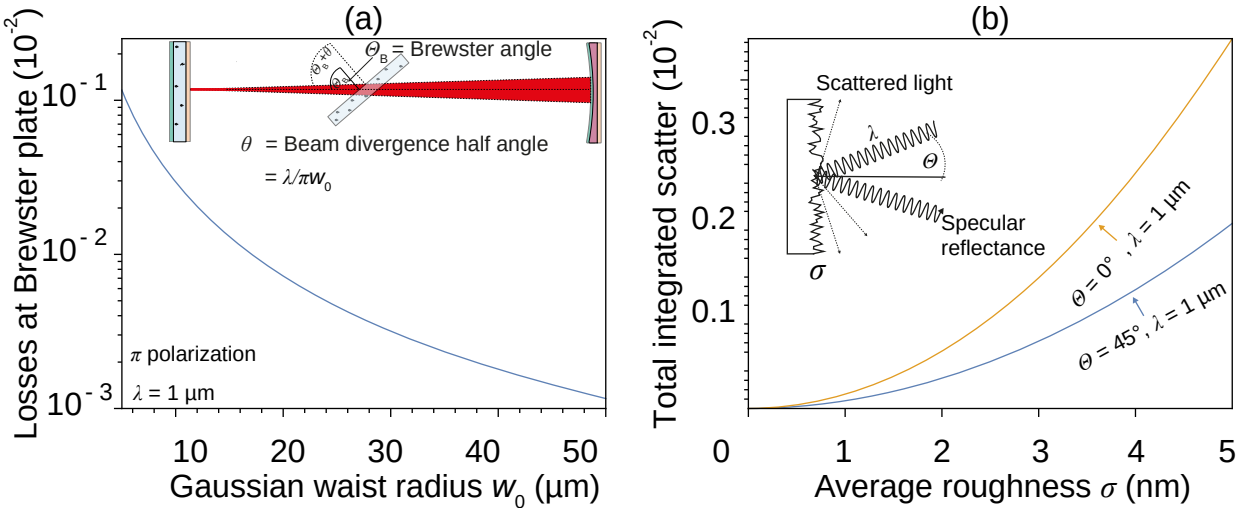

Figure 5.21: (a) Losses of a Gaussian beam at an optical window in the Brewster's angle due to intrinsic divergence which results in deviations of the outer beam parts from the Brewster's angle. (b) Scattering losses calculated according to Equation 2.83 for a wavelength of 1 µm for two angles.

Detailed investigations regarding intrinsic and induced polarization It can be distinguished between an intrinsic polarization and an induced polarization. The intrinsic polarization is shown in Figure 5.22 (a). The measurement without an optical defect exhibited a significant intrinsic polarization. A fit with a sine function revealed that the main axis was shifted by −24° against the vertical axis. The PER of the fitted function was 19:1. With a Brewster window, the PER of the OC transmitted power was larger than 100:1, and the one of the power reflected at the Brewster plate was 9:1.

The profile of the transmitted power in Figure 5.24 (a) shows deviations from a sine function. This can be explained by a lower stability of the intrinsic polarization. The intrinsic polarization can be caused by small differences of the original isotropic structure of the gain material. A stable laser can maintain the preference. When the system is disturbed, the preference can become less stable. The oscillation on the fundamental mode is beneficial for the intrinsic polarization, as every mode can maintain its independent polarization.

In the case of an optical defect, the behavior is perturbed, as it is shown in Figure 5.22 (a). This could have been caused by instabilities of the fundamental mode or due to absorption of the defect. Thus, the intrinsic polarization has the advantage of no additional elements having to be added to the resonator. The disadvantage can be seen in a lower PER, a lower reproducibility in respect to different laser disks and a lower stability. Due to the optical defect, the measurements were continued with Yb:$Y_3Al_5O_{12}$ (218). Further investigations of the intrinsic polarizations are depicted in Figure 5.23. Here (a) shows a polarization measurement. The PER of the intrinsic polarization is lower in comparison to Yb:$Y_3Al_5O_{12}$ (495). In addition, the contribution probability of higher order modes can be reduced by an aperture in the resonator. Results of the intrinsic polarization in dependence on the OC transmission for an open aperture and one with a diameter of 5 mm, can be gathered from

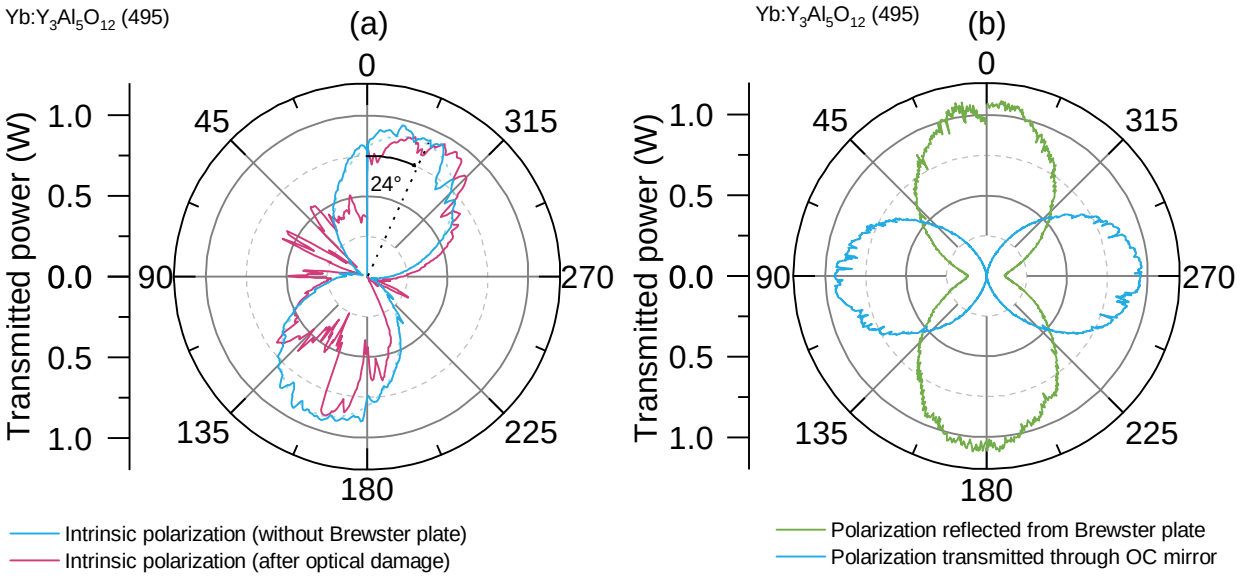

Figure 5.22: Polar graph of the transmitted power to (a) illustrate the intrinsic polarization and the impact by optical damage and (b) the polarization induced by a Brewster plate.

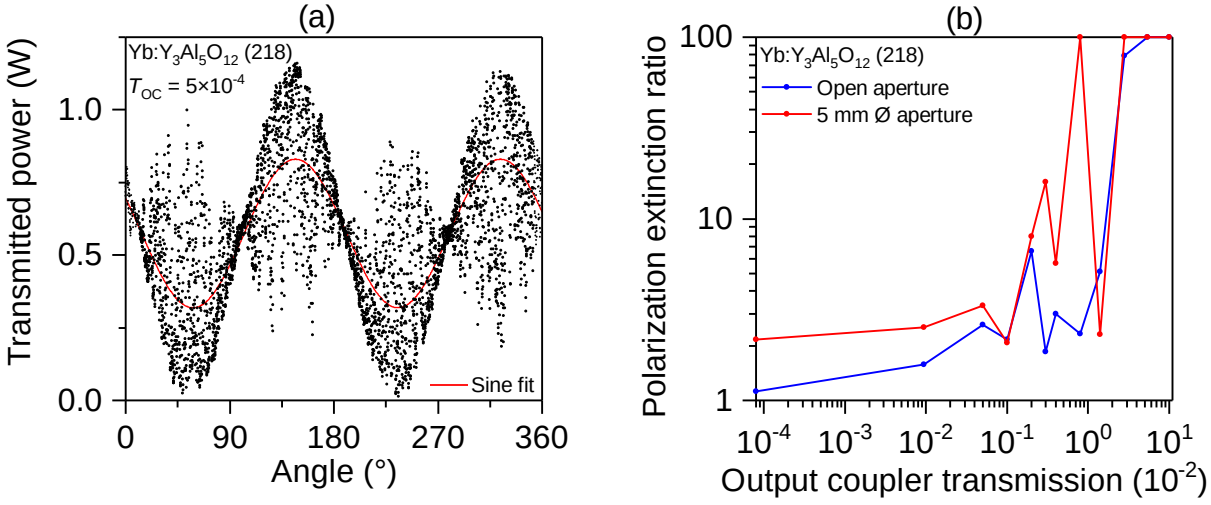

Figure 5.23: (a) Sine fit of the output power transmitted through a rotating polarizer behind the OC. (b) Polarization extinction ratio (PER) for the intrinsic polarization with an additional aperture.

Figure 5.23 (b). We can learn two things from this figure: First, the PER of the intrinsic polarization increases with the OC transmission. Second, an aperture yields to a higher PER for the same OC transmission, due to the reduced contribution of higher order modes. The impact of the OC on the PER transmission is difficult to estimate. However, at a lower OC transmission the laser tends to oscillate on many axial modes. For large OC transmissions, the laser oscillation wavelength becomes shorter and the number of modes decreases. This might augment the stability of the polarization of the independent laser modes and in addition, lower the influence of external perturbations.

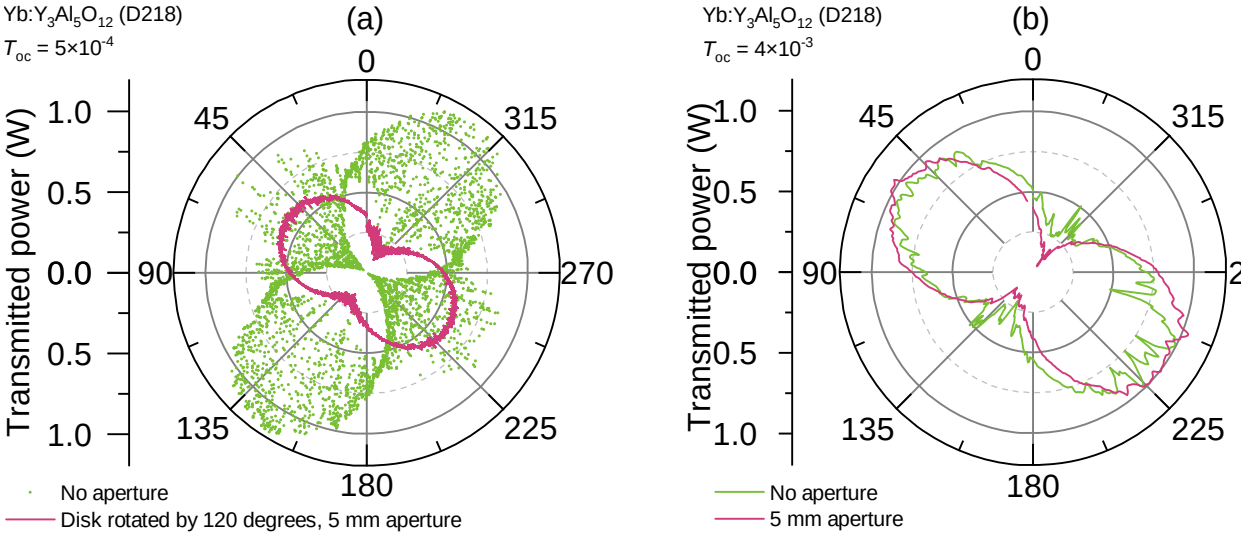

Figure 5.24: Polar graphs of the output power transmitted through a rotating polarizer behind the OC for Yb:$Y_3Al_5O_{12}$ (218) for two different OC transmissions.

5.3 Discussion of the results with linear resonators

Polarization selection Two types of polarization selection were observed. Polarization selective elements exhibited diverse losses for different polarizations and generated a preferred field direction. Experiments showed an OC transmission independent PER of more than 100:1 with a 1 mm thin fused silica window, limited only by the noise of the power meters. The intrinsic polarization significantly depended on the OC transmission. For low transmissions up to 10^{-2} the PER was between 1:1 and 10:1 and originated presumably from stress induced deviations of the isotropic structure. The responsible stress can come from the crystal growth, the mounting procedure on the heatsink, or from the coating. This yields to significant losses for an additional polarization selective element. Measurements determined the depolarization losses caused by the reflection of power at a Brewster plate in the order of 10^{-3} for a pump spot diameter of 1.2 mm.

Single-transverse-mode operation Single-transverse-mode operation was achieved by a suitable laser/pump mode overlap with an appropriate resonator design for a pump spot diameter of 1.2 mm. The small pump spot decreased the influence of optical defects and the predominant astigmatism, which was confirmed with an SHWFS. In the experiments with a short resonator an M^2 below 1.05 was measured for internal losses of 8.9×10^{-3}.

Intracavity powers higher than 100 kW Intracavity powers in the order of 200 kW and 150 kW were obtained with a pump spot diameter of 3.6 mm in multi-transverse-mode operation with Yb:Lu_2O_3 and Yb:$Y_3Al_5O_{12}$. The pump power was 270 W in the case of Yb:Lu_2O_3 and 150 W in the case of Yb:$Y_3Al_5O_{12}$. With a pump spot diameter of 1.2 mm, an intracavity power of 135 kW was measured for Yb:$Y_3Al_5O_{12}$. This corresponded to an enhancement by a factor of 2500 with respect to the incident pump power of 54 W, enabled by the low losses of state-of-the-art processed gain disks. In all experiments further scaling of the intracavity power was limited by optical damage at disks and mirrors. Generally, the observed optical damage of laser disks could be divided into two groups. The first group of disks showed transverse cracks through the entire disk, which can be explained by thermo-mechanical stress. The second group exhibited small nodular defects with diameter up to several µm. Most defects were found in the center close to the area of the highest beam intensity. Defects in the HR and AR coatings which absorb light and finally melt are plausible. Another reason for optical damage are high field-seeking dirt or dust molecules, which can be attracted to optical surfaces, where they can absorb photons.

Electric field intensity The required intensities of $10^{10}\,\mathrm{W\,cm^{-2}}$ to $10^{12}\,\mathrm{W\,cm^{-2}}$ were not achieved in the presented linear resonators. Those intensities require an intracavity focus for the available pump powers, which could not be achieved with the available laser disks in a linear resonator. Here, the highest intracavity intensities of approx. $11\,\mathrm{MW\,cm^{-2}}$ were obtained on the pump spot, which probably already caused several optical defects.

Resonator roundtrip losses The resonator's internal roundtrip losses were determined in a short and efficient multi-transverse-mode resonator for several disks. The losses were in the order of 3×10^{-4} for a pump spot diameter of 1.2 mm. No significant dependence of the resonator's internal losses on the known disk parameters could be determined. The independence on the disk's thickness suggests that the losses were caused at surfaces rather than in volumes. However, this could not be confirmed in experiments with a pump spot of 3.6 mm, which showed a comparable performance for low OC transmissions.

Measurements in a single-transverse-mode resonator with a pump spot of 1.2 mm exhibited losses of 9×10^{-3} and with an additional optical window in the Brewster's angle in the order of 1.5×10^{-2}. They could not be assigned to specific loss channels due to their comparable magnitudes. A combination of scattering, transmission, absorption, diffraction at the disk and the mirror, additional losses at the Brewster window and nodular defects is plausible. The losses at the Brewster window originate from depolarization and the angular difference of the outer parts of a Gaussian beam from the Brewster's angle. Finally, the determined resonator's internal roundtrip losses of 1.5×10^{-2} with a linear field polarization in single-transverse-mode operation might require pump powers of more than 200 W to achieve intracavity powers in the order of 100 kW.

Choice of the gain material Under consideration of the estimated inaccuracy of the loss determination in the order of 5 %–10 %, no gain material stands out from measurements of the internal losses or laser performance. The most relevant difference between the gain materials can be seen in their thermal conductivity. Spectral properties, such as gain cross-sections, have less importance and should not influence the resonator's internal losses, nor have a significant importance on the laser performance at low OC transmissions. In parallel, in respect to optical damage, no distinct advantage of one specific material was observed.

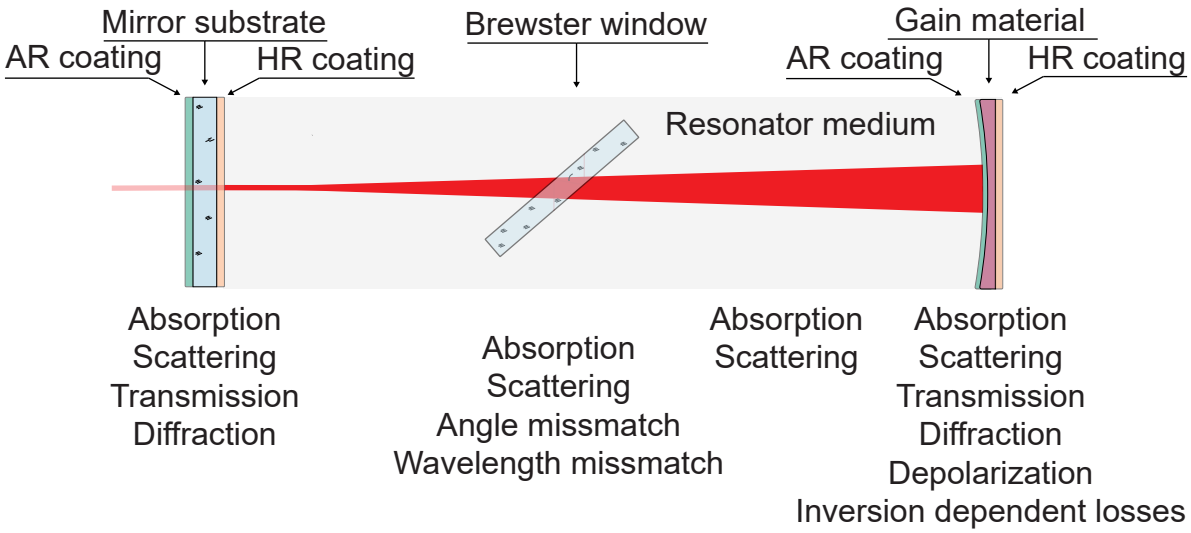

Figure 5.25: Overview about several loss mechanisms which can occur in a linear resonator with an optical window in the Brewster angle. Optical defects are not enlisted and can occur at all surfaces.

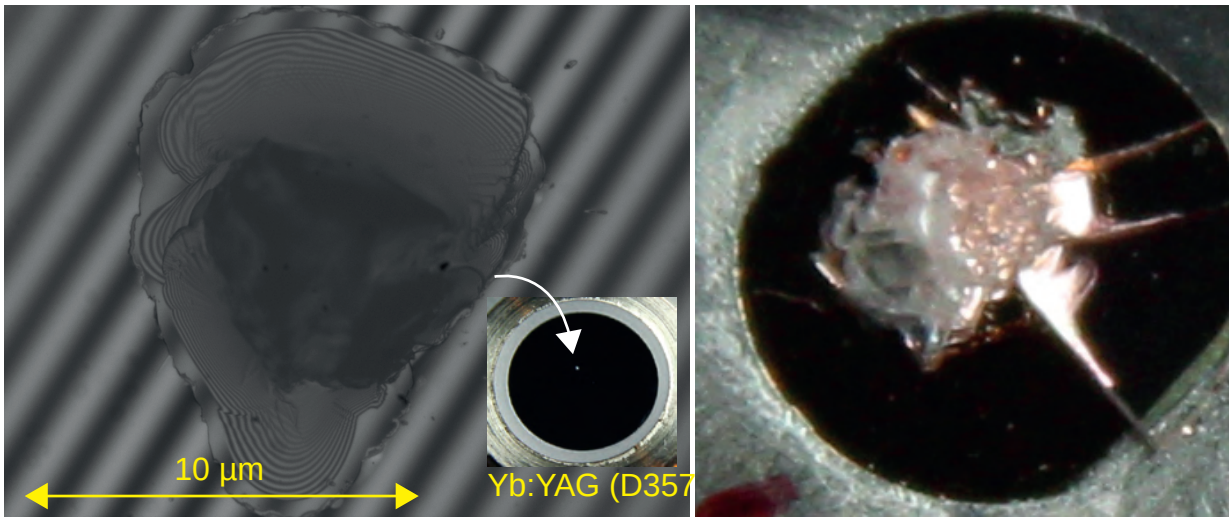

Figure 5.26: Left: microscopic picture of a small optical damage of a thin disk, presumably induced by point defects in the HR coating. Right: Transverse cracks through nearly the entire disk.

This points towards gain material independent losses and thus towards causes which they have in common, such as coatings and contacting. The monitoring of optical damage is difficult, as it would require a continuous image of the disk's surface in high resolution, to detect optical defects of µm size. In parallel, no specific range of the intracavity intensity and power could be determined yet, which would significantly reduce the risk of optical damage. The reason for the occurrence of optical damage in these experiments could not be finally assigned and needs further investigation.

A choice of the best suited host material can be made under consideration of the availability and commercial use of the gain materials. Yb:Lu_2O_3 bulk crystals nowadays are not commercially available in a constant optical quality, due to high requirements on the growth. In contrast, Yb:$Y_3Al_5O_{12}$ is industrially available since decades. This indicates, that production lines, such as polishing, coating or soldering, are adapted and optimized to the host material, which is not the case for Yb:Lu_2O_3. The same advantages are valid for Yb:$Lu_3Al_5O_{12}$, which can probably be found in commercial high power TDL, because of its higher thermal conductivity in comparison to Yb:$Y_3Al_5O_{12}$. Thus, considering the previous statements, at the moment, the suggested optical candidate for continuative experiments is Yb:$Lu_3Al_5O_{12}$. Due to the planned purpose of laser operation at potentially low OC transmissions, there is room for further optimizations. A decrease of the disk's thickness to reduce its temperature, or a reduction of the ytterbium doping concentration, which could improve the optical quality of the gain material, would be feasible.

5.4 Design of the folded resonators for thin-disk lasers

The experiments with folded resonators had the following purpose: they allowed comparing the determined losses and efficiencies with the ones from the linear resonators. The results can be different, as scattering and diffraction losses will increase with the number of optical elements. Furthermore, it is easier to set up resonators with a tight internal focus and to investigate further possible losses. Linear resonators can get meter long lengths, if they are designed for single-transverse-mode operation. In addition, if they contain the thermal lens of a laser disk [63] the adjustment sensitivity diverges for increasing pump powers, as the ROC of the disk tends to become larger [63, 214]. The schemes of different resonators and the abbreviations used in this chapter are depicted in Figure 5.27.

When the resonator is folded over a curved mirror, its focal length will change in dependency of the AOI. These astigmatic distortions can limit the performance and the beam quality. They can be corrected by folding the resonator out of the plane, by special mirrors or by optical windows [55, p.495].

The folded resonator's design is presented for three different cases, as shown in Figure 5.27. The first case (a) is a multi-transverse-mode resonator, which is folded via the disk. The second case depicts a single-transverse-mode resonator, which is also folded via the disk. The last case (b) is a single-folded resonator, folded via a mirror, designed for single-transverse-mode operation and with a strong internal focus.

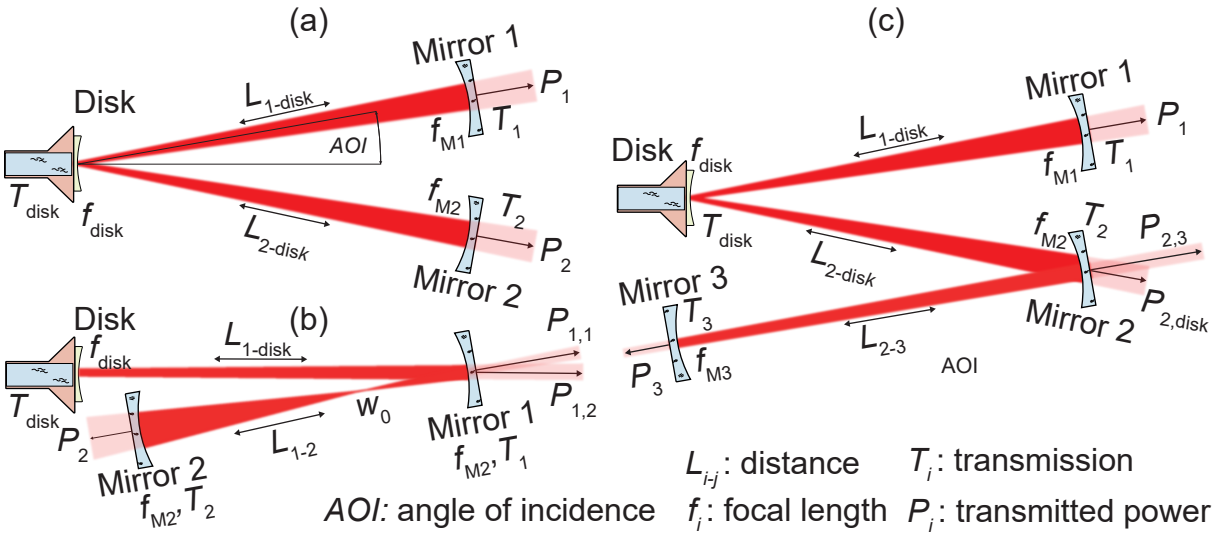

Figure 5.27: Scheme of folded (V) resonators. (a) the disk is the folding mirror. (b) the mirror M_1 is the folding mirror. (c) Scheme of one example of a two-folded Z-resonator.

Design of single folded multi-and single-transverse-mode resonators A calculation of the stability parameter of the roundtrip matrix $-1 < ((A+D)/2) < 1$ and of the Gaussian beam radius on the disk is shown for a resonator folded via the thin disk in Figure 5.28. In the symmetric case of $L_{1\text{-disk}} = L_{2\text{-disk}}$ and two equal OC mirrors (in (a) and (b)), the beam radius on the disk decreases for $L_{1\text{-disk}} = L_{2\text{-disk}} \rightarrow f_{M1}$. Therefore, this resonator is suitable for multi-transverse-mode operation. The asymmetric resonator, (calculated in (c) and (d)) can be more beneficial for fundamental mode operation, when the areas with a comparable beam radius are bigger. Single-transverse-mode operation can be achieved for $w_{\text{disk}} \approx 480\,\mu\text{m}$ for a pump spot of 1.2 mm. This yields to, e.g., $L_{1\text{-disk}} = 21\,\text{cm}$ and $L_{2\text{-disk}} = 71\,\text{cm}$. For almost equal resonator arm lengths, areas close to $L_{1\text{-disk}} \approx L_{2\text{-disk}} \approx 24\,\text{cm}$ at the edge of the stability zone can be used in case of a symmetric resonator design.

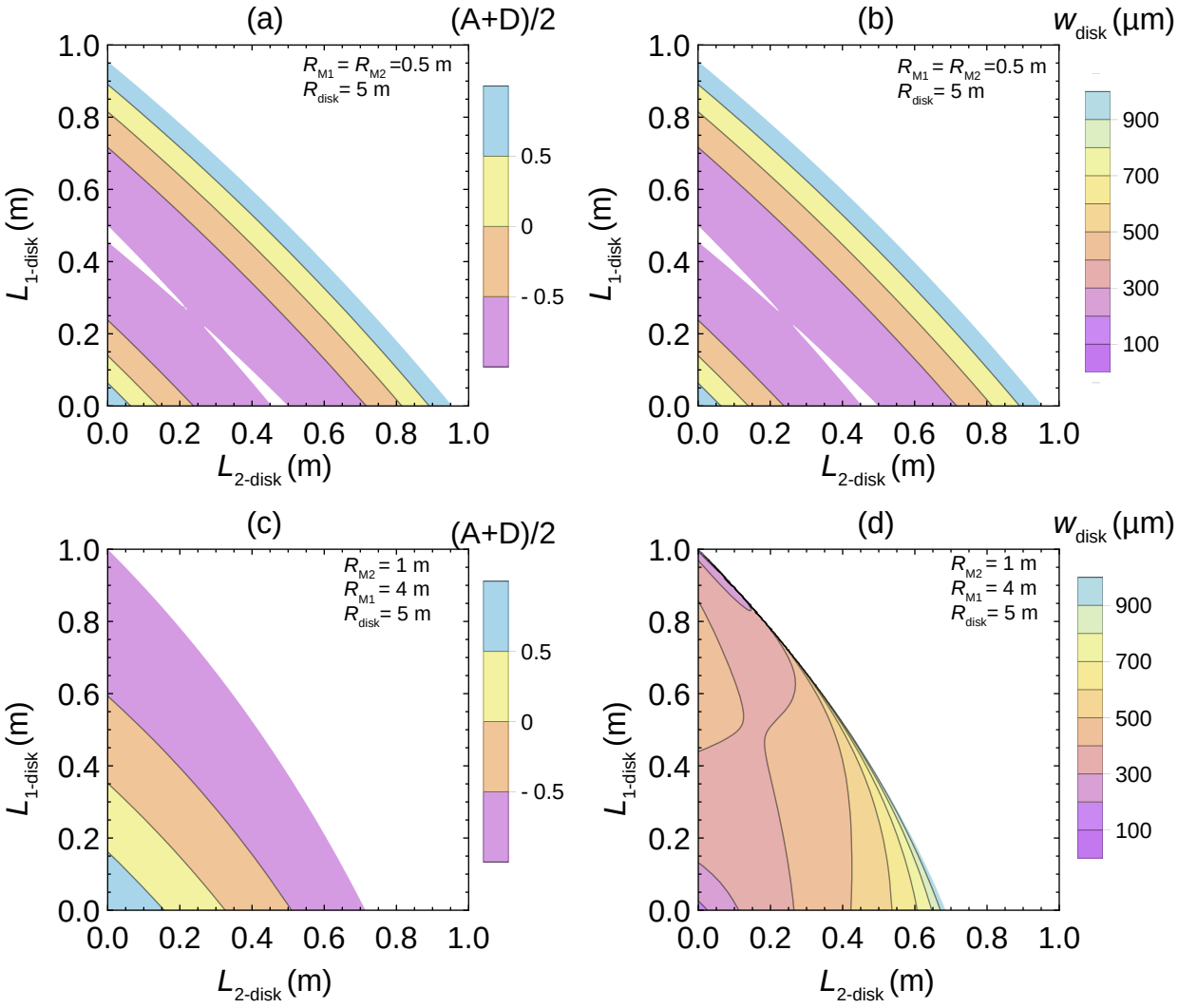

Figure 5.28: (a)/(c) Plot of the stability parameter and (b)/(d) Gaussian beam radius on the thin disk for a symmetric resonator in (b) and for an unsymmetric resonator in (d).

Resonator design of single-transverse-mode resonators with a small internal focus An internal focus can be achieved when the resonator is folded via a mirror with the ROC ROC_{M1}. For a small ROC this mirror can focus the beam in a distance of approx. $ROC_{M1}/2$. This focus can be imaged back onto this point by a 2f-2f image by a mirror with an ROC_{M2} in a distance from the mirror M_1 of approx. $ROC_{M1}/2+ROC_{M2}$. The mode size on the mirror M_2 can be controlled with ROC_{M2}. A larger ROC_{M2} requires a longer distance from the focus and because of the constant Rayleigh length the beam radius on M_2 increases.

Diffraction losses can become relevant for beam radii comparable to the mirror dimensions or for a low AOI on M_1. In this case the beam between the two mirrors can overlap with the beam coming from the disk to the first mirror. In addition, already for an AOI on M_1 of approx. 5°, the tangential and sagittal beam radii on the mirror M_1 can differ by 10 %. Caused by the astigmatism, which is also relevant for the pump spot, the probability of an oscillation of higher order modes can be increased. A free space of approx. 10 cm between the two mirrors suggests the use of $ROC_{M2} = 10\,\text{cm}$. The smallest ROC which was available at the time of the experiments was $ROC_{M1} = 5\,\text{cm}$. Thus, this corresponds to a length between M_1 and M_2 of approx. 12.5 cm. With the available mirror mounts, this leads to an AOI on the mirror M_2 larger than 3°. A beam, which is central pointed on the mirror M_2 necessitates a minimum AOI of approx. 6° for 1-inch optics. To find the working point, also the required Gaussian beam radius on the thin disk of 480 µm has to be considered. This suggests the minimization of a figure of merit (FOM) with the target beam radius on the disk $w_{\text{disk-want}}$ and the required waist radius $w_{0\text{-want}}$ according to

$$FOM = \sqrt{\left|\left(\frac{w_{\text{disk}}}{w_{\text{disk-want}}}\right)^2 - 1\right| + \left|\left(\frac{w_0}{w_{0\text{-want}}}^2\right) - 1\right|}. \tag{5.1}$$

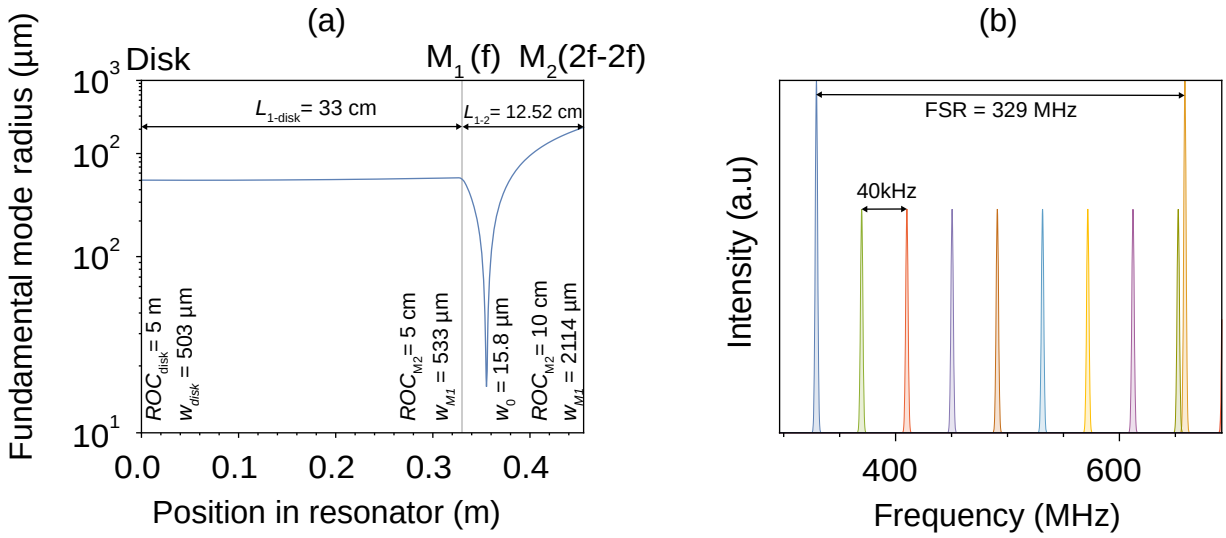

Figure 5.29: (a) Caustic of the resonator with a strong internal focus. (b) Frequency spectrum of the resonator. The linewidth has to be scaled in dependence on the resonator losses.

d_p (mm)	ROC_{disk} (m)	ROC_{M1} (cm)	ROC_{M2} (cm)	$L_{1\text{-disk}}$ (cm)	$L_{1\text{-}2}$ (cm)
1.2	5	5	10	33	12.52
1.4	5	7	15	54	18.5
1.8	5	8	13	55	17
2.7	5	11.2	11	88	16.54
3.6	5	15	10	75	17.38
5.4	5	20	20	125	29.75
10	5	30	15	200	29.29

Table 5.7: Suggested resonator designs for different pump spot diameters. The target beam radius on the disk was $0.4 \cdot d_{pump}$ and the target waist 20 µm.

The optimization of Equation 5.1 was performed for additional pump spot diameters larger than 1.2 mm to explore the general feasibility for larger pump powers. Inclusion of the ROC of the two OC as parameters into the optimization turned out to be necessary. In a second step, the optimized ROCs were set to common available ROCs and the optimization was performed again. Two examples are shown in Figure 5.32. The desired length of $L_{1\text{-}2}$ would have to be adjusted for a pump spot diameter of 3.6 mm to a precision better than 100 µm. In case of a pump spot diameter of 10 mm the necessary precision is increased to approx. 10 µm. The results of the resonator design and optimization can be obtained from Table 5.7. The alignment sensitivity of this resonator can be gathered from Figure 5.30 and Figure 5.31. In Figure 5.30 (a) the plot of the stability parameter is shown in dependency on L_{1-disk} and L_{1-2}. It can be seen, that the stable range of L_{1-2} decreases for an increasing L_{1-disk}. In Figure 5.30 (b) region plots of different requirements (inequalities) are depicted. The overlap of the three regions defines the target area of the resonator. The working point of Figure 5.29 is depicted by the horizontal and the vertical lines. A better insight into the

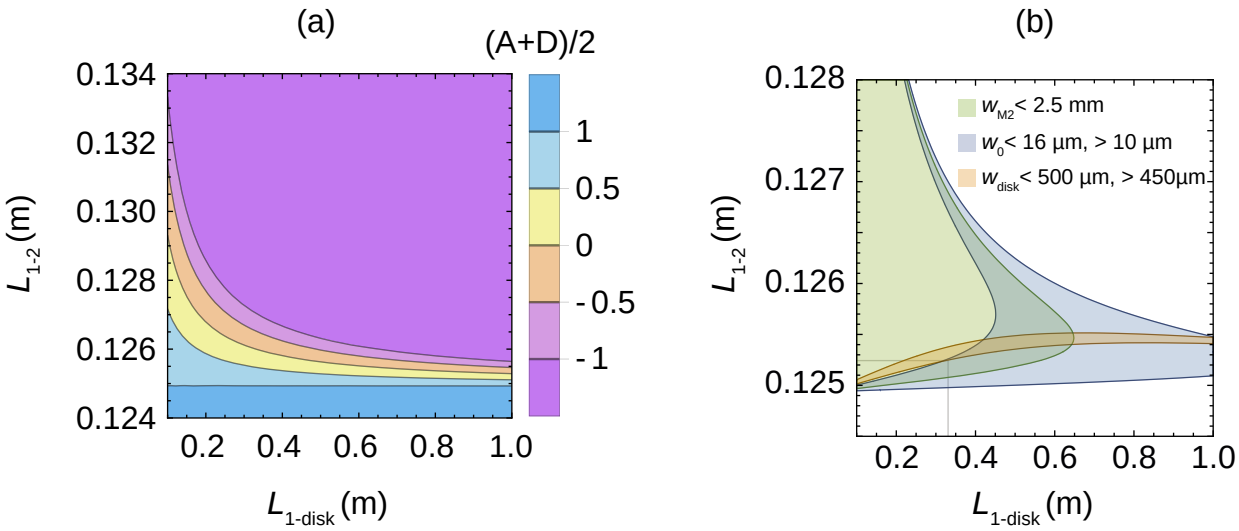

Figure 5.30: (a) Stability parameter for the resonator, shown in Figure 5.29.(b) Region plot for different inequalities of the resonator's properties.

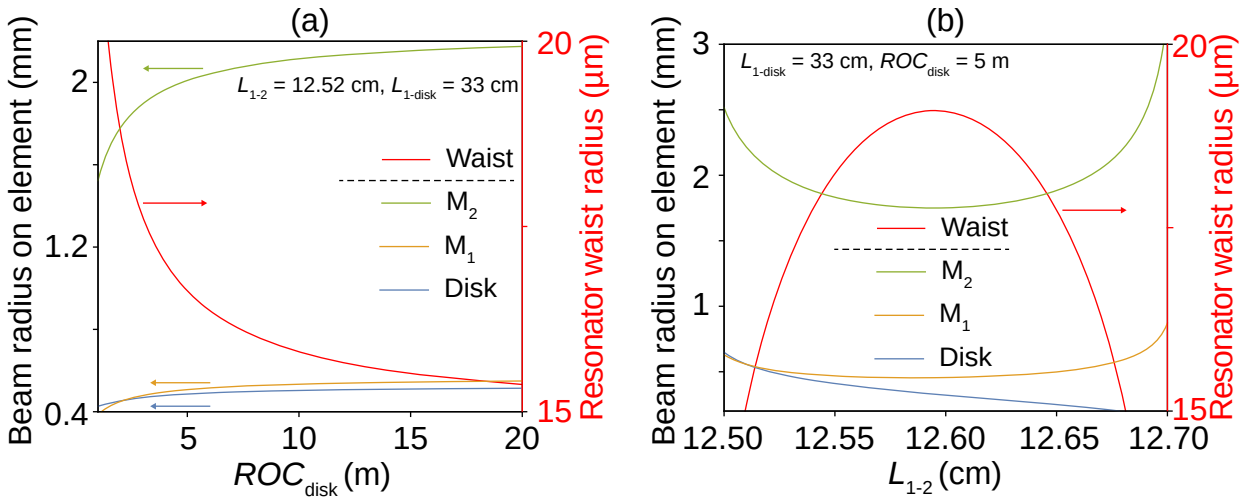

Figure 5.31: Variation of the beam and waist radius in dependence on the (a) ROC of the disk and (b) the length $L_{1\text{-}2}$ between the two focusing mirrors.

stability can be gained from Figure 5.31. In (a) the ROC of the disk is varied and in (b) the distance between the mirror M_1 and the mirror M_2 is. The remaining parameters are kept constant. An increase of the ROC yields to a lower waist radius, while the radius on the disk is nearly constant. Therefore, this resonator should not exhibit a large sensitivity in respect to changes of the ROC. In contrast, a strong dependence on the length can be seen.

A resonator design for fundamental mode operation and a 20 µm waist can be found for common pump spot diameters. At the same time one has to consider the astigmatism and possible losses by diffraction.

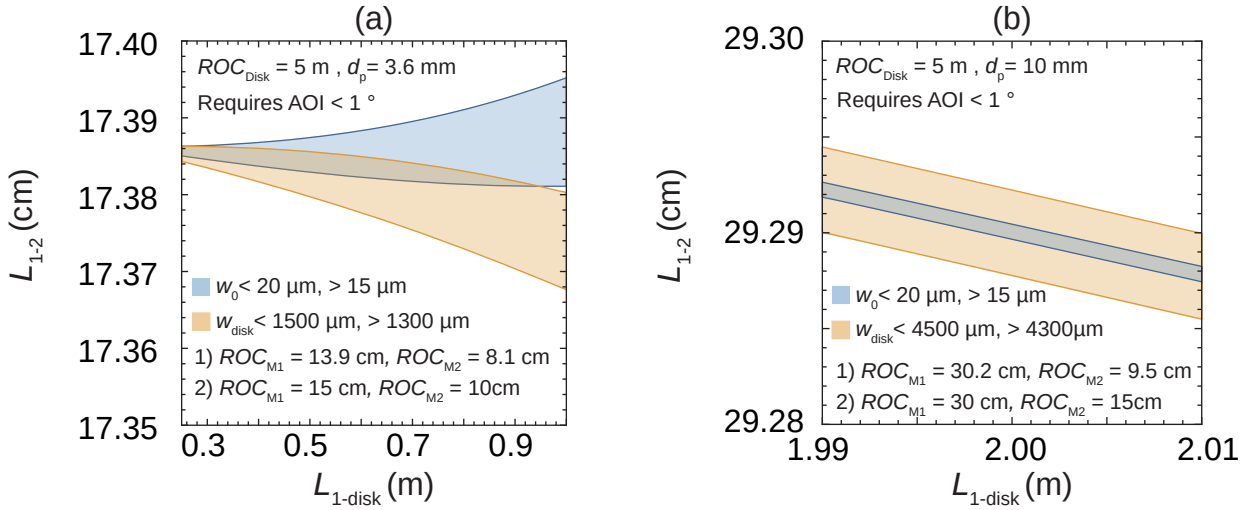

Figure 5.32: Stability zones for resonators with tight focus and a large pump spot of (a) 3.6 mm and (b) 10 mm. Further parameters of the resonators can be found in Table 5.7.

5.5 Results of laser experiments with folded resonators

5.5.1 Laser experiments with single-folded resonators

Specific setup All experiments were conducted with Yb:$Y_3Al_5O_{12}$ (218). The laser beam was folded via the disk. The observation of optical damage after the previously described experiments required a rotation of the disk and a slight shift of the pump spot. The multi-transverse-mode resonator was set up with $ROC_{M1} = ROC_{M2} = 0.5$ m. Both resonator arms had a length of approx. 25 cm. The AOI on the disk was 10°. Single-transverse-mode operation was achieved with an arm length of approx. 23.5 cm. For experiments with a polarization selection, a 1 mm thick fused silica Brewster window was added.

Laser performance The results of the laser performance are shown in Figure 5.33 (a) and listed in Table 5.8. For both the multi-transverse-mode resonator and the single-transverse-mode resonator, maximum slope efficiencies of 0.58 and 0.46 were measured at the OC transmission rates of 8×10^{-3} and 4×10^{-3} with a maximum output power of 7.2 W and 6 W, respectively. In this configuration, the maximum optical-to-optical efficiencies were 0.48 and 0.4. The high resonator losses and the low pump powers led to surface temperatures below 30 °C. For the single-transverse-mode resonator without a Brewster window the beam quality was lower than 1.1. The irregularities, which are visible in Figure 5.33 (b) may have been caused by optical defects or beam quality distortions. To increase the polarization preference, a Brewster window was inserted into the resonator. This decreased the beam quality for $T_{oc} < 8 \times 10^{-3}$. In addition, the results in Figure 5.33 (a) show a further decreased laser performance in comparison to the single-transverse-mode operation.

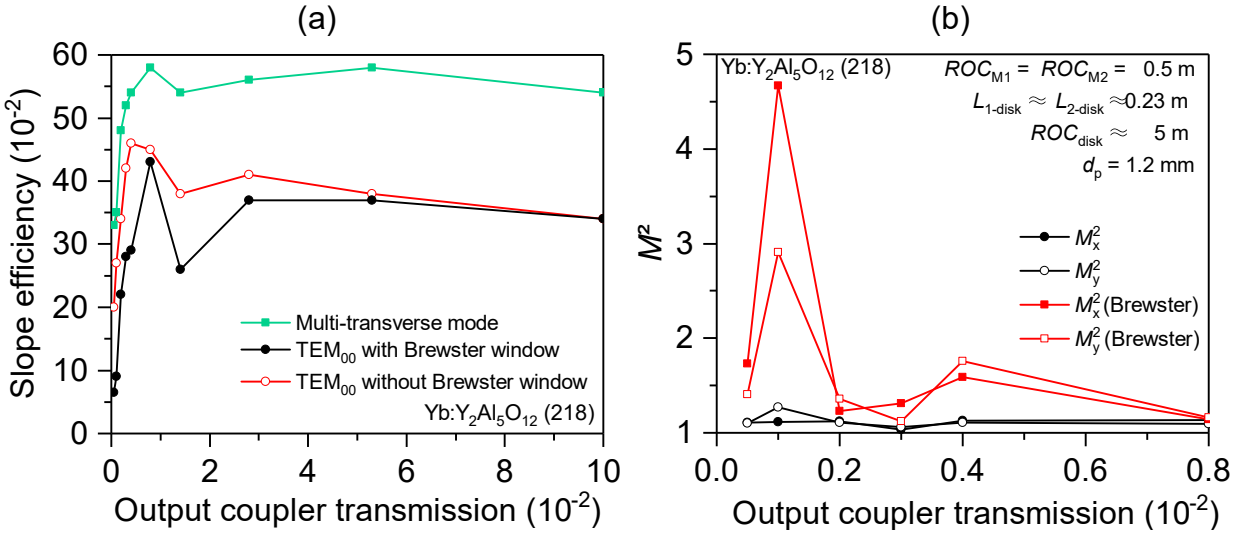

Figure 5.33: (a) Laser performance for different folded resonators.(b) Beam quality for the resonators designed for fundamental mode operation. The M^2 factor was below 1.1 for $T_{oc} > 8 \times 10^{-3}$.

Resonator	η_{sl} (10^{-2}) for output coupler transmission (10^{-2})										$P_{int\text{-}max}$(kW)
	0.05	0.1	0.2	0.3	0.4	0.8	1.4	2.4	5.4	10	
Multi-mode	33	35	48	52	54	58	54	56	**58**	54	8
Single-mode	20	27	34	42	**46**	45	38	41	38	34	3.5
Single-mode - Brewster	6.5	9	22	28	29	**43**	26	37	37	34	1.5

Table 5.8: Laser performance (10^{-2}) for single folded resonators for Yb:$Y_3Al_5O_{12}$ for $P_{p\text{-}max} = 15$ W.

Polarization selection To investigate the potential of the intrinsic polarization, measurements of the PER for the single-transverse-mode resonator without a polarization selective element are depicted in Figure 5.34 (a). The highest PER of 3.5:1 for an OC transmission below 4×10^{-3} was measured for $T_{oc} = 5 \times 10^{-4}$. The PER decreased to approx 2:1 for $T_{oc} = 4 \times 10^{-3}$. Finally, for $T_{oc} > 4 \times 10^{-3}$ the PER increased up to 29:1. For the resonator with the Brewster window, the PER was larger than 100:1. The trend for the intrinsic polarization differed to the one obtained in the linear resonator, which is shown in Figure 5.23. Here, the previous measurements showed an increasing trend over the entire range. An explanation for the different behaviors may be an influence of the optical defect, which was observed after the experiments in the linear resonator. In addition, defects can disturb the polarization and explain the unstable beam quality in Figure 5.33. For two selected OC transmissions the losses at the Brewster plate are depicted in Figure 5.34 (b). The power, reflected at the Brewster window could only be measured at one site of the folded resonator. Therefore, the total power was assumed to be $P_{B1} = P_{B2}$. Thus, the comparison to the power transmitted through the OC depicts an upper limit for the losses at the optical window. For the linear resonator and Yb:$Y_3Al_5O_{12}$ (495), losses of 10^{-3} were measured at the Brewster plate. In parallel, an increase of the losses for higher pump powers was observed.

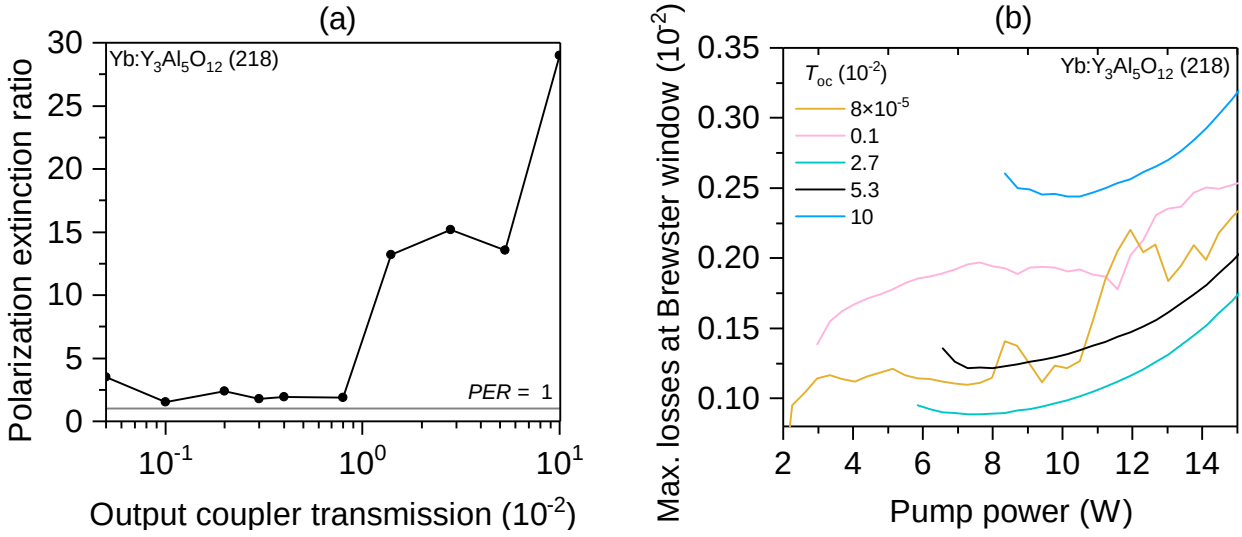

Figure 5.34: (a) Polarization extinction ratio for the single-transverse-mode resonator without polarization selective elements. (b) Losses at the Brewster window for different OC transmissions.

Resonator	Caird fit		Nonlinear model fit	
Yb:$Y_3Al_5O_{12}$ (218)	$L_{\text{int}}(10^{-4})$	$\eta_{\text{abs}} \cdot \eta_{\text{ov}}$	$L_{\text{int}}(10^{-4})$	$\eta_{\text{abs}} \cdot \eta_{\text{ov}}$
Multi-mode	3.9 (4.0)	0.63 (0.64)	5.1 (4.6)	0.67 (0.65)
Single-mode	8.0 (7.1)	0.57 (0.53)	10.6 (6.3)	0.62 (0.63)
Single-mode - Brewster	42 (39)	0.65 (0.62)	45 (22)	0.73 (0.51)

Table 5.9: Results of the Caird analysis for different single folded resonators of Figure 5.33. The values in brackets include OC transmissions between 5×10^{-4} and 2.8×10^{-2} while the ones without brackets cover only OC transmissions between 5×10^{-4} and 4.0×10^{-3}.

Resonator losses A Caird analysis was performed on the results, which are shown in Figure 5.33, to determine the resonator's internal losses. The results are listed in Table 5.9 together with the results of the direct nonlinear fit. The losses from the Caird method are larger for the multi-transverse-mode resonator and the single-mode resonator than the one, found for the linear resonators and disk 495, which are listed in Table 5.6. The differences between the resonators can be explained by an increase of scattering and diffraction losses due to the second mirror. In addition, the disk itself can exhibit a different roughness and different optical defects. The presence of an optical window in the Brewster's angle increased the discrepancy. A comparison to Figure 5.34 shows pump power dependent losses at the Brewster plate between 10^{-3} and 3×10^{-3}. The remaining losses in the order of 10^{-3} coincide with the losses from the single-transversal mode resonator.

The losses determined for the folded resonator are consistent with the ones obtained for the linear multi-mode and fundamental mode resonator. Inclusion of a Brewster window led to approx. 3× *higher losses compared to the linear resonator with a Brewster plate. The increase of losses can be explained by depolarization and scattering losses.*

5.5.2 Results of the folded laser resonators with an internal focus

Specific setup The first set of experiments was conducted with the Yb:$Y_3Al_5O_{12}$ disk 498. This disk was used for a pump spot diameter of 2.7 mm and pumped at the ZPL. The pump power was kept below 200 W. The targeted length between disk and the mirror M_1 was 50 cm and the distance $L_{1\text{-}2}$ between M_1 and M_2 was 14.65 cm. Both mirrors had an ROC of 10 cm. This corresponds with an AOI on M_1 of 5° to $w_t = 749\,\mu\text{m}$ and to $w_s = 1175\,\mu\text{m}$ on the disk and to a waist radius of $w_t = 23\,\mu\text{m}$ and $w_s = 15\,\mu\text{m}$. To ensure single-transverse-mode operation an aperture was used for this resonator. The second set of experiments was conducted with the Yb:$Y_3Al_5O_{12}$ disk 218 for a pump spot diameter of 1.2 mm. The distance from the disk to M_1 was 33 cm and between the two OC it was 12.54 cm. The ROCs of the mirrors M_1 and M_2 were 5 cm and 10 cm, respectively. The caustic and the stability are depicted in Figure 5.29 and Figure 5.31. No aperture was used in this resonator. It was observed that the planned AOI was unsuitable due to an insufficient beam quality. This was suppressed by shifting the beam close to the inner edge on M_2. This decreased the AOI on M_1 but increased the diffraction losses on M_2 because of clipping on the mirror's edges.

Disk	D_p (mm)	η_{sl} (10^{-2}) for output coupler transmission (10^{-2})									L_{int}(10^{-2})	M^2
		0.05	0.1	0.2	0.3	0.4	0.8	1.4	2.4	5.4		
218	1.2	0.7	1.6	3.3	3.8	5	7.2	11.7	9.5	3.7	<6.4	<1.1
498	2.7	9.3	11.7	20.9	28.2	31.5	38.3	42	40.9	43.8	<0.44	<1.1

Table 5.10: Laser performance for the folded resonators with a tight internal focus

Laser performance The results with the two disks are depicted in Figure 5.35 and listed in Table 5.10. The laser performance in the two resonators with an internal focus was lower than in the other experiments. For disk 218 and disk 498 maximum slope efficiencies of 0.12 and 0.44 were measured for an OC transmission rate of 1.4×10^{-2} and 5.4×10^{-2}, respectively. For the two disks, the maximum intracavity powers were 285 W and 29 kW. The pump power was increased in comparison to the previous experiments, to enable the imaging of the resonator's internal focus. A decreasing trend of the slope efficiency is shown in Figure 5.35, while the behavior is less prominent in Figure 5.35 (b). This can be explained by larger losses in case of disk 218. The larger internal losses increase the visibility of inversion dependent losses at lower OC transmissions. An intrinsic PER between 2:1 and 10:1 was observed, which was probably induced by a polarization preference of the disk or the mirror M_1. No laser operation was achieved with an added Brewster window, which could have been caused by the large alignment sensitivity. It must be noted, that the laser operation was very unstable and required regular re-alignment of both resonators. Furthermore, temperatures up to 80 °C were measured at opto-mechanics, which indicates a significant loss of power.

The low slope efficiencies and intracavity powers which were measured in resonators with a strong internal focus could not be compensated by the available pump powers to achieve the required intracavity powers.

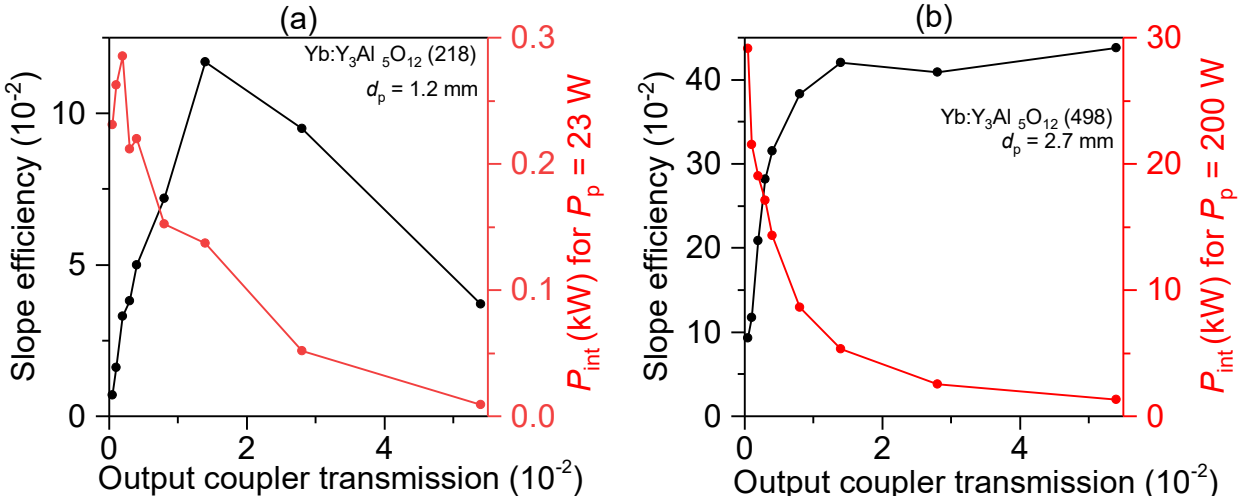

Figure 5.35: Slope efficiency and max. intracavity power P_{int} of resonators designed with an internal focus for (a) a pump spot diameter of 1.2 mm and (b) a pump spot diameter of 2.7 mm.

Resonator losses The loss analysis with the Caird method and the nonlinear fit yielded no reasonable results for both disks. However, the maximum losses can be estimated from the laser performance at the lowest OC of 5×10^{-4}. In this configuration, the maximum possible losses were 6.4×10^{-2} and 4.4×10^{-3}, for the disks 218 and 498. The laser spectrum was measured during the experiments. It was observed, that the laser oscillated at wavelengths around 1030 nm, even for low OC transmissions of 5×10^{-4}. All lasers in the previous experiments oscillated at a wavelength longer than 1050 nm for these transmissions. Therefore, this can explain an increase of the losses, as calculated and presented in Figure 2.8.

A comparison with the other experiments is required to understand the strong increase of the internal resonator losses. First, due to the large mode diameters on the mirror M_2, the scattering losses and the number of involved optical defects are increased. Second, the resonators are sensitive to external distortions due to their short stability zones. Here, small vibrations or length changes can have a big impact on the beam sizes at the mirrors. Third, it was observed in both resonators, that the fundamental mode operation could only be ensured by shifting the beam towards the edges of the mirror in case of the disk 218, or by the inclusion of an aperture in case of disk 498. Both mechanisms have the same impact. They augment the losses for higher order modes, which are caused by diffraction.

The diffraction losses of the resonators were calculated with OSCAR [233]. The calculations were performed with the assumption of one sphere with an ROC of 5 m for the disk, for one sphere with an ROC of 5 m and astigmatic distortions which were gained from wavefront measurements, and one with the raw surface profile of disk 218. The wavefront measurements shown in Figure 5.36 already indicate strong non-spherical distortions, which can potentially increase the diffraction losses.

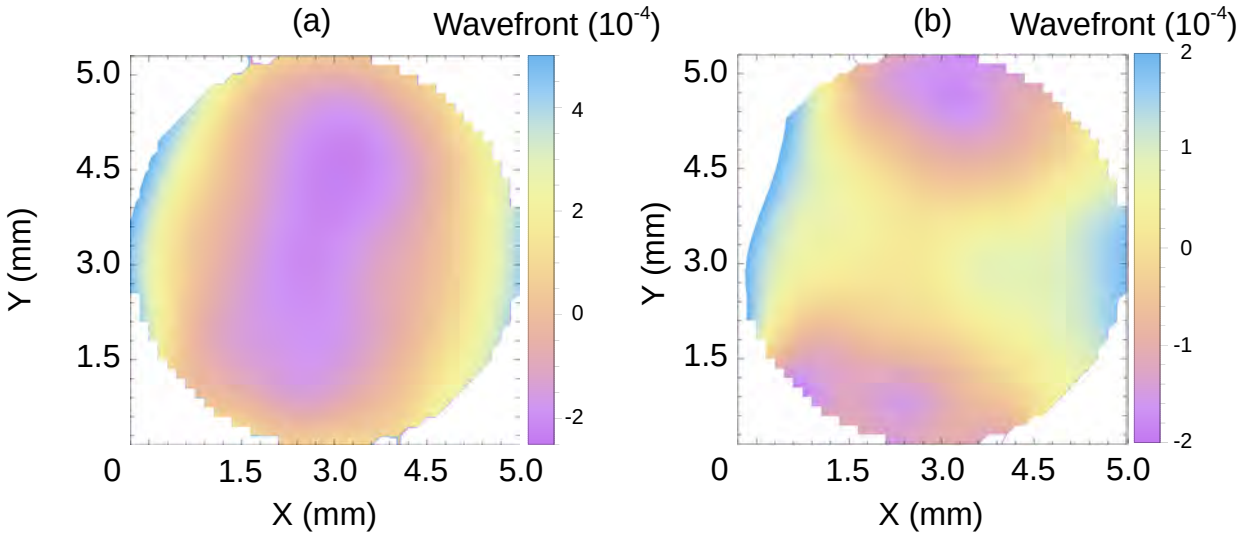

Figure 5.36: (a) Wavefront image of the disk 218 with substracted tilt and in addition with (b) a substracted sphere. The probe laser had a wavelength of 1064 nm.

The results of the calculation of the diffraction losses are shown in Figure 5.37. It must be considered, that neither the clear aperture of the laser on the mirror could be measured, nor the AOI and thus the position on the mirror. However, visual inspection with an infrared-viewer indicated that the outer parts of the beam were only in a distance of a few mm to the edge of the mirror. The maximum possible losses for this resonator, were in the order of 6.4×10^{-2}. A comparison with the results, given in Figure 5.37, shows that the losses could originate from diffraction losses. Thus, diffraction losses at the focusing mirrors might be an explanation for the resonator losses, which were measured for the setups with a tight internal focus. Despite the small fundamental mode volume of 0.9 cm^3 and an average density of 0.03 cm^{-3} of particles larger than a diameter of 0.5 µm in the laboratory air the regular trapping of particles was observed and must have caused additional losses.

Intracavity intensity Determination of the intracavity intensity requires measurement of the resonator's internal focus radius and the intracavity power. The latter was calculated with the power transmitted through an OC of known transmission. The spatial dimensions of the focus were measured with the previously described setup. The images which were used for the determination of the beam waist can be seen in Figure 5.38 (b) and (c). The first image in Figure 5.38 shows an example for an oscillation of a higher transverse mode. The different steps of the processing of the data are shown in Figure 5.39 for disk 218 and a pump spot of 1.2 mm. Here, a waist radius of 19.1 µm was determined. The waist corresponds to a deviation from the target length $L_{1\text{-}2}$ of only 0.6 mm. This yields to an intracavity peak intensity of 3.7×10^7 W cm^{-2} for an intracavity power of 230 W. The same data processing was done for the images which were obtained for disk 498 in the resonator with a pump spot of 2.7 mm. The evaluation yielded a waist radius of 52.4 µm, which corresponds to an intracavity peak intensity of 6.6×10^8 W cm^{-2}. A fundamental

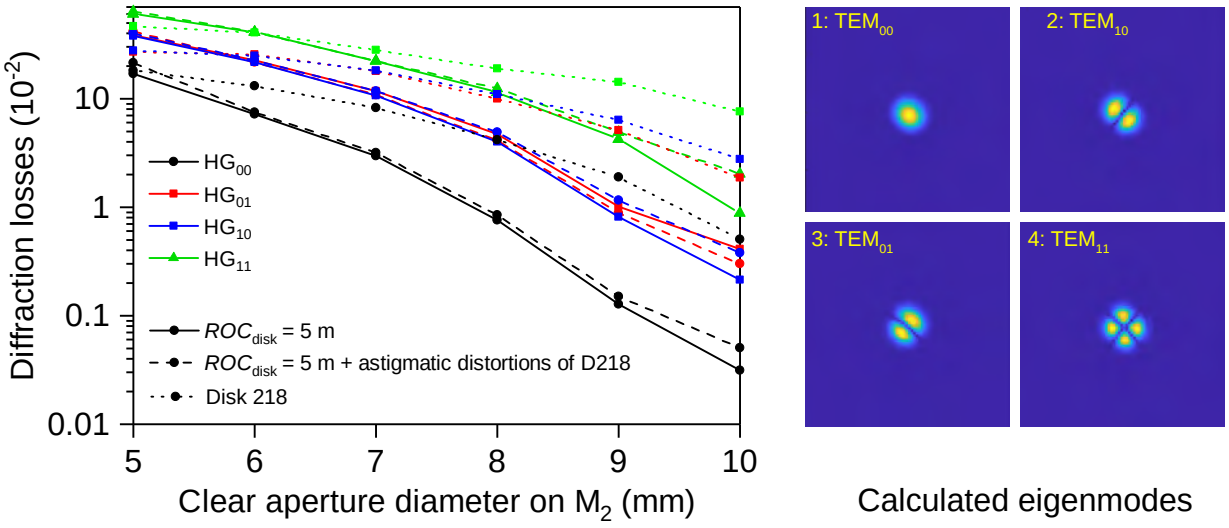

Figure 5.37: (a) Simulated diffraction losses and eigenmodes for the resonator with disk 218, a strong internal focus and a pump spot diameter of 1.2 mm.

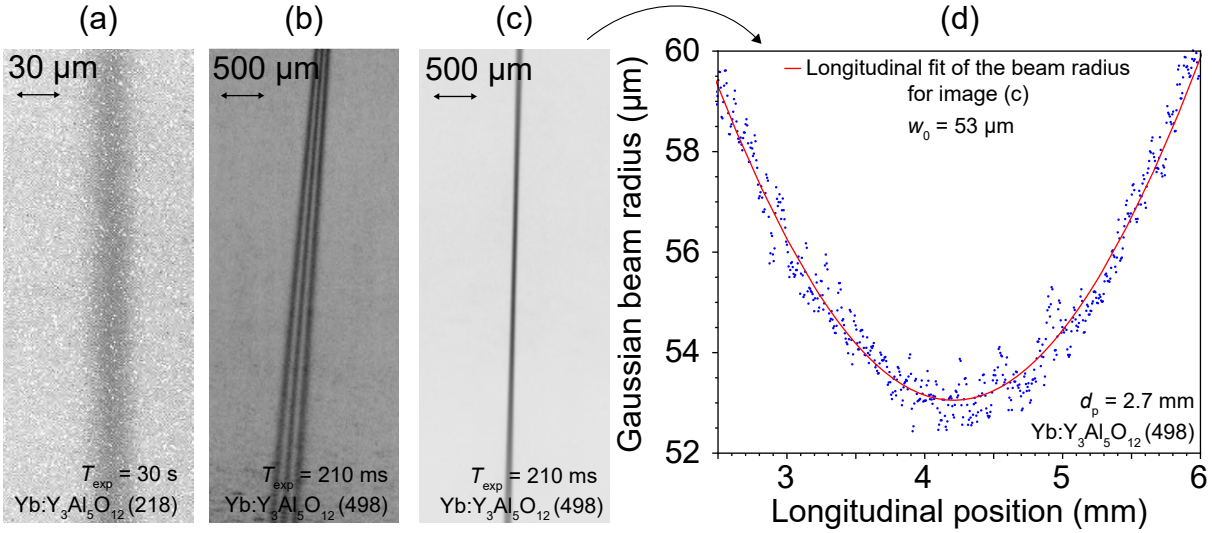

Figure 5.38: Rayleigh scattering at intracavity beams and (d) measured caustic for disk 498.

mode's waist of 55 µm is, according to mode radius calculations, not possible within the stable range of $L_{1\text{-}2}$ for the assumed curvatures of disks and mirrors. Here, the maximum possible waist radius is calculated to 32 µm. The deviations could have been caused, e.g., by local ROC variations of the disk or a thermal lense.

The set up of TDL resonators with an internal 20 µm waist was possible. The resonators exhibited losses of up to several percent, which could not be compensated by the available pump power. As a result, the necessary intracavity power was not achieved. Diffraction and scattering losses may have contributed to that in a great extent.

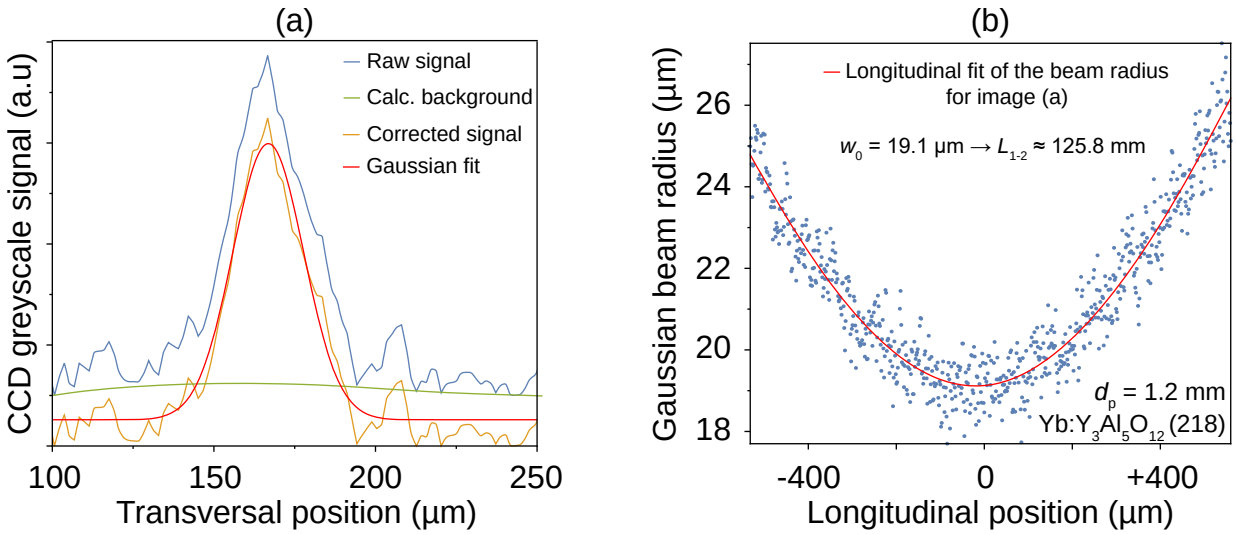

Figure 5.39: (a) Exemplaric data processing for the focus determination for Figure 5.38 (a). (b) Plot of the measured caustic for disk 218 and $d_p = 1.2\,\text{mm}$ for Figure 5.38 (a).

5.6 Discussion of the results with folded resonators

A defined polarization The polarization was analyzed for the intrinsic and the induced polarization. The intrinsic polarization was comparable in the linear and the folded resonator. In case of the latter, an additional preferred direction of polarization was induced by the AOI on the mirror, which in general might not coincide with the preferred direction induced by the disk. For the lowest OC transmission of 5×10^{-4} an intrinsic PER of 3.5 was measured. As this method does not add additional losses in form of depolarization or scattering to the resonator, further investigation to use the intrinsic polarization can be beneficial. When a Brewster window was included in the resonator, a PER higher than 100 was observed. This corresponds to the PER which is typically used for the alignment of linear molecules [36]. However, this method caused additional losses due to birefringence of the gain material.

Single-transverse-mode operation Single-transverse-mode operation was achieved in the resonators without a small focus by a suitable overlap between pump and laser mode. Experiments with a Brewster window showed a degradation of the beam quality for low OC transmissions. This behavior can be understood by considering the possible OPD caused by the optical window. For resonators with a small internal focus, the consideration of the pump and laser mode overlap was not sufficient to obtain stable single-transverse-mode operation. Here, diffraction losses for higher-transverse modes were added by the inclusion of apertures and by clipping losses at the mirror edges.

Intracavity electric field intensity Two resonators adapted for a pump spot diameter of 1.2 mm and 2.7 mm were set up. The designed intracavity waist was approx. 20 µm. The beam could be analyzed by imaging the Rayleigh scattering with a microscope objective on a CMOS camera. The evaluation of the data resulted in a waist of 19.1 µm and 52.4 µm for a maximum intracavity power of 230 W and 29 kW, respectively. This corresponded to maximum peak intensities of $3.7 \times 10^7\,\mathrm{W\,cm^{-2}}$ and $6.6 \times 10^8\,\mathrm{W\,cm^{-2}}$. Therefore, in case of the smaller waist, the required intensity could not be achieved, as the intracavity power was not sufficient. In case of the resonator with an intracavity power of 29 kW, the measured waist differed significantly from the one from the resonator design. The reason for the larger beam waist could not be assigned. Here, a decrease from 52.4 µm to 15 µm would be sufficient to achieve an intensity of approx. $1 \times 10^{10}\,\mathrm{W\,cm^{-2}}$.

Optical damage Similarly to the experiments that were obtained in the linear resonator, all disks and mirrors, which were used with folded resonators, accumulated optical defects. It did not matter whether the laser was operated under a flow box, or not. A suitable intracavity power which significantly reduced the risk of damage could not been found. It must be considered, that the optics and disks were not analyzed between the experiments as it would have reduced the comparability between the resonators. The drawback of this

is that the development of small defects would not have been noticed between the different experiments.

Resonator roundtrip losses The losses for the resonators, in which the laser was folded via the disk are listed in Table 5.9. They were determined in the order of 4×10^{-3} in the case of single-transverse-mode operation with an optical window in the Brewster's angle for polarization selection. A large depolarization in the thin disk, caused by thermo-mechanical stress might have been responsible for this. This assumption is encouraged by a comparison of the losses of folded resonators, with the ones measured for linear resonators, listed in Table 5.6, which are at least in the same order. Additionally, the folded resonator had increased scattering, absorption and diffraction losses because of the second mirror. No material specific advantages were noticed, as Yb:$Y_3Al_5O_{12}$ was taken as the only gain material because the Yb:Lu_2O_3 disks were not suitable for single-transverse-mode operation. The reason was a strong astigmatism, which was confirmed by D+G. In addition, the IFSW reported the observance of strong birefringence for these disks. The resonators with the strong internal focus showed a significant increase of the losses. Here, an estimation of the maximum possible losses yielded values of 6.4×10^{-2}. The high losses can be explained by large diffraction losses, which were induced by apertures and clipping losses at the mirrors to ensure single-transverse-mode operation. During the experiments, the trapping of dust and dirt particles in the focus was observed. The particles moved to the focus, where they were trapped for several seconds and burned, which was visible as sparks with the bare eye. It can be assumed that the density of high-field seeking particles in the focus increased. This would have led to increased scattering and absorption losses. To investigate this, operation of the resonator in vacuum would have been necessary. This could not be achieved due to the large alignment sensitivity of the cavity.

Comparability of the laser disks The laser experiments presented in this thesis were conducted with different disks. This was necessary, as all samples showed the occurrence of optical damage at different intracavity intensities. This includes disks as well as mirrors. Thus, the question arises, whether the results obtained for different resonators and disks are comparable. Indeed, constant transmission, losses and the number of defects of the optical resonator components cannot be ensured. However, the Yb:$Y_3Al_5O_{12}$ disks used in the experiments were all commercially available ones, obtained from D+G and DLR. Caused by the decade long development of the different manufacturing steps, the tested disks represent a statistical sample. This fact is unavoidable and an exchange of the laser disks in the planned setup should be possible without a new resonator concept. The continuation of laser experiments with the available Yb:Lu_2O_3 disks was avoided. The samples showed an excellent multi-transverse-mode performance. Despite that, they were not suitable for single-transverse-mode operation due to strong astigmatism and low spherical contour accuracy.

6. Conclusions and Outlook

6.1 Summary

The aim of this thesis was to develop a CW TDL with an intracavity electric field intensity of about $10^{10}\,\mathrm{W\,cm^{-2}}$ to $10^{11}\,\mathrm{W\,cm^{-2}}$. The laser's purpose of aligning molecules for x-ray diffraction experiments results in a beam waist of approx. 20 µm [40]. The electric field's polarization must be stable and defined. Furthermore, to ensure a smooth field distribution for a comparable alignment of the molecular ensemble, operation on the fundamental transverse mode is beneficial, while multi-longitudinal-mode operation avoids spatial hole burning in the gain material and ensures a homogeneous longitudinal field in the resonator's center. In this thesis the investigations focused on five aspects: choice and development of a suitable gain material, set up of a low loss laser system with a high intracavity power, fundamental mode operation, polarization selection and a 20 µm intracavity beam waist.

Choice and development of a suitable gain material High laser powers necessitate sufficient pump powers and gain materials with a large Stokes efficiency. This can be achieved with ytterbium-doped gain materials, such as Yb:$Y_3Al_5O_{12}$ and Yb:Lu_2O_3. The first one benefits from its commercial availability and can be obtained with constant and good optical quality. The second one exhibits a high thermal conductivity and excellent laser performances. While the Yb:$Y_3Al_5O_{12}$ disks were purchased, Yb:Lu_2O_3 crystals were grown in the ILP with the HEM. For this purpose, the growth was optimized by the means of in-growth-annealing to obtain color-free crystals. Furthermore, the CTE of Yb:Lu_2O_3 was refined in collaboration with the PTB. This allowed the manufacturing of CTE adapted heatsinks for the contacting of the Yb:Lu_2O_3. During the experiments, the use of Yb:$Y_3Al_5O_{12}$ disks gained priority due to their higher spherical form accuracy and optical quality.

Intracavity power and internal resonator losses More than 20 disks were characterized in a linear resonator. Resonator internal losses below 2×10^{-4} were determined. This is an order of magnitude lower than reported previously [136]. Most likely, the residual losses were caused by surface scattering and transmission of the disk's HR coating. Using a pump power of 54 W, an intracavity power of 135 kW was achieved for Yb:$Y_3Al_5O_{12}$ with a pump spot diameter of 1.2 mm. Average disk temperatures higher than 100 °C were observed for low OC transmissions. This tells that the disk represents a loss channel. Detailed investigations exhibit that the losses are likely to occur at surfaces. In addition, a TDL with a pump spot diameter of 3.6 mm was set up. 200 kW of intracavity power were achieved with a pump power of 270 W with Yb:Lu_2O_3. Optical damage restricted further power scaling in all experiments. Presumably, defects in the HR coatings were responsible for the damage.

Fundamental mode operation For linear and folded resonators, fundamental mode operation was realized by a suitable ratio of approx. 0.8 between the radius of the laser and the pump mode. A Caird analysis yielded losses of 9×10^{-4} for a 30 cm long resonator with a pump spot diameter of 1.2 mm, which is about one order of magnitude higher compared to multi-transverse-mode operation. The increase can be explained by absorption losses of the Gaussian mode in areas outside the pump spot. Resonators with astigmatism and a small internal focus showed a different behavior. Here, the fundamental mode operation could only be guaranteed by using apertures or by inducing large clipping losses.

Polarization A gain material tends to oscillate on one polarization if the gain or the losses differentiate between the two polarization directions. Thus, the gain material or optical elements can, for this purpose, induce a preferred direction of polarization. This happens even though Yb:$Y_3Al_5O_{12}$ and Yb:Lu_2O_3 are isotropic. This intrinsic polarization was only observed for single-transverse-mode operation. The polarization is an independent property of each mode and the oscillation on higher-order-modes does not imply equal losses. The PER was lower in case of the intrinsic polarization compared to the one induced by a Brewster element. Low differences of the gain and the losses in case of intrinsic polarization could be rated as the reason. Thus, external influences have a destabilizing effect. Parasitic losses can be caused by scattering, absorption and angular deviations of the outer parts of a laser beam from the central Brewster angle . The determined entire losses for resonators with a Brewster plate were 1.5×10^{-3} for a linear resonator and 4.2×10^{-3} for a resonator folded via the disk. The losses at the Brewster plate were 1×10^{-3} to 3×10^{-3}.

Intensity Two resonators were set up with a resonator design providing a waist of 20 µm. For a pump spot diameter of 1.2 mm, a waist of 19 µm was measured at an intracavity power of 230 W. In a thin-disk laser module with a pump spot diameter of 2.7 mm, a waist of 52 µm was obtained at an intracavity power of 30 kW. To measure the intracavity waist, the Rayleigh scattering of atmospheric molecules was imaged on a CMOS chip. Subsequent fitting of the transverse beam profile allowed determining the beam radius. In addition, the longitudinal trend of the measured beam profiles confirmed the operation on the fundamental mode. The resonators with strong internal foci exhibited losses up to 6.4×10^{-2}. A conceivable explanation for this observation are diffraction losses at the mirrors and scattering and absorption of atmospheric molecules, which were trapped in air in the resonator's focus. Every specific requirement of the aforementioned aspects of intracavity power, beam quality, polarization and waist could be fulfilled individually. However, the combination of focus, polarization, beam quality and intracavity power remained unachieved. Responsible for this are losses of several percent, which could not be compensated by the available pump power to achieve the required intracavity power. In case of low-loss resonators without an internal focus, optical damage limited further power scaling. Generally, within the framework of this thesis, no satisfying compromise to decrease the risk of optical damage and to obtain appropriate validity of the laser performance experiments with a sufficiently high pump power could be found.

6.2 Towards continuous-wave laser alignment of molecules

Based on the investigations in this thesis, recommendations can be given to accomplish the intended purpose. Those recommendations involve the investigation and subsequent reduction of the resonator's internal losses and in an increase of the intracavity power by an implementation of larger pump spots and pump powers.

The intracavity power can be augmented by two mechanisms: higher pump powers or lower losses. High pump powers and intensities mainly cause two effects. First, the temperature of the disks increases. This deteriorates the laser efficiency and can provoke thermo-mechanical stress, which can crack the disk. Second, a high intensity of pump and laser modes scales up the risk of optical damage, caused by microscopic defects in the coatings. The first effect has proven to be manageable in TDL, while the latter requires a preselection of the laser disks. In experiments described in [214], a pump spot diameter of 4.7 mm was used. Here, the remaining pump power deposited in the disk was still as high as 400 W without optical damage. However, it must be considered that these experiments were optimized for a high laser efficiency. Thus, the actual temperature of the disk at low OC transmissions can be higher. Thinner disks are beneficial to their temperature. A thickness of 100 µm can be sufficient to provide the necessary gain. The temperature of such a thin-disk can be in the order of 200 °C for a deposited power in the volume of the pump spot of 500 W. The high average temperatures can in principle be compensated by lower cooling temperatures, which is unproblematic in respect to water condensation for a laser operating in a vacuum chamber. The alignment of molecules has to be performed in a vacuum. Preliminary experiments with linear resonators in vacuum showed an increased stability and performance in accordance to previous results [239, 240]. However, operation of a TDL in a vacuum chamber can cause several problems. Depending on the pump power, efficient cooling systems are needed to remove the heat. This does not only include the heat removal of the gain material, but the cooling of opto-mechanics as well, which cannot efficiently dissipate heat due to the lack of convection. No physical limitations restricting an implementation of our setup are known.

The challenge is the amount of the required pump power. The overall feasibility with a TDL can be proven by means of commercial available high power thin-disk laser systems, even though the alignment sensitivity increases for large laser mode diameter on the disk [224]. This might be critical for resonators with a sharp focus, operating at the end of stability zones. Experiments indicated the possibility to extract an output power of 4 kW out of one disk in near fundamental-mode operation [158, 241]. As these lasers were optimized for high output powers, it can be assumed that they can provide a stable intracavity power of more than 100 kW. It must be considered that the use of higher pump powers also increases the technical challenges of the implementation of such a setup in vacuum. If high pump powers have to be avoided, the investigation and reduction of losses are important. The complexity of optimizing the different loss channels may be significantly reduced using thin-disks which are able to operate in commercial high-power systems.

6.2.1 In detail: decrease of the resonator losses

To avoid high pump powers, the resonator internal losses have to be reduced. Possible major losses are transmission losses at the disk's HR coatings, absorption losses in the coatings, losses due to optical defects, depolarization because of the disk and diffraction. A typical application of a thin-disk laser does not require an exceedingly high reflectivity of its HR coating, as the OC transmission is in many cases in the order of a few percent. By increasing the number of layer pairs, the reflectivity is improved at the cost of a higher thermal resistance. This impact can be reduced by coatings which are optimized for the specific pump and laser wavelengths. Absorption losses of the coatings can be reduced by annealing. In addition, the use of diamond heatsinks enables a high thermal conductivity of the system as well as spherical form accuracy, while reducing losses from astigmatism and diffraction. Scattering losses at surfaces can be reduced/minimized by advanced polishing techniques. Since we found optical defects at all disks and most mirrors as shown in Figure 6.1, it would be conceivable to use preselected thin-disks in future studies. Significantly higher densities of defects can be expected for laser disks and common resonator mirrors. Finally, an intended decrease of the losses would mostly benefit from an exact determination of the contribution of different channels. This would in parallel allow conclusions about the specific optimization potential. However, even without a precise knowledge several suggestions can be made.

- Diffraction. Use of larger optics and diamond contacted disks for higher form accuracy.
- Scattering. Use of super polished mirrors and disks as well as process optimization.
- Absorption. Annealing of the coatings. This could be beneficial for the disks as well.
- Defects. Use of more carefully preselected disks and mirrors.
- Depolarization. Investigation of depolarization-compensation and avoidance.

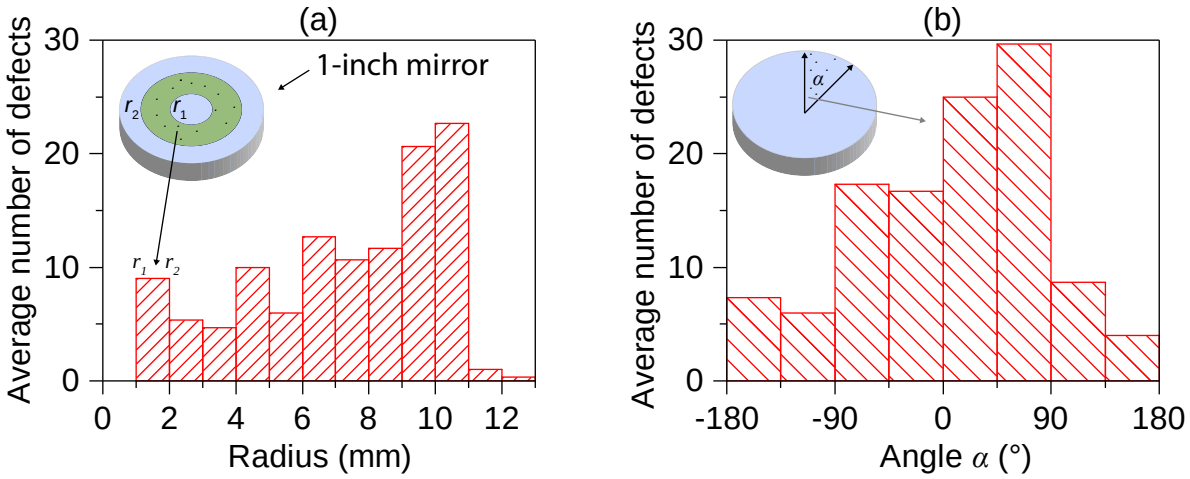

Figure 6.1: Statistics for optical defects larger than 2 µm for three preselected 1-inch mirrors. (a) Average number of defects in dependence on the circular disk segment and (b) on the angle.

6.2.2 In detail: increase of the pump power

An alternative to decreasing the resonator's losses is increasing the pump power to compensate for the present losses. Concerning recent results, e.g., in [158, 241, 242], disks should possibly be able to dissipate a heat load of approx. 3 kW. This can become relevant if the glue's temperature-resistiveness is exceeded, meaning that temperatures between 200 °C and 300 °C may already be critical. Therefore, under consideration of previous published dimensions and parameters in [173, 213], further developments of disks, glues, coatings and heatsinks might have been necessary to reduce the disks' temperatures. A decrease of the thicknesses of the glue, the CVD diamond heatsink and the disk might have been possible. Simulations, shown in Figure 6.2 imply that a thinner HR coating might have been required. However, this would reduce the HR coating's reflectivity. Therefore, for efficient laser operation higher OC transmissions are necessary, which subsequently reduce the intracavity power. Thus, even if pump powers higher than 10 kW are possible, the necessary optimizations of the thin-disks might make them unsuitable for high intracavity powers. Another possible limitation can be seen in the air-wedge in front of the disks, which is described in [141] and simulated in Figure 6.2 (b). The air convection in front of the disk leads to an up-shift of the beam. Nevertheless, this is only important for a laser concept with the pump module being outside of the vacuum chamber. While the beam's shift can be compensated [141], it might have a detrimental impact on resonators with an internal focus, operated at the edges of their stability zones. Despite the suggestion to set up the complete TDL module in vacuum, this can become technically challenging for such high pump powers, which might induce kilowatts of losses. These considerations do not imply a non-feasibility with a high-power laser but rather raise awareness for complications.

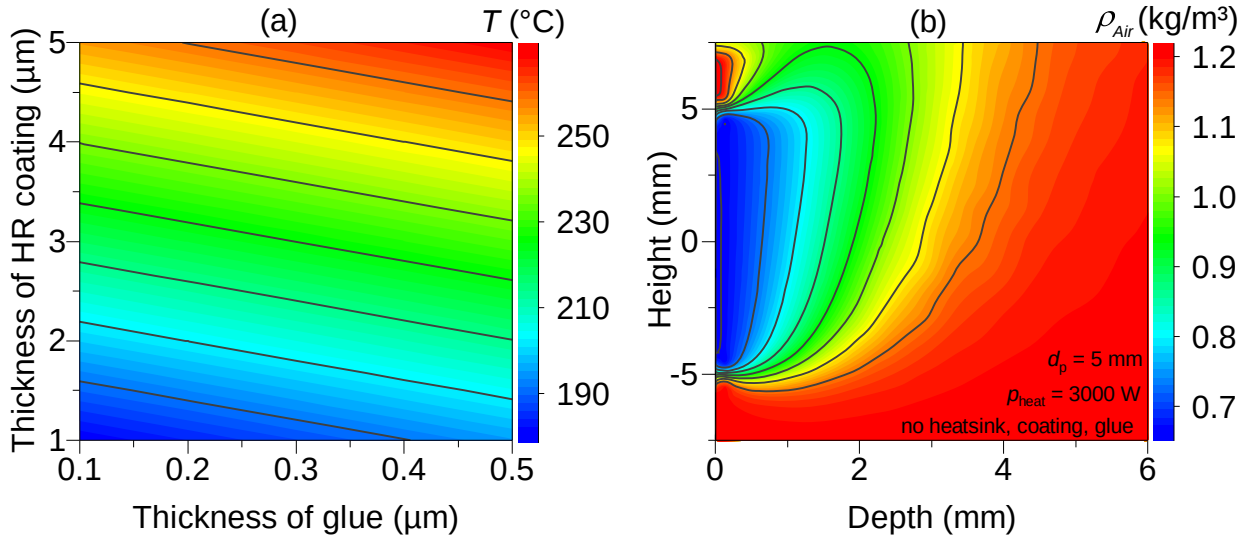

Figure 6.2: (a). Average temperature in a 1 cm pump spot in dependence on the thickness of the HR coating ($\lambda_{th} = 2\,\mathrm{W\,m^{-1}\,K^{-1}}$) and on the glue ($\lambda_{th} = 1\,\mathrm{W\,m^{-1}\,K^{-1}}$) for a 0.1 mm thin gain material ($\lambda_{th} = 8\,\mathrm{W\,m^{-1}\,K^{-1}}$). (b) Air density in front of a 100 µm thin-disk ($\lambda_{th} = 8\,\mathrm{W\,m^{-1}\,K^{-1}}$).

6.3 Outlook

In order to acquire a more profound understanding about the loss processes which were observed at low output-coupler transmissions, further research is necessary. Investigation into the kind of optical damage at thin-disks and mirrors would help to estimate the influence of point defects in the order of 10 µm. Disks and mirrors can be analyzed with high-resolution surface profilers. This enables the precise calculation of scattering and diffraction losses. Further laser experiments could be done with thinner and lower-doped gain materials. In addition, a reduction of the thickness and doping concentration can yield shorter laser wavelengths which allow the employment of thinner highly-reflective coatings due to the smaller required bandwidth. This would reduce the thermal resistance of the disk-coating system and therefore decrease the disk temperature. In turn, the cooling temperature of the disk can be further reduced. While this is avoided in air because of water condensation, it is beneficial in a vacuum chamber. Optical damage mainly resulted from defects in the highly reflective coatings on disks and mirrors. An optimization requires preselection of the laser disks, or the use of disks which have been proven to work at intracavity powers higher than 100 kW. A significant contribution to the losses originates from depolarization in the disk. An adapted cut direction of the crystals or various other compensation techniques have optimization potential [88, 145, 146]. Additionally, the resonator design can be improved. Astigmatism impairs the beam quality and forces to choose small incident angles on the curved mirrors. Therefore, astigmatism-compensation techniques should be investigated regarding suitability in high-power low-loss lasers [243, 244].

A purposive implementation of a CW alignment laser system would comprise a commercial high power TDL system in clean room environment. Such setups, disks and optics are most likely to handle high intracavity powers. Due to large possible pump powers such a setup would be less sensitive to existing and additional losses. Instead in a standing-wave cavity, the disk should be implemented into a ring resonator. Here, longitudinal single frequency operation could be achieved with an optical diode. This would facilitate a large stability and an excellent beam quality of the resonator in comparison to a multi-longitudinal-mode resonator. In addition, this would provide a significant optimization potential in respect to coatings on disks and mirrors. Additionally, an one-directional ring cavity with a TDL can provide further advantages for diffractive imaging, e.g., by the inclusion of waveplates into the resonator which enables the rotation of the polarization in local parts of the resonator. Generally, the coupling of the proposed laser system to a molecular beam could, besides diffractive imaging, be employed for the investigations of chemical scattering experiments on aligned or oriented molecules [245]. Additionally, this laser would allow for the trapping of atoms and molecules using the polarizability interaction [246, 247]. It would provide for traps of a few-Kelvin depth, sufficient for small molecules and even deeper traps for larger, more polarizable molecules. This could also be utilized for in-vacuo trapping and guiding of nanoparticles [248, 249]. The setup could be useful for many more strong-field experiments in atomic and molecular physics, for instance, at high-repetition-rate FELs [250]. Finally, such a system allows for diffraction experiments with repetition rates far higher than todays. Further applications are also possible at synchrotron facilities.

A. Overview of the laser disks

Disk	Material	Doping	Cryst. growth	Producer	Polishing	Coating	Contacting	Heatsink	l_c	σ	ROC_x	ROC_y	Wedge	η_{sl}-MM
		(at. %)							(µm)	(nm)	(m)	(m)		
495	Yb:$Y_3Al_5O_{12}$	7	n.a.	D+G	n.a.	n.a.	n.a.	n.a.	220	0.5	6.3	6.2	1	0.5
375	Yb:$Y_3Al_5O_{12}$	7	n.a.	D+G	n.a.	n.a.	n.a.	n.a.	220	0.4	7.1	6.2	1	0.53
498	Yb:$Y_3Al_5O_{12}$	7	n.a.	D+G	n.a.	n.a.	n.a.	n.a.	220	0.9	4.4	4.3	1	0.47
238	Yb:$Lu_3Al_5O_{12}$	10	SMC	DLR	LAYERTEC	LAYERTEC	DLR	W80/Cu20	142	0.3	10.1	10.3	1	0.56
228	Yb:$Y_3Al_5O_{12}$	9.75	SMC	DLR	LAYERTEC	LAYERTEC	DLR	W80/Cu20	144	0.4	5.6	5.4	1	0.43
218	Yb:$Y_3Al_5O_{12}$	7	FEE	DLR	LAYERTEC	LAYERTEC	DLR	W80/Cu20	286	0.3	13.1	13.1	1	0.46
121	Yb:Lu_2O_3	3	ILP	ILP	FEE	LAYERTEC	D+G	W90/Cu10	214	0.45	2.9	2.4	1	0.39
128	Yb:Lu_2O_3	3	ILP	ILP	FEE	LAYERTEC	D+G	W90/Cu10	150	0.4	2.2	1.7	0	0.49
129	Yb:Lu_2O_3	3	ILP	ILP	FEE	LAYERTEC	D+G	W90/Cu10	190	0.3	2.3	1.9	0	0.42
130	Yb:Lu_2O_3	3	ILP	ILP	FEE	LAYERTEC	D+G	W90/Cu10	200	1.1	2.7	2.3	0	0.4
131	Yb:Lu_2O_3	3	ILP	ILP	FEE	LAYERTEC	D+G	W90/Cu10	117	0.4	0.9	0.8	1	0.43
116	Yb:Lu_2O_3	3	ILP	ILP	FEE	LAYERTEC	D+G	W90/Cu10	165	0.4	1.3	1.1	1	0.42
118	Yb:Lu_2O_3	3	ILP	ILP	FEE	LAYERTEC	D+G	W90/Cu10	160	0.47	2	1.5	1	0.34
119	Yb:Lu_2O_3	3	ILP	ILP	FEE	LAYERTEC	D+G	W90/Cu10	214	0.5	3.5	2.8	1	0.29
124	Yb:Lu_2O_3	3	ILP	ILP	FEE	LAYERTEC	D+G	W90/Cu10	255	0.49	3.6	3.2	1	0.44
125	Yb:Lu_2O_3	3	ILP	ILP	FEE	LAYERTEC	D+G	W90/Cu10	107	0.4	1.1	0.8	0	0.44
126	Yb:Lu_2O_3	3	ILP	ILP	FEE	LAYERTEC	D+G	W90/Cu10	100	4	0.7	0.5	0	0.43
132	Yb:Lu_2O_3	3	ILP	ILP	FEE	LAYERTEC	D+G	W90/Cu10	115	0.4	0.9	0.8	1	0.48
122	Yb:Lu_2O_3	3	ILP	ILP	FEE	LAYERTEC	D+G	W90/Cu10	255	0.4	17.8	8.9	1	0.41
147	Yb:Lu_2O_3	3	ILP	ILP	FEE	LAYERTEC	D+G	CVD	160	0.3	1.01	0.98	1	0.53
138	Yb:Lu_2O_3	3	ILP	ILP	FEE	LAYERTEC	D+G	CVD	115	0.4	0.99	1.01	1	0.45
134	Yb:Lu_2O_3	3	ILP	ILP	FEE	LAYERTEC	D+G	CVD	160	1.7	1.03	1.03	1	0.45

Table A.1: Overview about the laser disks and their laser performance in a 7 cm short multimode resonator for $T_{oc} = 5 \times 10^{-4}$. For commercial Yb:$Y_3Al_5O_{12}$ disks from D+G informations about the disk processing process were not provided by the company. CVD stands for CVD diamond heatsinks. It has to be noted, that all disks accumulated optical defects during the laser experiments.

B. Properties of $Yb:Y_3Al_5O_{12}$ and $Yb:Lu_2O_3$

Gain material	$Yb:Lu_2O_3$	$Yb:Y_3Al_5O_{12}$	References
Lattice symmetry	cubic	cubic	[251–253]
Space group	$Ia\bar{3}$	Ia3d	[251–253]
Lattice constant (Å)	10.39	12.00	[192, 204, 254]
Density ($g\,cm^{-3}$)	9.42	4.56	[192, 254]
Cation density ($10^{20}\,cm^{-3}$)	285.2 (Lu^{3+})	138 (Y^{3+})	[192, 254]
Yb-Coordination number	6	8	[206, 255, 256]
Cation radius (Å)	0.86 (6-fold)	1.02 (8-fold)	[255, 257]
Dopant radius (Å)	0.868 (6-fold)	0.985 (8-fold)	[255, 257]
Site symmetry	C_2, C_{3i}	D_2	[252, 255]
Mohs hardness	6-6.5	8.5	[192, 258]
Melting point (°C)	2450	1940	[259, 260]
Transparency range (µm)	0.23-8	0.18-6	[182, 205]
Debye-temperature (K)	375	750	[182, 205]
Specific heat capacity ($J\,g^{-1}\,K^{-1}$)	0.25 (3 at. %)	0.58 (4 at. %)	[180, 201, 261, 262]
Thermal diffusivity ($10^{-6}\,m^2\,s^{-1}$)	5.6 (20 °C)	3.7-4.3 (20 °C)	[53, 176, 180]
Thermal conductivity $W\,m^{-1}\,K^{-1}$	12.6 (20 °C)	10.1-11.4 (20 °C)	[53, 176, 180]
Thermal expansion coefficient $\frac{dl}{dt}$ ($10^{-6}\,K^{-1}$)	5.88 (20 °C, 1.5 at. %)	6.2 (25 °C, undoped)	[136, 194, 263]
Thermo-optic coefficient $\frac{dn}{dt}$ ($10^{-6}\,K^{-1}$)	7.49 (20 °C,1064 nm)	7.65 (20 °C,1064 nm)	[198, 201]
Max. phonon energy (cm^{-1})	618 (300 K)	857 (300 K)	[182, 183, 264]
Refractive index	1.911 (1 µm)	1.816 (1 µm) (7 at. %)	[198, 200]
Max. absorption (nm)	976	968.8	[176, 253, 265]
Absorption bandwidth (FWHM) (nm)	2.9	2.6	[66, 265]
Max. absorption cross section ($10^{-21}\,cm^2$)	30	8.3	[66, 265]
Laser wavelengths (nm)	1033;1080	1030;1049	[66, 265]
Absorption cross section at laser wavelengths ($10^{-21}\,cm^2$)	0.7; <0.03	1.24; 0.1	[66, 265]
Max. emission cross section ($10^{-21}\,cm^2$)	12.6; 4.4	18.8. 2.9	[66, 265]
Emission bandwidth (FWHM) (nm)	13.0; 15.7	8.4; 8.3	[66, 265]
Fluorescence lifetime (µs)	820 (3 at. %)	950 (7 at. %)	[66, 265]
Stark levels $^2F_{7/2}$ (cm^{-1})	0; 427; 514; 903 (C_2)	0; 565; 612; 785	[182, 205, 206, 253]
Stark levels $^2F_{5/2}$ (cm^{-1})	10244; 10666; 11073 (C_2)	10327; 10624; 10679	[182, 205, 206, 253]
Partition function ratio Z_l/Z_u (30 °C)	1.066	0.817	[182, 205, 206, 253]

Table B.1: Recommended property values of $Yb:Lu_2O_3$ and $Yb:Y_3Al_5O_{12}$. Data are prefered if available for common ytterbium doping concentration (3 at. %. for $Yb:Lu_2O_3$ and 7 at. % for $Yb:Y_3Al_5O_{12}$). While only slight changes of the properties are expected for $Yb:Lu_2O_3$, they can be pronounced even more for $Yb:Y_3Al_5O_{12}$ due to the differences of ionic radii and masses.

List of Figures

List of Tables

Glossary and list of acronyms

1d one-dimensional

3d three-dimensional

AC alternating current

AOI angle of incidence

ASE amplified spontaneous emission

AR anti-reflective

BESSY Berliner Elektronenspeicherring-Gesellschaft für Synchrotronstrahlung

CCD charge-coupled device

CMOS complementary metal-oxide-semiconductor

CRD cavity ring down

CTE coefficient of thermal expansion

CVD chemical vapour deposition

CW continuous wave

DC direct current

DLR Deutsches Zentrum für Luft- und Raumfahrt

D+G Dausinger + Giesen

FEE Forschungsinstitut f. Mineral u. Metallische Werkstoffe Edelsteine Edelmetalle

FEL free-electron laser

FEM finite element method

FOM figure of merit

FSR free spectral range

FWHM full width at half-maximum

HEM heat exchanger method

HHG high harmonic generation

HR high-reflective

IBS ion beam sputtering

ILP Institut für Laser-Physik

LCLS Linac Coherent Light Source

OC output coupler

OPD optical path difference

PETRA Positron-Elektron-Tandem-Ring-Anlage

PER polarization extinction ratio

PTB Physikalisch-Technische Bundesanstalt

QWS quarter-wave stack

RF radio frequency

ROC radius of curvature

RMS root mean square

SHWFS Shack–Hartmann wavefront sensor

SHG second harmonic generation

SNR signal-to-noise ratio

TDL thin-disk laser

TIS total integrated scatter

THG third harmonic generation

VBG volume Bragg grating

VMI velocity map imaging

WHS WHS Sondermetalle

WLI white light interferometer

XFEL X-Ray Free-Electron Laser

ZPL zero-phonon line

Bibliography

[1] A. H. Zewail. *Femtochemistry: Atomic-Scale Dynamics of the Chemical Bond*. J. Phys. Chem. A **104** (24), 5660–5694 (2000), [doi:10.1021/jp001460h].

[2] M. Peplow. *The next big hit in molecule Hollywood*. Nature **544** (7651), 408–410 (2017), [doi:10.1038/544408a].

[3] J. Xu, C. I. Blaga, P. Agostini, and L. F. DiMauro. *Time-resolved molecular imaging*. J. Opt. Soc. Am. B **49** (11), 112001 (2016), [doi:10.1088/0953-4075/49/11/112001].

[4] A. Barty, J. Küpper, and H. N. Chapman. *Molecular Imaging Using X-Ray Free-Electron Lasers*. Annu. Rev. Phys. Chem. **64** (1), 415–435 (2013), [doi:10.1146/annurev-physchem-032511-143708].

[5] C. Kupitz, S. Basu, I. Grotjohann, R. Fromme, N. A. Zatsepin, K. N. Rendek, M. S. Hunter, R. L. Shoeman, T. A. White, D. Wang, D. James, J.-H. Yang, D. E. Cobb, B. Reeder, R. G. Sierra, H. Liu, A. Barty, A. L. Aquila, D. Deponte, R. A. Kirian, S. Bari, J. J. Bergkamp, K. R. Beyerlein, M. J. Bogan, C. Caleman, T.-C. Chao, C. E. Conrad, K. M. Davis, H. Fleckenstein, L. Galli, S. P. Hau-Riege, S. Kassemeyer, H. Laksmono, M. Liang, L. Lomb, S. Marchesini, A. V. Martin, M. Messerschmidt, D. Milathianaki, K. Nass, A. Ros, S. Roy-Chowdhury, K. Schmidt, M. Seibert, J. Steinbrener, F. Stellato, L. Yan, C. Yoon, T. A. Moore, A. L. Moore, Y. Pushkar, G. J. Williams, S. Boutet, R. B. Doak, U. Weierstall, M. Frank, H. N. Chapman, J. C. H. Spence, and P. Fromme. *Serial time-resolved crystallography of photosystem II using a femtosecond X-ray laser*. Nature **513** (7517), 261–265 (2014), [doi:10.1038/nature13453].

[6] J. Miao, T. Ishikawa, I. K. Robinson, and M. M. Murnane. *Beyond crystallography: Diffractive imaging using coherent x-ray light sources*. Science **348** (6234), 530–535 (2015), [doi:10.1126/science.aaa1394].

[7] E. Weckert. *The potential of future light sources to explore the structure and function of matter*. IUCrJ **2** (2), 230–245 (2015), [doi:10.1107/S2052252514024269].

[8] J. M. Martin-Garcia, C. E. Conrad, J. Coe, S. Roy-Chowdhury, and P. Fromme. *Serial femtosecond crystallography: A revolution in structural biology*. Arch. Biochem. Biophys. **602**, 32–47 (2016), [doi:10.1016/j.abb.2016.03.036].

[9] T. Seideman and E. Hamilton. *Nonadiabatic alignment by intense pulses. Concepts, theory, and directions*. Adv. Atom. Mol. Opt. Phys. **52**, 289–329 (2005), [doi:10.1016/S1049-250X(05)52006-8].

[10] H. Stapelfeldt and T. Seideman. *Colloquium: Aligning molecules with strong laser*

pulses. Rev. Mod. Phys. **75** (2), 543–557 (2003), [doi:10.1103/RevModPhys.75.543].

[11] L. Holmegaard, J. H. Nielsen, I. Nevo, H. Stapelfeldt, F. Filsinger, J. Küpper, and G. Meijer. *Laser-induced alignment and orientation of quantum-state-selected large molecules*. Phys. Rev. Lett. **102**, 023001 (2009), [doi:10.1103/PhysRevLett.102.023001], arxiv:0810.2307 [physics.chem-ph] .

[12] V. Kumarappan, C. Z. Bisgaard, S. S. Viftrup, L. Holmegaard, and H. Stapelfeldt. *Role of rotational temperature in adiabatic molecular alignment*. J. Chem. Phys. **125** (19), 194309 (2006), [doi:10.1063/1.2388273].

[13] H. N. Chapman. *Imaging beyond the limits*. In *Biology with FELs: Toward the Molecular Movie*. Lawrence Berkeley National Laboratory, Berkeley, CA 94720, USA (2011).

[14] S. Stern, L. Holmegaard, F. Filsinger, A. Rouzee, A. Rudenko, P. Johnsson, A. V. Martin, A. Barty, C. Bostedt, J. Bozek, R. Coffee, S. Epp, B. Erk, L. Foucar, R. Hartmann, N. Kimmel, K.-U. Kühnel, J. Maurer, M. Messerschmidt, B. Rudek, D. Starodub, J. ThÃ¸gersen, G. Weidenspointner, T. A. White, H. Stapelfeldt, D. Rolles, H. N. Chapman, and J. Küpper. *Toward atomic resolution diffractive imaging of isolated molecules with x-ray free-electron lasers*. Faraday Disc. **171**, 393 (2014), [doi:10.1039/c4fd00028e], arxiv:1403.2553 [physics.atom-ph] .

[15] S. Trippel, T. Mullins, N. L. M. Müller, J. S. Kienitz, K. Długołęcki, and J. Küpper. *Strongly aligned and oriented molecular samples at a kHz repetition rate*. Mol. Phys. **111**, 1738 (2013), [doi:10.1080/00268976.2013.780334], arxiv:1301.1826 [physics.atom-ph] .

[16] J. Yang, V. Makhija, V. Kumarappan, and M. Centurion. *Reconstruction of three-dimensional molecular structure from diffraction of laser-aligned molecules*. Struct. Dyn. **1** (4), 044101 (2014), [doi:10.1063/1.4889840].

[17] A. Fratalocchi and G. Ruocco. *Single-Molecule Imaging with X-Ray Free-Electron Lasers: Dream or Reality?* Phys. Rev. Lett. **106** (10), 105504 (2011), [doi:10.1103/PhysRevLett.106.105504].

[18] J. Küpper, F. Filsinger, G. Meijer, and H. Stapelfeldt. *Methods in Physical Chemistry*, chap. Manipulating the motion of complex molecules: Deflection, focusing, and deceleration of molecular beams for quantum-state and conformer-selection, 1–28. Wiley-VCH (2011). ISBN 9783527327454, [doi:10.1002/9783527636839].

[19] M. Lemeshko, R. V. Krems, J. M. Doyle, and S. Kais. *Manipulation of Molecules with Electromagnetic Fields*. Mol. Phys. **111** (12-13), 1648–1682 (2013), [doi:10.1080/00268976.2013.813595], arxiv:1306.0912 [physics.atom-ph] .

[20] E. Wrede. *Über die Ablenkung von Molekularstrahlen elektrischer Dipolmoleküle im inhomogenen elektrischen Feld*. Z. Phys. **44** (4-5), 261–268 (1927), [doi:10.1007/BF01391193].

[21] U. Even, J. Jortner, D. Noy, N. Lavie, and N. Cossart-Magos. *Cooling of large molecules below 1 K and He clusters formation*. J. Chem. Phys. **112**, 8068–8071 (2000), [doi:10.1063/1.481405].

[22] N. F. Ramsey. *Molecular Beams*. The International Series of Monographs on Physics. Oxford University Press, London, GB (1956), [doi:10.1093/acprof:oso/9780198520214.001.0001]. Reprinted in *Oxford Classic Texts in the Physical Sciences*

(2005).

[23] S. Y. T. van de Meerakker, H. L. Bethlem, and G. Meijer. *Taming molecular beams*. Nat. Phys. **4** (8), 595–602 (2008), [doi:10.1038/nphys1031].

[24] Y.-P. Chang, D. A. Horke, S. Trippel, and J. Küpper. *Spatially-controlled complex molecules and their applications*. Int. Rev. Phys. Chem. **34**, 557–590 (2015), [doi:10.1080/0144235X.2015.1077838], arxiv:1505.05632 [physics.chem-ph] .

[25] H. J. Loesch and A. Remscheid. *Brute force in molecular reaction dynamics: A novel technique for measuring steric effects*. J. Chem. Phys. **93**, 4779 (1990), [doi:10.1063/1.458668].

[26] B. Friedrich and D. R. Herschbach. *Spatial Orientation of Molecules in Strong Electric Fields and Evidence for Pendular States*. Nature **353**, 412–414 (1991), [doi:10.1038/353412a0].

[27] R. J. Bemish, E. J. Bohac, M. Wu, and R. E. Miller. *Photofragment vibrational, rotational, and translational distributions for N_2-HF (v=1)*. J. Chem. Phys. **101** (11), 9457–9468 (1994), [doi:10.1063/1.467977].

[28] J. Bulthuis, J. J. Vanleuken, and S. Stolte. *Hexapole state selection and focusing vs brute force orientation of beam molecules*. J. Chem. Soc. – Faraday Trans. **91**, 205–214 (1995), [doi:10.1039/FT9959100205].

[29] D. Normand, L. Lompre, and C. Cornaggia. *Laser-induced Molecular Alignment Probed By A Double-pulse Experiment*. J. Phys. B **25**, 497–503 (1992), [doi:10.1088/0953-4075/25/20/001].

[30] E. T. Karamatskos, S. Raabe, T. Mullins, A. Trabattoni, P. Stammer, G. Goldsztejn, R. R. Johansen, K. Długołęcki, H. Stapelfeldt, M. J. J. Vrakking, S. Trippel, A. Rouzée, and J. Küpper. *Molecular movie of ultrafast coherent rotational dynamics* (2018), arxiv:1807.01034 [physics.chem-ph] .

[31] W. Demtröder. *Experimentalphysik 3*, vol. 3. Springer Verlag, Berlin, 4 edn. (2010), [doi:10.1007/978-3-642-03911-9].

[32] S. Trippel, T. Mullins, N. L. M. Müller, J. S. Kienitz, J. J. Omiste, H. Stapelfeldt, R. González-Férez, and J. Küpper. *Strongly driven quantum pendulum of the carbonyl sulfide molecule*. Phys. Rev. A **89**, 051401(R) (2014), [doi:10.1103/PhysRevA.89.051401], arxiv:1401.6897 [quant-ph] .

[33] T. Kierspel, J. Wiese, T. Mullins, J. Robinson, A. Aquila, A. Barty, R. Bean, R. Boll, S. Boutet, P. Bucksbaum, H. N. Chapman, L. Christensen, A. Fry, M. Hunter, J. E. Koglin, M. Liang, V. Mariani, A. Morgan, A. Natan, V. Petrovic, D. Rolles, A. Rudenko, K. Schnorr, H. Stapelfeldt, S. Stern, J. Thøgersen, C. H. Yoon, F. Wang, S. Trippel, and J. Küpper. *Strongly aligned molecules at Free-Electron Lasers*. J. Phys. B **48** (20), 204002 (2015), [doi:10.1088/0953-4075/48/20/204002], arxiv:1506.03650 [physics.chem-ph] .

[34] T. Seideman. *On the dynamics of rotationally broad, spatially aligned wave packets*. J. Chem. Phys. **115**, 5965 (2001), [doi:10.1063/1.1400131].

[35] J. J. Larsen, K. Hald, N. Bjerre, H. Stapelfeldt, and T. Seideman. *Three dimensional alignment of molecules using elliptically polarized laser fields*. Phys. Rev. Lett. **85**, 2470–2473 (2000), [doi:10.1103/PhysRevLett.85.2470].

[36] S. Trippel. *Aligned Molecules for Reactive Scattering*. Ph.D. thesis, Universität Freiburg,

Germany (2010).

[37] J. J. Larsen. *Laser induced alignment of neutral molecules*. Ph.D. thesis, University of Aarhus, Denmark (2010).

[38] P. W. Atkins and R. S. Friedman. *Molecular Quantum Mechanics*. Oxford University Press, University of Michigan, 3 edn. (1997). ISBN 9780198559474, [doi:10.1080/00107514.2012.678277].

[39] H. W. Kroto. *Molecular Rotation Spectra*. Dover Publications, New York, NY, USA (1975). ISBN 9780486672595.

[40] J. Küpper, S. Stern, L. Holmegaard, F. Filsinger, A. Rouzée, A. Rudenko, P. Johnsson, A. V. Martin, M. Adolph, A. Aquila, S. Bajt, A. Barty, C. Bostedt, J. Bozek, C. Caleman, R. Coffee, N. Coppola, T. Delmas, S. Epp, B. Erk, L. Foucar, T. Gorkhover, L. Gumprecht, A. Hartmann, R. Hartmann, G. Hauser, P. Holl, A. Hömke, N. Kimmel, F. Krasniqi, K.-U. Kühnel, J. Maurer, M. Messerschmidt, R. Moshammer, C. Reich, B. Rudek, R. Santra, I. Schlichting, C. Schmidt, S. Schorb, J. Schulz, H. Soltau, J. C. H. Spence, D. Starodub, L. Strüder, J. Thøgersen, M. J. J. Vrakking, G. Weidenspointner, T. A. White, C. Wunderer, G. Meijer, J. Ullrich, H. Stapelfeldt, D. Rolles, and H. N. Chapman. *X-ray diffraction from isolated and strongly aligned gas-phase molecules with a free-electron laser*. Phys. Rev. Lett. **112**, 083002 (2014), [doi:10.1103/PhysRevLett.112.083002], arxiv:1307.4577 [physics.atom-ph] .

[41] S. Boutet, L. Lomb, G. J. Williams, T. R. M. Barends, A. Aquila, R. B. Doak, U. Weierstall, D. P. DePonte, J. Steinbrener, R. L. Shoeman, M. Messerschmidt, A. Barty, T. A. White, S. Kassemeyer, R. A. Kirian, M. M. Seibert, P. A. Montanez, C. Kenney, R. Herbst, P. Hart, J. Pines, G. Haller, S. M. Gruner, H. T. Philipp, M. W. Tate, M. Hromalik, L. J. Koerner, N. van Bakel, J. Morse, W. Ghonsalves, D. Arnlund, M. J. Bogan, C. Caleman, R. Fromme, C. Y. Hampton, M. S. Hunter, L. C. Johansson, G. Katona, C. Kupitz, M. Liang, A. V. Martin, K. Nass, L. Redecke, F. Stellato, N. Timneanu, D. Wang, N. A. Zatsepin, D. Schafer, J. Defever, R. Neutze, P. Fromme, J. C. H. Spence, H. N. Chapman, and I. Schlichting. *High-Resolution Protein Structure Determination by Serial Femtosecond Crystallography*. Science **337** (6092), 362–364 (2012), [doi:10.1126/science.1217737].

[42] B. Ziaja, H. N. Chapman, R. Fäustlin, S. Hau-Riege, Z. Jurek, A. V. Martin, S. Toleikis, F. Wang, E. Weckert, and R. Santra. *Limitations of coherent diffractive imaging of single objects due to their damage by intense x-ray radiation*. New J. Phys. **14** (11), 115015 (2012), [doi:10.1088/1367-2630/14/11/115015].

[43] G. Scoles. *Atomic and Molecular Beam Methods*. Oxford University Press (1988).

[44] A. T. J. B. Eppink and D. H. Parker. *Velocity map imaging of ions and electrons using electrostatic lenses: Application in photoelectron and photofragment ion imaging of molecular oxygen*. Rev. Sci. Instrum. **68** (9), 3477–3484 (1997), [doi:10.1063/1.1148310].

[45] J. Arthur et al. *Linac Coherent Light Source (LCLS) Conceptual Design Report*. Tech. rep., Stanford Linear Accelerator Laboratory (SLAC), Menlo Park, CA, USA (2002).

[46] M. Altarelli, R. Brinkmann, M. Chergui, W. Decking, B. Dobson, S. Düsterer, G. Grübel, W. Graeff, H. Graafsma, J. Hajdu, J. Marangos, J. Pflüger, H. Redlin, D. Riley, I. Robinson, J. Rossbach, A. Schwarz, K. Tiedtke, T. Tschentscher, I. Vartaniants,

H. Wabnitz, H. Weise, R. Wichmann, K. Witte, A. Wolf, M. Wulff, and M. Yurkov. *The Technical Design Report of the European XFEL*. Tech. rep., DESY, Hamburg, Germany (2007), [doi:10.3204/DESY_06-097].

[47] W. Decking and T. Limberg. *European XFEL post-TDR description*. Tech. rep., DESY (2013).

[48] Basic Energy Sciences Advisory Committee. *Report of the BESAC Subcommittee on Future X-ray Light Sources* (2013).

[49] H. Klingbeil, U. Laier, and D. Lens. *Theoretical foundations of synchrotron and storage ring RF systems*. Particle acceleration and detection. Springer Verlag (2015). ISBN 9783319071879, [doi:10.1007/978-3-319-07188-6].

[50] E. R. Peterson, C. Buth, D. A. Arms, R. W. Dunford, E. P. Kanter, B. Krässig, E. C. Landahl, S. T. Pratt, R. Santra, S. H. Southworth, and L. Young. *An x-ray probe of laser-aligned molecules*. Appl. Phys. Lett. **92** (9), 094106 (2008), [doi:10.1063/1.2890846].

[51] C. Benko, L. Hua, T. K. Allison, F. Labaye, and J. Ye. *Cavity-Enhanced Field-Free Molecular Alignment at a High Repetition Rate*. Phys. Rev. Lett. **114** (15), 153001–153005 (2015), [doi:10.1103/PhysRevLett.114.153001].

[52] J. C. H. Spence, K. Schmidt, J. S. Wu, G. Hembree, U. Weierstall, B. Doak, and P. Fromme. *Diffraction and imaging from a beam of laser-aligned proteins*. Acta Cryst. A **61** (Pt 2), 237–245 (2005), [doi:10.1107/S0108767305002710].

[53] S. T. Fredrich-Thornton. *Nonlinear losses in single crystalline and ceramic Yb:YAG thin-disk lasers*. Ph.D. thesis, Universität Hamburg (2010).

[54] J. Stark and G. Wendt. *Beobachtungen über den Effekt des elektrischen Feldes auf Spektrallinien. II. Längseffekt*. Ann. Phys. **348** (7), 983–990 (1914), [doi:10.1002/andp.19143480703].

[55] P. Cheo. *Handbook of Solid-State Lasers*. CRC Press (1988). ISBN 9780824778576, [doi:10.1080/09500349014550191].

[56] B. Denker and E. Shklovsky. *Handbook of Solid-State Lasers*. Materials, Systems and Applications. Elsevier (2013). ISBN 0857097504.

[57] W. Koechner. *Solid-state laser engineering*. Springer Verlag (2006). ISBN 9780387290942, [doi:10.1007/0-387-29338-8].

[58] R. C. Powell. *Physics of Solid-State Laser Materials*. Springer Verlag (1998). ISBN 9781563966583.

[59] D. E. McCumber. *Einstein Relations Connecting Broadband Emission and Absorption Spectra*. Phys. Rev. A **136** (4), 954–957 (1964), [doi:10.1103/PhysRev.136.A954].

[60] N. Hodgson and H. Weber. *Laser Resonators and Beam Propagation: Fundamentals, Advanced Concepts, Applications*. Springer Verlag (2005). ISBN 9780387400785, [doi:10.1007/b106789].

[61] A. Giesen, H. Hügel, A. Voss, K. Wittig, U. Brauch, and H. Opower. *Scalable concept for diode-pumped high-power solid-state lasers*. Appl. Phys. B **58** (5), 365–372 (1994), [doi:10.1007/BF01081875].

[62] A. Giesen and J. Speiser. *Fifteen years of Work on Thin-Disk Lasers: Results and Scaling Laws*. IEEE J. Sel. Top. Quantum. Electron. **13** (3), 598–609 (2007), [doi:10.1109/JSTQE.2007.897180].

[63] S. Erhard. *Pumpoptiken und Resonatoren für den Scheibenlaser*. Ph.D. thesis, Universität Stuttgart (2002).

[64] K. Schuhmann, T. W. Hänsch, K. Kirch, A. Knecht, F. Kottmann, F. Nez, R. Pohl, D. Taqqu, and A. Antognini. *Thin-disk laser pump schemes for large number of passes and moderate pump source quality*. Appl. Opt. **54** (32), 9400–9408 (2015), [doi:10.1364/AO.54.009400].

[65] C. Kränkel. *Ytterbium-dotierte Borate und Vanadate mit großer Verstärkungsbandbreite als aktive Materialien im Scheibenlaser*. Ph.D. thesis, Universität Hamburg (2008).

[66] A. Voss. *Der Scheibenlaser: Theoretische Grundlagen des Dauerstrichbetriebs und erste experimentelle Ergebnisse anhand Yb:YAG*. Ph.D. thesis, Universität Stuttgart (2002).

[67] K. Contag. *Modellierung und numerische Auslegung des Yb:YAG-Scheibenlasers*. Ph.D. thesis, Universität Stuttgart (2002).

[68] T. Taira, W. M. Tulloch, and R. L. Byer. *Modeling of quasi-three-level lasers and operation of CW Yb:YAG lasers*. Appl. Opt. **36** (9), 1867–1874 (1997), [doi:10.1364/AO.36.001867].

[69] P. Wittmuess, S. Piehler, T. Dietrich, M. A. Ahmed, T. Graf, and O. Sawodny. *Numerical modeling of multimode laser resonators*. J. Opt. Soc. Am. B **33** (11), 2278–2287 (2016), [doi:10.1364/JOSAB.33.002278].

[70] C. Stolzenburg. *Hochrepetierende Kurzpuls-Scheibenlaser im infraroten und grünen Spektralbereich*. Ph.D. thesis, Universität Stuttgart (2011).

[71] A. E. Siegman. *Lasers*. University Science Books, Sausalito, CA, USA (1986). ISBN 9780935702118.

[72] T. Graf. *Laser*. Springer Verlag (2015). ISBN 9783658079536.

[73] F. K. Kneubühl and M. W. Sigrist. *Laser*. B. G. Teubner, Stuttgart (1989).

[74] P. W. Milonni and J. H. Eberly. *Lasers*. John Wiley & Sons, 1 edn. (1988).

[75] W. Demtröder. *Laser Spectroscopy: Basic Concepts and Instrumentation*. Springer Verlag, Berlin, 3 edn. (2003). ISBN 3540652256.

[76] W. Demtröder. *Laser Spectroscopy: Basic Concepts and Instrumentation*. Springer Verlag, Berlin, 2 edn. (1998). ISBN 354057171.

[77] A. Yariv. *Quantum electronics*. John Wiley & Sons (1989). ISBN 0471617717.

[78] K. Arai and L. S. Collaboration. *On the accumulated round-trip Gouy phase shift for a general optical cavity. Technical Note LIGO-T1300189-v1*. Tech. rep., LIGO Scientific Collaboration (2013).

[79] J. Weitenberg, P. Rußbüldt, I. Pupeza, and T. Udem. *Geometrical on-axis access to high-finesse resonators by quasi-imaging: a theoretical description*. J. Opt **17** (2), 025609 (2015), [doi:10.1088/2040-8978/17/2/025609].

[80] H. Carstens, S. Holzberger, J. Kaster, J. Weitenberg, V. Pervak, A. Apolonski, E. Fill, F. Krausz, and I. Pupeza. *Large-mode enhancement cavities*. Opt. Exp. **21** (9), 11606–11617 (2013), [doi:10.1364/OE.21.011606].

[81] Q. Zhang, B. Ozygus, and H. Weber. *Degeneration effects in laser cavities*. Eur. Phys. J. AP **6** (3), 293–298 (1999), [doi:10.1051/epjap:1999186].

[82] R. Paschotta. *Beam quality deterioration of lasers caused by intracavity beam distortions*. Opt. Exp. **14** (13), 6069–6074 (2006), [doi:10.1364/OE.14.006069].

[83] A. L. Bullington, B. T. Lantz, M. M. Fejer, and R. L. Byer. *Modal frequency degeneracy in thermally loaded optical resonators*. Appl. Opt. **47** (15), 2840–2851 (2008), [doi:10.1364/AO.47.002840].

[84] D. Findlay and R. A. Clay. *The measurement of internal losses in 4-level lasers*. Phys. Lett. **20** (3), 277–278 (1966), [doi:10.1016/0031-9163(66)90363-5].

[85] J. A. Caird, S. A. Payne, P. R. Staver, A. J. Ramponi, L. L. Chase, and W. F. Krupke. *Quantum Electronic-Properties of the $Na_3Ga_2Li_3F_{12}$:Cr^{3+} Laser*. IEEE J. Quantum. Electron. **24** (6), 1077–1099 (1988), [doi:10.1109/3.231].

[86] U. Wolters. *Inversion Dependent Losses in Yb: YAG and Their Effects on Thin-Disk Laser Operation*. Ph.D. thesis, Universität Hamburg, Hamburg, Germany (2014).

[87] K. J. Weingarten, B. Braun, and U. Keller. *In situ small-signal gain of solid-state lasers determined from relaxation oscillation frequency measurements*. Opt. Lett. **19** (15), 1140–1142 (1994), [doi:10.1364/OL.19.001140].

[88] R. Paschotta. *Encyclopedia of Laser Physics and Technology*. John Wiley & Sons (2008). ISBN 9783527408283.

[89] W. A. Clarkson and D. C. Hanna. *Effects of Transverse-mode Profile on Slope Efficiency and Relaxation Oscillations in a Longitudinally-pumped Laser*. J. Mod. Opt. **36** (4), 483–498 (2007), [doi:10.1080/09500348914550561].

[90] J. Scherer, J. Paul, A. O'Keefe, and R. Saykally. *Cavity Ringdown Laser Absorption Spectroscopy: History, Development, and Application to Pulsed Molecular Beams*. Chem. Rev. **97** (1), 25–52 (1997), [doi:10.1021/cr930048d].

[91] G. Berden and R. Engeln. *Cavity Ring-Down Spectroscopy: Techniques and Applications*. John Wiley & Sons, Chichester, UK (2009). ISBN 9781444308242, [doi:10.1002/9781444308259].

[92] H. Zhao and A. Major. *Dynamic characterization of intracavity losses in broadband quasi-three-level lasers*. Opt. Exp. **22** (22), 26651–26658 (2014), [doi:10.1364/OE.22.026651].

[93] F. Träger. *Springer Handbook of Lasers and Optics*. Springer Verlag, Berlin, Heidelberg (2012). ISBN 3642194095, [doi:10.1007/978-3-642-19409-2].

[94] J. H. Seinfeld and S. N. Pandis. *Atmospheric Chemistry and Physics*. John Wiley & Sons (2016). ISBN 978-1-118-94740-1.

[95] A. J. Cox, A. J. DeWeerd, and J. Linden. *An experiment to measure Mie and Rayleigh total scattering cross sections*. Am. J. Phys **70** (6), 620 (2002), [doi:10.1119/1.1466815].

[96] M. Sneep and W. Ubachs. *Direct measurement of the Rayleigh scattering cross section in various gases*. J. Quant. Spectrosc. Radiat. Transfer **92** (3), 293–310 (2005), [doi:10.1016/j.jqsrt.2004.07.025].

[97] C. Tomasi, V. Vitale, B. Petkov, A. Lupi, and A. Cacciari. *Improved algorithm for calculations of Rayleigh-scattering optical depth in standard atmospheres*. Appl. Opt. **44** (16), 3320–3341 (2005), [doi:10.1364/AO.44.003320].

[98] H. E. Bennett and J. O. Porteus. *Relation Between Surface Roughness and Specular Reflectance at Normal Incidence*. J. Opt. Soc. Am. **51** (2), 123–129 (1961), [doi:10.1364/JOSA.51.000123].

[99] J. E. Harvey, S. Schröder, and N. Choi. *Total integrated scatter from surfaces with*

arbitrary roughness, correlation widths, and incident angles. Opt. Eng. **51** (1), 013402 (2012), [doi:10.1117/1.OE.51.1.013402].

[100] J. H. Rakels. *Influence of the surface height distribution on the total integrated scatter (TIS) formula*. Nanotechnology **7** (1), 43–46 (1996), [doi:10.1088/0957-4484/7/1/006].

[101] J. M. ELSON. *Diffraction and diffuse scattering from dielectric multilayers*. J. Opt. Soc. Am. **69** (1), 48–54 (1979), [doi:10.1364/JOSA.69.000048].

[102] P. Bousquet, F. Flory, and P. Roche. *Scattering from multilayer thin films: theory and experiment*. J. Opt. Soc. Am. **71** (9), 1115–1123 (1981), [doi:10.1364/JOSA.71.001115].

[103] C. Amra. *Light-scattering from multilayer optics .1. tools of investigation*. J. Opt. Soc. Am. **11** (1), 197–210 (1994), [doi:10.1364/JOSAA.11.000197].

[104] R. E. Hummel and K. H. Guenther. *Handbook of optical properties: thin films for optical coatings*. CRC Press (1995). ISBN 9780849324840.

[105] A. Duparré and S. Kassam. *Relation between light scattering and the microstructure of optical thin films*. Appl. Opt. **32** (28), 5475–5480 (1993), [doi:10.1364/AO.32.005475].

[106] D. L. Windt. *IMD - Software for modeling the optical properties of multilayer films*. Computers in Physics **12** (4), 360–370 (1998), [doi:10.1063/1.168689].

[107] M. Karszewski. *Scheibenlaser höchster Strahlqualität*. Ph.D. thesis, Universität Stuttgart (2000).

[108] L. S. Rothman, I. E. Gordon, Y. Babikov, A. Barbe, D. C. Benner, P. F. Bernath, M. Birk, L. Bizzocchi, V. Boudon, L. R. Brown, A. Campargue, K. Chance, E. A. Cohen, L. H. Coudert, V. M. Devi, B. J. Drouin, A. Fayt, J. M. Flaud, R. R. Gamache, J. J. Harrison, J. M. Hartmann, C. Hill, J. T. Hodges, D. Jacquemart, A. Jolly, J. Lamouroux, R. J. Le Roy, G. Li, D. A. Long, O. M. Lyulin, C. J. Mackie, S. T. Massie, S. Mikhailenko, H. S. P. Mueller, O. V. Naumenko, A. V. Nikitin, J. Orphal, V. Perevalov, A. Perrin, E. R. Polovtseva, C. Richard, M. A. H. Smith, E. Starikova, K. Sung, S. Tashkun, J. Tennyson, G. C. Toon, V. G. Tyuterev, and G. Wagner. *The HITRAN2012 molecular spectroscopic database*. J. Quant. Spectrosc. Radiat. Transfer **130**, 4–50 (2013), [doi:10.1016/j.jqsrt.2013.07.002].

[109] S. E. Watkins, J. P. Black, and B. J. Pond. *Optical scatter characteristics of high-reflectance dielectric coatings and fused-silica substrates*. Appl. Opt. **32** (28), 5511–5518 (1993), [doi:10.1364/AO.32.005511].

[110] K. H. Guenther. *Nodular defects in dielectric multilayers and thick single layers*. Appl. Opt. **20** (6), 1034–1038 (1981), [doi:10.1364/AO.20.001034].

[111] J. F. DeFord and M. R. Kozlowski. *Modeling of electric-field enhancement at nodular defects in dielectric mirror coatings*. In H. E. Bennett, L. L. Chase, A. H. Guenther, B. E. Newnam, and M. J. Soileau, eds., *Annual Boulder Damage Symposium Proceedings – Laser-Induced Damage in Optical Materials*, vol. 1848 of *Proc. SPIE*, 455–473 (1992), [doi:10.1117/12.147414].

[112] L. G. DeShazer, B. E. Newnam, and K. M. Leung. *Role of coating defects in laser-induced damage to dielectric thin films*. Appl. Phys. Lett. **23** (11), 607–609 (1973), [doi:10.1063/1.1654764].

[113] M. R. Kozlowski and R. Chow. *Role of defects in laser damage of multilayer coatings*. In H. E. Bennett, L. L. Chase, A. H. Guenther, B. E. Newnam, and M. J. Soileau, eds., *Laser-Induced Damage in Optical Materials*, vol. 2114 of *Proc. SPIE* (1993), [doi:10.1117/12.180876].

[114] R. H. Sawicki, C. C. Shang, and T. L. Swatloski. *Failure characterization of nodular defects in multilayer dielectric coatings*. In H. E. Bennett, A. H. Guenther, M. R. Kozlowski, B. E. Newnam, and M. J. Soileau, eds., *Laser-Induced Damage in Optical Materials*, vol. 2428 of *Proc. SPIE*, 333–343 (1995), [doi:10.1117/12.213718].

[115] X. Cheng, J. Zhang, T. Ding, Z. Wei, H. Li, and Z. Wang. *The effect of an electric field on the thermomechanical damage of nodular defects in dielectric multilayer coatings irradiated by nanosecond laser pulses*. Light Sci. Appl. **2** (6), e80 (2013), [doi:10.1038/lsa.2013.36].

[116] X. Cheng, A. Tuniyazi, Z. Wei, J. Zhang, T. Ding, H. Jiao, B. Ma, H. Li, T. Li, and Z. Wang. *Physical insight toward electric field enhancement at nodular defects in optical coatings*. Opt. Exp. **23** (7), 8609–8619 (2015), [doi:10.1364/OE.23.008609].

[117] H. Goldenberg and C. J. Tranter. *Heat flow in an infinite medium heated by a sphere*. Br. J. Appl. Sci. Technol. **3** (9), 296 (1952), [doi:10.1088/0508-3443/3/9/307].

[118] G. Rempe, R. J. Thompson, H. J. Kimble, and R. Lalezari. *Measurement of ultralow losses in an optical interferometer*. Opt. Lett. **17** (5), 363–365 (1992), [doi:10.1364/OL.17.000363].

[119] D. T. Carpenter, C. S. Wood, and O. Lyngnes. *Ultra low absorption glasses and optical coatings for reduced thermal focus shift in high power optic*. In E. Beyer and T. Morris, eds., *High Power Laser Materials Processing: Lasers, Beam Delivery, Diagnostics, and Applications*, vol. 8898 of *Proc. SPIE*, 82390Y (2012), [doi:10.1117/12.905462].

[120] H. J. Cho, J. C. Lee, and S. H. Lee. *Design and Development of an Ultralow Optical Loss Mirror Coating for Zerodur Substrate*. J. Opt. Soc. Korea **16** (1), 80–84 (2012), [doi:10.3807/JOSK.2012.16.1.080].

[121] T. Guang. *Influence of annealing temperature on structure, optical loss and laser-induced damage threshold of TiO_2 thin films*. Chin. Phys. Lett **24** (10), 2967 (2007), [doi:10.1088/0256-307X/24/10/070].

[122] M. Haque and S. Mahalakshmi. *Effect of Annealing on Structure and Morphology of Cadmium Sulphide Thin Film Prepared by Chemical Bath Deposition*. J. Appl. Phys. **3** (2), 159–162 (2014), [doi:10.1166/jap.2014.1116].

[123] M. Popovic, M. Novakovic, and N. Bibic. *Annealing effects on the properties of TiN thin films*. Processing and Application of Ceramics **9** (2), 67–71 (2015), [doi:10.2298/PAC1502067P].

[124] S. Kičas, U. Gimževskis, and S. Melnikas. *Post deposition annealing of IBS mixture coatings for compensation of film induced stress*. Opt. Mat. Exp. **6** (7), 2236–2243 (2016), [doi:10.1364/OME.6.002236].

[125] N. P. Barnes and P. J. Walsh. *Loss of Gaussian beams through off-axis circular apertures*. Appl. Opt. **27** (7), 1230–1232 (1988), [doi:10.1364/AO.27.001230].

[126] I. Pupeza, S. Holzberger, T. Eidam, and H. Carstens. *Compact high-repetition-rate source of coherent 100 eV radiation*. Nat. Photon. **7** (8), 608–612 (2013), [doi:10.1038/nphoton.2013.156].

[127] I. Pupeza, M. Högner, J. Weitenberg, and S. Holzberger. *Cavity-enhanced high-harmonic generation with spatially tailored driving fields*. Phys. Rev. Lett. **112** (10), 103902 (2014), [doi:10.1103/PhysRevLett.112.103902].

[128] M. Born and E. Wolf. *Principles of Optics*. Pergamon Press, Oxford, 7th edn. (1999). ISBN 0521642221, [doi:10.1016/S0030-3992(00)00061-X].

[129] S. M. Lee, D. G. Cahill, and T. H. Allen. *Thermal conductivity of sputtered oxide films*. Phys. Rev. B **52** (1), 253–257 (1995), [doi:10.1103/PhysRevB.52.253].

[130] J. A. Thornton and D. W. Hoffman. *Stress-related effects in thin-films*. Thin Solid Films **171** (1), 5–31 (1989), [doi:10.1016/0040-6090(89)90030-8].

[131] M. G. Gurov and A. K. Dmitriev. *Diffraction losses and selection of transverse modes in complex resonators*. Russ. Phys. J. **52** (5), 464 (2009), [doi:10.1007/s11182-009-9252-1].

[132] H. P. Kortz and H. Weber. *Diffraction losses and mode structure of equivalent TEM_{00} optical resonators*. Appl. Opt. **20** (11), 1936–1940 (1981), [doi:10.1364/AO.20.001936].

[133] B. Saleh and M. C. Teich. *Fundamentals of photonics*. John Wiley & Sons (2007). ISBN 9780471358329, [doi:10.1002/0471213748].

[134] A. G. Fox and T. Li. *Resonant modes in a maser interferometer*. Bell System Technical Journal **40** (2), 453 – 488 (1961), [doi:10.1002/j.1538-7305.1961.tb01625.x].

[135] A. E. Siegman and H. Y. Miller. *Unstable optical resonator loss calculations using the Prony method*. Appl. Opt. **9** (12), 2729–2736 (1970), [doi:10.1364/AO.9.002729].

[136] M. Larionov. *Kontaktierung und Charakterisierung von Kristallen für Scheibenlaser*. Ph.D. thesis, Universität Stuttgart (2009).

[137] F. Moglia. *Upconversion lasers and other applications of Er^{3+}-doped fluoride crystals*. Ph.D. thesis, Universität Hamburg (2014).

[138] D. Kouznetsov, J.-F. Bisson, J. Dong, and K.-i. Ueda. *Surface loss limit of the power scaling of a thin-disk laser*. J. Opt. Soc. Am. B **23** (6), 1074–1082 (2006), [doi:10.1364/JOSAB.23.001074].

[139] R. Paschotta, J. Speiser, and A. Giesen. *Comment on "Surface loss limit of the power scaling of a thin-disk laser"*. J. Opt. Soc. Am. B **24** (10), 2658–2658 (2007), [doi:10.1364/JOSAB.24.002658].

[140] Z. Lin, G. Zhu, W. Zhao, Y. Qiao, M. Wang, H. Wang, and X. Zhu. *Heat generation in quasi-three-level Yb:YAG thin-disk lasers*. J. Opt. Soc. Am. B **34** (8), 1669–1676 (2017), [doi:10.1364/JOSAB.34.001669].

[141] T. Dietrich, S. Piehler, C. Röcker, M. Rumpel, M. Abdou-Ahmed, and T. Graf. *Passive compensation of the misalignment instability caused by air convection in thin-disk lasers*. Opt. Lett. **42** (17), 3263–3266 (2017), [doi:10.1364/OL.42.003263].

[142] S. Piehler, T. Dietrich, P. Wittmüss, O. Sawodny, M. A. Ahmed, and T. Graf. *Deformable mirrors for intra-cavity use in high-power thin-disk lasers*. Opt. Exp. **25** (4), 4254–4267 (2017), [doi:10.1364/OE.25.004254].

[143] J. Speiser. *Scaling of thin-disk lasers––influence of amplified spontaneous emission*. J. Opt. Soc. Am. B **26** (1), 26–35 (2009), [doi:10.1364/JOSAB.26.000026].

[144] D. A. Copeland. *Amplified spontaneous emission (ASE) models and approximations for thin-disk laser modeling*. In W. A. Clarkson and R. Shori, eds., *Solid State Lasers XXII:*

Technology and Devices, vol. 8599 of *Proc. SPIE* (2013), [doi:10.1117/12.2005376].

[145] W. A. Clarkson, N. S. Felgate, and D. C. Hanna. *Simple method for reducing the depolarization loss resulting from thermally induced birefringence in solid-state lasers*. Opt. Lett. **24** (12), 820–822 (1999), [doi:10.1364/OL.24.000820].

[146] I. Shoji and T. Taira. *Intrinsic reduction of the depolarization loss in solid-state lasers by use of a (110)-cut $Y_3Al_5O_{12}$ crystal*. Appl. Phys. Lett. **80** (17), 3048–3050 (2002), [doi:10.1063/1.1475365].

[147] G. Fibich and A. L. Gaeta. *Critical power for self-focusing in bulk media and in hollow waveguides*. Opt. Lett. **25** (5), 335–337 (2000), [doi:10.1364/OL.25.000335].

[148] B. Erk, D. Rolles, L. Foucar, B. Rudek, S. W. Epp, M. Cryle, C. Bostedt, S. Schorb, J. Bozek, A. Rouzee, A. Hundertmark, T. Marchenko, M. Simon, F. Filsinger, L. Christensen, S. De, S. Trippel, J. Küpper, H. Stapelfeldt, S. Wada, K. Ueda, M. Swiggers, M. Messerschmidt, C. D. Schroter, R. Moshammer, I. Schlichting, J. Ullrich, and A. Rudenko. *Ultrafast charge rearrangement and nuclear dynamics upon inner-shell multiple ionization of small polyatomic molecules*. Phys. Rev. Lett. **110** (5), 053003 (2013), [doi:10.1103/PhysRevLett.110.053003].

[149] B. Rudek, S.-K. Son, L. Foucar, S.-W. Epp, B. Erk, R. Hartmann, M. Adolph, R. Andritschke, A. Aquila, N. Berrah, C. Bostedt, N. Bozek, Johnand Coppola, F. Filsinger, H. Gorke, T. Gorkhover, H. Graafsma, L. Gumprecht, A. Hartmann, G. Hauser, S. Herrmann, H. Hirsemann, P. Holl, A. Hömke, L. Journel, C. Kaiser, N. Kimmel, F. Krasniqi, K.-U. Kühnel, M. Matysek, M. Messerschmidt, D. Miesner, T. Möller, R. Moshammer, K. Nagaya, B. Nilsson, G. Potdevin, D. Pietschner, C. Reich, D. Rupp, G. Schaller, I. Schlichting, C. Schmidt, F. Schopper, S. Schorb, C.-D. Schröter, J. Schulz, M. Simon, H. Soltau, L. Strüder, K. Ueda, G. Weidenspointner, R. Santra, J. Ullrich, A. Rudenko, and D. Rolles. *Ultra-efficient ionization of heavy atoms by intense X-ray free-electron laser pulses*. Nat. Photon. **6**, 858–865 (2012), [doi:10.1038/nphoton.2012.261].

[150] R. A. Kirian, S. Awel, N. Eckerskorn, H. Fleckenstein, M. Wiedorn, L. Adriano, S. Bajt, M. Barthelmess, R. Bean, K. R. Beyerlein, L. M. G. Chavas, M. Domaracky, M. Heymann, D. A. Horke, J. Knoska, M. Metz, A. Morgan, D. Oberthuer, N. Roth, T. Sato, P. L. Xavier, O. Yefanov, A. V. Rode, J. Küpper, and H. N. Chapman. *Simple convergent-nozzle aerosol injector for single-particle diffractive imaging with x-ray free-electron lasers*. Struct. Dyn. **2** (4), 041717 (2015), [doi:10.1063/1.4922648].

[151] E. Shcherbakov, V. Fomin, A. Abramov, A. Ferin, D. Mochalov, and V. P. Gapontsev. *Industrial Grade 100 kW Power CW Fiber Laser*. In *Advanced Solid State Lasers*, ATh4A.2. Optical Society of America (2013), [doi:10.1364/ASSL.2013.ATh4A.2].

[152] L. N. Myrabo, T. R. Knowles, J. O. Bagford, D. B. Seibert, and H. M. Harris. *Laser-boosted light sail experiments with the 150-kW LHMEL II CO_2 laser*. In C. R. Phipps, ed., *High-Power Laser Ablation IV*, vol. 4760 of *Proc. SPIE* (2002), [doi:10.1117/12.482034].

[153] H. Aksakal and E. Arıkan. *A feasibility study of TAC IR-FEL project*. Nucl. Instrum. Meth. A **620** (2-3), 155–158 (2010), [doi:10.1016/j.nima.2010.04.016].

[154] S. Mustafiz, N. Bjorndalen, and M. R. Islam. *Lasing into the future: Potentials of laser drilling in the petroleum industry*. Pet Sci Technol. **22** (9-10), 1187–1198 (2004), [doi:10.1081/LFT-200034067].

[155] T. Y. Fan. *Laser beam combining for high-power, high-radiance sources*. IEEE J. Sel. Top. Quantum. Electron. **11** (3), 567–577 (2005), [doi:10.1109/JSTQE.2005.850241].

[156] G. Mourou, B. Brocklesby, T. Tajima, and J. Limpert. *The future is fibre accelerators*. Nat. Photon. **7** (4), 258–261 (2013), [doi:10.1038/nphoton.2013.75].

[157] A. Giesen. *Scaling Thin Disk Lasers to High Power and Energy*. In *CLEO: 2013*, CTu1O.1. Optical Society of America (2013), [doi:10.1364/CLEO_SI.2013.CTu1O.1].

[158] T. Gottwald, V. Kuhn, S.-S. Schad, C. Stolzenburg, and A. Killi. *Recent developments in high power thin disk lasers at TRUMPF Laser*. In *Technologies for Optical Countermeasures X; and High-Power Lasers 2013: Technology and Systems*, vol. 8898 of *Proc. SPIE* (2013), [doi:10.1117/12.2028656].

[159] M. Wolke, J. Klinner, H. Keßler, and A. Hemmerich. *Cavity Cooling Below the Recoil Limit*. Science **337** (6090), 75–78 (2012), [doi:10.1126/science.1219166].

[160] J. Ye and T. W. Lynn. *Applications of optical cavities in modern atomic, molecular, and optical physics*. Adv. At. Mol. Opt. Phy. **49**, 1–83 (2003), [doi:10.1016/S1049-250X(03)80003-4].

[161] I. Pupeza. *Power Scaling of Enhancement Cavities for Nonlinear Optics*. Ph.D. thesis, Universität München, München (2012), [doi:10.1007/978-1-4614-4100-7].

[162] H. Carstens, N. Lilienfein, S. Holzberger, C. Jocher, T. Eidam, J. Limpert, A. Tünnermann, J. Weitenberg, D. C. Yost, A. Alghamdi, Z. Alahmed, A. Azzeer, A. Apolonski, E. Fill, F. Krausz, and I. Pupeza. *Megawatt-scale average-power ultrashort pulses in an enhancement cavity*. Opt. Lett. **39** (9), 2595–2598 (2014), [doi:10.1364/OL.39.002595].

[163] P. Kwee, C. Bogan, K. Danzmann, M. Frede, H. Kim, P. King, J. Pöld, O. Puncken, R. L. Savage, F. Seifert, P. Wessels, L. Winkelmann, and B. Willke. *Stabilized high-power laser system for the gravitational wave detector advanced LIGO*. Opt. Exp. **20** (10), 10617–10634 (2012), [doi:10.1364/OE.20.010617].

[164] R. Dändliker. *Eigenstates of Polarization in Optical Resonators with Partial Polarizers*. J. Opt. Soc. Am. **58** (8), 1062–1069 (1968), [doi:10.1364/JOSA.58.001062].

[165] C. Yelland, J. Hong, M. J. Padgett, M. H. Dunn, and W. Sibbett. *A vector approach to the geometrical dependence of polarisation rotation in a non-planar cw Nd:YAG ring laser*. Opt. Comm. **109** (5-6), 451 (1994), [doi:10.1016/0030-4018(94)90497-9].

[166] H. R. Bilger, G. E. Stedman, and P. V. Wells. *Geometrical dependence of polarisation in near-planar ring lasers*. Opt. Comm. **80** (2), 133–137 (1990), [doi:10.1016/0030-4018(90)90374-3].

[167] W. Demtröder. *Molecular Physics*. John Wiley & Sons (2008). ISBN 3527618104, [doi:10.1002/9783527618095].

[168] T. Fan. *Heat generation in Nd:YAG and Yb:YAG*. IEEE J. Quantum. Electron. **29** (6), 1457–1459 (1993), [doi:10.1109/3.234394].

[169] S. Chenais, F. Balembois, F. Druon, G. Lucas-Leclin, and P. Georges. *Thermal lensing in diode-pumped ytterbium Lasers-Part I: theoretical analysis and wavefront measurements*. IEEE J. Quantum. Electron. **40** (9), 1217–1234 (2006), [doi:10.1109/JQE.2004.833198].

[170] T. Y. Fan, D. J. Ripin, and R. L. Aggarwal. *Cryogenic Yb^{3+}-doped solid-state lasers*.

IEEE J. Quantum. Electron. **13(3)**, 448–459 (2007), [doi:10.1109/JSTQE.2007.896602].

[171] J. Mende, E. Schmid, J. Speiser, G. Spindler, and A. Giesen. *Thin disk laser: power scaling to the kW regime in fundamental mode operation*. In W. A. Clarkson, W. Hodgson, and R. Shori, eds., *Solid State Lasers XVIII: Technology and Devices*, vol. 7193 of *Proc. SPIE* (2009), [doi:10.1117/12.809031].

[172] M. Okrusch and S. Matthes. *Mineralogie, 2009; Eine Einführung in die spezielle Mineralogie, Petrologie und Lagerstättenkunde*. Springer Verlag, Berlin Heidelberg (2009), [doi:10.1007/978-3-642-34660-6].

[173] K. Wentsch. *Analyse Ytterbium-dotierter Materialien für den Einsatz in ultrakurzgepulsten Scheibenlasersystemen*. Ph.D. thesis, Universität Stuttgart (2016).

[174] J.-H. Wolter, M. Abdou Ahmed, and T. Graf. *Thin-disk laser operation of Ti:sapphire*. Opt. Lett. **42** (8), 1624–1627 (2017), [doi:10.1364/OL.42.001624].

[175] A. Diebold, Z. Jia, I. J. Graumann, Y. Yin, F. Emaury, C. J. Saraceno, X. Tao, and U. Keller. *High-power Yb:GGG thin-disk laser oscillator: first demonstration and power-scaling prospects*. Opt. Exp. **25** (2), 1452–146 (2017), [doi:10.1364/OE.25.001452].

[176] K. Beil, S. T. Fredrich-Thornton, F. Tellkamp, R. Peters, C. Kränkel, K. Petermann, and G. Huber. *Thermal and laser properties of Yb:LuAG for kW thin disk lasers*. Opt. Exp. **18** (20), 20712–20722 (2010), [doi:10.1364/OE.18.020712].

[177] T. Dietrich, S. Piehler, M. Rumpel, P. Villeval, D. Lupinski, M. Abdou-Ahmed, and T. Graf. *Highly-efficient continuous-wave intra-cavity frequency-doubled Yb:LuAG thin-disk laser with 1 kW of output power*. Opt. Exp. **25** (5), 4917–4925 (2017), [doi:10.1364/OE.25.004917].

[178] Y. H. Peng, J. Cheng, Y. Y. Cheah, K. S. Lai, E. Lau, and S. K. Ang. *High brightness continuous wave ceramic Yb:LuAG thin-disk laser*. Opt. Exp. **23** (15), 19618–19623 (2015), [doi:10.1364/OE.23.019618].

[179] W. H. Zachariasen. *Untersuchungen über die Kristallstrukturen von Sesquioxiden und Verbindungen ABO_3*. Geologiska Foereningan i Stockholm. Foerhandlingar **51** (1), 123–123 (1929), [doi:10.1080/11035892909447062].

[180] R. Peters. *Ytterbium-dotierte Sesquioxide als hocheffiziente Lasermaterialien*. Ph.D. thesis, Universität Hamburg, Hamburg (2009).

[181] S. Hunklinger. *Festkörperphysik*. Oldenbourg Wissenschaftsverlag (2009). ISBN 9783486596410.

[182] E. Mix. *Kristallzüchtung, Spektroskopie und Lasereigenschaften Yb-dotierter Sesquioxide*. Ph.D. thesis, Universität Hamburg (1999).

[183] J. P. Hurrell, S. P. S. Porto, I. F. Chang, S. S. Mitra, and R. P. Bauman. *Optical Phonons of Yttrium Aluminum Garnet*. Phys. Rev. **173** (3), 851–856 (1968), [doi:10.1103/PhysRev.173.851].

[184] N. P. Padture and P. G. Klemens. *Low Thermal Conductivity in Garnets*. J. Am. Ceram. Soc. **80** (4), 1018–1020 (1997), [doi:10.1111/j.1151-2916.1997.tb02937.x].

[185] R. S. Krishnan, R. Srinivasan, and S. Devanarayanan. *Thermal Expansion of Crystals*. International Series in The Science of The Solid State. Elsevier (2013). ISBN 1483158071.

[186] T. Y. Fan, T. Crow, and B. Hoden. *Cooled Yb:YAG for high-power solid state lasers*. [doi:10.1117/12.323939].

[187] D. S. Sumida and T. Y. Fan. *Emission Spectra and Fluorescence Lifetime Measurements of Yb:YAG as a Function of Temperature*. In *Advanced Solid State Lasers*, YL4. Optical Society of America (1994), [doi:10.1364/ASSL.1994.YL4].

[188] K. Wang and R. R. Reeber. *Thermal expansion of copper*. High Temp. Mat. Sci. **35** (2) (1996).

[189] K. Wang and R. R. Reeber. *The role of defects on thermophysical properties: thermal expansion of V, Nh, Ta, Mo and W*. Mater. Sci. Eng. R. Rep. **23** (3), 101–137 (1998), [doi:10.1016/S0927-796X(98)00011-4].

[190] R. R. Reeber and K. Wang. *Thermal expansion, molar volume and specific heat of diamond from 0 to 3000K*. J. Electron. Mater. **25** (1), 63–67 (1996), [doi:10.1007/BF02666175].

[191] R. R. Reeber and K. Wang. *Lattice Parameters and Thermal Expansion of Important Semiconductors and Their Substrates*. MRS Proceedings **622**, T6.35.1 (2000), [doi:10.1557/PROC-622-T6.35.1].

[192] L. Gmelin. *Gmelin Handbuch der anorganischen Chemie: Seltenerdelemente, vol. C1*. Springer Verlag, Berlin (1974).

[193] R. Schödel, A. Walkov, M. Zenker, G. Bartl, R. Meeß, D. Hagedorn, C. Gaiser, G. Thummes, and S. Heltzel. *A new Ultra Precision Interferometer for absolute length measurements down to cryogenic temperatures*. Meas. Sci. Technol. **23** (9), 094004 (2012), [doi:10.1088/0957-0233/23/9/094004].

[194] P. A. Loiko, K. V. Yumashev, R. Schödel, M. Peltz, C. Liebald, X. Mateos, B. Deppe, and C. Kränkel. *Thermo-optic properties of Yb:Lu_2O_3 single crystals*. Appl. Phys. B **120** (4), 601–607 (2015), [doi:10.1007/s00340-015-6171-4].

[195] A. Fluegel. *Global model for calculating room-temperature glass density from the composition*. J. Am. Ceram. Soc. **90** (8), 2622–2625 (2007), [doi:10.1111/j.1551-2916.2007.01751.x].

[196] I. Moreno, J. J. Araiza, and M. Avendano-Alejo. *Thin-film spatial filters*. Opt. Lett. **30** (8), 914–916 (2005), [doi:10.1364/OL.30.000914].

[197] E. W. Marchand and H. Nishihara. *Gradient-index optics: introduction by the feature editors*. Appl. Opt. **29** (28), 3991– (1990), [doi:10.1364/AO.29.003991].

[198] D. E. Zelmon, J. M. Northridge, N. D. Haynes, D. Perlov, and K. Petermann. *Temperature-dependent Sellmeier equations for rare-earth sesquioxides*. Appl. Opt. **52** (16), 3824–3828 (2013), [doi:10.1364/AO.52.003824].

[199] U. Schlarb and K. Betzler. *Refractive indices of lithium niobate as a function of temperature, wavelength, and composition: A generalized fit*. Phys. Rev. B **48** (21), 15613–15620 (1993), [doi:10.1103/PhysRevB.48.15613].

[200] N. D. Haynes and D. E. Zelmon. *Optical and spectroscopic properties of Ytterbium-doped YAG*. In W. A. Clarkson and R. Shori, eds., *Solid State Lasers XXII: Technology and Devices*, vol. 4760 of *Proc. SPIE* (2013), [doi:10.1117/12.2000069].

[201] R. L. Aggarwal, D. J. Ripin, J. R. Ochoa, and T. Y. Fan. *Measurement of thermo-optic properties of $Y_3Al_5O_{12}$, $Lu_3Al_5O_{12}$, $YAlO_3$, $LiYF_4$, $LiLuF_4$, BaY_2F_8, $KGd(WO_4)_2$, and $KY(WO_4)_2$ laser crystals in the 80-300 K temperature range*. J. Appl. Phys. **98** (1),

103514 (2005), [doi:10.1063/1.2128696].

[202] G. A. Bogomolova, D. N. Vylegzhanin, and A. A. Kaminskii. *Spectral and lasing investigations of garnets with Yb^{3+} ions*. Sov. Phys. JETP **42**, 440–446 (1976).

[203] G. Liu and B. Jacquier. *Spectroscopic Properties of Rare Earths in Optical Materials*, vol. 83 of *Springer Series in Materials Science*. Springer Verlag, Berlin/Heidelberg (2006). ISBN 3540282092, [doi:10.1007/3-540-28209-2].

[204] C. H. Peng, H. T. Liu, K. T. Wu, Y. F. Chen, H. Chou, I. M. Jiang, and W. S. Tse. *Structural properties of host laser single crystal Yb:YAG*. Opt. Comm. **284** (21), 5164–5166 (2011), [doi:10.1016/j.optcom.2011.07.020].

[205] V. Peters. *Growth and spectroscopy of ytterbium doped sesquioxides*. Ph.D. thesis, Universität Hamburg (2001).

[206] Y. Guyot, M. Guzik, G. Alombert-Goget, J. Pejchal, A. Yoshikawa, A. Ito, T. Goto, and G. Boulon. *Assignment of Yb^{3+} energy levels in the C_2 and C_{3i} centers of Lu_2O_3 sesquioxide either as ceramics or as crystal*. J. Lumin. **170**, 513–519 (2016), [doi:10.1016/j.jlumin.2015.04.017].

[207] H. Kühn, S. T. Fredrich-Thornton, C. Kränkel, R. Peters, and K. Petermann. *Model for the calculation of radiation trapping and description of the pinhole method*. Opt. Lett. **32** (13), 1908–1910 (2007), [doi:10.1364/OL.32.001908].

[208] P. F. Moulton. *Spectroscopic and laser characteristics of Ti:Al_2O_3*. J. Opt. Soc. Am. B **3**, 125–133 (1986), [doi:10.1364/JOSAB.3.000125].

[209] T. Numai. *Fundamentals of Semiconductor Lasers*, vol. 93 of *Springer Series in Optical Sciences*. Springer Verlag, Tokyo (2014). ISBN 4431551484, [doi:10.1007/978-4-431-55148-5].

[210] W. W. Chow and S. W. Koch. *Semiconductor-Laser Fundamentals*. Physics of the Gain Materials. Springer Verlag, Berlin, Heidelberg (2013). ISBN 3662038803, [doi:10.1007/978-3-662-03880-2].

[211] P. Schmitz (LAYERTEC). personal communication (2015).

[212] E. Palik. *Handbook of Optical Constants of Solids*. Academic Press, San Diego CA (1998). ISBN 9780125444156, [doi:10.1016/B978-0-08-054721-3.50036-8].

[213] A. Voss, M. Huonker, and C. Schmitz. *EU Patent EP 1 178 579 A2: Laserverstärkeranordnung* (2001).

[214] C. R. E. Baer, O. H. Heckl, C. J. Saraceno, C. Schriber, C. Kränkel, T. Südmeyer, and U. Keller. *Frontiers in passively mode-locked high-power thin disk laser oscillators*. Opt. Exp. **20** (7), 7054–7065 (2012), [doi:10.1364/OE.20.007054].

[215] R. G. Lane and M. Tallon. *Wave-front reconstruction using a Shack–Hartmann sensor*. Appl. Opt. **31** (32), 6902 (1992), [doi:10.1364/AO.31.006902].

[216] B. C. Platt and R. Shack. *History and principles of Shack-Hartmann wavefront sensing*. J. Refract. Surg. **17** (5), 573–577 (2001).

[217] S. Awel, R. A. Kirian, N. Eckerskorn, M. Wiedorn, D. A. Horke, A. V. Rode, J. Küpper, and H. N. Chapman. *Visualizing aerosol-particle injection for diffractive-imaging experiments*. Opt. Exp. **24** (6), 6507–6521 (2016), [doi:10.1364/OE.24.006507], arxiv:1512.06231 [physics] .

[218] J. Guttman, J. Fleischer, and M. Minshall. *Beam scattering laser monitor* (2013). US Patent App. 13/636,339.

[219] D. Van Thourhout and J. Roels. *Optomechanical device actuation through the optical gradient force*. Nat. Photon. **4** (4), 211–217 (2010), [doi:10.1038/nphoton.2010.72].

[220] C. Savage. *Introduction to Light Forces, Atom Cooling, and Atom Trapping*. Aust. J. Phys. **49** (4), 745–7644 (1996), [doi:10.1071/PH960745].

[221] T. Graf and J. E. Balmer. *Laser beam quality, entropy and the limits of beam shaping*. Opt. Comm. **131** (1-3), 77–83 (1996), [doi:10.1016/0030-4018(96)00249-0].

[222] L. W. Hillman, J. Krasinski, J. A. Yeazell, and C. R. Stroud. *Intracavity power measurement by Rayleigh scattering*. Appl. Opt. **22** (22), 3474 (1983), [doi:10.1364/AO.22.003474].

[223] Y. H. Peng, Y. X. Lim, J. Cheng, Y. Guo, Y. Y. Cheah, and K. S. Lai. *Near fundamental mode 1.1 kW Yb:YAG thin-disk laser*. Opt. Lett. **38** (10), 1709–1711 (2013), [doi:10.1364/OL.38.001709].

[224] V. Magni. *Multielement stable resonators containing a variable lens*. J. Opt. Soc. Am. A **4** (1), 1962–1969 (1987), [doi:10.1364/JOSAA.4.001962].

[225] K. Mikami, K. A. Tanaka, M. Fujita, S. Motokoshi, T. Jitsuno, and T. Somekawa. *Temperature dependence of laser-induced damage threshold of optical coatings at different pulse widths*. Opt. Exp. **21** (23), 28719–28728 (2013), [doi:10.1364/OE.21.028719].

[226] FLIR Systems. *ThermaCAM Researcher Pro Manual* (2010).

[227] J. A. King. *Materials Handbook for Hybrid Microelectronics*. Artech House (1988). ISBN 0890063257.

[228] X. Xu, Z. Zhao, P. Song, B. Jiang, G. Zhou, J. Xu, P. Deng, G. Bourdet, J. Christophe Chanteloup, J.-P. Zou, and A. Fulop. *Upconversion luminescence in Yb^{3+}-doped yttrium aluminum garnets*. Physica B Condens. Matter **357** (3-4), 365–369 (2005), [doi:10.1016/j.physb.2004.11.088].

[229] R. J. Tench, R. Chow, and M. R. Kozlowski. *Characterization of defect geometries in multilayer optical coatings*. J. Vac. Sci. Technol. **12** (5), 2808–2813 (1994), [doi:10.1364/AO.36.001867].

[230] T. Y. Fan. *Aperture guiding in quasi-three-level lasers*. Opt. Lett. **19** (8), 554–556 (1994), [doi:10.1364/OL.19.000554].

[231] M. C. Gupta and J. Ballato. *The Handbook of Photonics, Second Edition*. CRC Press (2006). ISBN 1420004697.

[232] P. Barriga, B. Bhawal, L. Ju, and D. G. Blair. *Numerical calculations of diffraction losses in advanced interferometric gravitational wave detectors*. J. Opt. Soc. Am. A **24** (6), 1731–1741 (2007), [doi:10.1364/JOSAA.24.001731].

[233] J. Degallaix. *OSCAR a Matlab based optical FFT code*. J. Phys.: Conf. Ser. **228** (1), 012021 (2010), [doi:10.1088/1742-6596/228/1/012021].

[234] M. L. Grilli, T. Aumann, D. Ristau, M. Dieckmann, F. von Alvensleben, and E. Masetti. *Thermal conductivity of e-beam and IBS coatings*. In *Specification, Production, and Testing of Optical Components and Systems*, vol. 2775 of *Proc. SPIE* (1996), [doi:10.1117/12.246766].

[235] R. Kitamura, L. Pilon, and M. Jonasz. *Optical constants of silica glass from extreme ultraviolet to far infrared at near room temperature*. Appl. Opt. **46** (33), 8118–8133

(2007), [doi:10.1364/AO.46.008118].

[236] C. Stewen. *Scheibenlaser mit Kilowatt-Dauerstrichleistung*. Ph.D. thesis, Universität Stuttgart (2000).

[237] I. Moshe, S. Jackel, and A. Meir. *Production of radially or azimuthally polarized beams in solid-state lasers and the elimination of thermally induced birefringence effects*. Opt. Lett. **28** (10), 807–809 (2003), [doi:10.1364/OL.28.000807].

[238] O. Puncken, H. Tünnermann, J. J. Morehead, P. Weßels, M. Frede, J. Neumann, and D. Kracht. *Intrinsic reduction of the depolarization in Nd:YAG crystals*. Opt. Exp. **18** (19), 20461–20474 (2010), [doi:10.1364/OE.18.020461].

[239] C. J. Saraceno, F. Emaury, O. H. Heckl, C. R. E. Baer, M. Hoffmann, C. Schriber, M. Golling, T. Südmeyer, and U. Keller. *275 W of output power from a femtosecond thin disk oscillator operated in a vacuum environment*. Opt. Exp. **20** (21), 23535–23541 (2012), [doi:10.1364/OE.20.023535].

[240] B. Weichelt, D. Blazquez-Sanchez, A. Austerschulte, A. Voss, T. Graf, and A. Killi. *Improving the brightness of a multi-kW thin disk laser with a single disk by an aspherical phase-front correction*. 77210M. [doi:10.1117/12.854549].

[241] S.-S. Schad, V. Kuhn, T. Gottwald, V. Negoita, A. Killi, and K. Wallmeroth. *Near fundamental mode high-power thin-disk laser*. [doi:10.1117/12.2046689].

[242] S.-S. Schad, T. Gottwald, V. Kuhn, M. Ackermann, D. Bauer, M. Scharun, and A. Killi. *Recent development of disk lasers at TRUMPF*. 972615. [doi:10.1117/12.2212789].

[243] H. Kogelnik, E. Ippen, A. Dienes, and C. Shank. *Astigmatically compensated cavities for CW dye lasers*. IEEE J. Quantum. Electron. **8** (3), 373–379 (1972), [doi:10.1109/JQE.1972.1076964].

[244] W. Qiao, L. Guowen, Z. Xiaojun, L. Zongsen, W. Yonggang, L. Ji, and N. Hanben. *Exact Analytical Solution for the Mutual Compensation of Astigmatism Using Curved Mirrors in a Folded Resonator Laser*. IEEE Photon. J. **6** (6), 1–13 (2014), [doi:10.1109/JPHOT.2014.2366160].

[245] H. J. Loesch. *Orientation and alignment in reactive beam collisions - recent progress*. Annu. Rev. Phys. Chem. **46**, 555–594 (1995), [doi:10.1146/annurev.pc.46.100195.003011].

[246] B. Friedrich and D. Herschbach. *Alignment and Trapping of Molecules in Intense Laser Fields*. Phys. Rev. Lett. **74** (23), 4623–4626 (1995), [doi:10.1103/PhysRevLett.74.4623].

[247] R. Grimm, M. Weidemüller, and Y. B. Ovchinnikov. *Optical Dipole Traps for Neutral Atoms*. In *Advances In Atomic, Molecular, and Optical Physics*, vol. 42, 95–170. Elsevier (2000), [doi:10.1016/S1049-250X(08)60186-X].

[248] A. Ashkin. *Acceleration and Trapping of Particles by Radiation Pressure*. Phys. Rev. Lett. **24** (4), 156–159 (1970), [doi:10.1103/PhysRevLett.24.156].

[249] N. Eckerskorn, L. Li, R. A. Kirian, J. Küpper, D. P. DePonte, W. Krolikowski, W. M. Lee, H. N. Chapman, and A. V. Rode. *Hollow Bessel-like beam as an optical guide for a stream of microscopic particles*. Opt. Exp. **21** (25), 30492–30499 (2013), [doi:10.1364/OE.21.030492].

[250] T. Mazza, M. Ilchen, A. J. Rafipoor, C. Callegari, P. Finetti, O. Plekan, K. C. Prince, R. Richter, M. B. Danailov, A. Demidovich, G. De Ninno, C. Grazioli, R. Ivanov,

N. Mahne, L. Raimondi, C. Svetina, L. Avaldi, P. Bolognesi, M. Coreno, P. O'Keeffe, M. Di Fraia, M. Devetta, Y. Ovcharenko, T. Möller, V. Lyamayev, F. Stienkemeier, S. Düsterer, K. Ueda, J. T. Costello, A. K. Kazansky, N. M. Kabachnik, and M. Meyer. *Determining the polarization state of an extreme ultraviolet free-electron laser beam using atomic circular dichroism*. Nat. Commun. **5**, 3648 (2014), [doi:10.1038/ncomms4648].

[251] H. S. Yoder and M. L. Keith. *Complete substitution of aluminium for silicon-the system 3MNO. AL_2O_3. $3SIO_2$-$3Y_2O_3$. $5AL_2O_3$*. Am. Miner. **36**, 519–533 (1950).

[252] L. Pauling and M. D. Shappell. *8. The Crystal Structure of Bixbyite and the C-Modification of the Sesquioxides*. Z. Kristallog. – Cryst. Mater. **75** (1), 128–142 (1930), [doi:10.1515/zkri-1930-0109].

[253] T. Böttger, C. W. Thiel, R. L. Cone, Y. Sun, and A. Faraon. *Optical spectroscopy and decoherence studies of Yb^{3+}:YAG at 968 nm*. Phys. Rev. B **94** (4), 045134 (2016), [doi:10.1103/PhysRevB.94.045134].

[254] F. Euler and J. A. Bruce. *Oxygen coordinates of compounds with garnet structure*. Acta Cryst. A **19** (6), 971–978 (1965), [doi:10.1107/S0365110X65004747].

[255] A. A. Kaminskii. *Laser Crystals*. Their Physics and Properties. Springer Verlag (2013). ISBN 3540707492.

[256] L. Dobrzycki, E. Bulska, D. A. Pawlak, Z. Frukacz, and K. Woźniak. *Structure of YAG crystals doped/substituted with erbium and ytterbium*. Inorg. Chem. **43** (24), 7656–7664 (2004), [doi:10.1021/ic049920z].

[257] R. D. Shannon. *Revised effective ionic radii and systematic studies of interatomic distances in halides and chalcogenides*. Acta Cryst. A **32** (5), 751–767 (1976), [doi:10.1107/S0567739476001551].

[258] W. Schumann. *Minerals of the World*. Sterling (2008). ISBN 140275339X.

[259] V. Peters, A. Bolz, K. Petermann, and G. Huber. *Growth of high-melting sesquioxides by the heat exchanger method*. J. Cryst. Growth **237-239**, 879–883 (2002), [doi:10.1016/S0022-0248(01)02054-1].

[260] J. L. Caslavsky and D. J. Viechnicki. *Melting behaviour and metastability of yttrium aluminium garnet (YAG) and $YAlO_3$ determined by optical differential thermal analysis*. J. Mater. Sci. **15** (7), 1709–1718 (1980), [doi:10.1007/BF00550589].

[261] H. Mun, A. Jouini, A. Yoshikawa, and J. H. Kim. *Thermal and optical properties of Yb-doped Lu_2O_3 single crystal grown by the micro-pulling-down method*. J. Ceram. Process. Res. **14** (5), 636–640 (2013), [doi:10.1364/JOSAB.21.000543].

[262] H. Qiu, P. Yang, J. Dong, P. Deng, J. Xu, and W. Chen. *The influence of Yb concentration on laser crystal Yb:YAG*. Mater. Lett. **55** (1-2), 1–7 (2002), [doi:10.1016/S0167-577X(01)00608-5].

[263] Y. Sato and T. Taira. *Highly accurate interferometric evaluation of thermal expansion and dn/dT of optical materials*. Opt. Mat. Exp. **4** (5), 876–888 (2014), [doi:10.1364/OME.4.000876].

[264] S. Kostić, Z. Ž. Lazarević, V. Radojević, A. Milutinović, M. Romčević, N. Ž. Romčević, and A. Valčić. *Study of structural and optical properties of YAG and Nd:YAG single crystals*. Mater. Res. Bull. **63**, 80–87 (2015), [doi:10.1016/j.materresbull.2014.11.033].

[265] R. Peters, C. Kränkel, K. Petermann, and G. Huber. *Broadly tunable high-power Yb:Lu_2O_3 thin disk laser with 80 % slope efficiency*. Opt. Exp. **15** (11), 7075–7082 (2007), [doi:10.1364/OE.15.007075].

List of Publications

Publications in scientific journals

- I. J. Graumann, A. Diebold, C. G. E. Alfieri, F. Emaury, B. Deppe, M. Golling, D. Bauer, D. Sutter, C. Kränkel, C. J. Saraceno, C. R. Phillips, and U. Keller. *Peak-power scaling of femtosecond Yb:Lu_2O_3 thin-disk lasers.* Optics Express **25** (19), 22519 - 22536 (2017).
- C. Paradis, N. Modsching, V. J. Wittwer, B. Deppe, C. Kränkel, and T. Südmeyer. *Generation of 35-fs pulses from a Kerr lens mode-locked Yb:Lu_2O_3 thin-disk laser.* Optics Express **25** (13), 14918 - 14925 (2017).
- B. Deppe, G. Huber, C. Kränkel, and J. Küpper. *High-intracavity-power thin-disk laser for the alignment of molecules.* Optics Express **23** (22), 28491 - 28500 (2015).
- K. Hasse, T. Calmano, B. Deppe, C. Liebald, and C. Kränkel. *Efficient Yb^{3+}:$CaGdAlO_4$ bulk and femtosecond laser-written waveguide lasers.* Optics Letters **40** (15), 3552 - 3555 (2015).
- P. A. Loiko, K. V. Yumashev, R. Schödel, M. Peltz, C. Liebald, X. Mateos, B. Deppe, and C. Kränkel. *Thermo-optic properties of Yb:Lu_2O_3 single crystals.* Applied Physics B **120** (4), 601 - 607 (2015).
- K. Beil, B. Deppe, and C. Kränkel. *Yb:$CaGdAlO_4$ thin-disk laser with 70% slope efficiency and 90 nm wavelength tuning range.* Optics Letters **38** (11), 1966-1968 (2013).

Contributions to international conferences

- C. Paradis, N. Modsching, F. Labaye, M. Gaponenko, F. Emaury, A. Diebold, I. Graumann, B. Deppe, C. Kränkel, V. J. Wittwer, and T. Südmeyer. *Kerr lens mode-locked thin-disk lasers delivering 30-fs pulses from Yb:CALGO and 35-fs pulses from Yb:Lu_2O_3.* Ultrafast Optics Conference XI, Jackson Hole, USA, (2017).
- C. Paradis, N. Modsching, M. Gaponenko, F. Labaye, F. Emaury, A. Diebold, I. Graumann, B. Deppe, C. Kränkel, V. J. Wittwer, and T. Südmeyer. *Sub-50-fs Kerr Lens Mode-Locked thin-Disk Lasers.* Conference on Lasers and Electro-Optics (CLEO/Europe-EQEC), Munich, Germany, post deadline talk PD-1.4 (2017).

- N. Modsching, C. Paradis, V. J. Wittwer, B. Deppe, C. Kränkel, and T. Südmeyer. *64-fs pulses from a Kerr-lens modelocked Yb:LuO thin-disk laser.* Conference on Lasers and Electro-Optics (CLEO/Europe-EQEC), Munich, Germany, talk CA-7.1 (2017).
- I. J. Graumann, A. Diebold, F. Emaury, B. Deppe, C. R. Phillips, M. Golling, D. Bauer, P. Heu, D. Follmann, G. D. Cole, M. Aspelmeyer, D. Sutter, C. Kränkel, C. J. Saraceno, and U. Keller. *Peak-power scaling of femtosecond SESAM-modelocked Yb:Lu_2O_3 thin-disk lasers.* Conference on Lasers and Electro-Optics (CLEO/Europe-EQEC), Munich, Germany, talk CF-5.4 (2017).
- C. Paradis, N. Modsching, V. J. Wittwer, B. Deppe, C. Kränkel, T. Südmeyer. *128-fs Pulses from a Kerr-Lens Modelocked Yb:LuO Thin-Disk Laser.* Conference on Lasers and Electro-Optics (CLEO2017), San Jose, USA, talk SM1I.3 (2017).
- I. Graumann, A. Diebold, F. Emaury, B. Deppe, C. Kränkel, C. Saraceno, and U. Keller. *High-power modelocked Yb:Lu_2O_3 thin-disk laser with 10-MW sub-500 fs pulses.* Advanced Solid-State Lasers Conference, Boston, USA, talk ATU1A.3 (2016).
- C. Kränkel, B. Deppe, G. Huber, and J. Küpper. *Megawatt continuous wave intracavity power thin disk laser for the alignment of molecules.* Conference on Advanced Laser Technologies (ALT'16), Galway, Ireland, talk LSM-3-3 (invited) (2016).
- I. J. Graumann, A. Diebold, F. Emaury, B. Deppe, C. Kränkel, C. J. Saraceno, and U. Keller. *10-MW sub-500 fs high power SESAM-modelocked Yb:Lu_2O_3 thin disk laser.* 7th EPS-QEOD Europhoton Conference, Vienna, Austria, talk 32.2 (invited) (2016).
- B. Deppe, G. Huber, C. Kränkel, and J. Küpper. *High intracavity power thin-disk lasers for continuous-wave strong alignment of molecules.* IEEE Photonics Conference (IPC), Reston, USA, talk MB2.2 (2016).
- B. Kreipe, J. R. Cardoso de Andrade, B. Deppe, C. Kränkel, and U. Morgner. *160 fs pulses from a Kerr-lens mode-locked Yb^{3+}:Lu_2O_3 thin-disk oscillator.* 7th EPS-QEOD Europhoton Conference, Vienna, Austria, poster 25.30 (2016).
- B. Deppe, G. Huber, J. Küpper, and C. Kränkel. *Thin-disk lasers with high intracavity power for the continuous alignment of molecules.* Conference on Lasers and Electro-Optics (CLEO/Europe-EQEC), Munich, Germany, talk CA-7.2 (2015).
- K. Hasse, B. Deppe, C. Kränkel, and T. Calmano. *Femtosecond-laser-written Yb^{3+}:$CaAlGdO_4$ waveguide laser.* Conference on Lasers and Electro-Optics (CLEO/Europe-EQEC), Munich, Germany, talk CJ-6a.2 (2015).
- S. Trippel, T. Mullins, N. L. M. Müller, J. Kienitz, B. Deppe, J. Wiese, C. Kränkel, R. González Férez, and J. Küpper. *Controlled molecules to investigate ultrafast chemical dynamics directly in the molecular frame.* Femto 12, Hamburg, Germany, poster P1-22 (2015).
- C. Kränkel, K. Hasse, B. Deppe. *Czochralski growth of high quality CALGO.* French-German Workshop on Oxide/Laser Crystals, Idar-Oberstein, Germany, talk Fr3 (2014).

- C. Kränkel, K. Beil, B. Deppe, and K. Petermann. *Growth by the heat exchanger method and laser operation of rare-earth doped sesquioxides.* 6th International Workshop on Crystal Growth Technology, Berlin, Germany, talk S2 / oral 2 (invited) (2014).
- K. Beil, B. Deppe, and C. Kränkel. *Broadly tunable Yb:CALGO thin disk laser with high efficiency.* Advanced Solid-State Lasers Conferenc, Paris, France, talk AF3A.1 (2013).
- K. Beil, B. Deppe, and C. Kränkel. *Yb:$CaGdAlO_4$ thin disk laser with 70 % slope efficiency.* Conference on Lasers and Electro-Optics (CLEO/Europe-EQEC), Munich, Germany, talk CA-5.3 (2013).
- B. Deppe, A. Heuer, K. Beil, C. Kränkel, and G. Huber. *Broadly tunable OPS pumped Yb:CALGO laser.* 5th EPS-QEOD Europhoton Conferenc, Stockholm, Sweden, talk FrA.9 (2012).

Contributions to national conferences

- B. Deppe, G. Huber, J. Küpper and C. Kränkel. *Toward multi-MW continuous-wave intracavity power lasers for the alignment of molecules.* Frühjahrstagung der Deutschen Physikalischen Gesellschaft, Hanover, Germany, talk MO21.3 (2016).
- K. Hasse, B. Deppe, T. Calmano, and C. Kränkel. *Efficient Yb:$CaGdAlO_4$ bulk and waveguide lasers.* Frühjahrstagung der Deutschen Physikalischen Gesellschaft, Heidelberg, Germany, talk Q30.4 (2015).
- B. Deppe, G. Huber, J. Küpper, and C. Kränkel. *High finesse thin-disk laser for adiabatic alignment of molecules.* Frühjahrstagung der Deutschen Physikalischen Gesellschaft, Heidelberg, Germany, talk Q30.2 (2015).
- B. Deppe, G. Huber, J. Küpper, and C. Kränkel. *High intracavity power thin-disk lasers for the continuous alignment of molecules.* CUI Symposium , Hamburg, poster (2015).
- B. Deppe, K. Beil, G. Huber, and J. Küpper. *Yb:Lu_2O_3 thin disk laser for intracavity cw-alignment of molecules.* Frühjahrstagung der Deutschen Physikalischen Gesellschaft, Berlin, Germany, poster Q 30.55 (2014).
- B. Deppe, K. Beil, C. Kränkel, G. Huber, and J. Küpper. *High-intracavity-power lasers for molecule alignment.* Frühjahrstagung der Deutschen Physikalischen Gesellschaft, Hannover, Germany, poster MO 19.12 (2013).
- B. Deppe, K. Beil, C. Kränkel, and G. Huber. *Yb:$CaGdAlO_4$ und Yb:$SrAl_{12}O_{19}$ als breitbandig emittierende Lasermaterialien.* Frühjahrstagung der Deutschen Physikalischen Gesellschaft, Stuttgart, Germany, talk Q18.7 (2012).

Statutory declaration

I hereby declare in lieu of an oath that I have independently completed the above thesis. The thoughts taken directly or indirectly from external sources are properly marked as such. This thesis has not previously been submitted to another academic institution or published elsewhere. The submitted written version is identical to the one on the submitted electronic storage device. Furthermore, I give my permission for publication of this thesis.

Hiermit bestätige ich, dass die vorliegende Arbeit von mir selbständig verfasst wurde und ich keine anderen als die angegebenen Hilfsmittel – insbesondere keine im Quellenverzeichnis nicht benannten Internet-Quellen – benutzt habe und die Arbeit von mir vorher nicht einem anderen Prüfungsverfahren eingereicht wurde. Die eingereichte schriftliche Fassung entspricht der auf dem elektronischen Speichermedium. Ich bin damit einverstanden, dass diese Arbeit veröffentlicht wird.

Ort, Datum Unterschrift (Vor- und Nachname)